Arrayed functional genomic screening of Parkinson's disease candidate risk genes identifies modifiers of α-synuclein aggregation and mitophagy in human neurons



Rachel Heon-Roberts

Lady Margaret Hall

Department of Physiology, Anatomy and Genetics

University of Oxford

A thesis submitted for the degree of

Doctor of Philosophy

Trinity 2025

To my family, Caroline, Simon and Sam

Abstract

Parkinson's disease is an age-related neurodegenerative disease, characterised by the death of neurons in the substantia nigra and other brains regions such as the cortex in late-stage disease. Lewy bodies and Lewy neurites composed of the aggregated pre-synaptic protein α-synuclein are a diagnostic finding in affected brain regions at autopsy. This aggregation process is thought to cause neuronal dysfunction, contributing to cell death in substantial part through impairing the function of organelles such as the mitochondria. Environmental toxins targeting mitochondria or mutations in the mitophagy-associated proteins PINK1 and PRKN can also cause PD.

Treatment of human iPSC-derived cortical neurons with *in vitro* aggregated α-synuclein pre-formed fibrils modelled α-synuclein aggregation, triggering the aggregation of endogenous monomer. Using up-to-date methodology significantly reduced batch-to-batch variability and increased the robustness of PFF-induced α-synuclein aggregation in cell models, though these improvements were only weakly correlated with measured parameters such as fibril length, suggesting unknown factors influence a preparation's aggregation efficacy. CRISPRi-mediated knockdown of *SNCA* abolished PFF-seeded aggregation in human iPSC-derived cortical neurons, confirming that endogenous monomer is required for the process of aggregation. In addition, co-localisation of the mitochondrial mitophagy marker phospho-serine 65 ubiquitin (pS65Ub) and pathological α-synuclein aggregates marked by phosphorylation at serine 129 (pS129) was found in PFF-treated neurons. This association was influenced by aggregate size and time post-seeding, suggesting a pathological cascade where α-synuclein aggregation results in accumulation of pS65Ub.

Recent studies have demonstrated a contribution of 134 risk loci to the development of PD. The mechanism by which these genes increase disease risk is undefined and we hypothesised that these genes might regulate the rate of α-synuclein aggregation or impede the process of mitochondrial autophagy. A library of 71 candidate risk and 4 monogenic PD genes was screened in iPSC-derived cortical neurons and validated in iPSC-derived dopaminergic neurons, identifying several novel and previously-published genes which may modulate the levels of α-synuclein aggregation or of the

mitophagy marker phospho-serine 65 ubiquitin. Understanding the underlying mechanisms of risk gene contribution to disease aetiology is expected to enable idiopathic patient stratification and personalised medicine.

Acknowledgements

There are a large number of people I would like to thank, as without their advice, help, support or encouragement, the journey to completion of my PhD would have been far more arduous than it already was.

First, thank you to Dr Brent Ryan for your unwavering support and supervision, and for giving me the opportunity to tackle this challenge. I have learnt so much through your guidance, your scientific excellence, your unrelenting dedication, ambition and belief in all of us who you supervise. I would also like to thank Prof Richard Wade-Martins for your support, and for providing a path to come to Oxford when, due to lack of funding, I was unable to take up a place on the Master's degree course. It is safe to say that I would not be here today without you.

Second, thank you to the people who have enriched my journey with their friendship and support. Millie Smith, Sarah Franks, Dr Elena Britti and Dr Kalina Naidoo, your friendship has been and will forever be treasured. You are all fantastic friends and wonderful colleagues. Thank you also to Dr Maria Claudia Caiazza and Dr Naroa Ibarra-Aizpurua for being amazing friends as well as colleagues and for your endless support, kindness and advice – that has meant so much. I'd like to especially thank Cassandra Rose, Ida Derish, Alex Laskaris, Marie-Ève Cloutier, Félix Breton, David Derish, Geneviève Leblanc, Daphné Chabot and Léonie Lampron-Nadeau for your love and support from afar. Thank you to Dr Sarah Pearce for bringing the fun wherever you go, as well as for all your help and support. Thank you to Féodora Bertherat, Johanna Hoffmann for all the fantastic chats; the support from both of you has been far more meaningful than you realise. Dr Benjamin Vallin and Dr Camille Loiseau, thank you for your friendship and making me practice my French. Thank you also, in no particular order and amongst a large number of people who I cannot all name, to Anna Lavayssière, Dr Billy McGuinness, Victoria Lievens, Sandor Szunyogh, Katrina Savory, Martha Lavelle, Lorraine Dyson, Katie Thomas, Iona Thomas-Wright, Akansha Mehta, Aishwarya Vedula, and Dr Ajantha Abey, who made our lab environment a friendly place to work.

Thank you in particular to Brian and Debbie Walter for fantastic conversation, infinitely-appreciated love and support, as well as for your help in my times of need. Spending time with you has been one of the highlights of my time at Oxford.

An immense thank you goes, of course, to my family – my mother Caroline, my father Simon and my brother Samuel – I would not have believed in my ability to undertake this had you not believed in me first. Your support and unconditional love have been the single most influential factors in my life.

Lastly, thank you to the Department of Physiology, Anatomy and Genetics, the Rosetrees Trust, and my college Lady Margaret Hall for your financial support, without which none of this would have been possible.

Declaration

I declare that the work presented in this thesis is my own, with help gratefully acknowledged from several colleagues. The schematic of the *NGN2*-expressing differentiation cassette in Figure 1a of this thesis is reproduced unchanged from Figure 1A of Wang *et al.* (2017), licensed under CC BY-NC-ND 4.0 (https://creativecommons.org/licenses/by-nc-nd/4.0/). The schematic of the dCas9-expressing cassette in Figure 1a of this thesis is reproduced unchanged from CRISPR Interference-Based Platform for Multimodal Genetic Screens in Human iPSC-Derived Neurons, Vol 104, by Tian *et al*, 2019, p.239-255, with permission from Elsevier. Dr Charmaine Lang and Dr Stephanie Giussani provided helpful advice on flow cytometry. Sarah Franks performed half the lentiviral packaging for the CRISPR interference library and Elly Robles Rodriguez prepared six of the lentiviruses. Dr Maria Claudia Caiazza genetically engineered the 156, 856, 831-1 and 831-3 iPSC lines to introduce dCas9 expression. Katrina Savory transduced and selected the SNCA-EGFP-overexpressing SH-SY5Y cells used for quality control of α-synuclein pre-formed fibrils. Dr Brent Ryan, Sarah Franks and Millie Smith all provided additional help with the screening experiments by preparing the lentiviral source plate for nanodispensing. Dr Camille Loiseau provided a batch of α-synuclein pre-formed fibrils for testing and helpful advice with α-synuclein fibril aggregation, as well as expertise and method development with correlative light and electron microscopy, training on the Zeiss confocal and electron microscopes, and image acquisition for the light microscopy images presented in section 4.3.1. Dr Nora Bengoa-Vergniory developed the first iteration of the α-synuclein fibril aggregation protocol. Dr Stewart Humble and Peter Holderrieth cloned 41 of the CRISPR interference vectors utilised in this study, and both cloned and lentivirally-packaged another 30, out of a total of 225 vectors. Dr Lothar Schermelleh acquired the structured illumination microscopy images presented in this work, and I gratefully acknowledge the Micron Bioimaging Facility for their support & assistance. Dr Kalina Naidoo proofread parts of the manuscript in line with University of Oxford guidance. Sections 1.4, 1.4.1 to 1.4.3 of this thesis' introduction are adapted from Franks and Heon-Roberts, *et al*, 2024. The sections adapted were written by me and are used here with written permission from co-authors.

List of Abbreviations

BCA	Bicinchoninic acid
BDNF	Brain-derived neurotrophic factor
BSLII	Biological safety level II
Cas	CRISPR-associated
CCCP	Carbonyl cyanide m-chlorophenyl hydrazone
CLEM	Correlative light and electron microscopy
CMV	Cytomegalovirus
CNQX	Cyanquixaline
CQ	Chloroquine
CRISPR	Clustered, regularly-interspersed, short palindromic repeats
CRISPRa	CRISPR activation
CRISPRi	CRISPR interference
CRISPRn	Nuclease-active CRISPR/Cas9
crRNA	CRISPR-derived RNA
CTSB	Cathepsin B
DaN	Dopaminergic neuron
dCas9	Dead Cas9
ddH_2O	Double distilled H_2O
DIV	Day *in vitro*
DLB	Dementia with Lewy bodies
DPBS	Dulbecco's PBS
EDTA	Ethylenediaminetetraacetic acid
eQTL	Expression quantitative trait locus
ETC	Electron transport chain
FACS	Fluorescence-activated cell sorting
FBS	Foetal bovine serum
FCB	Flow cytometry buffer
FCCP	Carbonyl cyanide 4-(trifluoromethoxy)phenylhydrazone
Gcase	Glucocerebrosidase
GDH	Glutamate dehydrogenase
GWAS	Genome-wide association study
IM	Induction medium
iPSC	Induced pluripotent stem cell
KRAB	Krüppel-associated box
LIR	LC3-interacting region
MAM	Mitochondria-associated endoplasmic reticulum membrane
MDS-UPDRS	Movement Disorder Society-sponsored Revision of the Unified Parkinson's Disease Rating Scale
MMSE	Mini-Mental State Examination
MoCA	Montreal Cognitive Assessment
mPTP	Mitochondrial permeability transition pore
NT	Non-targeting
NT-3	Neurotrophin-3
PB	Phosphate buffer
PBS	Phosphate-buffered saline

PD	Parkinson's disease
PEI	Polyethyleneimine
PFF	Pre-formed fibril
PLO	Poly-L-ornithine
pS129	α-Synuclein phosphorylated at serine 129
pS65Ub	Phospho-serine 65 ubiquitin
RIPA	Radioimmunoprecipitation assay
RNAi	RNA interference
ROS	Reactive oxygen species
SEM	Standard error of the mean
sgRNA	Single guide RNA
shRNA	Short hairpin RNA
SNpc	Substantia nigra pars compacta
TBS	Tris-buffered saline
TBS-T	Tris-buffered saline with Tween
TCA	Tricarboxylic acid
TH	Tyrosine hydroxylase
tracrRNA	Trans-encoded RNA
TSS	Transcription start site
TWAS	Transcriptome-wide association study

List of Publications

Meade RM, Allen SG, Lopez AJ, Williams C, Thomas-Wright I, Heon-Roberts R, Carey-Wood M, Tang TMS, Sero JE, Hunt VL et al (2025) Stabilizing a Native Fold of Alpha-Synuclein with Short Helix-Constrained Peptides. *JACS Au* 5: 4321–4336

Schmidt SI, Okarmus J, Madsen DA, Hansen JS, Gregersen E, Gram H, Winkelmann LS, Oliveira AS, Heon-Roberts R, Ryan BJ et al (2025) Formation of seeding-competent α-synuclein aggregates in parkin-deficient iPSC-derived human neurons. *NPJ Parkinsons Dis* 11: 180

Franks SNJ*, Heon-Roberts R*, Ryan BJ (2024) CRISPRi: a way to integrate iPSC-derived neuronal models. *Biochem Soc Trans* 52: 539–551

Williamson MG, Madureira M, McGuinness W, Heon-Roberts R, Mock ED, Naidoo K, Cramb KML, Caiazza M-C, Malpartida AB, Lavelle M et al (2023) Mitochondrial dysfunction and mitophagy defects in LRRK2-R1441C Parkinson's disease models. *Hum Mol Gen* 32: 2808–2821

Bogetofte H, Ryan BJ, Jensen P, Schmidt SI, Vergoossen DLE, Barnkob MB, Kiani LN, Chughtai U, Heon-Roberts R, Caiazza MC et al (2023) Post-translational proteomics platform identifies neurite outgrowth impairments in Parkinson's disease GBA-N370S dopamine neurons. *Cell Rep* 42: 112180

*Co-first authors

Table of Contents

Abstract 2

Acknowledgements 4

Declaration 6

List of Abbreviations 7

List of Publications 9

Table of Contents 10

List of Figures 16

List of Tables 19

1 Introduction 20

1.1 Overview of Parkinson's disease 20

1.1.1 α-Synuclein in the pathogenesis of PD 21

1.1.2 Consequences of α-synuclein misregulation 23

1.1.3 Genetic architecture of PD 25

1.2 Overview of mitochondrial function 28

1.2.1 Pathways of mitochondrial autophagy 29

1.3 Mitochondrial dysfunction in PD 31

1.3.1 Mitochondrial function impairment 32

1.3.2 Alterations of mitophagy 33

1.4 Overview of CRISPRi technology 34

1.4.1 Development of CRISPRi 35

1.4.2 Advantages and limitations of CRISPRi 36

1.4.3 Genome-wide CRISPRi screening 37
1.4.4 Arrayed CRISPRi screening 38
1.4.5 Applications of CRISPRi to disease modelling 39
1.5 Aims 39
2 Materials and Methods 41
2.1 Cell culture 41
2.1.1 iPSC-derived i^3 cortical neurons 41
2.1.2 SH-SY5Y 45
2.1.3 HEK-293T 46
2.1.4 iPSC-derived dopaminergic neurons 46
2.2 Immunocytochemistry 49
2.3 qRT-PCR 51
2.4 *In vitro* aggregation of α-synuclein fibrils 53
2.4.1 Fibril aggregation 53
2.4.2 Electron microscopy 53
2.4.3 Quality control 54
2.5 α-Synuclein aggregation 54
2.5.1 Cortical neurons 54
2.5.2 Dopaminergic neurons 54
2.6 MitoSOX live assay 55
2.7 CellTiter-Glo® 2.0 live assay 55
2.8 JC-10 live assay 56
2.9 DQ™ Red BSA live assay 57

2.10 Preparation and cloning of sgRNAs for CRISPRi 57
2.10.1 Annealing sgRNAs 57
2.10.2 Digestion of the lentiviral backbone 58
2.10.3 Ligation of sgRNAs into the lentiviral backbone 59
2.10.4 Transformation of ligated plasmids into competent bacteria 59
2.10.5 Plasmid amplification, isolation and sequencing 60
2.11 Lentivirus packaging 60
2.12 Titration of CRISPRi sgRNAs 61
2.13 Arrayed CRISPRi screening in i^3 cortical neurons 62
2.13.1 Experimental design 62
2.13.2 Screen analysis 63
2.14 Flow cytometry 64
2.14.1 Initial protocol 64
2.15 Correlative light and electron microscopy 65
2.16 Statistical analyses 67
3 Results: Modelling Parkinson's Disease Using α-Synuclein Pre-Formed Fibrils 69
3.1 Characterisation of iPSC-derived i^3 cortical neurons 70
3.1.1 i^3 Neurons adopt glutamatergic and cortical neuronal identity 70
3.1.2 Neurodegeneration-relevant proteins are expressed in i^3 neurons 75
3.2 α-Synuclein pre-formed fibrils to model the process of aggregation 76
3.2.1 Characterisation of *in vitro*-generated α-synuclein recombinant fibrils 76
3.2.2 α-Synuclein PFFs trigger formation of phospho-serine 129-positive aggregates in a dose-dependent manner 77

3.2.3 High batch-to-batch variability of recombinant α-synuclein PFFs 80
3.2.4 Optimisation of recombinant α-synuclein aggregation 82
3.2.5 Predicting seeding efficiency of α-synuclein PFF preparations 88
3.3 pS129-positive aggregates co-localise with a marker of mitophagy 94
3.3.1 α-Synuclein aggregates trigger formation of pS65Ub 94
3.3.2 pS129 and pS65Ub interaction at a single-aggregate level 98
3.3.3 PFF-induced pS65Ub formation is dependent on PINK1 100
3.4 Discussion 101
3.4.1 Maturity of iPSC-derived i^3 cortical neurons 103
3.4.2 i^3 Neurons as a model of Parkinson's disease 104
3.4.3 Methods of modelling α-synuclein aggregation in a dish 106
3.4.4 Factors influencing α-synuclein PFF-induced aggregation 107
3.4.5 α-Synuclein fibrils template the aggregation of endogenous α-synuclein monomer 109
3.4.6 pS129 aggregation induces pS65Ub accumulation 110
4 Results: Organellar health and morphology under PD-relevant insults 113
4.1 Mitochondrial defects resulting from α-synuclein PFF treatment 114
4.1.1 Confocal microscopy reveals mitochondrial network changes in response to the mitochondrial toxin CCCP 114
4.1.2 α-Synuclein aggregation induces alterations to mitochondria in neurons without aggregates 116
4.1.3 Functional assays reveal altered mitochondrial respiration 118
4.2 Lysosomal alterations with α-synuclein PFF treatment 120
4.2.1 Lysosomal content is reduced in aggregate-negative neurons 120

4.2.2 Lysosomal proteolytic activity is effectively measured by DQ-BSA imaging 122

4.2.3 α-Synuclein PFF treatment has no effect on lysosomal activity 124

4.2.4 Lysosomal activity is impaired by treatment with amyloid-β 124

4.3 High resolution microscopy for the evaluation of organellar morphology 126

4.3.1 Optimisation of correlative light and electron microscopy 129

4.3.2 Optimisation of structural illumination microscopy 131

4.4 Discussion 133

4.4.1 Mitochondrial uncoupling results in fragmentation of the network 133

4.4.2 Mitochondrial morphology is differentially altered in pS129-positive and negative neurons 135

4.4.3 Mitochondrial function is impaired by α-synuclein PFF treatment 136

4.4.4 α-Synuclein PFF treatment in i^3 neurons does not induce lysosomal impairment ... 138

4.4.5 Super-resolution microscopy to confirm and extend the findings of this study 139

5 Functional genomic screening identifies candidate genes modulating pS129 and pS65Ub formation 141

5.1 Cloning and validating an arrayed CRISPRi PD GWAS candidate risk gene library .. 142

5.1.1 Library design and candidate risk gene selection 145

5.1.2 sgRNA cloning and lentiviral packaging 147

5.2 Optimisation of arrayed CRISPRi screening 149

5.2.1 sgRNAs and dCas9 machinery are not silenced over maturation 151

5.2.2 Optimisation of screening workflow and analysis 154

5.2.3 Optimisation of the analysis pipeline 157

5.3 Primary screening of PD GWAS risk candidate genes 159

5.3.1 Screen plate design and controls 159
5.3.2 Readout correlation and unified scoring 163
5.3.3 Identification of putative modulators of pS129-positive aggregate formation and α-synuclein PFF-induced pS65Ub 167
5.3.4 Cellular pathways underlying pS129 and pS65Ub regulation 171
5.3.5 Correlation of pS129 and pS65Ub levels in screening data 173
5.4 Validation screening in iPSC-derived dopaminergic neurons 174
5.5 Prioritisation of hit genes for mechanistic follow-up 178
5.5.1 Future directions 182
5.6 Discussion 184
5.6.1 Targeted arrayed screening provides a rich and complex dataset 184
5.6.2 Screening design 185
5.6.3 Prioritised genes reflect mostly mitochondrial and lysosomal biology 187
5.6.4 A PD-centred approach to α-synuclein biology 190
6 Discussion 192
6.1 pS129-positive aggregate formation is linked with PINK1-dependent mitophagy in PFF-treated conditions 192
6.2 Functional characterisation of candidate risk genes at PD risk loci to enable aetiological stratification of patients 194
6.3 Conclusions 200
Appendix 201
References 230

List of Figures

Figure 1. Genetically engineered G3dCas9 iPSCs differentiate in a one-step process to neurons. 71

Figure 2. i^3 Neurons express cortical, excitatory, neuronal markers. 72

Figure 3. Increased excitatory firing in i^3 neurons over the course of maturation. 74

Figure 4. Neurodegeneration-related SNCA and tau are expressed in i^3 neurons. 76

Figure 5. Characterisation of α-synuclein fibrils aggregated from purified monomer. 78

Figure 6. α-Synuclein PFFs seed pS129-positive aggregation in a dose-dependent manner. 79

Figure 7. Comparison of α-synuclein PFF preparations. 81

Figure 8. Development of a functional validation assay for α-synuclein PFF preparations. 83

Figure 9. Comparison of α-synuclein PFF aggregation methods. 85

Figure 10. Characterisation of α-synuclein PFF preparations aggregated using different methods. 87

Figure 11. Preparations of in vitro aggregated α-synuclein show reduced experimenter-induced variability. 89

Figure 12. Preparations of in vitro aggregated α-synuclein show reduced batch-to-batch variability. 90

Figure 13. Comparison of all available α-synuclein PFF preparations to predict seeding efficiency. 91

Figure 14. Predicting the seeding efficacy of PFF preparations based on multiple measurable parameters. 93

Figure 15. Seeding pS129-positive aggregation later in maturation does not significantly increase levels of pS129. 95

Figure 16. Time-dependent pS129 and pS65Ub accumulation over time post-seeding with PFFs. 97

Figure 17. Relationship of pS129 and pS65Ub puncta over aggregation time course. 99

Figure 18. PFF-induced pS65Ub accumulation is dependent on the kinase PINK1. 102

Figure 19. Mitochondrial morphology changes induced by the mitochondrial toxicant CCCP. 115

Figure 20. α-Synuclein PFF treatment induces mitochondrial network morphology alterations in pS129-negative neurons. 117

Figure 21. Mitochondrial function is altered by treatment with α-synuclein PFFs. 119

Figure 22. LAMP1-positive endolysosomal content and morphology is unchanged with α-synuclein PFF treatment. 121
Figure 23. Lysosomal alkalising agent chloroquine reduces proteolytic activity in a dose-dependent manner. 123
Figure 24. Optimisation of DQ-BSA incubation time and dosage in i^3 neurons. 125
Figure 25. α-Synuclein PFF treatment has no effect on DQ-BSA signal intensity. 127
Figure 26. Amyloid-β oligomers impair lysosomal proteolytic activity in a dose-dependent manner. 128
Figure 27. Optimisation of correlative light and electron microscopy in i^3 neurons. 130
Figure 28. Comparison of fixation reagents, concentrations and incubation times and their effects on immunostaining pattern and intensity. 132
Figure 29. Preliminary trial of structure illumination microscopy (SIM) for the evaluation of mitochondrial morphology. 134
Figure 30. Flow cytometry optimisation for single-cell measurement of pS129 and pS65Ub levels. 143
Figure 31. Sensitivity of the pS129 immunocytochemical assay. 144
Figure 32. Design of the arrayed PD GWAS candidate risk gene CRISPRi screening library. 146
Figure 33. Cloning CRISPRi sgRNAs into lentiviral vectors at scale. 148
Figure 34. Lentiviral library functional titration in i^3 neurons. 150
Figure 35. Functional characterisation of CRISPRi silencing at DIV 10 and 31. 153
Figure 36. Preliminary screening to optimise arrayed screening workflow. 156
Figure 37. Screen plate design and controls. 158
Figure 38. Correlation of screening readouts and composite readouts. 160
Figure 39. Primary GWAS candidate risk gene screening. 167
Figure 40. Primary screening of sgRNAs targeting proteomics hit genes. 170
Figure 41. Identification of cellular pathways and processes underlying pS129 and pS65Ub accumulation. 173
Figure 42. Regulation of pS129 and pS65Ub is largely independent. 175
Figure 43. Differentiation efficiency of iPSC-derived dopaminergic neurons. 178

Figure 44. Quantification of internal assay controls in iPSC-derived dopaminergic validation screening. 179
Figure 45. Validation screening in iPSC-derived dopaminergic neurons. 181
Figure 46. Interaction network of prioritised genes for mechanistic follow-up 183
Figure 47. Automated analysis pipeline in Harmony for the analysis of arrayed CRISPRi screens measuring pS129 and pS65Ub. 202
Figure 48. Lysosomal alkalinising agent chloroquine (CQ) potentiates pS129-positive aggregation. 203
Figure 49. Comparison of pS129 antibodies in PFF-treated i^3 neurons. 211
Figure 50. Preliminary screening internal controls. 212
Figure 51. Harmony analysis pipeline optimisation. 214
Figure 52. Primary screening readouts in cortical neurons. 221
Figure 53. Primary screening readouts for genes in the proteomics datasets in cortical neurons. 225
Figure 54. Screening readouts for the mechanistic library of genes targeting mitochondria, lysosomes and autophagy. 229

List of Tables

Table 1. Induction medium composition for i^3 cortical neurons 44

Table 2. Maturation medium composition for i^3 cortical neurons 44

Table 3. DMEM KO KSR base medium composition 47

Table 4. NNB base medium composition 48

Table 5. NB base medium composition 48

Table 6. Growth factors and small molecules for dopaminergic neuron differentiation 48

Table 7. Details of primary antibodies and dilutions 50

Table 8. Details of secondary antibodies and dilutions 50

Table 9. Primer sequences for qPCR 51

Table 10. 2X annealing buffer composition 57

Table 11. Digestion of the sgRNA backbone with BlpI 58

Table 12. Digestion of the sgRNA backbone with BstXI 58

Table 13. NEBuffer 2.1 to 3.1 spike composition 58

Table 14. Ligation reaction (per sgRNA) 59

Table 15. Details of primary antibodies used for CLEM 66

Table 16. Details of secondary antibodies used for CLEM 66

Table 17. Screening Harmony pipeline readouts and interpretation 161

Table 18. Top upregulating sgRNAs ranked by readout score in the primary screen 168

Table 19. Top downregulating sgRNAs ranked by readout score in the primary screen 168

Table 20. Top upregulating sgRNAs ranked by readout score in the validation screen 176

Table 21. Top downregulating sgRNAs ranked by readout score in the validation screen 177

Table 22. Genes targeted by the top-ranked up or downregulating sgRNAs in both primary and validation screening 182

Table 23. Details of CRISPRi sgRNAs used in this study 204

1 Introduction

1.1 Overview of Parkinson's disease

Parkinson's disease (PD) was first described by James Parkinson in 1817, based on observations in patients of resting tremor, weakness and a bent posture (Parkinson, 2002). The cardinal motor symptoms, namely bradykinesia, muscular rigidity, resting tremor as well as postural and gait impairments, remain the most recognisable feature of the condition (reviewed in Kalia & Lang, 2015). Furthermore, clinically-relevant non-motor symptoms have been identified which accompany the motor manifestations. These include autonomic dysfunction (orthostatic hypotension), cognitive dysfunction (impaired memory, concentration, and mood as well as increased anxiety, apathy and visual hallucinations), sleep disturbances (dream re-enactment and daytime sleepiness) and gastrointestinal dysfunction (constipation) (Khoo *et al*, 2013). Several of these features pre-date the onset of motor symptoms by more than 10 years (Kalia & Lang, 2015). PD is a progressive disease with late stages presenting motor and non-motor symptoms that are increasingly resistant to treatment, with falls, dysphagia, dysautonomia, dysarthria and dementia showing strong association with institution admission and mortality (reviewed in Coelho & Ferreira, 2012).

The development of PD is determined by a complex interaction of genetic, lifestyle and environmental factors, with ~85% of cases being idiopathic in nature. By far the highest risk factor is increasing age, but gender and ethnicity also contribute to an individual's risk profile (Pringsheim *et al*, 2014; Kalia & Lang, 2015). Being a non-smoker, having low alcohol or increased caffeine consumption, having depression, epilepsy, daytime sleepiness and early menarche increase risk for PD (Noyce *et al*, 2012; Jacobs *et al*, 2020), as does exposure to pesticides, head injury, living in rural areas, taking β-blockers, having an agricultural occupation or drinking well water (Noyce *et al.*, 2012). Furthermore, a first degree relative with PD, tremor, or dementia is a strong risk factor for the disease (Noyce *et al.*, 2012; Jacobs *et al.*, 2020), and several mutations have been associated with autosomal dominant or recessive,

early or late-onset PD (Polymeropoulos *et al*, 1997; Kitada *et al*, 1998; Krüger *et al*, 1998; Singleton *et al*, 2003; Chartier-Harlin *et al*, 2004; Ibáñez *et al*, 2004; Valente *et al*, 2004). The most recent genome-wide association study (GWAS) has identified 134 loci associated with increased risk of PD, confirming the involvement of genetic factors in idiopathic cases of the disease (The Global Parkinson's Genetics & Leonard, 2025).

Despite the fact that PD prevalence is second only to Alzheimer's disease and is projected to affect up to 9.3 million people by 2030 (Dorsey *et al*, 2007; Kalia & Lang, 2015), and that age-standardised prevalence has risen 21.7% between 1990 and 2016 (Dorsey *et al*, 2018), treatment of PD remains symptomatic with disease-modifying therapies having so far failed at various stages of development. This may be partly explained by a growing recognition that PD might be more than a single disease, a fact which could have confounded clinical trials. From a motor syndrome characterised early on by a few cardinal manifestations, to a complex disorder having both a non-motor and motor component (Langston, 2006), to more recently an umbrella term for multiple separate but related entities (Espay *et al*, 2020; Farrow *et al*, 2022a), the concept of PD has evolved as the understanding of the disease mechanisms and aetiology has progressed. Research is currently underway to classify subclusters of patients based on symptomology and progression in an effort to find common targets for therapeutics (Jankovic *et al*, 1990; Lawton *et al*, 2018), though this is controversial as it places emphasis on clinical manifestations whose underlying mechanisms may be diverse (Mestre *et al*, 2021). Instead, several researchers are proposing a personalised medicine approach, based on molecular pathogenesis, to disease-modifying treatments (Weiner, 2008; Espay *et al*, 2017; Bloem *et al*, 2021). Consequently, identification of aetiology and disease mechanisms are currently a predominant area of focus.

1.1.1 α-Synuclein in the pathogenesis of PD

As early as 1912, post-mortem staining and microscopy on PD patient brain slices revealed the presence of proteinaceous inclusions within the soma and neurites of several neuronal populations (Goedert *et al*, 2013). These inclusions were associated with areas of neuronal loss, in particular in the substantia nigra pars compacta. These inclusions and filaments were respectively named Lewy bodies and Lewy neurites in 1919 (Goedert *et al*, 2013). Their composition was subsequently dissected, revealing that

they were composed of several different proteins such as ubiquitin (Kuzuhara *et al*, 1988) and p62 (Kuusisto *et al*, 2001). In 1997, the protein α-synuclein was discovered as a major component of these Lewy bodies and neurites, implicating it in the pathogenesis of PD (Spillantini *et al*, 1997). These findings were extended a year later to demonstrate that α-synuclein was the most sensitive marker for Lewy bodies and neurites as it stained more Lewy-like structures than ubiquitin (Spillantini *et al*, 1998) or p62 (Kuusisto *et al*, 2003). α-Synuclein is a small pre-synaptic protein of 140 amino acids, whose endogenous localisation and physiological function are still under investigation. It has been implicated in the clustering of synaptic vesicles in a Ca^{2+}-dependent manner at the pre-synaptic terminal, organising the vesicle pool (Fusco *et al*, 2016; Lautenschläger *et al*, 2018). α-Synuclein may also multimerise at the presynaptic plasma membrane and chaperone SNARE complex assembly (Burré *et al*, 2014).

There is growing evidence for a role of α-synuclein in PD pathogenesis. Mutations in the gene encoding α-synuclein, *SNCA*, were shown to cause autosomal dominant PD in kindreds with high rates of PD (Polymeropoulos *et al.*, 1997; Krüger *et al.*, 1998; Singleton *et al.*, 2003; Chartier-Harlin *et al.*, 2004; Ibáñez *et al.*, 2004). Similarly, certain variants in the *SNCA* promoter (Pals *et al*, 2004) and certain *SNCA* polymorphisms are associated with PD risk (reviewed in Campêlo & Silva, 2017). Lastly, the genetic dosage of *SNCA* correlates with the age at onset for PD, with patients carrying triplications of the *SNCA* gene having the earliest age-at-onset (Book *et al*, 2018).

The appearance and spread of α-synuclein aggregates in the brain are correlated with neuronal loss and disease severity, as demonstrated in post-mortem brain samples and experimental models (Braak *et al*, 2003; Luk *et al*, 2012b). Lewy bodies and neurites affect multiple brain areas such as the substantia nigra pars compacta (SNpc), limbic system, motor system, amygdala, hypothalamus and cortex. This demonstrates that despite large focus on the severe and characteristic loss of SNpc dopaminergic neurons (DaNs) which produces many of the characteristic motor symptoms, degeneration of other brain regions is also an important component of the disease (Braak & Braak, 2000). Further microscopy studies have shown that Lewy bodies and neurites are composed of a matrix of α-synuclein which adopts a range of morphologies, from clusters of discrete puncta to large, compact circular aggregates through

a range of intermediate morphologies (Kuusisto *et al.*, 2003). Analysis of small to large aggregates revealed that the inclusions are formed first by α-synuclein and there is subsequent incorporation of ubiquitin and p62. Furthermore, it was shown by correlative light and electron microscopy (CLEM) that inclusions also contain a large number of membranous vesicular organelles that are similar to lysosomes, as well as mitochondria with distorted internal architecture (Shahmoradian *et al*, 2019). Aggregated α-synuclein was found to be tagged by phosphorylation at serine 129 (pS129) (Fujiwara *et al*, 2002). Despite this, evidence suggests that Lewy bodies and neurites do not themselves cause toxicity, but rather it is the smaller, soluble α-synuclein assemblies such as oligomers and small fibrils which are toxic (Alam *et al*, 2019; Cascella *et al*, 2022; Emin *et al*, 2022). It is possible these may exert toxic gain-of-function roles in the cell as well as depleting the levels of endogenous α-synuclein monomer, possibly leading to loss-of-function phenotypes (Chandra *et al*, 2005; Burre *et al*, 2010; Volpicelli-Daley *et al*, 2011).

1.1.2 Consequences of α-synuclein misregulation

As suggested by the engulfment of various organelles in Lewy bodies, α-synuclein aggregation has been implicated in the disruption of multiple organelles in the cell (reviewed in Saramowicz *et al*, 2023). These include mitochondria, the endoplasmic reticulum and Golgi apparatus, as well as autophagosomes and lysosomes. The impacts of α-synuclein aggregation on mitochondria will be covered in section 1.3.

α-Synuclein has been localised to mitochondria-associated endoplasmic reticulum membranes (MAMs) and loss of this localisation was associated with PD-linked mutations in *SNCA*, increased mitochondrial fragmentation and decreased function of the MAMs (Guardia-Laguarta *et al*, 2014). Increased levels of α-synuclein were also found to disrupt MAMs and interfere with ATP production and Ca^{2+} flux between the endoplasmic reticulum and mitochondria (Paillusson *et al*, 2017). α-Synuclein upregulation and aggregation has been linked to sarco/endoplasmic reticulum calcium ATPase (SERCA) pump (Betzer *et al*, 2018) and unfolded protein response activation (Hoozemans *et al*, 2007; Bellucci *et al*, 2011; Colla *et al*, 2012; Chung *et al*, 2013; Valdés *et al*, 2014; Heman-Ackah *et al*, 2017) as well as trafficking defects between the endoplasmic reticulum and Golgi apparatus (Cooper *et al*, 2006).

α-Synuclein, both unmodified and tagged with pS129, has been identified in the nucleus of post-mortem human patients with dementia with Lewy bodies (DLB) (Koss *et al*, 2022). However, the nuclear localisation of α-synuclein and its aggregates is contested, as a different group were unable to identify α-synuclein inclusions in the nucleus of DLB cases, but did identify such aggregates in multiple system atrophy cases (Weston *et al*, 2022). Further research will be required in this area for a definitive conclusion to be reached.

There is far less controversy regarding impairment of the autophagy-lysosomal pathway in PD by pathologically elevated or aggregated α-synuclein. Reductions of lysosomal proteins LAMP1 and CTSD were found in post-mortem brain tissues from PD patients, with the largest reduction found in neurons bearing α-synuclein aggregates (Chu *et al*, 2009). Reductions in LAMP2A and HSC70 were also found in patient SNpc samples and were associated with increased α-synuclein stability (Alvarez-Erviti *et al*, 2010). LAMP1 and LAMP2 were significantly decreased in PD patient cerebrospinal fluid samples (Boman *et al*, 2016). These data are consistent with findings of reduced lysosomal mass in a toxin-induced mouse model of PD linked to lysosomal membrane permeabilisation by reactive oxygen species (ROS) (Dehay *et al*, 2010), as well as with lysosomal depletion and enlargement in α-synuclein pre-formed fibril (PFF)-treated conditions (Tanik *et al*, 2013). Studies in model systems using PFFs to trigger α-synuclein aggregation showed that early, small aggregates of α-synuclein were cleared in lysosome-dependent manner but not mature aggregates (Lee *et al*, 2004; Watanabe *et al*, 2013). Wild-type α-synuclein has been shown to be degraded by chaperone-mediated autophagy, but mutant α-synuclein (A53T and E46K) was found to block the receptor, leading to accumulation (Cuervo *et al*, 2004). Culturing *SNCA*-overexpressing neurons for hundreds of days led to reduced activity of proteases in acidic cell compartments and, in this study, an increase in lysosomal mass. These effects were dependent both on α-synuclein levels and aggregation and resulted from impaired hydrolase trafficking at the Golgi (Mazzulli *et al*, 2016a). α-Synuclein was also shown to impair Rab1a activity, resulting in an autophagy defect (Winslow *et al*, 2010). Furthermore, there is a genetic link between PD autophagy-lysosomal system dysfunction, with lysosomal gene variants (Ngo *et al*, 2024), mutations in *ATP13A2* (Dehay *et al*, 2012), and *VPS35* (Tang *et al*, 2015) contributing to PD risk.

These data suggest many disease-relevant interactions exist between PD-linked α-synuclein upregulation or aggregation and several organelles such as the endoplasmic reticulum, autophagosome and lysosome.

1.1.3 Genetic architecture of PD

The genetic component of PD was first studied in monozygotic and dizygotic twins, which showed there was low concordance of PD status between the siblings with onset after 50 years of age, whereas the concordance was higher if the onset was before 50 years of age (Tanner *et al*, 1999). This suggested a genetic component to PD with an early age at onset. Study of kindreds with high rates of PD showed not only mutations in *SNCA*, as discussed in 1.1.1, but mutations in *LRRK2* and *GBA* which caused autosomal dominant PD (Aharon-Peretz *et al*; Sidransky *et al*; Paisán-Ruíz *et al*, 2004; Zimprich *et al*, 2004). Mutations in the genes *PINK1*, *PARK7*, and *PRKN* were shown to cause autosomal recessive PD (Kitada *et al.*, 1998; Bonifati *et al*, 2003; Valente *et al.*, 2004). Other genes implicated in monogenic PD with variable scientific consensus, penetrance and age-at-onset include *VPS35*, *PLA2G6*, *FBXO7*, *ATP13A2*, *POLG*, *DNAJC6*, *DNAJC13*, *TMEM230*, *SYNJ1*, *VPS13C*, *CHCHD2*, and *DCTN1* (reviewed in Day & Mullin, 2021).

Early studies provided evidence that the majority of PD cases were sporadic and not caused by mutations of large effect size in single genes (reviewed in Pankratz & Foroud, 2007). Instead, common variants at many different loci might contribute to risk. However, GWAS studies at the time were significantly underpowered and did not yield robust or consistent results in sporadic cases (Maraganore *et al*, 2005; Fung *et al*, 2006). Analysis of the genomes of patients reporting a first-degree relative with PD compared to normal controls revealed an association with the genes *MAPT* and *SNCA*, as well as other candidates such as *DGKQ/GAK* (Pankratz *et al*, 2009). These studies also highlighted evidence that certain genes, such as *SNCA*, confer risk for both sporadic disease as well as familial disease depending on the presence of variants or mutations. Similarly, common genetic variants, such as those identified by GWAS, as well as rare variants identified using more focussed approaches, have been found to increase the risk of PD (Robak *et al*, 2017; Sun *et al*, 2025), increasing the complexity of identifying individuals at high likelihood of developing PD.

Subsequent studies in populations of European ancestry with increasingly large numbers of patients and controls have now identified common variants at up to 134 loci which are significantly associated with PD risk (Edwards *et al*, 2010; Hamza *et al*, 2010; Do *et al*, 2011; Nalls *et al*, 2011; Lill *et al*, 2012; Pihlstrøm *et al*, 2013; Nalls *et al*, 2019; The Global Parkinson's Genetics & Leonard, 2025). Identifying the genes mediating the increased risk has proven more challenging. A study by two leading consortia used gene expression and methylation analysis in post-mortem brains from patients and controls to identify molecular mechanisms and candidate genes at 11 PD-associated loci, which identified alterations in *PARK16*, *GPNMB*, and *STX1B* (International Parkinson's Disease Genomics & Wellcome Trust Case Control, 2011). Li and colleagues (2019c) conducted a transcriptome-wide association study to identify differential expression or splicing associated with PD in post-mortem brains and peripheral monocytes from patients and controls. Candidate risk genes were subsequently prioritised by combining this analysis with PD GWAS datasets to identify differentially-expressed or spliced genes that may confer risk for PD (Li *et al*, 2019c). Combining the datasets with methylation and expression data in a Mendelian randomisation framework (Nalls *et al.*, 2019) or integrating expression quantitative trait loci (eQTL) datasets (Grenn *et al*, 2020) have yielded promising candidates that now require further study to confirm their role in PD as well as underlying molecular mechanisms.

Another aspect of genetic susceptibility to PD resides in identifying genomic regions which influence specific outcomes related to the disease, such as motor progression, cognitive decline, or age-at-onset. Genetic variants in *COMT*, for example, may be associated with earlier age-at-onset of PD in males, but not in females (Klebe *et al*, 2013), or with levodopa therapy-induced dyskinesia (Yin *et al*, 2021) without modulating risk for the disease (Martín-Bórnez *et al*, 2025). However, the association of *COMT* with dyskinesia and other clinical symptoms is contested (Martín-Bórnez *et al*, 2025). Other loci such as *MAPT* (Kobayashi *et al*, 2006; Das *et al*, 2009; Gan-Or *et al*, 2012; Davis *et al*, 2016), *SNCA* (Brockmann *et al*, 2013; Blauwendraat *et al*, 2019; Pedersen *et al*, 2021) and *GBA1* (Clark *et al*, 2007; Nichols *et al*, 2009; Sidransky *et al*, 2009; Davis *et al*, 2016a; Blauwendraat *et al*, 2019) have been consistently linked to PD risk and age-at-onset, with variants in or near *GBA1* and *SNCA* leading to earlier onset and a variant in MAPT leading to later onset. *GBA1* variants, which are some of the most

common genetic risk factors for PD, have also been clearly linked with faster motor progression (Winder-Rhodes *et al*, 2013; Brockmann *et al*, 2015; Davis *et al*, 2016a; Davis *et al*, 2016b; Iwaki *et al*, 2019) and cognitive decline (Winder-Rhodes *et al*, 2013; Davis *et al*, 2016b; Mata *et al*, 2016; Liu *et al*, 2016; Iwaki *et al*, 2019), whereas different variants in *SNCA* have been associated with faster and slower motor progression (Ritz *et al*, 2012; Cooper *et al*, 2016; Szwedo *et al*, 2021). *LRRK2* variants may instead be associated with increased symptom severity but slower progression (Saunders-Pullman *et al*, 2018; Sun *et al*, 2024).

Though it could be thought that genes associated with monogenic forms of PD may not be representative of idiopathic PD cases due to their larger effect size, there is evidence to suggest that polygenic risk scores derived from risk variants of low effect size identified by GWAS in idiopathic patients may also be associated with earlier age-at-onset (Escott-Price *et al*, 2015), suggesting that these variants may have, cumulatively, an influence on the initiation of PD. Indeed, a large age-at-onset GWAS has identified a significant effect of variants in *SNCA* and *TMEM175* and nominally significant effects of *BST1*, *GBA1*, *IPP5F/BAG3*, *FAM47E/SCARB2*, and *MCCC1* variants on age-at-onset, many of which, the authors note, have been associated with α-synuclein aggregation or lysosomal clearance (Blauwendraat *et al*, 2019). A later study provided additional evidence to the involvement of *TMEM175*, *SNCA*, and *BST1* in modulating age-at-onset (Grover *et al*, 2022).

Genomic loci of low effect size have also been investigated for their effect on motor progression and cognitive decline in idiopathic patients, though these studies are inherently more difficult due to variation arising from the type of test administered (Movement Disorder Society-Sponsored Revision of the Unified Parkinson's Disease Rating Scale (MDS-UPDRS) versus Hoehn and Yahr, or Mini Mental State Examination (MMSE) versus Montreal Cognitive Assessment (MoCA)), difficulty harmonising clinical outcomes across cohorts (reviewed in Blauwendraat *et al*, 2020), the effect of medication such as dopamine replacement therapy on the patient and natural daily variation in disease symptomology (Blauwendraat *et al*, 2020). Variants at *APOE* (Iwaki *et al*, 2019; Liu *et al*, 2021; Tan *et al*, 2021; Real *et al*, 2023), *RIMS2* (Liu *et al*, 2021), *TMEM108* (Liu *et al*, 2021), *TMEM106B* (Tropea *et al*, 2019), and *LRP1B* (Real *et al*, 2023) were found to be nominally significant or significant at

genome-wide level for association with cognitive decline. Genome-wide analyses of loci associated with motor progression initially identified one variant in *SLC44A1* (Iwaki *et al*, 2019), one haplotype at *GJA5* (Martínez Carrasco *et al*, 2023) and one nominal variant in *ATP8B2* (Tan *et al*, 2021). The *MORN1, ASNS, PDE5A* and *XPO1* loci have since been associated with progression to a Hoehn and Yahr stage 3, and analysis of SNPs associated with PD risk did not show association with motor progression, with the exception of one nominally significant variant in *CLCN3* (Tan *et al*, 2024). This study did not show replication of the association at *SLC44A1*. These data suggest that genetic variants modulating the risk for PD and disease initiation may be different to those regulating disease progression, as underpinned by a recent meta-analysis (Nguyen *et al*, 2025), and that larger datasets with increased standardisation and correlation of clinical measures are likely to uncover more progression variants as well as increase the validity and reproducibility of progression variants identified.

1.2 Overview of mitochondrial function

Mitochondria are the organelle which produce the majority of the cells' energy (Siekevitz, 1957) but it is reductive to conceptualise mitochondria only as 'powerhouses'. In fact, mitochondria have multiple functions in addition to their role in energy production, such as participating the synthesis of various biomolecules, acting as a hub for signalling and managing certain cellular waste products.

When performing their function as energy producers, mitochondria utilise pyruvate, produced in the cytoplasm by the reactions of glycolysis. It is transformed into acetyl-CoA and fed into the tricarboxylic acid (TCA) cycle which over multiple enzymatic oxidation steps produces reduced forms of NADH and $FADH_2$ that act as electron stores, subsequently donating their electrons to the electron transport chain (ETC) for oxidative phosphorylation (Walsh *et al*, 2018). Complexes I, III and IV of the ETC use the free energy of donated electrons to power the pumping of H^+ ions into the intermembrane space, creating an electrochemical gradient that powers the F_1F_0 ATP synthase; through conformational changes, it phosphorylates ADP into ATP (Sazanov, 2015). Fatty acids can also be converted to acetyl-

CoA for use in energy production via β-oxidation, and branched-chain amino acids may also provide acetyl-CoA through transamination and a series of decarboxylating enzymatic reactions (Pietrocola *et al*, 2015).

Mitochondria also have a prominent role in the synthesis of several molecules such as nucleotides, glucose, haem, fatty acids, cholesterol and amino acids such as glutamate and aspartate (Spinelli & Haigis, 2018). The energy-producing TCA cycle is intimately linked to anabolism as many intermediates and enzymes of the TCA cycle are involved in the synthesis of fatty acids or glucose (Owen *et al*, 2002). Acetyl-CoA is also an important precursor for lipid synthesis (Pietrocola *et al.*, 2015). Similarly, waste products from mitochondrial activities, such as ammonia, ROS and hydrogen sulphide can also be utilised in synthetic or signalling pathways (Spinelli & Haigis, 2018). For example, ammonia that is produced in the synthesis of amino acids is used in the reaction to make glutamate by the enzyme glutamate dehydrogenase (GDH) in a bidirectional reaction (Spinelli *et al*, 2017).

Mitochondria also serve as a signalling hub and can both sense and signal the metabolic state of the cell through ions, metabolites, proteins and other chemicals such as ROS. Hormone receptors for oestrogen and testosterone, G protein-coupled receptors, metabolite and ion transporters, as well as concentrations of metabolites and substrates all serve to sense signals either from the cell or from the mitochondrion itself. This allows for a response such as shifting the equilibria of various metabolic reactions to promote biosynthesis, mitochondrial fission or fusion, increased or decreased interaction with other organelles, or a signalling output such as a transcription factor to effectuate nuclear gene expression change (Picard & Shirihai, 2022).

1.2.1 Pathways of mitochondrial autophagy

Given the complexity and dynamic nature of mitochondria, mitochondrial quality control and turnover is an equally diverse and highly specialised process. Several pathways of mitochondrial autophagy (mitophagy) exist and are deployed for different types of mitochondrial damage. Perhaps the best studied and understood pathway is the PINK1/PRKN-dependent pathway of mitophagy. PINK1 is a mitochondrially-targeted kinase which is constitutively degraded by the protease PARL in

physiological conditions, but is stabilised by proteolytic inhibition at the outer mitochondrial membrane when the mitochondrial membrane potential is dissipated (Jin *et al*, 2010; Matsuda *et al*, 2010; Narendra *et al*, 2010). Activated PINK1 phosphorylates PRKN, an E3 ubiquitin ligase, as well as ubiquitin at serine 65 (phospho-serine 65 ubiquitin, pS65Ub), leading to the full activation of PRKN and generation of pS65Ub chains on various PRKN targets at the outer mitochondrial membrane, such as mitofusins, VDACs, and mitochondrial protein import proteins (Sarraf *et al*, 2013; Koyano *et al*, 2014). This leads to the clearance of mitochondria by interaction with p62/SQSTM1 (Geisler *et al*, 2010a), NDP52 or Optineurin (Lazarou *et al*, 2015) and autophagic degradation (Narendra *et al*, 2008).

In another layer of regulatory complexity, the PINK1/PRKN-dependent pathway of mitophagy is also regulated by deubiquitylases and phosphatases. The deubiquitylase USP30 negatively regulates the process of mitophagy by removing the ubiquitin tag added by PRKN on outer mitochondrial membrane proteins (Bingol *et al*, 2014). Ubiquitin ligase FBXO7 has also been implicated in mitophagy by rescuing Parkin- but not Pink1-mutant *Drosophila*, though it regulated basal mitophagy which occurred independently of Pink1 and Parkin via basal ubiquitination of substrates (Sanchez-Martinez *et al*, 2023). The phosphatase PPEF2, on the other hand, was found to antagonise the phosphorylation of ubiquitin by PINK1, thereby limiting mitophagy (Wall *et al*, 2019).

Despite the fact that the PINK1/PRKN-dependent pathway has been extensively implicated in conditions of mitochondrial stress, *Pink1* KO mice have no phenotypes despite displaying disruption of depolarisation-induced mitophagy in mouse embryonic fibroblasts and basal mitophagy occurred to a similar level in both control and *Pink1* KO brains (McWilliams *et al*, 2018). This suggested that either PINK1-dependent mitophagy is not the main pathway used by neurons at baseline, or that there was compensation in these mice by other mitophagy pathways. Indeed, several PINK1-independent pathways of mitophagy exist.

Mitophagy via the autophagy receptor BNIP3L/NIX was found to mediate mitochondrial clearance in the maturation process of reticulocytes, in a manner independent to its role in pro-apoptotic pathways. In reticulocytes derived from *Nix* KO mice, mitochondria were incorrectly localised to the outside of autophagosomes, resulting in incomplete degradation of mitochondria (Schweers *et al*, 2007). Gene

expression for both NIX and related protein BNIP3 is induced in conditions of hypoxia (Bruick, 2000; Sowter *et al*, 2001). Upon induction of mitophagy, NIX is activated by phosphorylation (Rogov *et al*, 2017) and homo- or heterodimerisation with BNIP3 (Marinković *et al*, 2021). This enables its binding to LC3 and GABARAP through an LC3-interacting motif (LIR) and degradation of mitochondria via WIPI/ATG13-mediated autophagy (Adriaenssens *et al*, 2025). In addition to BNIP3 and NIX, there exists several other mitophagy receptors with a similar mechanism of action, namely FUNDC1 (Liu *et al*, 2012b), BCL2L13 (Murakawa *et al*, 2015), and FKBP8 (Bhujabal *et al*, 2017). Importantly, KO of any one PINK1/PRKN-independent receptors (BNIP3, NIX, BCL2L13, FUNDC1, FKBP8) does not lead to complete reduction of mitophagy in HeLa cells, suggesting that elimination of individual receptors allows for compensation. However, double-knockout of NIX and BNIP3 results in complete abrogation of hypoxia-induced mitophagy (Yamashita *et al*, 2024). The importance, physiological roles and triggers of each pathway of mitophagy is an area of active investigation.

1.3 Mitochondrial dysfunction in PD

Several lines of evidence suggest that mitochondrial dysfunction is at least a prominent feature of, if not a causative factor in PD. Users of a synthetic drug developed severe and chronic parkinsonism after intravenous injection of a substance contaminated with N-methyl-4-phenyl-1,2,3,6-tetrahydropyridine (MPTP) (Langston *et al*, 1983). Indeed, parenteral injection of MPTP in mice led to a severe decrease in the number of substantia nigra dopaminergic neurons, whereas nucleus accumbens or hypothalamus neurons were unaffected (Heikkila *et al*, 1984). The MPTP metabolite MPP+ was found to be selectively uptaken by dopaminergic neurons (Javitch & Snyder, 1984; Langston *et al*, 1984), inhibiting the oxidation of NADH-linked substrates (Nicklas *et al*, 1985) and resulting in a highly dopaminergic-neuron specific mitochondrial toxin. The mitochondrial toxins rotenone and paraquat have also been linked to PD (Tanner *et al*, 2011) and rotenone has been extensively used to model PD both in mice and in induced pluripotent stem cell (iPSC)-derived neurons (Betarbet *et al*, 2000; Ryan *et al*, 2013; Fernandes *et al*, 2020; Van Laar *et al*, 2023). Furthermore, mutations in the mitophagy genes *PINK1*

and *PRKN* result in early-onset PD (Kitada *et al.*, 1998; Valente *et al.*, 2004), as does mutations in the gene *PARK7* (van Duijn *et al*, 2001; Bonifati *et al.*, 2003) and *UQCRC1* (Jing *et al*, 2025). The majority of patients with mutations in *PRKN* and some patients with mutations in *PINK1* do not present with Lewy pathology post-mortem, suggesting that mitochondrial dysfunction alone can cause degeneration of dopaminergic neurons in the SNpc (Samaranch *et al*, 2010; Doherty *et al*, 2013; Takanashi *et al*, 2016; Nybø *et al*, 2020). Finally, work in human iPSC-derived dopaminergic neurons has shown that cells from patients carrying mutations in *SNCA* (A53T, triplication or duplication), *LRRK2* or *GBA* show alterations to the levels of mitochondrial transcripts, impaired mitochondrial respiration and membrane potential, complex I inhibition, altered mitochondrial morphology and reduced ATP levels (Devi *et al*, 2008; Ryan *et al*, 2018; Zambon *et al*, 2019; Baden *et al*, 2023; Beccano-Kelly *et al*, 2023; Williamson *et al*, 2023). These findings implicate mitochondrial dysfunction both as a cause and consequence of PD pathogenesis.

1.3.1 Mitochondrial function impairment

An array of mitochondrial phenotypes have been described in PD post-mortem patient brains or experimental models. A deficiency in the activity of complex I in post-mortem PD patient brains was noted in 1990 by Schapira and colleagues, in the absence of a reduction in protein levels (Schapira *et al*, 1990a). In a follow-up study, the activity of complex I, but not of any other oxidative phosphorylation complex, was found to be reduced 42% in the substantia nigra and not in any other brain region studied (Schapira *et al*, 1990b). More recently, differences in the distribution and severity of complex I deficiency were found to underlie tremor-dominant or postural instability and gait disorder PD (Fløtnes *et al*, 2024), two subclassifications of PD made on the basis of motor or cognitive symptomology, onset and progression (Jankovic *et al.*, 1990). The finding that complex I deficiency, to various extents, is a common feature in PD in patients, combined with the known effect of complex I-targeting toxins such as rotenone on PD aetiology underlines the importance of complex I in the aetiology of PD.

Overexpression of *SNCA* in cell models resulted in mitochondrial uptake of α-synuclein and a reduction in complex I-linked respiration (Devi *et al.*, 2008; Chinta *et al*, 2010). The localisation of α-synuclein

at mitochondria was found to be increased in mitochondrial fractions from the substantia nigra and striatum of PD patient brains, but not from the cerebellum, perhaps indicating that α-synuclein localisation at mitochondria is associated with disease pathogenesis (Devi *et al.,* 2008). Other studies utilising similar overexpression models showed that α-synuclein induced nitric oxide and cytochrome c release in associated with mitochondrial permeability transition pore (mPTP) opening (Parihar *et al,* 2008). However, in these models, overexpression of α-synuclein may be inducing mislocalisation of α-synuclein at mitochondria (Parihar *et al.,* 2008).

Studies utilising aggregated α-synuclein species such as oligomers and fibrils have found similar effects of α-synuclein in iPSC-derived neurons and other models, though mediated by various mechanisms. Aggregated α-synuclein, unlike physiological α-synuclein, was found to localise to mitochondria in a pathological gain-of-function phenotype, resulting in respiration defects (Wang *et al,* 2019). Treatment of cells with aggregated α-synuclein species resulted in complex I inhibition, reduced ATP and complex I-mediated opening of the mPTP (Luth *et al,* 2014; Reeve *et al*, 2015). Oligomers of α-synuclein were found to inhibit protein import by directly binding TOM20, resulting in competitive displacement of mitochondrial-targeted proteins, reduced respiration and membrane potential as well as increased ROS (Di Maio *et al*, 2016). Binding of α-synuclein to TOM20 was also found to disrupt mitochondrial morphology, gene expression, and respiration (Zambon *et al.*, 2019). Oligomeric α-synuclein may also interact with ATP synthase (Ludtmann *et al*, 2018; Serdiuk *et al*, 2025) or bind mitochondrial membranes through interaction with cardiolipin (Ryan *et al.,* 2018; Choi *et al*, 2022) resulting in opening of the mPTP and apoptosis, or alteration of mitophagy. Alternative mechanisms include modulation of mitochondrial biogenesis and function by the interaction of α-synuclein and the transcription factor REST (Ryan *et al,* 2021) or by nitrosylation of MEF2C (Ryan *et al.*, 2013).

1.3.2 Alterations of mitophagy

PINK1 and *PRKN* are both involved in mitophagy and cause early-onset PD, suggesting that impairment of this process could contribute to wider mitochondrial dysfunction and PD aetiology. Indeed, in sporadic PD patient brains, increases in the PINK1/PRKN-dependent mitophagy marker pS65Ub were found based on PD affectation status and correlated with disease severity in several brain regions (Hou

et al, 2018; Hou *et al*, 2023). However, using a different labelling and quantification technique, a separate study identified decreases in pS65Ub as well as PINK1 and PRKN in PD cases (Chen *et al*, 2023), indicating that further investigation is required.

Furthermore, mitophagy disruptions, such increased or decreased mitophagy, have been described in several studies in iPSC-derived PD models. Measurement of mitophagy in SNCA A53T and E46K iPSC- and ESC-derived DaNs showed increased mitophagy (Ryan *et al.*, 2018). However, work in LRRK2 R1441C rat primary cultures and human iPSC-derived DaNs showed reduced mitophagy and pS65Ub levels (Williamson *et al.*, 2023). In both LRRK2 G2019S and SNCA A53T mutant DaNs, mitophagy was found to be delayed (Hsieh *et al*, 2016; Shaltouki *et al*, 2018). In VPS35-mutant iPSC-derived DaNs, deficits in the autophagy-lysosomal pathway were linked to failed degradation of mitochondria under stress conditions (Hanss *et al*, 2021). These studies demonstrate consistent involvement of the mitochondrial quality control pathways in PD experimental models but little consensus on the direction and mechanism governing these alterations.

1.4 Overview of CRISPRi technology

Sections 1.4-1.4.3 are adapted from the sections I wrote in Franks and Heon-Roberts, *et al*, 2024, with permission from co-authors.

The foundation of the bacterial immune system are sequences of short, repetitive DNA. These clustered, regularly interspersed, short palindromic repeats enable the transcription of two RNA molecules, the CRISPR-derived RNA (crRNA) and the trans-encoded CRISPR RNA (tracrRNA). These associate with CRISPR-associated (Cas) proteins, forming a ribonucleoprotein complex that is targeted to foreign DNA and introduces double-stranded breaks (reviewed in Wiedenheft *et al*, 2012). It was subsequently shown that fusing the tracrRNA and crRNA into a single guide RNA (sgRNA) retained full functionality of the ribonucleoprotein complex, increasing the potential of this new technology for application in genetic engineering (Jinek *et al*, 2012). The technology gained recognition with independent studies

demonstrating the practicality of CRISPR/Cas9 in editing the genomes of human cell models (Cho *et al*, 2013; Cong *et al*, 2013; Mali *et al*, 2013).

The advent of CRISPR technology rapidly enabled genome-wide genetic screening in multiple mammalian cell models (Koike-Yusa *et al*, 2014; Shalem *et al*, 2014; Wang *et al*, 2014; Wang *et al*, 2015), for example providing insight into genes essential for cell survival. However, it was soon shown that the nuclease-active CRISPR system (CRISPRn) targeted to endogenous loci produced a negative selection pressure in bacteria as well as human cells due to DNA cleavage (Qi *et al*, 2013; Aguirre *et al*, 2016; Munoz *et al*, 2016; Rosenbluh *et al*, 2017). The development of a nuclease-dead Cas9 (dCas9) provided targeted silencing of endogenous loci (Qi *et al.*, 2013) without reducing cell survival (Rosenbluh *et al.*, 2017).

1.4.1 Development of CRISPRi

Relying on steric hindrance to silence genes in human cells through impairment of transcription initiation and elongation resulted in low levels of gene knockdown. The technology, renamed CRISPR interference (CRISPRi), was improved by Gilbert and colleagues via fusion of a transcriptional repressor domain, the Krüppel-associated box (KRAB) region of the KOX1 transcription factor, to the dCas9 protein. This increased the levels silencing of CRISPRi technology, resulting in stable reductions in gene expression over time in culture (Gilbert *et al*, 2013). In the following years, the Cas9 and dCas9 proteins were engineered to further expand the range of CRISPR technologies via fusion of alternative transcription regulation domains. Attachment of four copies of the transcriptional activator VP16 to dCas9 resulted in upregulation of endogenous genes targeted by the dCas9-VP16 complex (CRISPR activation, CRISPRa) (Gilbert *et al.*, 2013), whereas fusion of histone methylation and demethylation domains enabled heritable silencing or activation (CRISPRoff and CRISPRon, respectively) (Liu *et al*, 2016; Nuñez *et al*, 2021). These technologies, alone or in combination, enabled the study of a wide range of complex biological systems, in particular when paired with transcriptomics, proteomics or other high-content readouts.

The CRISPRi system was further refined by improvements in the CRISPR/dCas9 system (Alerasool *et al*, 2020) and the identification of sequence features improving sgRNA potency. This enabled more effective silencing with improved genome-wide libraries (Gilbert *et al*, 2014; Sanson *et al*, 2018; Replogle *et al*, 2022). CRISPRi technology has been applied in targeted as well as genome-wide screening paradigms in both immortalised cell lines and human iPSC-derived neurons (Fulco *et al*, 2016; Liu *et al*, 2017; Tian *et al*, 2019; Tian *et al*, 2021).

1.4.2 Advantages and limitations of CRISPRi

In comparison with pre-dating technology, namely RNA interference (RNAi), CRISPRi demonstrates several advantages, including increased specificity, fewer off-target effects (Heintze *et al*, 2013; Hsu *et al*, 2013; Qi *et al.*, 2013; Evers *et al*, 2016; Morgens *et al*, 2016), and increased reproducibility (Shalem *et al.*, 2014; Wang *et al.*, 2014). As CRISPRi exerts its action in the nucleus by repressing gene transcription, it can be targeted to promoters, enhancers and other genomic regulatory regions (Fulco *et al*, 2016), unlike RNAi which mediates the degradation of mRNA. This enables the interrogation of a broader range of genetic elements for their effects on screen readouts. However, as RNAi is mediated by the delivery of short hairpin RNAs (shRNAs), relying on endogenous systems to degrade targeted mRNA, this technology is applicable to more varied cell-types without requiring genetic engineering, such as patient-derived iPSCs. CRISPRi, unlike RNAi, is more effective in cell lines engineered to express dCas9 or which can be easily transduced with sgRNA and Cas9-expressing lentiviral vectors, potentially limiting its applicability in some cell types.

The major advantage of CRISPRi over CRISPRn is its ability to silence gene expression without introducing permanent modifications in the genome. This enables reversible knockdown of gene expression (Mandegar *et al*, 2016), and is an advantage for the longitudinal study of gene silencing due to reduced compensation with CRISPRi than CRISPRn (Rossi *et al*, 2015). Furthermore, the phenotypic study of essential genes, which impact cell survival when mutated using CRISPRn, is better suited to the incomplete gene silencing induced by CRISPRi (Wang *et al.*, 2015). In particular, as individual sgRNAs have been shown to be more or less effective, the level of silencing or activating effect can be tuned to study the consequences of increased or decreased gene modulation (Jost *et al*, 2020). This may

be particularly useful for the screening of candidate genes identified by GWAS at risk loci, as CRISPRi or CRISPRa may phenocopy the effects of single nucleotide polymorphisms at larger scale than CRISPRn-mediated genome editing. Indeed, genomic modification by CRISPRn also results in a mixed population of cells with variable levels of protein activity, gene expression or gene splicing.

The sgRNA/dCas9 complex of CRISPRi is effective when targeted to a narrow window (-50 to 300 bp) around the transcription start site (TSS) (Gilbert *et al.*, 2014). Consequently, silencing genes which possess multiple TSSs or cryptic TSSs with a single sgRNA may be ineffective using CRISPRi and may instead require targeting by several sgRNAs to achieve silencing of all isoforms. Targeting loci at bidirectional promoter may also produce off-target effects as CRISPRi has been shown not to be strand specific (Howe *et al*, 2017). Additionally, as CRISPRi silences gene expression through transcription initiation, it effectively targets isoforms arising from alternative splicing but does not provide a mean of modulating the levels of individual isoforms. As CRISPRn is able to induce specific changes in splice sites, it may be advantageous in these applications to enable the production of specific isoforms or enabling exon removal (Wang *et al*, 2024).

1.4.3 Genome-wide CRISPRi screening

The first genome-wide CRISPRn screens demonstrated that robust results in complex biological systems could be obtained on a large scale, providing evidence that CRISPR technology is applicable to genetic screening (Koike-Yusa *et al.*, 2014; Shalem *et al.*, 2014; Wang *et al.*, 2014; Wang *et al.*, 2015). Pathway and gene discovery, therapeutic target discovery, and mechanistic interrogation are all possible applications of genome-scale screening, typically utilising a simple readout such as cell survival or proliferation (Li *et al*, 2019b; Tian *et al.*, 2019; Tian *et al.*, 2021; Guo *et al*, 2023). The use of fluorescence-activated cell sorting (FACS) also enables the identification of populations of interest on the basis of a fluorescently-linked phenotype (Kanfer *et al*, 2021; Sanchez *et al*, 2021; Wu *et al*, 2022), for example enabling the identification of genes regulating the levels of endogenous α-synuclein expression (Santhosh Kumar *et al*, 2024).

Several studies have demonstrated that the parallel use of CRISPRi and CRISPRa enables the generation of highly complementary datasets (Gilbert *et al.*, 2014; le Sage *et al*, 2017; Schmidt *et al*, 2022) which provide increased insight into the complex regulation of biological processes. This approach uncovered the role of the lysosomal protein prosaposin in lipid processing at the lysosome and in regulating cellular ROS (Tian *et al.*, 2021). Recent areas of advancement have been in increasing the number of readouts that can be obtained from pooled screens, such as integrating microscopy information in flow cytometry workflows (Tsubouchi *et al*, 2024) or adapting pooled screens to high-content microscopy (reviewed in Walton *et al*, 2022).

1.4.4 Arrayed CRISPRi screening

Unlike pooled screens which typically have a single, easily-measured readout, arrayed screens generate information-rich datasets which can be subsequently mined for information on cell survival, morphology, and levels of proteins of interest through multiplex immunocytochemistry or cell-painting assays (Franks *et al*, 2024). Arrayed screens have also historically sacrificed throughput and scale to achieve higher sensitivity to weak phenotypes. For example, an arrayed CRISPR screen for host factors essential for the infection of HeLa cells by coxsackievirus B3 identified 8 candidate hit genes, whereas pooled screening only identified a single gene, attributable at least in part to increased signal-to-noise ratios (Kim *et al*, 2018). Arrayed CRISPR screens have also outperformed arrayed siRNA screens due to increased consistency of sgRNAs targeting the same gene (Tan & Martin, 2016).

Due to more complex delivery and requirement for automated liquid handling, early arrayed CRISPR screens were more limited in scale, but as these technologies have become increasingly advanced the scale of screens has also increased exponentially (Hultquist *et al*, 2016; Strezoska *et al*, 2017). Arrayed CRISPR screens are now being conducted at the scale of the druggable genome, with 7795 genes having recently been screened for their effects on the delivery of mRNA into cells by lipid nanoparticles (Ross-Thriepland *et al*, 2020). A new method for the generation of genome-wide CRISPRi, CRISPRa and CRISPRn arrayed libraries will no doubt soon enable arrayed genome-wide CRISPR screens to be performed (Yin *et al*, 2025).

1.4.5 Applications of CRISPRi to disease modelling

CRISPR technologies enable the genetic modification of model systems such as iPSCs and iPSC-derived cell lines to recapitulate disease-associated mutations and phenotypes. CRISPRi and CRISPRa are particularly useful in an isogenic background, allowing direct comparisons of gene expression modifications. In this way, study of phenocopying models allows the identification of mechanisms and pathways underlying phenotypes, providing greater understanding of disease-causing mutations (Franks *et al.*, 2024).

1.5 Aims

Given the link between α-synuclein aggregation, mitochondrial dysfunction and the alteration of mitophagy, as well as the lack of functional information on candidate risk genes at GWAS-identified loci, the aims of this thesis are as follows:

1. Investigate the accumulation of pS65Ub secondary to pS129-positive aggregate formation in a human iPSC-derived neuronal model.
    a. Optimise and validate *in vitro*-aggregated α-synuclein PFFs as a means of modelling the process of α-synuclein aggregation in iPSC-derived neurons.
    b. Investigate the spatial and temporal association of pS65Ub and pS129 in the seeded aggregation model.
2. Study the impact of α-synuclein aggregation on mitochondrial and lysosomal function in human neurons.
    a. Identify morphological consequences of α-synuclein PFF-seeded aggregation in mitochondria and lysosomes.
    b. Study the effect of pS129-positive aggregate formation on mitochondrial membrane potential, ROS and ATP production.
    c. Determine the effect of PFF treatment on lysosomal protease function.

3. Identify candidate risk genes that modulate the rate of α-synuclein aggregation or the α-synuclein-induced accumulation of pS65Ub.
    a. Construct a library of CRISPRi sgRNA-expressing lentiviruses targeting candidate genes at PD GWAS risk loci.
    b. Conduct an arrayed screen to identify risk genes that alter the levels of PFF-seeded pS129 and pS65Ub in iPSC-derived cortical neurons.
    c. Validate pS129 and pS65Ub-modulating preliminary hits in human iPSC-derived dopaminergic neurons.

2 Materials and Methods

2.1 Cell culture

2.1.1 iPSC-derived i^3 cortical neurons

2.1.1.1 Thawing

The cryopreserved G3dCas9 iPSC line was obtained from the Michael Ward laboratory (National Institute of Health, USA) and thawed as follows. Matrigel (Corning) was prepared by diluting a 2.5 mg/ml aliquot in cold KnockOut™ DMEM medium (Gibco) to a final concentration of 100 µg/ml. A T75 flask (Corning) per line was coated with 4 to 5 ml of cold Matrigel and incubated at 37°C for at least one hour. In the meantime, 10 ml of KnockOut™ DMEM medium was added to a 15 ml conical tube (Corning) and warmed to 37°C. Just before thawing, the Matrigel was aspirated from the coated flask and replaced with mTeSR™1 Plus (STEMCELL Technologies) medium supplemented with 10 µM Rho-associated kinase (ROCK) inhibitor (ApexBio). Cryovials were kept on dry ice until the moment of thaw, where they were placed in a 37°C water bath until almost completely melted. 1 ml of KnockOut™ DMEM from the prepared 15 ml conical tube was added to the cryovial, the contents resuspended and transferred to the conical tube. The cells were pelleted by centrifugation at 300 *x g* for 5 minutes at room temperature. The pellet was resuspended in mTeSR™1 medium supplemented with 10 µM ROCK inhibitor and the contents of the conical tube were transferred to the coated T75 flask. The culture was placed in an incubator at 37°C, 5% CO_2.

2.1.1.2 Maintenance of iPSC cultures

The culture and maintenance of G3dCas9 iPSCs was conducted as published by Fernandopulle and colleagues (Fernandopulle *et al*, 2018), with minor modifications. Briefly, iPSC cultures were given a full media change every other day, with 15 ml mTeSR™1 Plus medium warmed to room temperature. Cells were colony passaged 1:6 when they reached 60-70% confluency. A 0.05M

ethylenediaminetetraacetic acid (EDTA) solution was prepared by diluting a 0.5M EDTA solution (Invitrogen) in phosphate-buffered saline (PBS). The medium was aspirated from the flask and the cells were washed once with EDTA. 5 ml of 0.05M EDTA was added to the flask and incubated at 37°C until the cells became rounded and close to detachment. The EDTA solution was then aspirated, and the cells vigorously washed off the culture surface with mTeSR™1 Plus medium, using a serological pipette and pipette controller. The cell suspension was immediately transferred to a previously prepared Matrigel-coated flask with mTeSR™1 Plus medium.

2.1.1.3 Differentiation of i^3 cortical neurons

Induction

G3dCas9 iPSC cultures were replated for induction when they achieved ~70% confluency, on day *in vitro* (DIV) 0. The cells were briefly washed with PBS, then enzymatically lifted by incubating for 5 minutes at 37°C with StemPro™ Accutase™ (Life Technologies). The Accutase™ was neutralised and the cells washed off the culture surface using 5 ml of KnockOut™ DMEM and the whole cell suspension was transferred to a 15 ml conical tube. After thorough mixing using a serological pipette and pipette controller, 20 µl of the cell suspension was transferred to two new tubes for cell counting. The 15 ml conical tube was centrifuged at 300 *x g* for 5 minutes, at room temperature, to pellet the cells. 1 µl of Solution 18 (ChemoMetec) was added to the counting tubes and mixed. 10 µl of this cell suspension was subsequently added to an A8 slide NC-Slide A8™ (ChemoMetec) and the cells quantified using the NucleoCounter NC-250™ automated cell counter (ChemoMetec).

Following centrifugation, the cell pellets are resuspended in 1 ml of mTeSR1™ Plus medium supplemented with 10 µM ROCK inhibitor, and 10-15 million cells plated in a T75 flask containing 15 ml of Induction medium (IM) which is composed of DMEM/F12 (Gibco™), 1X N2 supplement (Gibco™), 1X non-essential amino acids (Gibco™), 1X Glutamax (Gibco™) and supplemented with 10 µM ROCK inhibitor and doxycycline at a final concentration of 2 µg/ml.

Differentiation

During the differentiation, the medium was fully changed daily with IM supplemented with 2 µg/ml doxycycline but no ROCK inhibitor until DIV 3, when the cells were again replated similarly to the procedure outlined above.

Coating

On DIV 0, the final experimental plates were pre-coated with 2% polyethylenimine (PEI), by diluting 100 µl PEI solution in 4.8 ml borate buffer (100 mM boric acid, 25 mM sodium tetraborate, 75 mM sodium chloride, pH 8.4 in H_2O). This 10X stock solution was then diluted 1:10 in ddH_2O and added to culture plates at half the culture volume (25 µl for half-area 96 well plates). The plates were then incubated at 37°C overnight. In early experiments, plates were instead coated with poly-L-ornithine (PLO) by diluting 10 mg of powdered PLO in 5 ml borate buffer, which was further diluted 1:10 in ddH_2O.

On DIV 1, the plates were washed six times with sterile ddH_2O. Following the washes, the plates were dried using the laminar air flow in a tissue culture biological safety level two cabinet (BSLII).

On DIV 2, the dried plates were coated with 180 µg/ml Geltrex™ (or 10 µg/ml laminin (Sigma-Aldrich), in early experiments) diluted in cold DMEM KO medium (ThermoFisher Scientific). This was again incubated at 37°C overnight. Prior to replating the neurons on DIV 3, the laminin or Geltrex™ was aspirated from the cells and half the normal cell culture volume of maturation medium was added to the wells.

Replating

On DIV 3, cells were lifted using Accutase™, counted, centrifuged and subsequently resuspended in maturation medium to 720,000 cells per ml for plates destined for confocal microscopy, and 2,000,000 cells per ml for plates destined for biochemical analyses such as Western Blot and qRT-PCR. The maturation medium was composed of BrainPhys™ (STEMCELL Technologies), supplemented with 1X B27 supplement (Gibco™), 10 µg/ml brain-derived neurotrophic factor (BDNF) (PeproTech), 10 µg/ml neurotrophin-3 (NT-3) (Peprotech), 2 µg/ml doxycycline (Sigma-Aldrich), and 1 µg/ml laminin

(Gibco™). Half a normal culture medium volume of the cell suspension was added to the final experimental plates.

Following replating, half the culture medium was replaced biweekly with maturation medium as described above, minus the doxycycline, until the experimental timepoint was achieved.

Freezing

Cells at the iPSC or differentiated (DIV 3) stage were lifted using Accutase™, counted, centrifuged and resuspended at a density of 3.5 million cells/ml (at the iPSC stage) or ~25-30 million cells/ml (at DIV 3 stage) in 10% DMSO in FBS. The vials were quickly transferred to a freezing container (Corning), and frozen overnight at -80°C. The vials were then stored long term in liquid nitrogen.

Table 1. Induction medium composition for i^3 cortical neurons

Reagent	Final concentration	Manufacturer	Catalogue number
DMEM F/12	-	Gibco™	11320033
100X N2 supplement	1X	Gibco™	17502048
100X non-essential amino acids	1X	Gibco™	11140050
100x L-glutamine	2 mM	Gibco™	25030081
Doxycycline	2 ng/ml	Sigma-Aldrich	D9891

Table 2. Maturation medium composition for i^3 cortical neurons

Reagent	Final concentration	Manufacturer	Catalogue number
BrainPhys™	-	STEMCELL Technologies	05790
50X B27 supplement	1X	Gibco™	17504044
BDNF	10 ng/ml	PeproTech	450-02
NT-3	10 ng/ml	PeproTech	450-03
Laminin	1 µg/ml	Gibco™	23017015
Doxycycline (only on day 3)	2 ng/ml	Sigma-Aldrich	D9891

2.1.1.4 Generation of stable cell CRISPRi knockdown lines

The G3dCas9 cell lines were thawed as described above and expanded until they achieved ~70% confluency, at which point they were replated at a density of 800,000 cells/well in a 6-well cell culture plate (Corning) coated with Matrigel. The iPSCs were replated into mTeSR1™ Plus medium containing 30 µl lentiviral vectors expressing a non-targeting sgRNA (NT), or expressing a sgRNA against *PINK1*, *PRKN*, *USP30*, *PPEF2*, *NIX*, *BNIP3* or *SNCA*. One the day following replating and transduction, the

medium was removed, the cells were washed 5 times with PBS, and the medium was replaced once more with mTeSR1™ Plus. Two days after transduction, the medium was replaced with mTeSR1™ Plus containing 1 µg/ml of puromycin to begin selection of cells expressing the sgRNA vector. The cells were selected for 7-9 days and passaged once with puromycin selection, until >95% of cells were positive for the sgRNA cassette, as assessed by nuclear mTagBFP2 reporter expression. The iPSC lines generated were frozen down as described above.

2.1.2 SH-SY5Y

Neuroblastoma SH-SY5Y cells were obtained from the European Collection of Authenticated Cell Cultures (ECACC), expanded and cryopreserved prior to my arrival in the laboratory. My colleague Katrina Savory transduced SH-SY5Y with a lentiviral *SNCA*-EGFP overexpression vector and sorted the cells by flow cytometry to obtain high-expressing, medium-expressing and low-expressing populations, expanded and banked for future use (unpublished data).

2.1.2.1 Thawing

SH-SY5Y vials were placed on dry ice until thawing in a water bath at 37°C. A 15 ml conical tube was prepared containing 10 ml of DMEM/F12 (Gibco™), 10% foetal bovine serum (FBS) (Merck Life Science) and 1% penicillin and streptomycin (Life Technologies). Once the vial was almost completely thawed, 1 ml of medium was added to the cryovial, mixed, and the contents of the cryovial transferred back into the conical tube. The cells were then centrifuged at 300 *x g* for 5 minutes, the supernatant was aspirated and the pellet was resuspended in 1 ml of medium. The cells were plated in T75 flasks containing 15 ml of medium.

2.1.2.2 Maintenance

Cultures of SH-SY5Y cells were split when they reached approximately 80% confluency. Cells were lifted by removing the medium and incubating for 5 minutes at 37°C in 0.25% trypsin-EDTA (Life Technologies). The trypsin solution was neutralised by adding a 7 ml of medium (DMEM/F12, 10% FBS and 1% penicillin, streptomycin) and the cell suspension was transferred to a 15 ml conical tube. The cells were centrifuged at 300 *x g* for 5 minutes at room temperature, the supernatant aspirated and

the pellet resuspended in 5 ml of medium. 500-1000 µl of cell suspension were transferred to a new T75 flask containing 15 ml of medium, for a 1:10 or 1:5 split.

2.1.3 HEK-293T

The HEK 293T Lenti-X™ cell line was obtained from Takara Bio Inc. This HEK cell line has high transfection rate, making them ideal for lentiviral vector production (Takara).

2.1.3.1 Thawing

Vials of HEK 293T cells were transferred from liquid nitrogen to dry ice until thawing. Thawing was performed similarly to the SH-SY5Y lines, except the culture medium was 10% FBS in DMEM (Gibco™), and without penicillin and streptomycin.

2.1.3.2 Maintenance

HEK 293T cultures were split at ~80% confluence. The medium was aspirated and replaced with 0.25% trypsin-EDTA, and incubated at 37°C for 3 minutes, until the cells were detached from the surface of the plate. Culture medium (10% FBS in DMEM) was added to neutralise the trypsin-EDTA, and the contents of the flask were transferred to 15 ml conical tubes. The cells were centrifuged and resuspended as described in 2.1.2.2. 500-1000 µl of cell suspension were transferred to new flasks, for a 1:5 or 1:10 split.

2.1.4 iPSC-derived dopaminergic neurons

2.1.4.1 Thawing

Control and *SNCA* triplication patient iPSC lines were obtained from StemBANCC and genetically engineered to express a hygromycin-selectable dCas9-KRAB construct by Dr Maria Claudia Caiazza (unpublished data). 2 wells of a 6-well plate (Corning) per iPSC line were coated with Matrigel and incubated at 37°C for 1 hour. Vials were transferred from liquid nitrogen to dry ice, then thawed quickly in a 37°C water bath and the contents transferred to 10 ml of DMEM KO medium in a 15 ml falcon tube. The cells were pelleted by centrifugation at 300 x g for 5 minutes at room temperature, the supernatant aspirated and the pellet resuspended in 2 ml mTeSR™1 Plus (STEMCELL Technologies)

medium. The Matrigel-coated wells were prepared by aspirating the coating and replacing it with 1 ml/well of mTeSR™1 Plus medium. 1 ml of cell suspension was transferred to each coated well, the plate was swirled in a figure eight pattern to distribute the cells, and the plates incubated at 37°C, 5% CO_2.

2.1.4.2 Maintenance and antibiotic selection of iPSC cultures

iPSC cultures were given a full media change every other day with mTeSR™1 Plus medium. Upon reaching ~50% confluency after thawing, cultures were fed with medium containing 50 µg/ml hygromycin B (Life Technologies) for 2 days, refreshing the medium each day, before selection medium was replaced for another 2 days by mTeSR™1 Plus without hygromycin. Pulses of selection were applied in this manner, 2 days on, 2 days off, with passages in medium without selection, until >90% of the cells showed positivity for the nuclear mNeon Green signal reporting dCas9-KRAB construct positivity. As a final step, the cells were then passaged in medium containing hygromycin, yielding cultures >95% dCas9-KRAB-positive. Cells were passaged as colonies as described in section 2.1.1.2.

2.1.4.3 Differentiation of dopaminergic neurons

iPSC cultures were differentiated to dopaminergic neurons as previously described (Williamson *et al.*, 2023; Williamson *et al*, 2025), with modifications. iPSCs were plated at 1.2 million cells/well in 6-well plates two days prior to the start of differentiation, and differentiation commenced only when all the lines reached >90% confluency.

Table 3. DMEM KO KSR base medium composition

Reagent	Amount/Concentration	Manufacturer	Catalogue number
DMEM KO	410 ml	Gibco™	10829018
KSR serum replacement	75 ml	Gibco™	10828010
β-Mercaptoethanol	10 µM	Sigma-Aldrich	M6250
L-glutamine	2 mM	Gibco™	25030081
100X non-essential amino acids	1X	Gibco™	11140050

Table 4. NNB base medium composition

Reagent	Amount/Concentration	Manufacturer	Catalogue number
Neurobasal	500 ml	Gibco™	21103049
100X N2 supplement	0.5X	Gibco™	17502048
50X B27 supplement	0.5X	Gibco™	12587010
L-glutamine	2 mM	Gibco™	25030081

Table 5. NB base medium composition

Reagent	Amount/Concentration	Supplier	Catalogue number
Neurobasal	500 ml	Gibco™	21103049
50X B27 supplement	1X	Gibco™	12587010
L-glutamine	2 mM	Gibco™	25030081

Table 6. Growth factors and small molecules for dopaminergic neuron differentiation

Reagent	Stock concentration	Final concentration	Dilution	Supplier	Catalogue number
LDN	1.179 mM	118 nM	1:10,000	Sigma-Aldrich	ab120797
SB	10 mM	10 µM	1:1000	Bio-Techne	1614
SHH	100 µg/ml	100 ng/ml	1:1000	Bio-Techne	1845-SH-500
FGF8a	500 µg/ml	100 ng/ml	1:5000	Stratech	16124-HNAE-SIB
Purmorphamine	10 mM	2 µM	1:5000	Bio-Techne	4551/10
CHIR	10 mM	3 µM	1:3333	Bio-Techne	4423
ROCK inhibitor	10 mM	10 µM	1:1000	Tocris	1254
BDNF	100 µg/ml	20 ng/ml	1:5000	PeproTech	450-02
GDNF	100 µg/ml	20 ng/ml	1:5000	PeproTech	450-10
TGFβ3	10 µg/ml	1 ng/ml	1:10,000	PeproTech	100-36E
DAPT	100 mM	10 µM	1:10,000	Abcam	ab120633
Ascorbic acid	0.2 M	0.2 mM	1:1000	Sigma-Aldrich	A4544
dcAMP	100 mM	0.5 mM	1:200	Sigma-Aldrich	D0627
Antibiotic/antimycotic	100X	1X	1:100	Thermo-Fisher	15240062

iPSCs were fed on DIV 0 with DMEM KO KSR medium supplemented with LDN and SB. The medium was changed on DIV 1 to include LDN, SB, SHH, FGF8a and purmorphamine, and half-changed with fresh medium on DIV 2. This same medium was prepared on DIV 3 and 4, supplemented with CHIR. On DIV 5 through 10, DMEM KO KSR basal medium was mixed stepwise with NNB basal medium, from 75% DMEM KO KSR, 25% NNB on DIV 5 and 6, 50% of both on DIV 7 and 8, and 25% DMEM KO KSR, 75% NNB on DIV 9 and 10. The mixed basal medium was combined with LDN, SHH,

purmorphamine, FGF8a and CHIR on DIV 5 and 6, and only LDN and CHIR through DIV 7 to DIV 10.

Neurons were split 2 wells to 3 wells on DIV 10 + 1 by washing cells with PBS, aspirating the wash and incubating the cells with 1 ml/well Accutase™. 1 ml DMEM KO was used to wash cells from the surface and transfer them to a 15 ml falcon tube for centrifugation at 300 x g for 5 minutes at room temperature. The pellets were resuspended in DIV 10 medium supplemented with 10 µM ROCK inhibitor, and the cell suspension was distributed to fresh Geltrex-coated wells. 24 hours post-splitting, the medium was fully changed to DIV 10 medium, composed of 25% DMEM KO KSR, 75% NNB, supplemented with LDN and CHIR. The medium was half-changed or fully changed in alternation each day following until DIV 10 + 7.

On DIV 11, the fully was fully changed to maturation medium, which was composed of NB, CHIR, BDNF, GDNF, TGFβ3, DAPT, ascorbic acid, and dcAMP. On subsequent days, the medium was fully changed or half changed in alternation, removing CHIR on DIV 13. On DIV 16, the cells were replated as described in section 2.1.1.3 on poly-L-ornithine and Geltrex-coated plates, in dopaminergic neuron maturation medium composed of NB, BDNF, GDNF, TGFβ3, DAPT, ascorbic acid, dcAMP, ROCK inhibitor and antibiotic/antimycotic. The cells were maintained until the final experimental timepoint by half-feeding neurons three times a week in maturation medium with antibiotic/antimycotic, removing the ROCK inhibitor after DIV 16.

2.2 Immunocytochemistry

Mature cortical neurons or SH-SY5Y cells were fixed by removal of the medium and incubation with 4% paraformaldehyde (Life Technologies) for 15 minutes at room temperature. The fixing solution was then replaced with PBS containing 0.02% sodium azide and the plates were stored at 4°C until immunocytochemistry was performed.

The cells were permeabilised for 15 minutes in 0.1% Triton X-100 (Merck) in PBS and subsequently blocked in 10% FBS in PBS for 1 hour at room temperature. The primary antibodies were diluted in

blocking buffer (10% FBS in PBS) at the concentrations in Table 7 and the cells were incubated with this solution overnight at 4°C, in a sealed plate to prevent evaporation. The cells were subsequently washed three times with PBS for 5 minutes, after which secondary antibodies targeting the primary antibody's species were diluted at 1:1000 in blocking buffer (10% FBS in PBS). The secondary antibody solution was incubated for one hour at room temperature, after which the cells were washed three times once more. If using the rabbit anti-pS129 antibody (Abcam) in combination with the rabbit anti-pS65Ub antibody directly conjugated to Alexa Fluor 488 (Millipore), the neurons were first stained with the anti-pS129 antibody (Abcam) and anti-MAP2 antibody (Millipore) overnight at 4°C, then washed as described and stained with species-specific secondary antibodies for one hour at room temperature. A second blocking step was performed for one hour at room temperature, following which the neurons were incubated overnight with the directly-conjugated anti-pS65Ub antibody (Millipore) at 4°C, then washed three times. The plates were stored in PBS at 4°C until imaging on the PerkinElmer Opera Phenix confocal microscope.

For 384-well format plates, the steps described were performed using the CyBio-Felix liquid handler (Analytik Jena).

Table 7. Details of primary antibodies and dilutions

Protein target	Clone	Host	Dilution	Manufacturer	Catalogue number
pS65Ub	E62JT	Rabbit	1:1500	Cell Signalling	62802
pS65Ub-AF488	-		1:500	Sigma-Aldrich	ABS1514-I-AF488
pS65Ub-AF647	E5T1W	Rabbit		Cell Signalling	83816
α-Synuclein	EP1536Y	Rabbit	1:3000	Abcam	ab51253
α-Synuclein	81A	Mouse	1:40,000	Abcam	ab184674
TOM20	F-10	Mouse	1:500	Santa Cruz	sc-17764
TOM20	-	Rabbit	1:500	Abcam	ab220822
MAP2	-	Chicken	1:2000	Millipore	AB5543
LAMP1	H4A3	Mouse	1:500	Santa Cruz	sc-20011
TH	-	Rabbit	1:500	Millipore	AB152

Table 8. Details of secondary antibodies and dilutions

Protein target	Fluorophore	Host	Dilution	Manufacturer	Catalogue number
Rabbit IgG	488	Donkey	1:1000	Invitrogen	A21206
Chicken IgG	555	Goat	1:1000	Invitrogen	A32932
Mouse IgG	647	Donkey	1:1000	Invitrogen	A31571
Rabbit IgG	555	Donkey	1:1000	Invitrogen	A31572
Rabbit IgG	647	Donkey	1:1000	Invitrogen	A31573

Sheep IgG	488	Donkey	1:1000	Invitrogen	A11015
Rabbit IgG	647	Donkey	1:1000	Invitrogen	A32795

2.3 qRT-PCR

Samples were collected by resuspending cells in medium, collecting the suspension in 1.5 ml Eppendorf tubes and centrifuging at 300 x g for 5 minutes. The supernatants were removed and the pellets were frozen and stored at -80°C. RNA extraction was performed using the RNeasy Mini kit (QIAGEN), as per manufacturer's instructions and the RNA yield quantified using the Nanodrop™ spectrophotometer (ThermoFisher). Up to 0.5 µg of RNA was reverse transcribed into cDNA with the High-Capacity RNA-to-cDNA™ kit (ThermoFisher), as per manufacturer's instructions, and the yield was quantified using the Nanodrop™ spectrophotometer.

qRT-PCR in a 384-well format was performed by combining PowerUp™ SYBR™ Green Master Mix (ThermoFisher), 0.5 µl each of forward and reverse primers, 1.5 µl of PCR-grade double distilled H_2O (ddH_2O), and 2.5 µl of 1:10 diluted cDNA in each well. The QuantStudio™ ViiA 7 system was used to perform the qPCR reaction, and the data analysed using the ΔΔCT method. The data was normalised to the housekeeping gene *GAPDH*.

Table 9. Primer sequences for qPCR

Gene	Forward	Reverse
ANK2	AGCACTCTTTCCCCAAACTC	TCTCTGATGTTTCTGTTCCTGG
MAP2	CAGGAGACAGAGATGAGAATTCC	CAGGAGTGATGGCAGTAGAC
TUBB3/TUJ1	TTTGGACATCTCTTCAGGCC	TTTCACACTCCTTCCGCAC
VGLUT1/SLC17A7	TCAATAACAGCACGACCCAC	TCCTGGAATCTGAGTGACAATG
SYN1	CCCCAATCACAAAGAAATGCTC	ATGTCCTGGAAGTCATGCTG
PSD95/DLG4	AGTCAGAAATACCGCTACCAAG	CCGTTCACCTGCAACTCATATC
CUX1	TCACCTCTTCATAGTCAGCCT	CAGCCAGATCTCACAGCTTG
PAX6	GCCCTCACAAACACCTACAG	TCATAACTCCGCCCATTCAC
NESTIN	TGCGGGCTACTGAAAAGTTC	GGCTGAGGGACATCTTGAG
NGN2	TACCTCCTCTTCCTCCTTCA	GACATTCCCGGACACACAC
SNCA	ATTCGACGACAGTGTGGTGT	GTTTTCTCAGCAGCAGCCAC
GAPDH	TCATCATCTCTGCCCCCTCT	TCATGGATGACCTTGGCCAG

2.4 Western Blot

i^3 Neurons were plated at a density of two million cells per well in a 6-well plate format and harvested at several timepoints over the course of maturation by resuspending the cells in maturation medium, centrifuging at 300 x g for 5 minutes at 4°C, followed by careful and complete removal of the medium. The dry pellet was stored at -80°C. Pellets were resuspensed in 100 µl radioimmunoprecipitation assay (RIPA) buffer supplemented with phosphatase and protease inhibitors (Roche) and sonicated for a total of 5 minutes in a bath sonicator (Qsonica) at 20 kHz, 20% amplitude for 10 seconds on, 10 seconds off at 5°C. The protein concentration was quantified using a bicinchoninic acid (BCA) assay. Briefly, the samples were diluted 1:4 in ddH_2O, and 4 ul/well of sample was added to a clear 384-well plate, in triplicate. A 1:50 solution of BCA reagent A to BCA reagent B (ThermoFisher™) was prepared and 32 µl of reagent was added to each well. The concentration of each sample was measured after 20 minutes incubation at 37°C, and the protein concentration determined against a standard curve ranging from 2 mg/ml to 62.5 µg/ml bovine serum albumin.

The protein concentration of each sample was normalised to 0.5 µg/µl and Laemmli buffer was added to a final concentration of 1X. The samples were boiled at 95°C for 5 minutes. 15 µg of protein were run in a Mini-Protean TGX pre-cast gel (Bio-Rad) at 200 V in 25 mM Tris, 192 mM glycine and 0.1% SDS at pH 8.3 and transferred to a PVDF membrane using the Trans-Blot Turbo transfer system and transfer pack (Bio-Rad) for 11 minutes at 2 amps. The membrane was immediately fixed in 4% PFA for 15 minutes at room temperature. The membrane was subsequently blocked in 5% milk in tris-buffered saline (TBS) with 0.1% Tween (TBS-T) for one hour at room temperature, then incubated with a primary antibody solution (anti-α-synuclein, MJRF1, ab138501, Abcam) at 1:10,000 overnight at 4°C. The membrane was washed three times in TBS-T, then incubated for 1 hour at room temperature in secondary antibody dilution in 5% milk in TBS-T (goat anti-rabbit, 1706515, Bio-Rad) at 1:5000. The membrane was again washed three times in TBS-T, then developed using Immobilon chemiluminescence substrate (Sigma-Aldrich) and the Chemidoc imaging system (Bio-Rad). The membrane was washed three more times in TBS-T and incubated for one hour at room temperature in

primary antibody solution (anti-β-actin, ab49900, Abcam), then developed again. The density of α-synuclein bands was normalised to the density of the β-actin bands prior to fold change normalisation and graphing.

2.5 *In vitro* aggregation of α-synuclein fibrils

2.5.1 Fibril aggregation

1 mg of α-synuclein monomer was obtained commercially (Stratech) and resuspended in 1 ml of ddH_2O to a concentration of 1 mg/ml. The protein suspension was aliquoted into 500 µl aliquots in 1.5 ml Eppendorf tubes and aggregated by shaking at 1000 rpm, 37°C for 7 days. Following aggregation, the fibrils were sonicated using a probe sonicator (Hieschler) at 0.2 s interval, 25% amplitude in 5-10 minute intervals for 25 minutes, or for 12 minutes in a bath sonicator (QSonica) at 45% amplitude and 3 s on, off intervals.

2.5.2 Electron microscopy

3 mm size 300 mesh carbon-coated copper grids (TAAB) were prepared for staining using plasma coating (PELCO EasiGlow). The fibrils were diluted 1:3 in PBS and then incubated on the grid for 2 minutes by inverting the grid on 10 µl droplets of the sample. The grid was incubated on 20 µl 2% uranyl acetate, followed by a wash in ddH_2O, then dried fully before imaging at the JEOL 1400 120kV transmission electron microscope. Images were processed in Image J by overlaying the fibrils with selections of the same length. The fibrils from 6 fields of view a 20,000x objective were quantified and plotted as a distribution, or counted to estimate the relative number of fibrils per preparation. The Euclidean distance was calculated as a measure of fibril coagulation by measuring the distance between the centre points of each fibril within a field of view.

2.5.3 Thioflavin T fluorescence measurement

α-Synuclein fibrils were diluted to a final concentration of 100 µg/ml in PBS. Thioflavin T (ThT) (Sigma-Aldrich) powder was dissolved to a stock concentration of 1 mM in PBS and stored at 4°C. α-Synuclein fibrils and ThT solution were combined in 120 µl of PBS to a final concentration of 7 µg/ml

fibrils and 25 µM, respectively. The solution was incubated in the dark at 37°C, without agitation, prior to fluorescence reading on the Pherastar spectrophotometer (BMG Labtech).

2.5.4 Quality control

SH-SY5Y overexpressing the *SNCA* gene under a cytomegalovirus (CMV) promoter were seeded in a 96-well half area plate (Greiner) at a density of 1500 cells/well, incubated at 37°C, 5% CO_2 until settled on the dish, then treated with 0.12-2.4 uM of aggregated α-synuclein fibrils diluted in cell culture medium. The medium was fully changed 24 hours after treatment with fibrils, and the cells were grown for a further 4 days. The cells were fixed as described in Section 2.2 and stained using immunocytochemistry for phospho-serine 129, a marker of α-synuclein aggregation. Each new batch of fibrils was directly compared with the previous batch, and an approximate, relative measure of seeding efficacy was calculated by determining the fold-change difference between two preparations and multiplying it to the seeding efficacy score of the previous preparation. The first preparation, 2021_11, was given a seeding efficiency score of 1.

2.6 α-Synuclein aggregation

2.6.1 Cortical neurons

Cortical neurons were seeded at 18,000 cells/well in a 96-well half area plate (Greiner). At DIV 10, the cortical neurons were treated with aggregated α-synuclein fibrils at final concentration 10 µg/ml diluted in media. The fibrils were incubated with the cells for 48 hours, after which the media was changed fully. The cells were then fed as described in 2.1.1.3, as normal, until DIV 24, the timepoint at which cells were assayed or fixed for immunocytochemistry.

2.6.2 Dopaminergic neurons

Dopaminergic neurons were seeded at 16,000 cells per well in a 384-well format on DIV 16. Cells were maintained by half-feed with dopaminergic maturation medium three times a week until DIV 35. α-Synuclein PFFs were diluted to 20 µg/ml in medium and the cells were treated using a half-feed with fibril-containing medium, for a final concentration of 10 µg/ml. After 48 hours, the medium was

changed fully and the cells maintained normally until DIV 49, where they were fixed and immunostained.

2.7 MitoSOX live assay

i^3 Cortical neurons were seeded at a density of 18,000 cells/well in a 96-well half area plate (Greiner). Stocks of the MitoSOX™ mitochondrial superoxide indicator (Invitrogen™) were prepared by dissolving 50 µg vials of the MitoSOX™ reagent with 26 µl of DMSO, for a final concentration of 2.5 mM, and aliquoted into 4.5 µl aliquots. These stocks were stored at -20°C until use. At the final experimental timepoint of DIV 10 or DIV 24, the neuronal cell medium was half-changed and control wells were treated with rotenone at a final concentration of 10 µM, experimental wells, with an equal concentration of DMSO, 3 hours before the start of the assay. Following incubation with DMSO or rotenone, MitoSOX™ reagent was diluted to 2.5 µM in cortical neuron maturation medium, prepared with basal BrainPhys medium without phenol red. The medium was fully changed to load cells with the MitoSOX™ reagent, and the cells were incubated for 10 minutes at 37°C, 5% CO_2. Following incubation, the medium was fully changed to fresh, phenol red-free medium without MitoSOX™. The neurons were then imaged using the 40x water immersion objective on the Opera Phenix high content imaging microscope, using a temperature-controlled chamber set to 37°C, 5% CO_2.

2.8 CellTiter-Glo® 2.0 live assay

The CellTiter-Glo® 2.0 cell viability reagent (Promega) stock (100 ml) was thawed on ice and aliquoted into 4 ml aliquots, then stored, protected from light, at -20°C. i^3 Cortical neurons were seeded at a density of 18,000 cells/well in a 96-well half area plate, and the cells were cultured until the experimental timepoint of DIV 10, or DIV 24. Control wells were treated with 30 µM of the mitochondrial toxin carbonyl cyanide m-chlorophenyl hydrazone (CCCP), whereas experimental wells were treated with an equal concentration of DMSO, for 3 hours prior to the assay. During incubation, the number of nuclei was imaged by either treating with NucBlue™ Live ReadyProbes™ Reagent (Invitrogen™), or using the mTagBFP2 nuclear reporter, using the Opera Phenix with a 20x objective.

Following treatment, the medium was then removed and replaced with 100 µl of CellTiter-Glo® reagent, diluted 1:1 in PBS. The plate was incubated with the reagent for 10 minutes at room temperature, protected from light. Subsequently, 90 µl of the supernatant was removed at transferred to an opaque, white 96-well lumitrac plate (Greiner), in the same orientation as the original plate. This plate was then loaded into the PHERAstar (BMG Labtech) and well luminescence was measured, with the gain adjusted to 20% of the highest plate value. The raw luminescence values were divided by total nuclear count, and the results expressed as luminescence intensity per nucleus, as a measure of ATP per nucleus.

2.9 JC-10 live assay

The JC-10 reagent (AAT Bioquest) is purchased as a 3 mM stock solution, thawed upon receipt and aliquoted into 6.5 µl aliquots and stored at -20°C. Cortical neurons were plated at a density of 18,000 cells/well, in a 96-well plate half area (Greiner). On the day of the assay, control wells were treated with 30 µM of CCCP, whereas experimental wells were treated with equivalent concentrations of DMSO, for 2 hours. Following incubation with the mitochondrial toxin, the JC-10 reagent was diluted to 3 µM in phenol red-free cortical maturation medium, and cells were loaded with the reagent for 1 hour, as well as re-treated with DMSO and CCCP. After the hour, the medium was removed and 50 µl of fresh, phenol red-free medium was added to each well and the plate was incubated at 37°C, atmospheric CO_2 for 15 minutes. The plate was then loaded into the PHERAstar (BMG Labtech) for imaging at excitation 485 and 520 nm, emission at 520 nm (monomeric) and 590 nm (aggregated). 5 cycles of measurements were taken, with 20 µl of 35 µM CCCP were injected on the third cycle to depolarise mitochondrial membranes. The raw data was processed by taking the ratio of the fluorescence intensity at 590 nm over the intensity at 520 nm, averaging the values of the first and second cycle as a basal measurement, as well as the fourth and fifth cycle, post-CCCP, in each well. The data was expressed as the difference between the basal measurement average and the average measurement after CCCP injection.

2.10 DQ™ Red BSA live assay

Cortical neurons were seeded at a density of 25,000 cells/well on DIV 3, and assayed at DIV 10 or DIV 31. DQ™ Red BSA 1 mg lyophilised stock was resuspended in 1 ml of PBS, to a final concentration of 1 mg/ml. 48 hours prior to assaying, control wells were treated with 0, 1, 5, 10, 20, or 40 µM of chloroquine (CQ) using a full medium change, and the cells incubated at 37°C, 5% CO_2. On the day of assaying, DQ™ Red BSA was spiked into the wells to a final concentration of 3 µg/ml, and incubated for 4 hours, 20 minutes in the cell culture incubator. The medium was then changed fully and NeuroFluor™ NeuO was added to a concentration of 1:1000 in cortical maturation medium, along with 2 drops per ml of NucBlue™ Live ReadyProbes™ Reagent. The cells were further incubated for 40 minutes, after which the cells were imaged on the Opera Phenix confocal microscope, using the 40x objective.

2.11 Preparation and cloning of sgRNAs for CRISPRi

2.11.1 Annealing sgRNAs

25 nM of top and bottom sgRNA oligonucleotides were obtained premixed in lyophilised powder format from Integrated DNA Technologies (IDT) in 96-well PCR plates. The lyophilised sgRNAs were reconstituted by dissolving in 100 µl of ddH_2O, to a stock concentration of 100 µM. To anneal the sgRNAs, 2 µl of 100 µM, premixed top and bottom oligonucleotides were combined with 25 µl of annealing buffer and 23 µl of RNase-, DNase-free ddH_2O, for a total reaction volume of 50 µl.

Table 10. 2X annealing buffer composition

Reagent	Concentration
Potassium acetate	200 mM
HEPES-KOH pH 7.4	60 mM
Magnesium acetate	4 mM

The oligonucleotides were denatured by incubation at 95°C for 5 minutes in a thermocycler (BioRad). Subsequent cooling at room temperature for 20 minutes allowed for the annealing process. The annealed oligonucleotides were stored on ice or at -20°C until the ligation step.

2.11.2 Digestion of the lentiviral backbone

The lentiviral backbone was obtained from the Michael Ward laboratory (National Institute of Health, USA) and was prepared for sgRNA ligation by double restriction enzyme digestion. The initial digestion was performed by combining the following in a 1.5 ml Eppendorf tube:

Table 11. Digestion of the sgRNA backbone with BlpI

Reagent	Amount
NEBuffer 2.1 (New England Biolabs)	2 µl
BlpI (New England Biolabs)	3 µl
Lentiviral backbone	10 µg
RNase-, DNase-free ddH_2O	To 20 µl

The digestion preparation was incubated overnight at 37°C.

Following overnight incubation, components of the second digestion reaction were added to the initial preparation in the following amounts:

Table 12. Digestion of the sgRNA backbone with BstXI

Reagent	Amount
NEBuffer 2.1 to 3.1 spike	5 µl
BstXI (New England Biolabs)	3 µl
RNase-, DNase-free ddH_2O	2 µl

Table 13. NEBuffer 2.1 to 3.1 spike composition

Reagent	Amount
NaCl	17.5 mg
Tris-HCl	29.1 mg
10X NEB buffer 2.1	200 µl
ddH_{2O}	800 µl

The preparation was incubated overnight at 37°C. The next morning, the digested backbone was purified using the Qiaquick PCR cleanup kit, as per manufacturer's instructions. The DNA concentration was quantified using the Nanodrop™ spectrophotometer. To verify the success of the digestion reaction, 100 ng of the digested product was run on a 0.8-1% agarose gel, using a previously digested sample and an undigested sample as controls. The digestion product was stored at -20°C until the ligation step.

2.11.3 Ligation of sgRNAs into the lentiviral backbone

Prior to the start of the ligation reaction, the annealed sgRNAs were diluted 1:20 in ddH_2O in a 96-well PCR plate (Starlab). The ligation reaction master mix was prepared in the following manner, scaling based on the number of sgRNAs:

Table 14. Ligation reaction (per sgRNA)

Reagent	Amount
Digested, purified backbone	20 ng
Annealed guide oligonucleotides (1:20)	0.5 µl
2X Mighty Mix Quick Ligase buffer (Takara Biosciences)	2.5 µl
RNase-, DNase-free ddH_2O	To 5 µl

The reaction was incubated at 16°C for 30 minutes, and the product was stored at -20°C until the transformation step.

2.11.4 Transformation of ligated plasmids into competent bacteria

Luria broth (LB) with agar was prepared by dissolving 37 g of powdered LB agar (Invitrogen) into 1 L of ddH_2O and autoclaving the solution. LB agar was subsequently melted by microwaving in short bursts and cooled slightly before adding carbenicillin (Gibco) to a final concentration of 100 µg/ml. 15 ml LB agar was dispensed to each petri dish, which were then left to cool and solidify at room temperature.

0.5 µl of the ligated plasmids were mixed with 10 µl STBL3 chemically-competent *E. coli* (Invitrogen) and incubated on ice for 5 minutes before streaking onto the prepared petri dishes. The petri dishes were incubated at 37°C overnight to allow for colony formation.

2.11.5 Plasmid amplification, isolation and sequencing

LB was prepared by dissolving 25 g of powdered LB into 1 L of ddH_2O and autoclaving the resulting solution. Single colonies were picked and inoculated into 6 ml of LB containing 100 µg/ml ampicillin, then incubated with agitation at 37°C, 250 rpm for 16 hours. The bacteria were pelleted by centrifugation at 2000 x g for 10 minutes at room temperature and the supernatant was removed by decanting the liquid.

Plasmids were isolated from bacterial pellets using the QIAprep Spin Miniprep kit (Qiagen) on a vacuum manifold as per the manufacturer's instructions, eluting into 1.5 ml DNA lo-bind Eppendorf tubes (Eppendorf). The DNA concentration was quantified using a NanoDrop Microvolume Spectrophotometer (ThermoFisher Scientific).

Each plasmid was prepared for sequencing by combining 5 µl 100 ng/µl plasmid DNA and 5 µl of 5 pmol/µl sequencing primer (C31, sequence: GAC ATG ATA AGA TAC ATT GA) into Mix2Seq pre-labelled tubes. Sanger sequencing was performed by Eurofins Genomics GmbH.

Vectors which failed sequencing were discarded and a new colony was picked, amplified and sequenced until sequence-verified plasmids were obtained for all newly-created guides in the study.

2.12 Lentivirus packaging

Low passage HEK-293T cells were thawed and cultured as described in section 2.1.3. 15 cm dishes (Corning) were coated with poly-L-ornithine 0.1 mg/ml (Merck) in 10% borate buffer and 90% ddH_2O (see section 2.1.1.3 on coating for borate buffer composition) and incubated for 1 hour at 37°C, 5% CO_2. The coating solution was then aspirated and the dishes left to dry slightly open in the cell culture hood.

HEK-293T cells at ~70% confluency were passaged and plated at 45 x 10^6 cells per dish in 20 ml of medium then incubated overnight to allow for cell attachment. Transfection of the plasmids was performed by combining into 1 15 ml falcon tube per plasmid 2.4 ml of room-temperature Opti-MEM™ medium (Gibco™) and 30 µl Lipofectamine™ 3000 (ThermoFisher Scientific), mixing gently and incubating this solution for 20 minutes. In another 15 ml falcon, the following reagents were combined per vector: 2.4 ml Opti-MEM™, 30 µl P3000 reagent (Lipofectamine™ Transfection Reagent, ThermoFisher), 26.4 µg psPAX6, 9 µg pMD2G, 3.6 µg pAdVantage (Addgene) and 39 µg of plasmid DNA. This reaction was mixed by gently flicking the tube and incubated for 20 minutes. Both tubes were subsequently combined and mixed, then added dropwise to the dishes of HEK-293T cells while swirling to mix the media evenly. The dishes were incubated at 37°C, 5% CO_2 for 24 hours.

A full media change was performed using 72 µl of ViralBoost Reagent (ALSTEM) and 36 ml of DMEM 1X, 10% FBS per dish and the cells were subsequently incubated for another 3 days. The medium was harvested in a 50 ml falcon tube, centrifuged at 500 x g for 10 minutes at room temperature, and the supernatant transferred to a clean 50 ml falcon tube. 12 ml of Lenti-X Concentrator (Takara Bio) was added and mixed with the supernatant by inversion, then incubated at 4°C for 3 days, during which the lentivirus particles were precipitated from the medium.

The lentivirus particles were pelleted by centrifugation at 1,500 x g for 45 minutes at 4°C and the supernatant was carefully removed without disturbing the pellet. The pellet was resuspended in 360 µl of PBS and aliquoted into 12 µl aliquots in 8-strip PCR tubes (StarLab), then stored at -80°C.

2.13 Titration of CRISPRi sgRNAs

To determine the optimal concentration to use for transduction, i^3 neurons at DIV 3 were replated at 16,000 cells/well in 25 µl medium/well in 384-well plates (Revvity). sgRNA-expressing lentiviruses were diluted 1:5 then added to a 384-well source polypropylene plate (Greiner) and the ECHO acoustic Nanodispenser (Beckman Coulter) was used to dispense 25-1500 nl of lentivirus onto the neurons. The cells were incubated overnight in lentivirus-containing medium before the virus-containing media was changed by full feeding the plates with fresh medium. The cells were subsequently fed as described in

section 2.1.1.3 for 3-4 days, when the cells were given a media change containing HCS Nuclearmask™ Deep Red (Invitrogen) at 0.5X concentration to highlight all nuclei and imaged on the Opera Phenix confocal microscope using the 20x water immersion objective at 37°C and 5% CO_2.

Dose-response curves between the percentage of transduced, mTagBFP2-positive nuclei and the amount of virus dispensed (in nl) was computed and the minimal virus dose which transduced ~70% of neurons was determined and carried forward into the screening experiments.

2.14 Arrayed CRISPRi screening in i^3 cortical neurons

2.14.1 Experimental design

Screening plate layouts were designed to account for plate-by-plate normalisation and systemic spatial effects. Five NT controls were distributed across each of the screening plates, and the sgRNA technical replicates were distributed in two groups accounting for central and peripheral as well as left- and right-hand side positioning. Control, *SNCA*, *PRKN* and *PINK1*-expressing stable iPSC lines (see section 2.1.1.4) were selected to provide positive and negative controls for the pS129 and pS65Ub assays. Control sgRNA-expressing neurons were left untreated or were treated with α-synuclein PFFs and CCCP to upregulate pS129 and pS65Ub, respectively. *SNCA*, *PRKN* and *PINK1*-expressing cells were treated with PFFs, with the *SNCA* line expected to reduced pS129 levels, the *PINK1* line expected to reduced pS65Ub levels and the *PRKN* line expected to moderately increase pS129 levels, as we have recently published (Schmidt *et al*, 2025).

After differentiation of iPSCs into i^3 cortical neurons, the cells were replated DIV 3 as described in section 2.1.1.3, with modifications. 16,000 cells/well were seeded into PEI/Geltrex™-coated 384-well Phenovue plates (Revvity) and sgRNA-expressing lentiviruses were diluted 1:3 in PBS and prepared into a source plate for dispensing using the ECHO acoustic nanodispenser as described in section 2.13. A lower dilution of the virus was used in these experiments to minimise the dispensing time, which is performed at room temperature and atmospheric CO_2 levels, and increase cell viability. The concentration of each virus was adjusted based on the titre of that virus as well as the lower dilution

used in the screening experiments (1:3 vs 1:5). The virus-containing medium was fully changed 24 hours after transduction and the cells were fed normally until DIV 10, where the cells were treated with 10 µg/ml α-synuclein PFFs as per section 2.6. On DIV 24, control wells were treated with 15 µM CCCP, carbonyl cyanide 4-(trifluoromethoxy)phenylhydrazone (FCCP) or 2 µM oligomycin/antimycin to induce pS65Ub formation for 6 hours at 37°C, 5% CO_2 and the cells subsequently fixed with 4% PFA for 15 minutes at room temperature. The PFA was removed and replaced with PBS, and the plates were sealed and stored at 4°C. The plates were subsequently stained by immunocytochemistry using antibodies against pS129 (Abcam, clone EP1536Y, Cat # 51253), MAP2 (Millipore, Cat # AB5543) and pS65Ub (Millipore, Cat # ABS1513-I-AF488) as described in section 2.2. All liquid handling steps in 384-well format were performed using the CyBio-Felix robotic liquid handler (Analytik Jena).

2.14.2 Screen analysis

The images were analysed in Harmony 5.2 software (Revvity) using a bespoke analysis pipeline detailed in Appendix Figure 47. Briefly, mTagBFP2-positive nuclei were identified and MAP2-positive cytoplasm was segmented, retaining live MAP2-positive cells on the basis of the morphology of the nucleus and the intensity of MAP2. pS129-positive aggregates were identified, their area, intensity and number evaluated and their location mapped to either the soma or neurites. Their morphology (round versus elongated) was also assessed. pS65Ub spots were identified and their area, intensity, number and co-localisation with pS129 assessed. The mean per well data was exported and further processed using R. The following analysis was performed on a per plate basis using each well as a technical replicate. The data was processed by removing wells with fewer than 500 nuclei/well to account for cell death and spatial effects on the pS129 and pS65Ub readouts were adjusted readout-by-readout using a linear model applied to both rows and columns on a per plate basis. The data was log transformed and the Z-score of each guide was calculated using the following formula, where x is the observed value and μ and σ are the mean and standard deviation of the combined 5 control sgRNAs on the plate, respectively,

$$Z = \frac{(x - \mu)}{\sigma}$$

Once the Z-score was calculated, the data from all plates was combined for downstream graphing. Graphs were generated in R using several packages: tidyverse, ggplot2, ggbreak (Xu *et al*, 2021), ggrepel and corrplot. Three independent primary screening replicates were processed in this manner and subsequently integrated by taking the mean and standard deviation of the replicate Z-scores for each sgRNA. Likely hits were identified using a Z-score threshold of ± 2. However, due to the high variability of the pS129 aggregation assay, a threshold of ± 1.5 was used to identify sgRNAs to follow up.

2.15 Flow cytometry

2.15.1 Initial protocol

Reagent	Preparation	Manufacturer	Catalogue number
Trypsin-EDTA	-	Sigma-Aldrich	T4049
FBS	-	Sigma-Aldrich	F7524
PBS	-	Gibco™	10010023
DPBS	-	Gibco™	14190136
LIVE/DEAD™ near infra-red	Reconstitute in DMSO	Thermo-Fisher	L10119
Defined trypsin inhibitor	-	Thermo-Fisher	R007100
Triton X-100	-	Merck	648466
4% PFA	Dilute 4X in PBS	Thermo-Fisher	11586711

Flow cytometry of iPSC-derived cortical neurons was performed as described previously (Sandor *et al*, 2017), with minor modifications. Differentiated i^3 neurons were seeded at 2M/well in pre-coated 6 well-plates or at 1M/well in pre-coated 12-well plates and maintained until DIV 10 or 24 as described in section 2.1.1.3.

The neurons were washed with 1 ml warm Dulbecco's PBS (DPBS) then dissociated with 900 µl warm trypsin-EDTA. After 5 minutes incubation, the cells were washed off the dish using 1200 µl defined trypsin inhibitor mix by pipetting into a single-cell solution. The solution was pipetted through a pre-wetted cell strainer (Corning) into a 50 ml falcon tube. Cold PBS was used to wash the strainer and the neurons were centrifuged at 300 x g for 5 minutes at 4°C to pellet the cells. The supernatant was aspirated, the cells then placed on ice and resuspended in 500 µl PBS. The solution was transferred to a DNA Lo-Bind tube (Eppendorf) and the cells pelleted once more by centrifugation.

One tube was re-suspended in 500 µl LIVE/DEAD™ near infra-red at 1:1000 in PBS and incubated on ice for 10 minutes, then centrifuged and the supernatant removed. The other tubes were resuspended in 30 µl PBS. 200 µl 4% PFA was added to all tubes and incubated on ice for 10 minutes. The cells were washed once with 200 µl blocking buffer (0.1% Triton X-100, 10% FBS in PBS) by centrifuging, resuspending and centrifuging once more. The cells were incubated in 200 µl blocking buffer for 1 hour at room temperature. 50 µl of cell suspension from one tube was removed and set aside as an unstained control. The cells were centrifuged and resuspended in primary antibody solution in blocking buffer (1:100 for pS129 and 1:100 for pS65Ub), then incubated for 1 hour at 4°C, on a spinning rotor. The cells labelled with the directly conjugated pS65Ub-AF488 antibody (ABS-I-AF488, Millipore) were then washed three times by pelleting and resuspending in PBS. The cells labelled with the pS129 antibody (ab51253, Abcam) were washed three times, then incubated for another hour at 4°C in secondary antibody (1:100, A32795, Invitrogen), then washed again before processing.

Flow cytometry analysis was performed on the BD LSRFortessa™ X-20 Cell Analyzer. Cells were gated first by forward and side scatter to eliminate debris as well as doublets and then by using the LIVE/DEAD™ dye to remove dead cells. pS65Ub or pS129-positivity was determined by gating based on the IgG control and vehicle-treated cells.

2.16 Correlative light and electron microscopy

For CLEM, preliminary trials were conducted on i^3 cortical neurons seeded on DIV 3 at very low density (32,000 cells/well) on 14 mm diameter, no. 1.5 alpha-numeric gridded coverslips (MatTek). On DIV 10, these cells were treated with 30 µm CCCP for 6 hours, then fixed for CLEM using 0.1% glutaraldehyde, 4% PFA in PBS at pH 7.4. After three washed in PBS, the cells were blocked for 1 hour at room temperature in blocking buffer composed of 0.1% Saponin, 10% FBS in PBS. The neurons were then incubated in primary antibody diluted in blocking buffer (see Table 15) overnight at 4°C. The neurons were then washed three more times in PBS and incubated with secondary antibodies diluted in blocking buffer at room temperature for one hour, before being washed again in PBS. The neurons were mounted on coverslips and imaged on the LSM 880 AxioImager 2 confocal microscope (Zeiss), using

the 5x and 63x oil immersion objectives. The positions of clusters of neurons on the grid were noted for downstream processing and resin embedding.

Table 15. Details of primary antibodies used for CLEM

Protein target	Clone	Host	Dilution	Manufacturer	Catalogue number
pS65Ub	E62JT	Rabbit	1:1500	Cell Signalling	62802
MAP2	-	Chicken	1:2000	Millipore	AB5543
TOM20	F-10	Mouse	1:500	Santa Cruz	sc-17764

Table 16. Details of secondary antibodies used for CLEM

Protein target	Fluorophore	Host	Dilution	Manufacturer	Catalogue number
Rabbit IgG	488	Donkey	1:1000	Invitrogen	A21206
Chicken IgG	555	Goat	1:1000	Invitrogen	A32932
Mouse IgG	647	Donkey	1:1000	Invitrogen	A31571

The neurons were unmounted and fixed for 20 minutes in 2% glutaraldehyde in 0.1 M phosphate buffer (PB) at pH 7.4, then washed three more times in 0.1 M PB. The grids were incubated for 1 hour at room temperature in 1% osmium tetroxide. After washing once with 0.1 M PB, the samples were dehydrated by 10-minute incubation on ice with steps of 30% and 50% ice cold ethanol. The samples were then incubated in 1% uranyl acetate in 70% ethanol for 30 minutes in the dark, followed by 10-minute steps on ice of 80%, 90% and 95% ethanol. The samples were further dehydrated for 20 minutes on ice with dry ethanol then another 20 minutes at room temperature, followed by 100% acetone for 15 minutes, twice. One hour incubations in 3:1, 1:1 and 1:3 acetone:resin with rotation started the resin embedding process, which was continued with 100% durcupan resin overnight at room temperature. Resin-filled Beem capsules were then upturned onto the grid location of interest and the samples polymerised in a 60°C oven for 24 hours.

After polymerisation, the coverslips were removed by sequential immersion in liquid nitrogen and boiling water, and the resin block was subsequently trimmed by hand and sectioned on an EM UC7 ultramicrotome (Leica) using a diamond knife. The sections were floated onto EM grids and imaged on the HT7800 electron microscope (Hitachi) using the 3000x and 5000x objectives.

2.17 Statistical analyses

Outputted spreadsheets from the PheraStar or from the Harmony software were processed in Excel or in R and graphed using Graphpad Prism (Graphpad) or R. Technical replicates were averaged and normalised to a control within each differentiation, producing a fold change dataset that was subsequently combined with subsequent biological replicates. The data were tested for normality using the Shapiro-Wilk test and the examination of QQ plots prior to further graphing, and parametric or non-parametric statistical tests (and corresponding post-tests) were implemented based on the result of the normality test. Fold change-normalised data generated from independent differentiations was considered a paired dataset during statistical testing.

For comparison of two conditions using fold change-normalised data arising from multiple independent differentiations or from one experiment with measurements repeated before and after treatment, a parametric paired t-test or non-parametric Wilcoxon's test was used. For unpaired data, Welch's t-test was used to account for differences in variance between groups. When comparing three or more conditions with one independent variable, using fold-change normalised data from multiple differentiations, a parametric, repeated measures one-way ANOVA with Dunnett's multiple comparisons test or a non-parametric Friedman test with Dunn's multiple comparisons test was used. When comparing technical replicates from single experiment, a parametric ordinary one-way ANOVA with Tukey's multiple comparisons test (comparing all conditions pairwise) or Dunnett's multiple comparisons test (comparing all conditions to the control), or a non-parametric Kruskal-Wallis test with Dunn's multiple comparisons test was used. The Tukey or Dunnett's multiple comparisons tests were chosen to calculate 95% confidence intervals. Similarly, when comparing conditions with two independent variables for a single experiment, a two-way ANOVA with Tukey's multiple comparisons test was used. For comparison of conditions across two independent variables using fold change-normalised data from multiple differentiations, a repeated measures two-way ANOVA or a paired mixed-effects model (if data was missing) with Tukey's multiple comparisons test was used. For the

statistical testing of correlation between two variables, Spearmann's correlation test was used to account for the possibility of nonlinear relationships between the two measured variables.

The data were plotted using the standard error of the mean (SEM) as an estimate of the precision of the mean, rather than a measure of data spread. This was particularly relevant for the α-synuclein aggregation data in neurons, where high cell-to-cell variability existed in all treated conditions. Data plotted in R used several packages such as the tidyverse, ggplot2, and rstatix (Kassambra, 2023). Data points on graphs represent independent differentiations, unless specified in the figure legend, and data are plotted using the mean ± SEM unless otherwise stated.

3 Results: Modelling Parkinson's Disease Using α-Synuclein Pre-Formed Fibrils

Modelling *de novo* α-synuclein aggregation in iPSC-derived neurons is a challenge as there is a temporal component that governs increasing likelihood of aggregation in human brain as well as in cell models of the disease (Diao *et al*, 2021). One of the strongest risk factors for the development of Parkinson's disease is advancing age, and many studies have highlighted the difficulty in modelling ageing, as well as phenotypes linked to ageing, in iPSC-derived neurons (Cornacchia & Studer, 2017). Consequently, researchers have turned to triggering aggregation through exogenous methods, either through overexpression of monomeric α-synuclein or through the use of recombinant or brain-derived α-synuclein aggregates (Volpicelli-Daley *et al*, 2011; Cavaliere *et al*, 2017).

Extraction of α-synuclein proteinopathic seeds from the brain tissues of Parkinson's disease patients has generated highly disease-relevant insight into the process and consequences of α-synuclein aggregation (Masuda-Suzukake *et al*, 2013; Cavaliere *et al.*, 2017) but is limited by low yield and paucity of brain materials to extract from. Seeded amplification assays, allowing for the de novo generation of aggregation-prone seeds from patient brain-extracted materials, should theoretically circumvent the aforementioned difficulty in sourcing disease-specific aggregated α-synuclein, but in practice results in seeds that adopt a different conformation to the brain-derived materials from which they originate (Lövestam *et al*, 2021; Yang *et al*, 2022). Treatment of human neurons with α-synuclein PFFs has been shown to recapitulate the formation of Lewy body-like aggregates (Mahul-Mellier *et al*, 2020). How the formation of these aggregates impact cellular processes and components is an area of active study.

The aim of this chapter is to investigate the accumulation of pS65Ub secondary to pS129-positive aggregate formation in a human iPSC-derived neuronal model. To do this, I will:

1. Optimise and validate *in vitro*-aggregated α-synuclein PFFs as a means of modelling the process of α-synuclein aggregation in iPSC-derived neurons.
2. Investigate the spatial and temporal association of pS65Ub and pS129 in the seeded aggregation model.

3.1 Characterisation of iPSC-derived i^3 cortical neurons

3.1.1 i^3 Neurons adopt glutamatergic and cortical neuronal identity

The G3dCas9 (hereafter, i^3) iPSC line carries two genetic modifications which enable its specialised use for high-throughput biological experiments. A doxycycline-inducible neurogenin-2 expression cassette was inserted into the AAVS1 safe-harbour locus (Wang *et al*, 2017) and a dCas9-BFP-KRAB construct was integrated into the CLYBL safe-harbour locus, enabling constitutive expression of an enzyme-deficient form of Cas9 linked to the repressor domain KRAB (Tian *et al.*, 2019) (Figure 1a). Upon addition of doxycycline, these cells differentiate in a one-step, 3-day process to cortical excitatory neurons, a method which facilitates generating large quantities of neurons whilst using fewer resources than more traditional small molecule-based differentiation protocols (Figure 1b). The resulting population is composed of 97.4% MAP2-positive neurons (95% CI [96.55, 98.31]) and exhibits typically polarised neuronal morphology with extensive arborisation (Figure 1c).

The differentiation and cell fate identity of the i^3 neuron has been extensively characterised elsewhere (Zhang *et al*, 2013; Wang *et al.*, 2017; Chen *et al*, 2020; Rosa *et al*, 2020; Lam *et al*, 2024). As an initial step, the expression of key markers indicating neuronal, cortical and glutamatergic identity was confirmed over the course of differentiation and maturation.

PAX6 and *NES* are genes expressed in neuronal progenitor cells and the expression of both was upregulated at DIV 3, though only *PAX6* trended towards being upregulated ($p = 0.097$) with time in culture (Figure 2a), a timepoint during differentiation at which the cells have adopted a neuronal

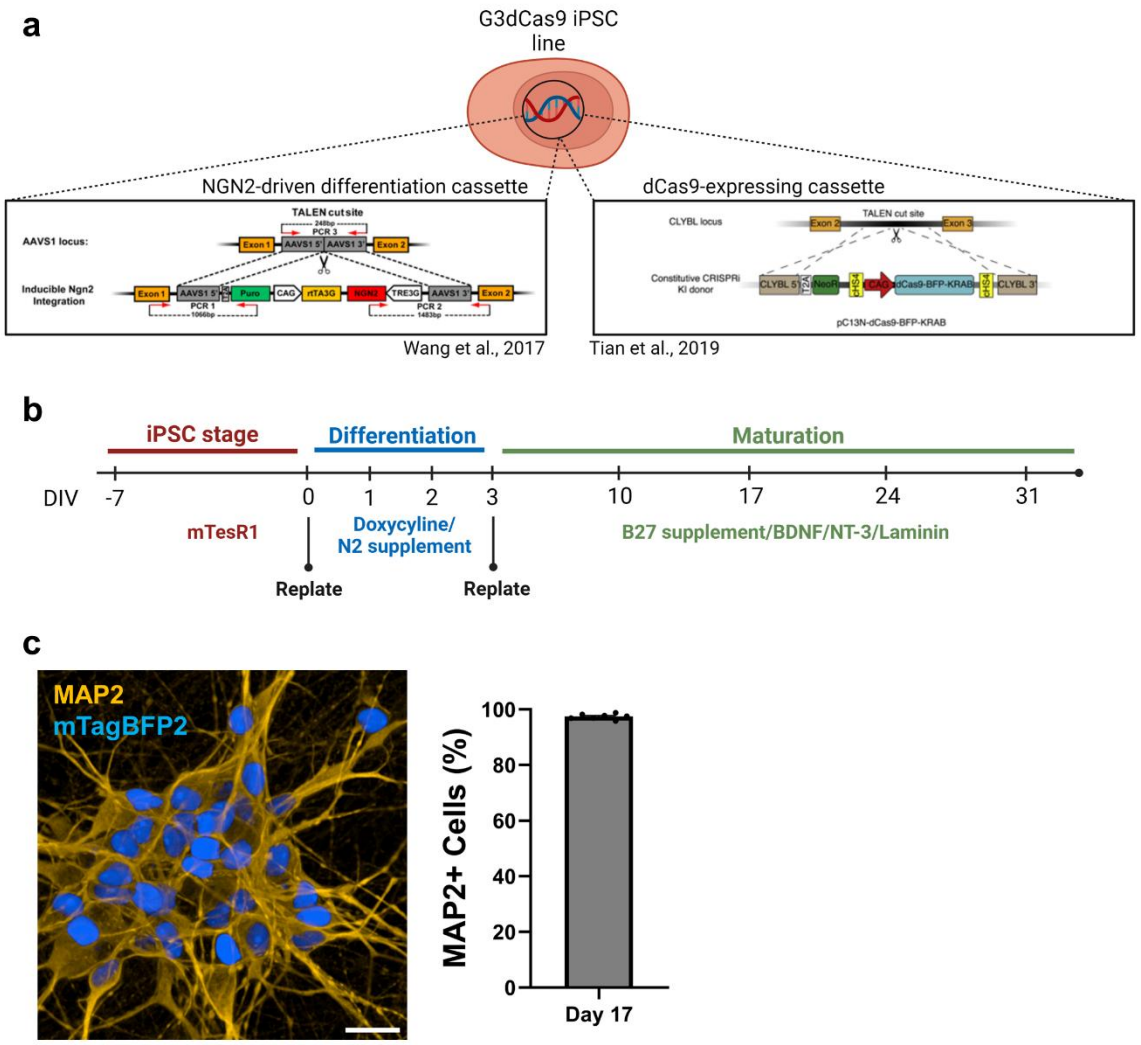


Figure 1. Genetically engineered G3dCas9 iPSCs differentiate in a one-step process to neurons. a) In previous work by the Ward and Kampmann labs, an inducible neurogenin-2 expression cassette was stably integrated at the *AAVS1* locus (Wang et al, 2017) and a constitutively-expressed dCas9 cassette was integrated at the *CLYBL* locus (Tian et al, 2019) of a healthy control line, WTC11, generating the G3dCas9 line. Left schematic: *NGN2*-expressing cassette, reproduced unchanged from Fig. 1A of Wang *et al*, 2017, licensed under CC BY-NC-ND 4.0. Right schematic: dCas9-expressing cassette, reproduced unchanged from Tian *et al*, 2019 with permission from Elsevier. b) Schematic representation of differentiation of G3dCas9 iPSCs to cortical, glutamatergic neurons. c) Representative image of differentiated i3 neurons at DIV 17, expressing the neuronal marker MAP2 by immunocytochemistry. Scale bar = 20 µm. Quantification of the number of MAP2-positive cells reveals that 97.4% of cells are MAP2-positive. N = 1 independent differentiations, each datapoint represents a technical replicate. Data is presented as the mean ± SEM. Panels 1a and 1b created with Biorender.com.

morphology. The expression of these markers at this time suggests that despite their appearance, these neurons are highly immature. Expression of *PAX6* was increased at DIV 10, whereas the levels of *NES* were similar to baseline. From DIV 17 to DIV 31, expression of both *PAX6* and *NES* showed no change

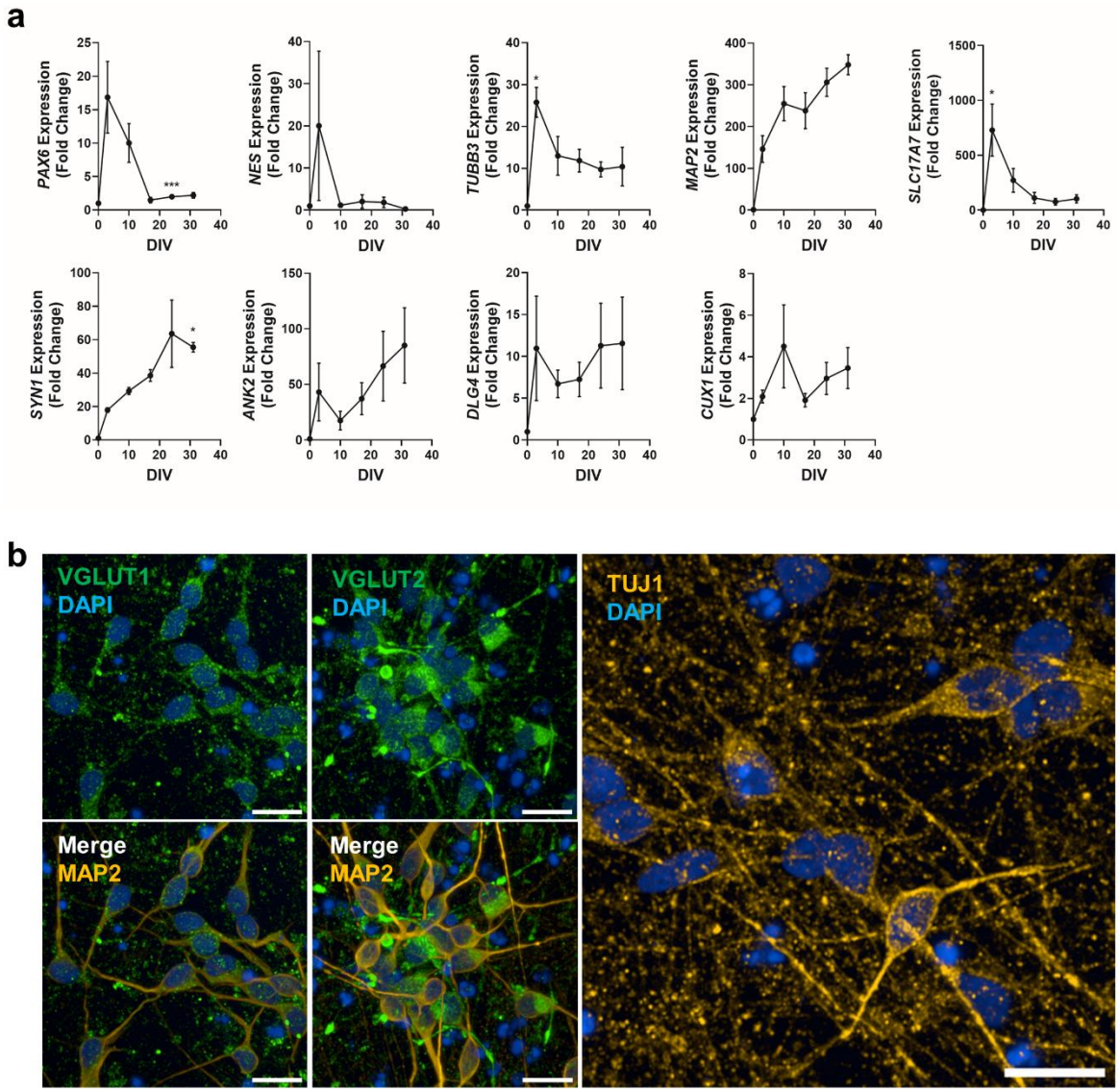


Figure 2. i^3 Neurons express cortical, excitatory, neuronal markers.

a) qPCR analysis of several neuronal progenitor cell, neuronal, glutamatergic, synaptic and cortical markers in i^3 neurons over the course of maturation at DIV 0, 3, 10, 17, 24 and 31. N = 2-3 independent differentiations. Statistical test: Repeated measures one-way ANOVA with Dunnett's multiple comparisons test or Friedman test with Dunn's multiple comparisons test. b) Immunocytochemistry in DIV 10 i^3 neurons for the glutamatergic markers *VGLUT1* and *VGLUT2* as well as for the neuronal markers *MAP2* and *TUJ1*. 40x water immersion objective on the Opera Phenix. Scale bar = 20 µm. N = 1 independent differentiations. Data is presented as the mean ± SEM. * $p < 0.05$, ** $p < 0.01$, *** $p < 0.001$, **** $p < 0.0001$.

from baseline (with the exception of *PAX6* at DIV 24, $p = 0.0002$), suggesting that the cells may acquire a more mature expression profile with increased time in culture.

Pan-neuronal markers *TUBB3* (encoding TUBB3/TUJ1) and *MAP2* (encoding MAP2) showed increased expression from DIV 0 to DIV 3 over the course of differentiation, though only *TUBB3* showed statistical significance ($p = 0.0376$), indicating adoption of a neuronal cell fate (Figure 2a). The expression of *MAP2* trended to increase over time ($p = 0.0681$ for the effect of culture time), whereas after an initial increase with differentiation, *TUBB3* expression was reduced and achieved a plateau over the course of maturation. *SLC17A7*, which encodes for VGLUT1, showed a similar trend to *TUBB3* ($p = 0.0083$ for the effect of time in culture, $p = 0.0376$ at DIV 3) (Figure 2a). This is consistent with rapid neurite outgrowth and synapse formation at earlier stages of maturation, which transitions to slower outgrowth and increased maintenance of existing neurites later in maturation. Interestingly, *SYN1* which encodes SYNAPSIN1, a pre-synaptic synaptic vesicle protein, and *ANK2*, a cytoskeletal adapter protein at synaptic terminals, showed increased expression over the course of maturation ($p = 0.0014$ and $p = 0.1389$), whereas the post-synaptic marker *DLG4*, encoding PSD95 at the post-synapse, maintained constant expression following differentiation (Figure 2a).

Expression of the cortical marker *CUX1* showed no statistical difference from DIV 0 over the course of differentiation and maturation, consequently the levels of VGLUT1, VGLUT2, TBR1 and CUX2 were investigated by immunocytochemistry in DIV 10 neurons to determine the potential for excitatory neurotransmission and ascertain superficial or deep cortical layer identity (Figure 2b). The neurons showed expression of both VGLUT1 and VGLUT2. Immunocytochemistry for TBR1 and CUX2 resulted in strong, unspecific staining of neurites and cell bodies, unlikely locations of physiological function for two transcription factors (data not shown).

Culturing i^3 neurons in multi-electrode array (MEA) plates allowed for the longitudinal assaying of neuronal activity over time. This technique allows for a broader measurement of neuronal firing at a population level. The mean firing rate remained at a low level until DIV 35 and 45, when a time-dependent increase in neuronal activity was observed ($p = 0.0199$ over time in culture, $p = 0.0137$ at DIV 45) (Figure 3a). Local and disseminated network firing, measured through burst frequency and network burst frequency, were absent until DIV 30 then increased over time ($p = 0.0444$ and $p = 0.0382$). Similarly, the synchronisation index of the network was increased over DIV 30-45 ($p = 0.0455$)

(Figure 3a). Overall, this suggests that i^3 neurons in culture lack functional maturity until ~DIV 30, and progressively acquire physiological firing capacities over extended culturing times.

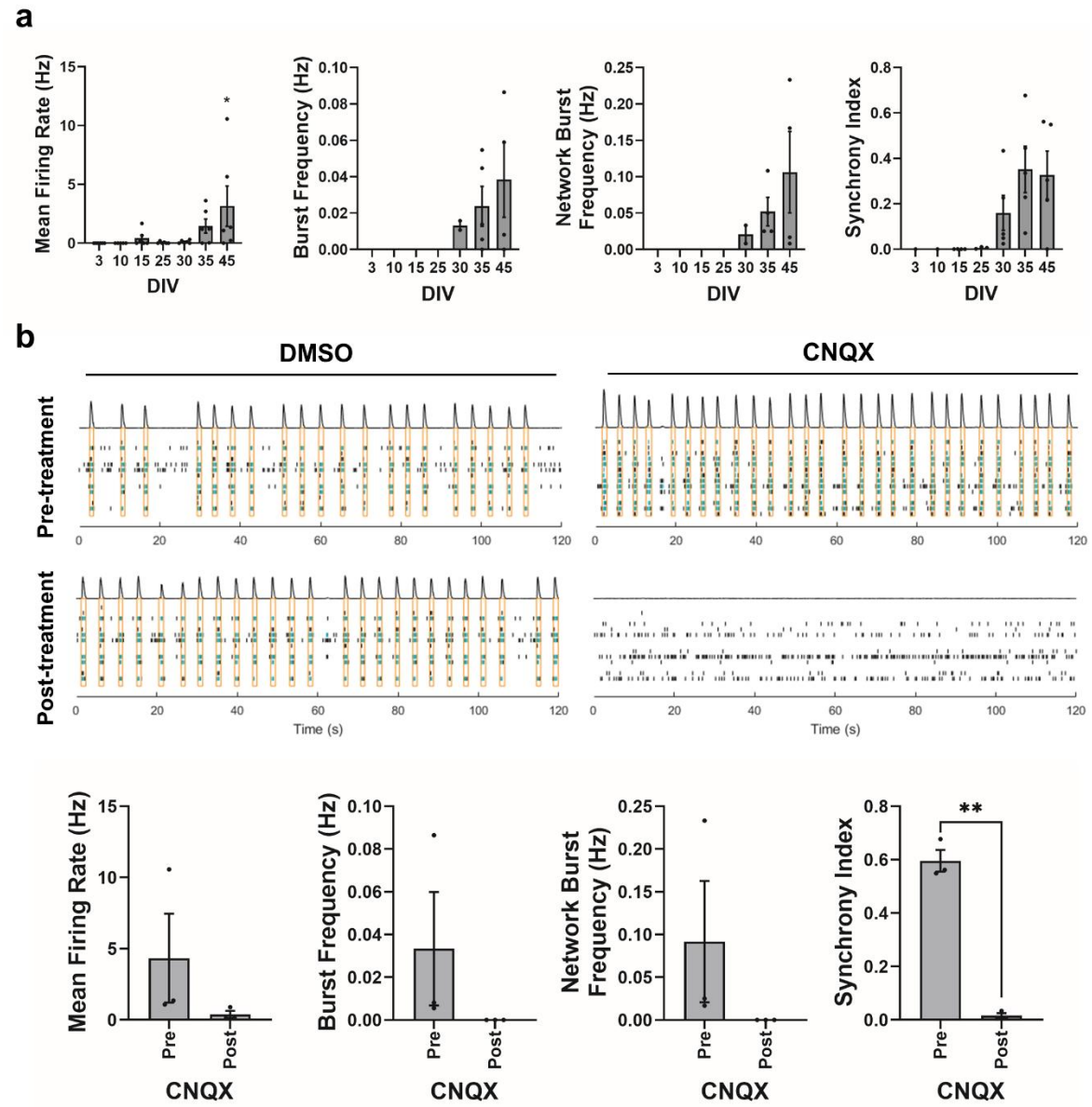


Figure 3. Increased excitatory firing in i^3 neurons over the course of maturation. a) Mean firing rate, burst frequency, network burst frequency and synchrony index were measured by multi-electrode array (MEA) over the course of maturation of i^3 neurons. These parameters were increased over the course of maturation, particularly from DIV 30 onwards. Statistical test: Ordinary one-way ANOVA with Dunnett's multiple comparisons test. b) Raster plots of network bursting (yellow boxes identify network bursts) with and without 10 µM cyanquixaline (CNQX) or an equivalent concentration of DMSO. CNQX is an AMPA and kainate receptor antagonist and completely abrogates i^3 neuron firing at DIV 45, as demonstrated by quantification of firing rate and bursting behaviour of the neurons. N = 1 independent differentiations, each datapoint represents a technical replicate. Statistical test: Paired t-test or Wilcoxon's test. Data is presented as the mean ± SEM. * $p < 0.05$, ** $p < 0.01$, *** $p < 0.001$, **** $p < 0.0001$.

Excitatory glutamatergic neurons express AMPA receptors, kainate receptors and NMDA receptors, with AMPA and kainate receptors generally modulating fast synaptic signalling and NMDA receptors regulating synaptic plasticity. Cyanquixaline (CNQX) is a potent AMPA and kainate receptor antagonist, and treatment of neurons was expected to inhibit firing and network activity.

Complete abrogation of several measures of local and network firing was observed upon treatment (Figure 3b), whereas DMSO-treated conditions showed no alterations to firing patterns. These data confirm that the population of neurons produced by NGN2-directed differentiation have an excitatory, glutamatergic profile.

3.1.2 Neurodegeneration-relevant proteins are expressed in i^3 neurons

To further characterise i^3 neurons, the expression of several neurodegenerative disease-associated proteins in i^3 neurons was measured over the course of differentiation and maturation. *SNCA* expression was increased over the course of maturation ($p = 0.0292$ for the effect of time in culture) until DIV 17, at which time it stabilised over the subsequent timepoints (Figure 4a). *APP* showed no significant increase in expression with differentiation. *APOE*, on the other hand, showed a marked decrease over the course of differentiation and early maturation – its expression was significantly reduced from DIV 10 onwards ($p = 0.0028$, $p < 0.0001$, $p = 0.0002$ and $p = 0.0012$ at DIV 10 to 31). *MAPT* showed strongly increased expression through differentiation and maturation ($p = 0.0083$ for the effect of time in culture). Overall, these data suggest that i^3 neurons have high levels of α-synuclein and tau expression in comparison with iPSCs, but show no change in amyloid-β-encoding gene expression.

The protein levels of α-synuclein and tau showed a similar trend to the gene expression data, as assessed by Western Blotting (Figure 4b). However, there was a strong upregulation of α-synuclein protein between DIV 17 and 24, whereas gene expression was already at maximal levels at DIV 17. Overall, these data suggest that the expression of aggregation-prone protein increases with the age and maturity levels of neurons in culture.

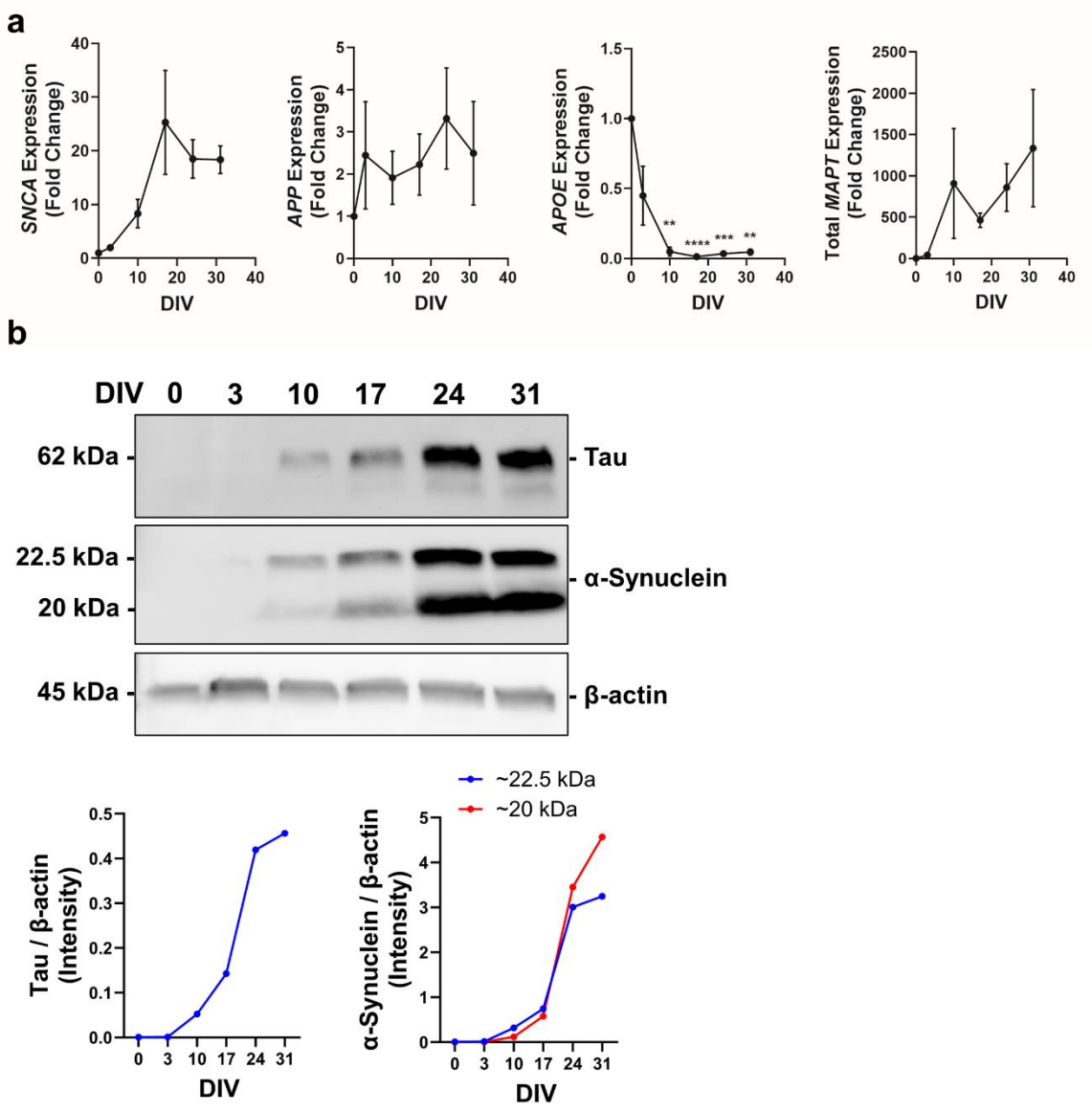


Figure 4. Neurodegeneration-related SNCA and tau are expressed in i^3 neurons.
a) Gene expression of neurodegeneration-related genes measured by qPCR over the course of maturation in i^3 neurons shows increased levels of *SNCA* and *MAPT* with time in culture. N = 2-3 independent differentiations. Statistical test: Repeated measures one-way ANOVA with Dunnett's multiple comparisons test or Friedman test with Dunn's multiple comparisons test. b) Measurement of SNCA and tau protein levels in i^3 neurons over the same timepoints reveals strong increases in SNCA and tau expression at DIV 24 and 31. N = 1 independent differentiation. Data is presented as the mean ± SEM. * $p < 0.05$, ** $p < 0.01$, *** $p < 0.001$, **** $p < 0.0001$.

3.2 α-Synuclein pre-formed fibrils to model the process of aggregation

3.2.1 Characterisation of *in vitro*-generated α-synuclein recombinant fibrils

α-Synuclein PFFs were first aggregated *in vitro* following a protocol developed by Dr Nora Bengoa-Vergniory (Bengoa-Vergniory *et al*, 2020) with modifications. α-Synuclein monomer sourced from the Oxford Protein Production Small Research Facility (5 mg/ml) was agitated at 37°C, 250 rpm for 31 days. The successful production of proteinaceous fibrils was monitored by visually tracking the turbidity of the solution, which increased over the course of aggregation (data not shown). At 31 days, the aggregation was stopped and the fibrils stored at room temperature until sonication. A probe sonicator (Hieschler) was used to sonicate the fibrils at 25% amplitude, 0.2 seconds cycle in 10-minute bursts, and the resulting fibrils imaged by electron microscopy, until the fibrils reached an average length of ~200 nm (Figure 5a).

Analysis of the PFFs under the electron microscope was performed by manually measuring the length of fibrils using ImageJ software (section 2.5) (Figure 5b). A density distribution of the fibrils lengths was then generated to allow the quantification of mean fibril length, and visualise the overall distribution of the fibril sizes in the studied batch (Figure 5c). The distribution of the fibrils within the 2021_11 preparation suggested that most fibrils were longer than 100 μm, whereas shorter α-synuclein fibrils, especially those <50 nm, have been shown to be more effective at seeding pS129-positive aggregation *in vitro* and *in vivo* (Tarutani *et al*, 2016).

3.2.2 α-Synuclein PFFs trigger formation of phospho-serine 129-positive aggregates in a dose-dependent manner

Treatment of primary neurons with α-synuclein PFFs has been shown to induce the formation of pS129-tagged α-synuclein aggregates in the cytoplasm of cells, which replicate many of the markers of Lewy bodies and neurites found in patient brains at autopsy (Mahul-Mellier *et al*, 2020). However, recombinant fibrils are recognised to have strong batch-to-batch variability (Polinski *et al*, 2018). To determine the effectiveness and treatment dosage of our preparation of α-synuclein fibrils, I conducted a dose-response of 2 to 50 μg/ml of PFFs in i^3 cortical neurons and measured the accumulation of pS129 by immunocytochemistry at day 14 post-seeding (Figure 6a). pS129-positive α-synuclein aggregates formed in a dose-dependent manner, as assessed by measurements of staining

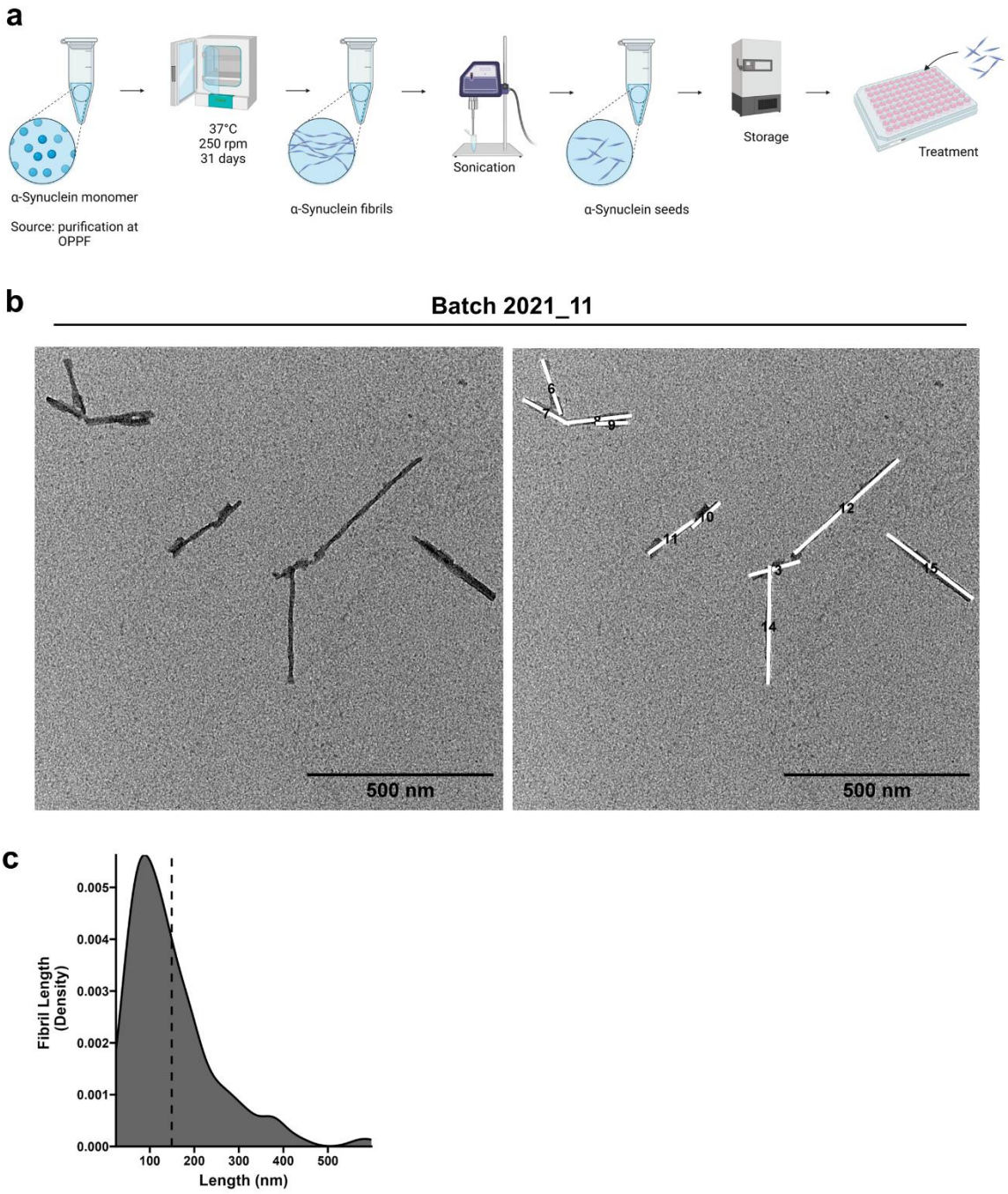


Figure 5. Characterisation of α-synuclein fibrils aggregated from purified monomer. a) Schematic representation of the method used in the *in vitro* aggregation of α-synuclein monomer into PFFs. b) Electron micrographs of the first PFF batch produced, 2021_11, and overlay of the selection used to quantify fibril length. 23,000x objective, JEOL 1400 KV electron microscope. c) Density distribution plot of the fibril lengths from batch 2021_11. Dashed vertical line represents the mean of the distribution. N = 179 fibrils. Panel 1a created with Biorender.com.

area and intensity (Figure 6b). In addition, there was no decrease in the average number of nuclei per well on the basis of dosage, suggesting no toxicity of the PFFs or of the aggregation process at the timepoint examined. This suggests that PFF treatment at DIV 10 in human cortical neurons may

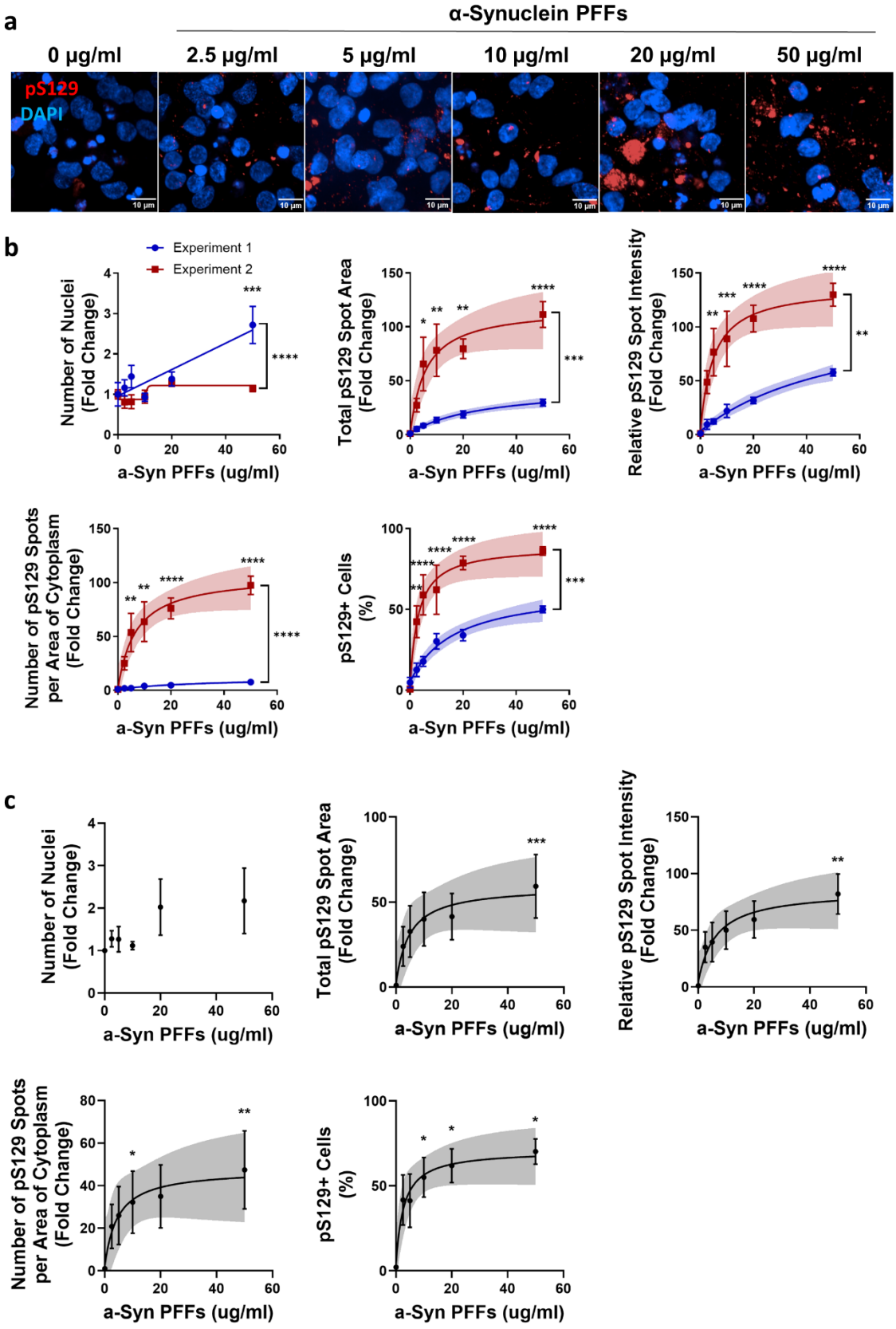


Figure 6. α-Synuclein PFFs seed pS129-positive aggregation in a dose-dependent manner. a) Confocal microscopy images of i^3 neurons treated with increasing doses of α-synuclein PFFs show increasing levels of pS129-positive aggregates. Scale bar = 10 µm, 40x water immersion objective,

Opera Phenix confocal microscope. b) Quantification of the levels of pS129 reveals significant differences between experimental replicates. Statistical analysis: Ordinary two-way ANOVA with Tukey's multiple comparisons test. N = 2 independent differentiations, each datapoint represents a biological replicate. c) Quantification of dose-dependent levels of PFF-seeded pS129 levels in i^3 neurons. N = 4 independent differentiations. Statistical test: Friedman test with Dunn's multiple comparisons test. Data is presented as the mean ± SEM. * $p < 0.05$, ** $p < 0.01$, *** $p < 0.001$, **** $p < 0.0001$.

model the early stages of α-synuclein aggregation, prior to advanced disease and cell death. The increase in pS129 levels was non-linear, suggesting that the process of aggregation quickly reaches saturation whereupon increases in fibrillar seeds does not produce further increases in aggregation (Figure 6b).

Statistically significant changes in the magnitude of PFF-induced pS129 aggregation were found between experimental replicates for the total pS129 spot area (effect of experiment, $p < 0.0001$, treatment, $p = 0.0018$), relative pS129 spot intensity (effect of experiment, $p < 0.0001$, treatment, $p < 0.0001$), number of spots per area of cell (effect of experiment, $p < 0.0001$, treatment, $p = 0.0021$, interaction, $p = 0.0097$) and percentage of pS129-positive cells (effect of experiment, $p < 0.0001$, treatment, $p < 0.0001$) (Figure 6b). This indicates that experiment-to-experiment variability is a strong component of overall variability, in addition to within-experiment variability assessed by technical replicates. Combining several independent replicates, each expressed as a fold change normalised to the untreated control, showed that the relationship between α-synuclein PFFs concentration and the levels of pS129 was nevertheless consistent across experiments (Figure 6c).

3.2.3 High batch-to-batch variability of recombinant α-synuclein PFFs

Another possibility for strong experiment-to-experiment variability was batch effects from different α-synuclein PFFs preparations, prompting an investigation into the reproducibility of our fibrils. As α-synuclein aggregation protocols have been found to be variable both batch-to-batch and across laboratories, I compared fibrils generated by myself and Dr Bengoa-Vergniory (batch 2021_11) to fibrils generated by myself (batch 2022_09) or generated by my colleague Ajantha Abey (batch 2023_02) using the same method of aggregation. Electron microscopy analysis revealed no morphological differences between the fibril preparations (Figure 7a). Comparison of the mean fibril length across each batch revealed that there was no significant difference between batches 2021_11

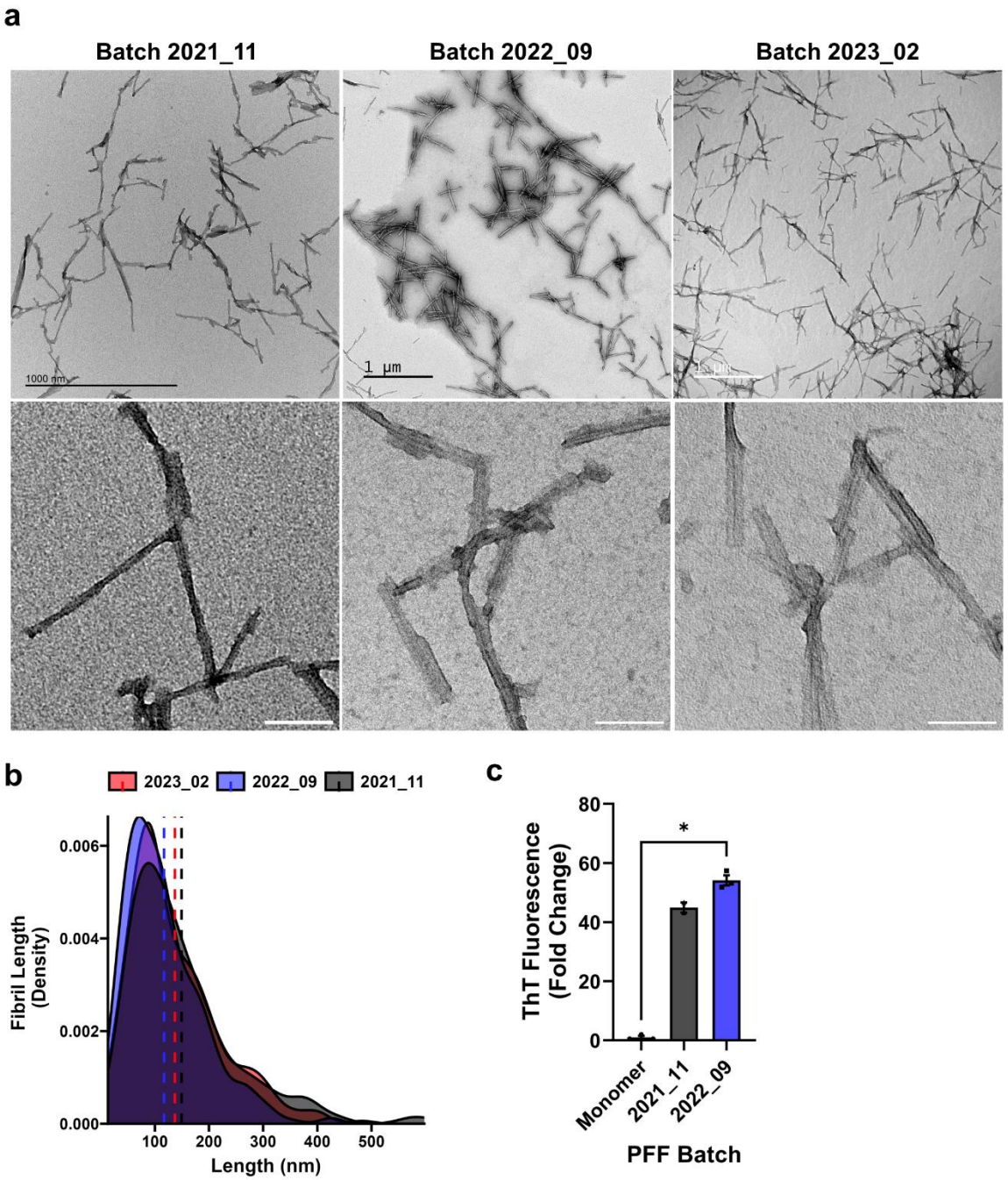


Figure 7. Comparison of α-synuclein PFF preparations. a) Electron micrographs of batches 2021_11, 2022_09 and 2023_02 prepared by 3 independent experimenters show similar fibril morphology and length. 6000x objective on Jeol 1400 KV electron microscope. Scale bars = 1 µm and 100 nm. b) Distribution density plot of fibril lengths of all three preparations. Dashed vertical lines represent the mean of each preparation. N = 179 fibrils for 2021_11, N = 379 fibrils for 2022_09 and N = 304 fibrils for 2023_02. Statistical test: Kruskal-Wallis test with Dunn's multiple comparisons. c) Preparations 2021_11 and 2022_09 show significantly increased intensity of ThT in comparison to monomeric SNCA. N = 1 independent experiment, each datapoint represents a technical replicate. Statistical test: Kruskal-Wallis test with Dunn's multiple comparisons post-test. Data is presented as the mean ± SEM. * $p < 0.05$, ** $p < 0.01$, *** $p < 0.001$, **** $p < 0.0001$.

and 2023_02, but that the mean length of batch 2022_09 was significantly shorter than both batches 2023_02 ($p = 0.0084$) and 2021_11 ($p = 0.0012$) (Figure 7b). Thioflavin T fluorescence analysis of the 2022_09 and 2021_11 fibrils showed strongly increased fluorescence for both fibrillar batches (Figure 7c), indicating the fibrils have adopted a β-sheet conformation.

To rapidly and consistently assess α-synuclein PFF functional efficacy, I utilised a previously-established immunocytochemical assay in SH-SY5Y cells overexpressing α-synuclein under the control of the CMV promoter (Katrina Savory, unpublished data). Briefly, *SNCA*-T2A-GFP expressing SH-SY5Y cells were seeded at low confluency into a 96-well plate format, treated with a dose-response of α-synuclein PFFs and the levels of pS129 assessed as a readout of α-synuclein aggregation five days post-seeding (Figure 8a). Treatment with α-synuclein fibrils led to a significant dose-dependent increase in pS129-positive aggregates, which appeared predominantly as i) large, perinuclear solid masses, and to a lesser extent as ii) dense cores with fibrillar offshoots, iii) fibrils or iv) a collection of puncta (Figure 8c).

Comparison of the three α-synuclein fibril batches with this assay demonstrated high variability between the three preparations. Batch 2021_11 showed the highest efficacy in inducing formation of pS129-positive aggregates, whereas batches 2022_09 and 2023_02 showed reduced potency (Figure 8b-d). At the maximal PFF treatment concentration, 2021_11 had a significantly increased percentage of pS129 positive cells compared to both 2022_09 ($p = 0.0014$) and 2023_02 ($p < 0.0001$), and 2022_09 showed significantly more pS129-positive cells than 2023_02 ($p = 0.0002$) (Figure 8b-d). Overall, these data suggested that the protocol for α-synuclein PFF aggregation produced high batch-to-batch variability, which would create challenges in the design and implementation of α-synuclein PFFs-based screening assays. Given that the objectives of the project relied on effective and reliable α-synuclein aggregation, it became imperative to optimise fibril generation to minimise batch effects.

3.2.4 Optimisation of recombinant α-synuclein aggregation

A collaboration was established with the Magill lab, whose fibril preparations showed robust aggregation in mouse models of PD (unpublished data). Through curation of the literature as well as

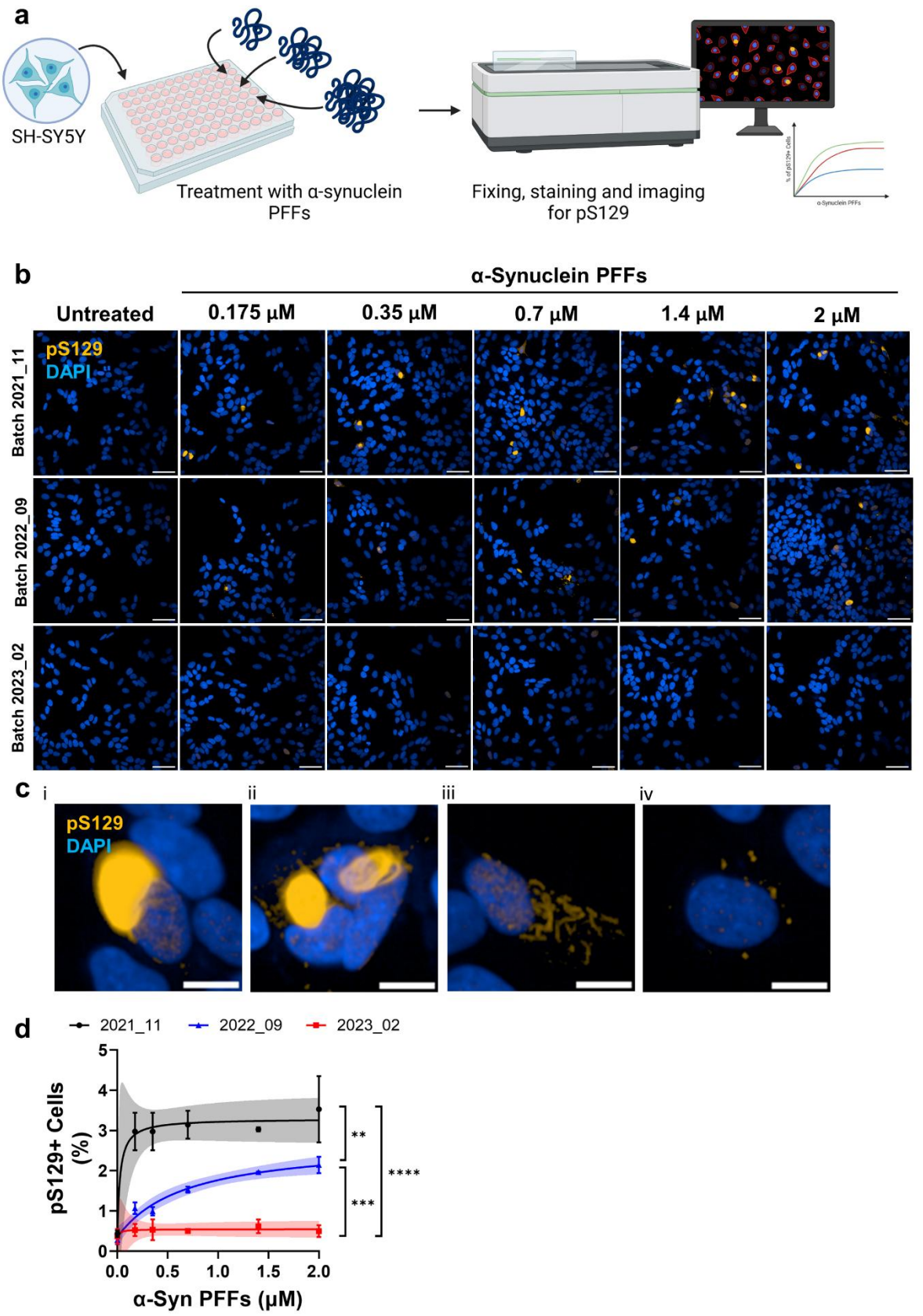


Figure 8. Development of a functional validation assay for α-synuclein PFF preparations. a) Schematic of the method employed to functionally assess the PFF-induced seeding efficiency of each individual preparation. b) Representative confocal images of SH-SY5Y cells seeded with increasing

concentrations of α-synuclein fibrils and stained with immunocytochemistry for pS129 and DAPI. Scale bars = 50 μm. 40x water immersion objective, Opera Phenix confocal microscope. c) Magnification of various aggregate morphologies found at 2 μM PFF. Scale bars = 10 μm. 40x water immersion objective, Opera Phenix confocal microscope. d) Quantification of the percentage of pS129-positive cells from the images in b). Preparation 2021_11 demonstrates a significantly higher induction of PFF-seeded aggregation in comparison to preparation 2023_02, and a non-significant increase over 2022_09. N = 1 independent experiments. Statistical test: Two-way ANOVA with multiple comparisons test. Data is presented as the mean ± SEM. * $p < 0.05$, ** $p < 0.01$, *** $p < 0.001$, **** $p < 0.0001$. Panel 1a created with Biorender.com.

discussion with the Magill and Volpicelli-Daley laboratories, 3 changes were made to the original protocol (Figure 9).

First, the source and consistency of the α-synuclein monomeric starting material, and the buffer conditions it is supplied in, are crucial considerations in the aggregation process of α-synuclein, and standardisation of these two factors is recommended by prominent laboratories in the field (Polinski *et al.*, 2018). The monomer used in the aggregation of batches 2021_11, 2022_09 and 2023_02 was sourced from the Protein Production Small Research Facility (Oxford), which produced α-synuclein on an ad hoc basis. α-Synuclein monomer commercially available from rPeptide was used for subsequent preparations.

Second, the aggregation rotation was increased from 250 rpm to 1000 rpm, which significantly shortened the time required for fibril formation. Stronger agitation has been shown to increase fibril formation, and this in spite of changes to ionic strength, monomer concentration or addition of compounds into the reaction solution (reviewed in Narkiewicz *et al*, 2014), suggesting that increased shaking could mitigate small experiment-to-experiment variations.

Third, though it was widely recommended throughout the literature to sonicate α-synuclein fibril aliquots after storage and immediately prior to use, to increase the aliquot-to-aliquot consistency of the preparations, the fibrils were sonicated in large volumes prior to storage and use. As quality control was performed on the original fibril aliquot, this increased how representative the electron micrographs taken were of the individual aliquots and minimised inconsistencies which may have arisen from sonication of each small aliquot independently. It should also be noted that recommendations in the field have evolved significantly over the past decade, and at least one

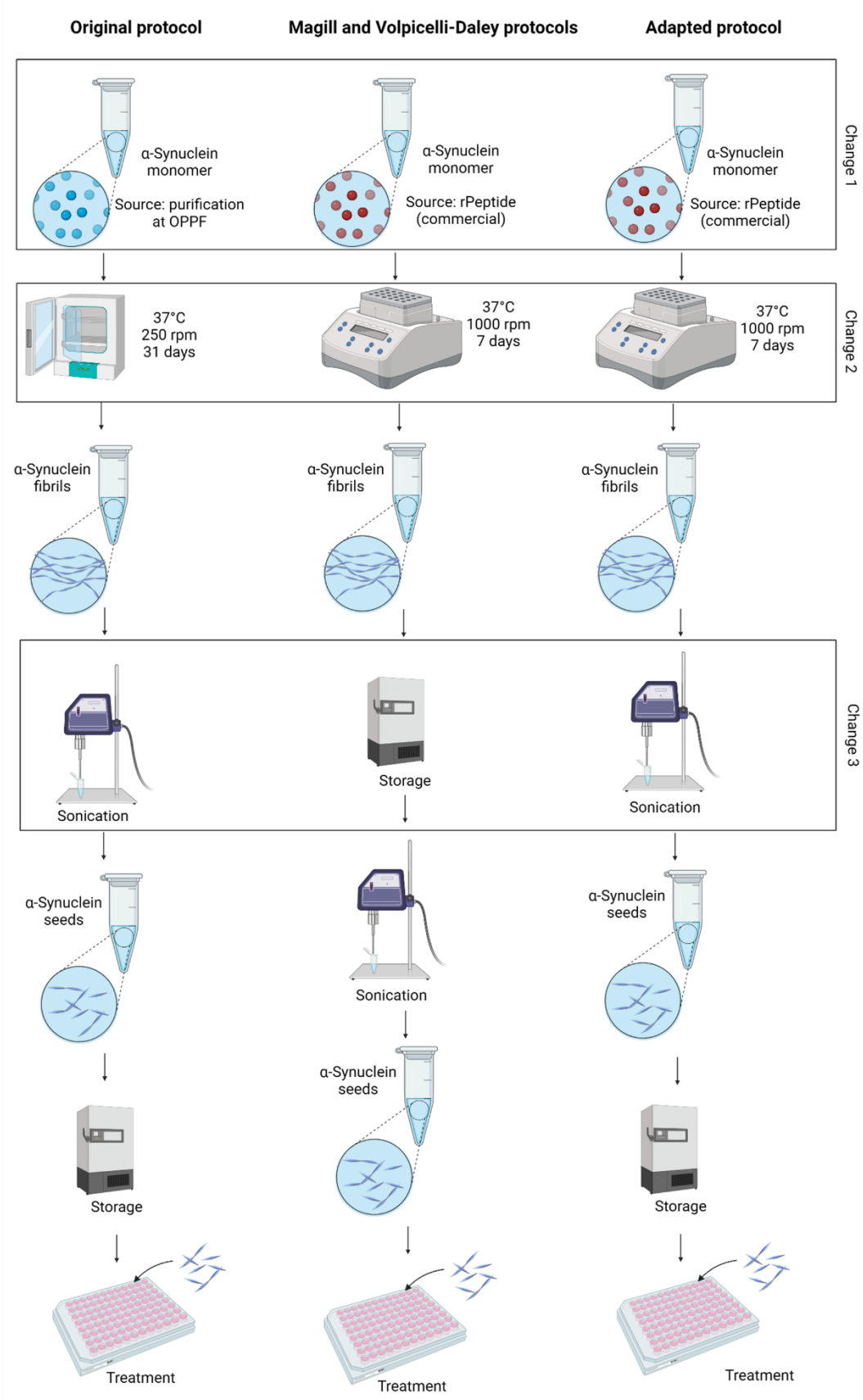


Figure 9. Comparison of α-synuclein PFF aggregation methods. Diagram comparison of three methods for *in vitro* aggregation of α-synuclein monomer. Black boxes highlight changes made to the original protocol in the final protocol (adapted protocol). Created with Biorender.com.

laboratory which once advised against sonication prior to storage has, after further testing, adhered to this method.

To compare the performance of the new α-synuclein PFF aggregation protocol, human recombinant α-synuclein fibrils were obtained sonicated and frozen from the Volpicelli-Daley laboratory (batch 2023_04) through the Aligning Science Across Parkinson's (ASAP) consortium initiative to distribute well-characterised fibrils. These were compared both to the newly-generated fibrils (batch 2023_05) (Figure 10a) and the fibrils generated using the previous aggregation protocol (batch 2022_09). Electron micrographs did not reveal differences in structure or conformation of the fibrils, but analysis of the fibril length distribution showed that batch 2023_04 had a mean length of 37 nm, whereas the mean length of the fibrils for batches 2022_09 and 2023_05 were 100 nm and 76 nm, respectively. All three PFF preparations showed statistically significant differences in their mean length in all pairwise comparisons ($p < 0.0001$) (Figure 10b and f).

ThT fluorescence analysis revealed that the 2023_04 fibril batch showed the highest fold change increase in intensity (109-fold) compared to batch 2022_09 which showed only a 44.3-fold increase in intensity and 2023_05 which showed a 13.5-fold increase in intensity over the α-synuclein monomer (Figure 10c). However, these results have limited interpretation without access to the starting material for batch 2023_04, which was aggregated by the Volpicelli-Daley laboratory. In direct contrast to the ThT assay results, functional validation of the α-synuclein fibrils in SH-SY5Y showed that batch 2023_05 outperformed both 2023_04 ($p < 0.0001$) and 2022_09 ($p < 0.0001$), with batch 2022_09 also outperforming batch 2023_04 ($p = 0.0451$) (Figure 10d-e). These data show that the newly-adopted α-synuclein fibril aggregation method produces fibrils that are able to induce pS129 aggregation.

A crucial aspect of adopting this new protocol was to increase batch-to-batch consistency of the fibrils. Three new batches were prepared in accordance with the new protocol – batches 2023_08_2 and 2023_08_1 were prepared by my colleagues Sarah Franks and Dr Elena Britti. Functional validation revealed much more consistency between the three preparations, though one of the preparations, 2023_08_1, showed significantly increased levels of pS129 compared to 2023_08_2

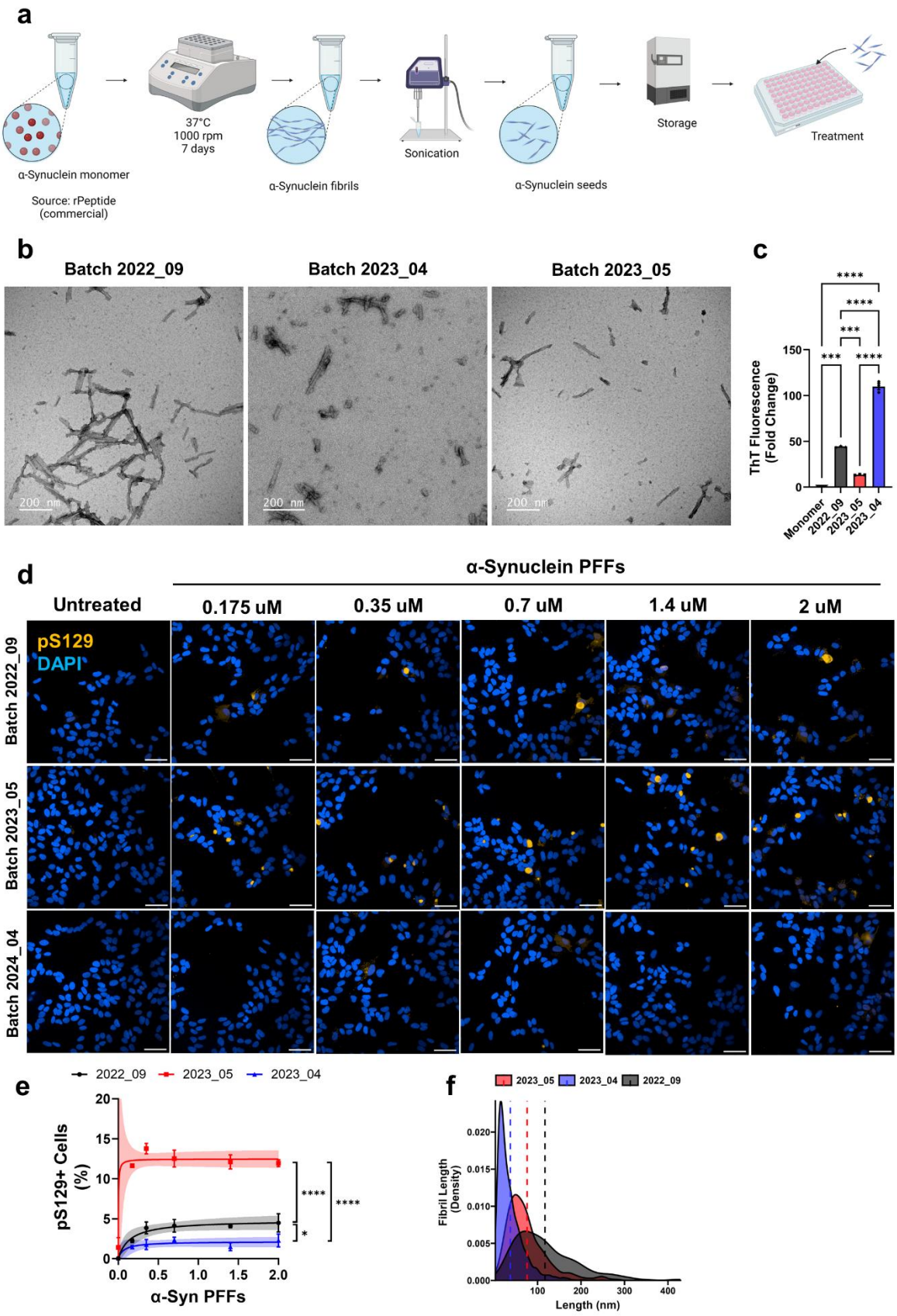


Figure 10. Characterisation of α-synuclein PFF preparations aggregated using different methods. a) Schematic of the new method developed for the aggregation of α-synuclein monomer. A commercial α-synuclein monomer is agitated at 1000 rpm and 37°C for 7 days prior to sonication

and storage. b) Electron micrographs of batch 2022_09, prepared following the original protocol, batch 2023_04, obtained from the Volpicelli-Daley laboratory and batch 2023_05 prepared following the new, adapted method. Scale bars = 200 nm. 20,000x objective, JEOL 1400 KV electron microscope. c) Fibril preparations show increased ThT fluorescence in comparison to monomeric SNCA. N = 1 independent experiment, each datapoint represents a technical replicate. Statistical test: Ordinary one-way ANOVA with Tukey's multiple comparisons test. d) Confocal microscopy images of functional seeding efficiency validation of each preparation in SH-SY5Y cells, immunostained for pS129 and DAPI. Scale bars = 50 µm. 40x water immersion objective, Opera Phenix confocal microscope. e) Quantification of the microscopy images measuring the percentage of pS129-positive cells at each concentration shows a statistically significant difference between batch 2023_05 and the other two preparations. N = 1 independent experiment. Statistical test: Two-way ANOVA with Tukey's multiple comparisons test. f) Distribution density plots of fibril lengths for each preparation. Vertical dashed lines represent the mean of the distribution for each batch. N = 329 fibrils for 2022_09, N = 1398 fibrils for 2023_04 and N = 262 fibrils for 2023_05. Data is presented as the mean ± SEM. * $p < 0.05$, ** $p < 0.01$, *** $p < 0.001$, **** $p < 0.0001$. Panel 1a created with Biorender.com.

($p = 0.0008$) and 2024_03 ($p < 0.0001$) (Figure 11a-b). Importantly, all three preparations showed a significant effect of PFF treatment (0 µM versus 2 µM, $p < 0.0001$), whereas two previous preparations had failed to show a significant effect of treatment (2023_02 and 2023_04). Interestingly, batch 2023_08_1 showed significantly increased mean length of fibrils compared to both other preparations ($p < 0.0001$) (Figure 11c). Another batch was prepared in 2025 and functionally evaluated using pS129 as a readout. It was shown to perform on par with the previous two preparations, with all three batches demonstrating a significant effect of treatment at doses of 0.175 µM to 2 µM ($p < 0.0209$) (Figure 12a-b). These data suggest reduced variability across preparations of fibrils, and that the protocol is more robust to experimenter-induced variation.

3.2.5 Predicting seeding efficiency of α-synuclein PFF preparations

Given that early α-synuclein preparations showed increased batch-to-batch variability but few clear differences in fibril morphology, we sought to identify parameters measured in the process of quality control which might predict the seeding efficacy of a preparation. The electron micrographs of all the previous α-synuclein preparations over the past three years were revisited (Figure 13 and Figure 14), which revealed changes in the lengths of the fibrils within each preparation, but no apparent changes in fibril morphology or conformation, such as helices. However, the natural variability existing within fibril preparations as well as heterogeneity in the contrast of the positive staining confounded the comparison of preparations on the basis of their appearance in EM micrographs.

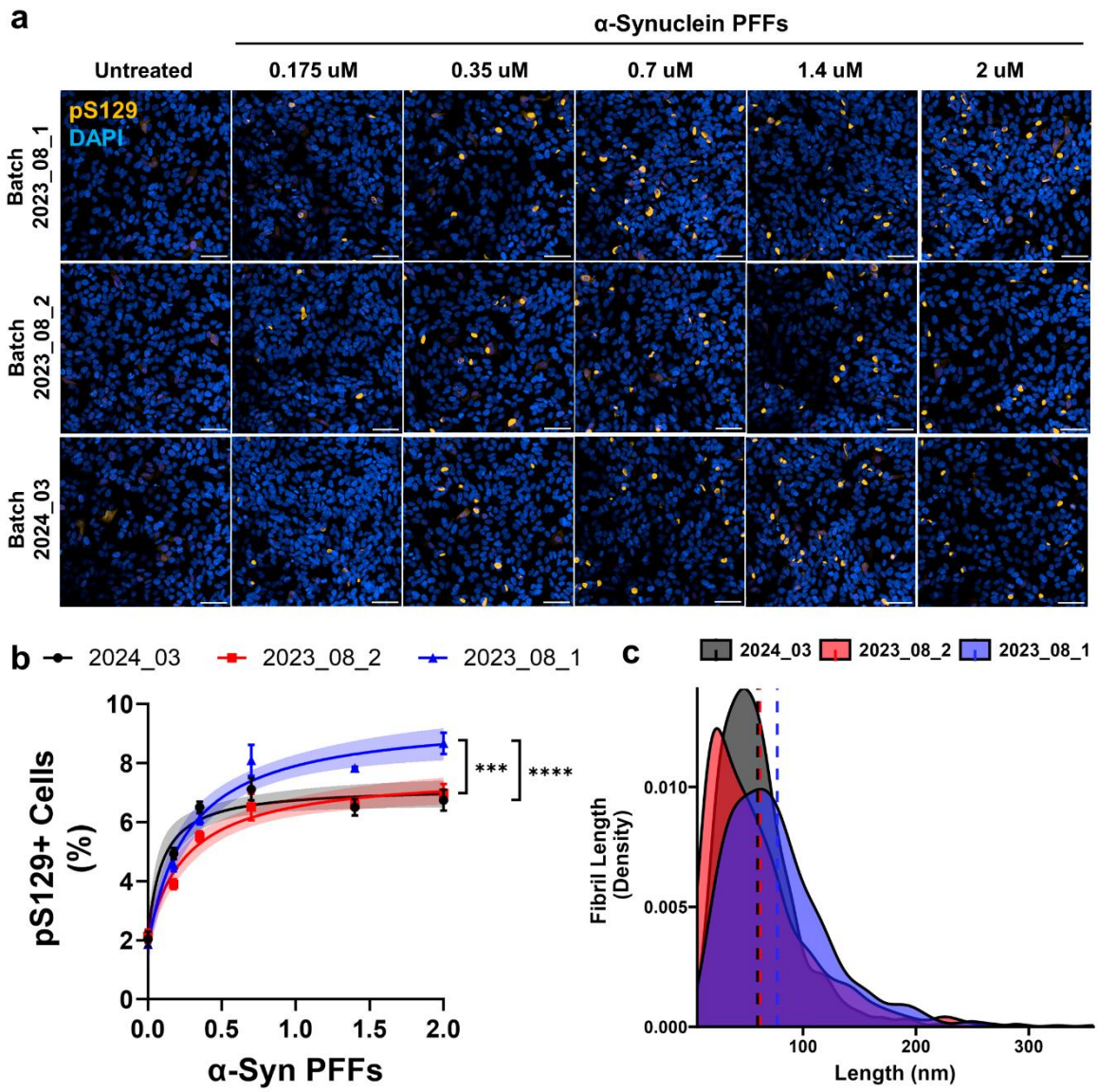


Figure 11. Preparations of in vitro aggregated α-synuclein show reduced experimenter-induced variability. a) Preparations were aggregated *in vitro* by three independent experimenters and subjected to functional characterisation in *SNCA*-GFP SH-SY5Y. Confocal microscopy images showed that all three preparations show similar dose-dependent increases in pS129-positive aggregation. Scale bars = 50 µm. 20x water immersion objective, Opera Phenix confocal microscope. b) Quantification of the number of pS129-positive cells shows a small significant increase in the percentage of positive cells for batch 2023_08_1. N = 1 independent experiments. Statistical test: Two-way ANOVA with Tukey's multiple comparisons test. c) Density distribution plot of fibril lengths for each preparation. Vertical dashed lines indicate the distribution mean. N = 501 fibrils for 2024_03, N = 489 fibrils for 2023_08_1 and N = 804 fibrils for 2023_08_02. Data is presented as the mean ± SEM. * $p < 0.05$, ** $p < 0.01$, *** $p < 0.001$, **** $p < 0.0001$.

Plotting the fibril length distributions of all the preparations revealed a statistically significant reduction in the mean fibril length over time ($p = 0.0080$ for 2022_09_thawed and $p > 0.0001$ for

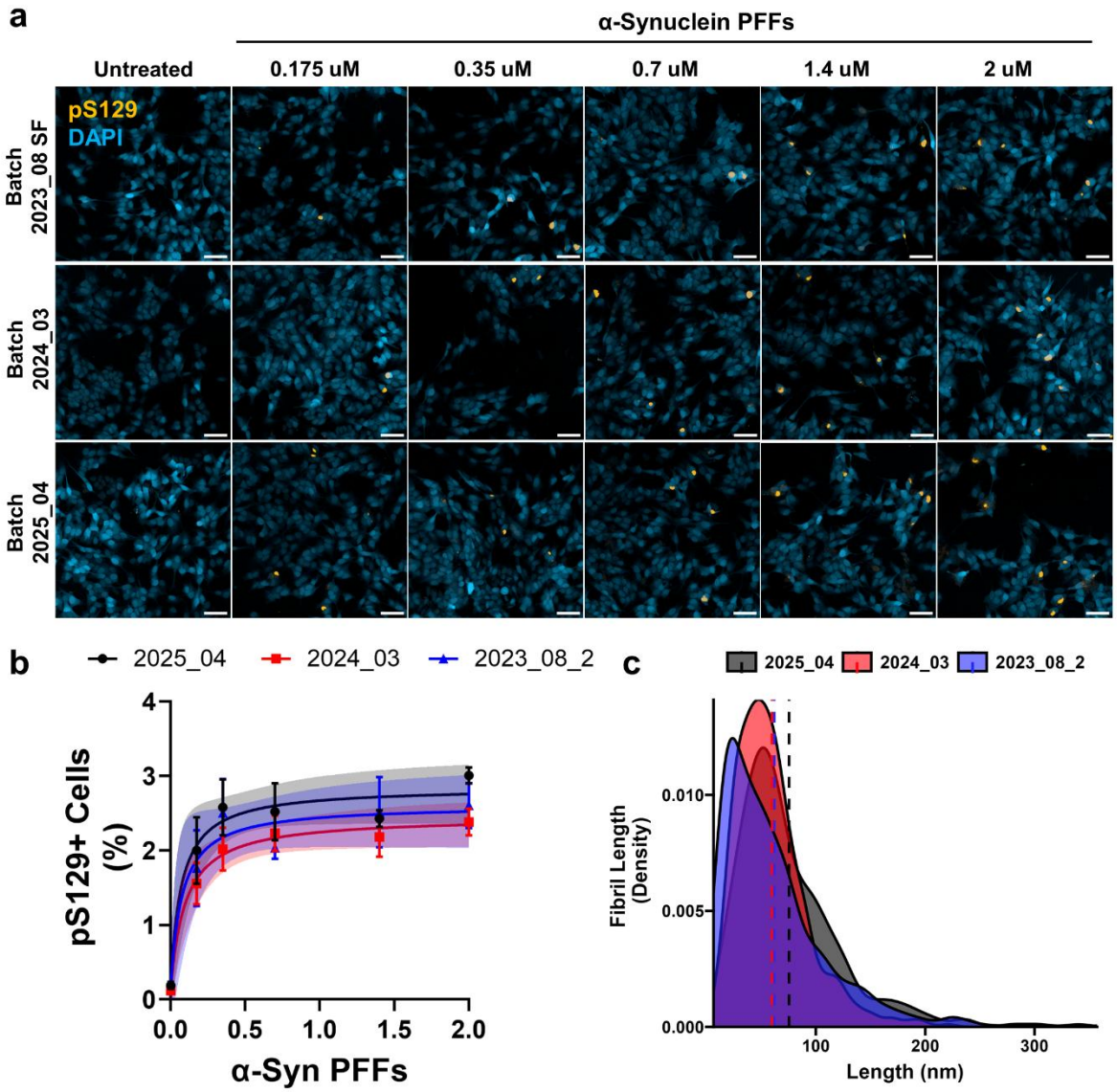


Figure 12. Preparations of in vitro aggregated α-synuclein show reduced batch-to-batch variability. a) Three preparations were aggregated *in vitro* and functionally characterised in SH-SY5Y overexpressing *SNCA*. Confocal microscopy images showed that all three preparations show similar dose-dependent increases in pS129-positive aggregation. Scale bars = 50 µm. 20x water immersion objective, Opera Phenix confocal microscope. b) Quantification of the number of pS129-positive cells showed no difference across all preparations. N = 1 independent experiment. Statistical test: two-way ANOVA with Tukey's multiple comparisons test. c) Density distribution plot of fibril lengths for each preparation. Vertical dashed lines indicate the distribution mean. N = 501 fibrils for 2024_03, N = 804 fibrils for 2023_08_02 and N = 339 fibrils for 2025_04. Data is presented as the mean ± SEM. * $p < 0.05$, ** $p < 0.01$, *** $p < 0.001$, **** $p < 0.0001$.

2023_03 to 2025_05). This is particularly evident when comparing the first preparation produced (batch 2021_11) compared to the last (batch 2025_05), which showed respective mean fibril lengths of 149.2 and 33.5 nm, respectively (Figure 14a). Binning the fibrils based on their length reveals that this appears to be driven by a loss of fibrils >200 nm in length, and a gain in the proportion of fibrils between 0-50

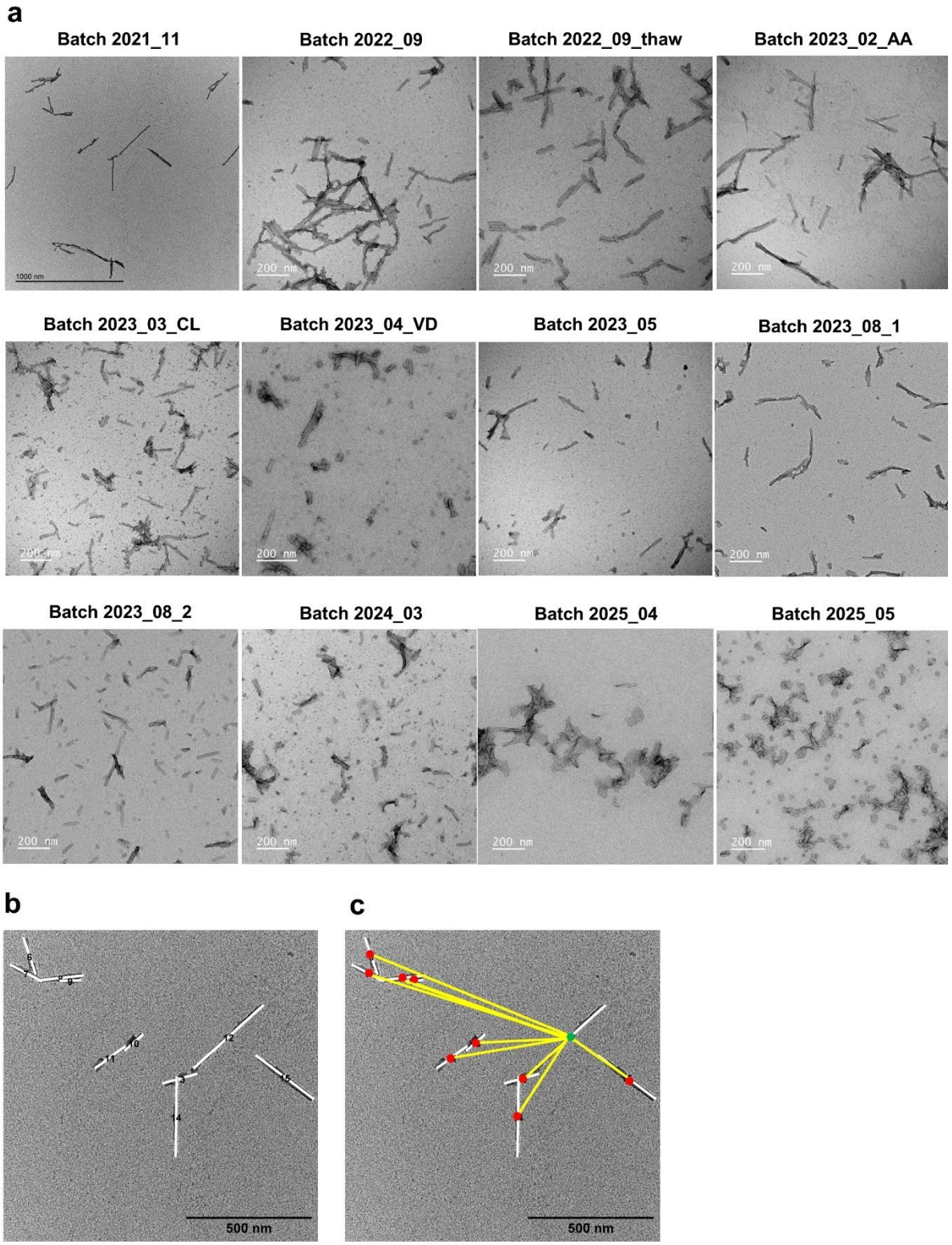


Figure 13. Comparison of all available α-synuclein PFF preparations to predict seeding efficiency.

a) Electron micrographs of *in vitro*-aggregated α-synuclein preparations. All preparations show similar overall morphology despite significant differences in the contrast of positive staining. The fibrils show varying lengths, numbers per field and sideways packing of fibrils. Scale bars = 200 nm, except for batch 2021_11, scale bar = 1000 nm. 20,000x objective on JEOL 1400 KV electron microscope. b) Fibril length was measured using Image J software. c) The Euclidean distance was measured from the centre point of another fibril. This measurement was repeated for all fibrils in a

field of view, generating a distribution of distance measurements. 23,000x objective on JEOL 1400 120 kV electron microscope.

nm in length (Figure 14b). Plotting the mean fibril lengths and the total fibril counts also reveals a possible inverse relationship between these two parameters (Figure 14c-d). Seeding efficiency was determined in a relative manner by comparing the maximal levels of pS129 induced by each preparation and normalising the value to the maximal levels of the previous preparation included in the comparison (see section 2.5). The seeding efficiency shows an increase following the adoption of the new aggregation method and although it shows batch-to-batch variability, this variability is reduced in scale compared to the first three preparations (Figure 14e).

To analyse the degree of protein aggregation and coagulation within α-synuclein fibril preparations, which is likely to effectively reduce the concentration of active seeds, the distance between the centre of each fibril and each of the neighbouring fibrils in the electron micrographs was measured per field of view, then mapped as a distribution (Figure 13c and Figure 14f). This highlighted increased distances between fibrils in preparation 2021_11, and decreased distance (and increased aggregation) in preparation 2025_04, visible in the electron micrographs of these two preparations (Figure 13a).

Finally in order to understand which measured parameters are most informative of a preparation's seeding efficiency, the mean length, mean Euclidean distance, fibril count and monomer source were correlated to the efficiency score of each preparation. This revealed no parameter had a statistically significant effect on seeding efficiency, though the mean length showed a Spearmann's $\rho = -0.25$ and the monomer source and aggregation protocol showed a Spearmann's $\rho = 0.317$ (Figure 14f). The effect of length on fibril uptake kinetics into cells has been well characterised, and it is possible that the α-synuclein monomer itself or the buffer composition, contaminants, or the aggregation method are contributing factors in the efficiency of the final preparation. Increasing the numbers of replicates may increase the statistical power of the correlation. Interestingly, neither the Euclidean distance nor the fibril count showed any correlation with the efficiency score, suggesting that the coagulation of the fibrils and the number of fibrils, measured in this manner, does not have an influence on the levels of pS129 generated (Figure 14f).

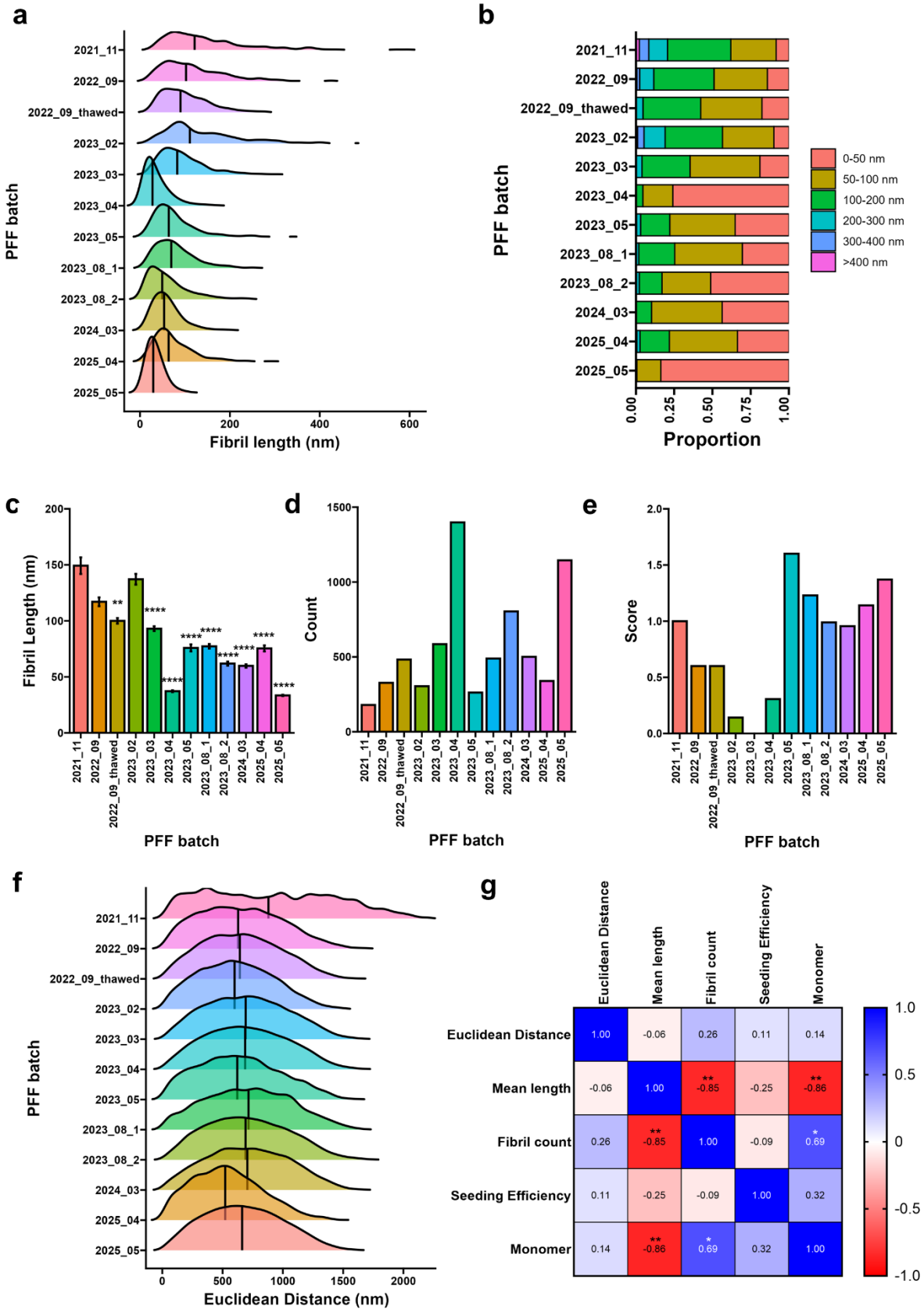


Figure 14. Predicting the seeding efficacy of PFF preparations based on multiple measurable parameters.

a) Distribution density plots of the fibril lengths for each preparation. Black vertical lines represent the mean of each distribution. N = 179 fibrils for 2021_11, N = 327 for 2022_09, N = 482 for 2022_09_thawed, N = 304 for 2023_02, N = 585 for 2023_03, N = 1398 for 2023_04, N = 262 for 2023_05, N = 489 for 2023_08_1, N = 804 for 2023_08_2, N = 501 for 2024_03, N = 339 for 2025_04 and N = 1145 for 2025_05. b) Fibril length was quantified and binned into categories based on length. The proportion of the number of fibrils in each bin is presented as a bar plot. Over time, the preparations have had fewer fibrils >200 nm and more fibrils <50 nm. c) Mean length of each fibril preparation shows a significant decrease of mean length over time when compared to batch 2021_11. See a) for N. Statistical test: Kruskal-Wallis test with Dunn's multiple comparisons test. d) Count of the number of fibrils in all the fields of view combined for each preparation reveals a trend towards increased numbers of fibrils. N = 1 independent experiment. e) The seeding efficiency score was computed for each batch relative to previous preparations and was overall increased and less variable in batches prepared with the adapted protocol. N = 1 independent experiment. f) Distribution density plot of the Euclidean distance between fibrils, measured from the centre position of a fibril to the centre position of another fibril within a field of view, for each preparation. N = 2590 measurements for 2021_11, N = 9304 measurements for 2022_09, N = 19,565 measurements for 2022_09_thawed, N = 7694 measurements for 2023_02, N = 28,179 measurements for 2023_03, N = 165,263 measurements for 2023_04, N = 5767 measurements for 2023_05, N = 20,448 measurements for 2023_08_1, N = 53,722 measurements for 2023_08_2, N = 21,643 measurements for 2024_03, N = 10,685 measurements for 2025_04, N = 116,586 measurements for 2025_05. g) Spearmann correlation plot of the parameters measured in relation to the seeding efficiency score of the fibril preparations. N = 1 independent experiment. Statistical test: Spearmann's correlation test. Data is presented as the mean ± SEM. * $p < 0.05$, ** $p < 0.01$, *** $p < 0.001$, **** $p < 0.0001$.

3.3 pS129-positive aggregates co-localise with a marker of mitophagy

Implementation of the α-synuclein PFF-induced pS129 assay into i^3 cortical neurons allows for the study of a basic, neuronal biological model that is highly tractable and has shorter experimental timeframes. With the integration of the dCas9-expressing cassette, having the possibility of knocking down genes of interest allows dissection of the molecular process of α-synuclein aggregation and its downstream effects.

3.3.1 α-Synuclein aggregates trigger formation of pS65Ub

It has been widely reported that α-synuclein pre-formed fibrils act as seeds which trigger the aggregation of endogenous α-synuclein monomer. Examination of the *SNCA* gene expression (section 3.1.2) suggested that *SNCA* is upregulated after differentiation and over maturation, suggesting increased levels of pS129 could be seeded with PFF treatment later in maturation. To investigate the impact of α-synuclein monomer expression over culture time on seeded aggregation, i^3 neurons were treated with

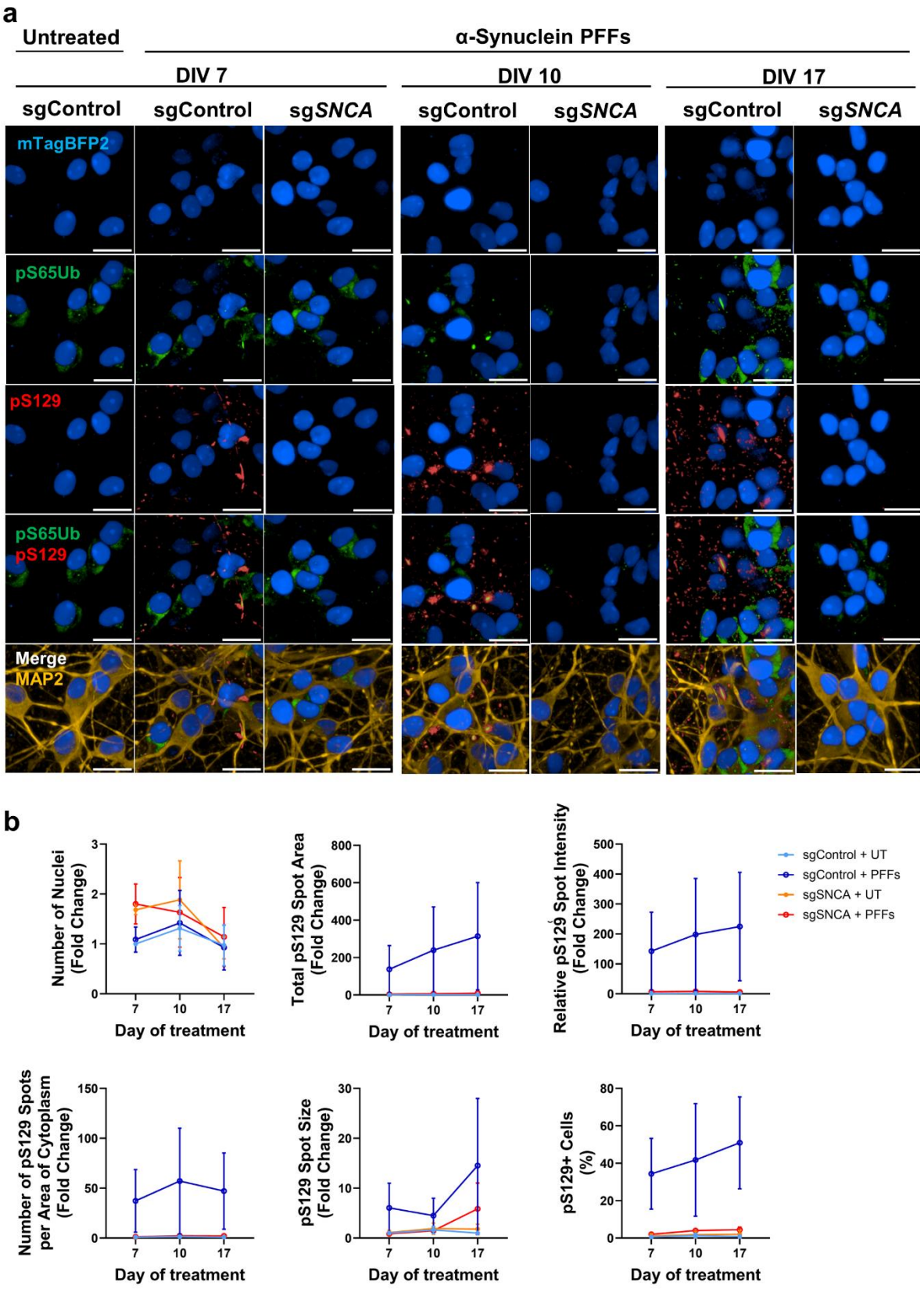


Figure 15. Seeding pS129-positive aggregation later in maturation does not significantly increase levels of pS129.

a) Confocal microscopy images of PFF-seeded pS129-positive aggregation in i^3 neurons 14 days after PFF treatment at DIV 7, 10 or 17. Immunocytochemistry for pS65Ub and pS129 highlights similar levels of both markers with treatment later in maturation. Scale bar = 20 μm. 40x water

immersion objective, Opera Phenix confocal microscope. b) Quantification of the pS129 staining in the images in panel a) shows no statistically significant differences in measured parameters with PFF treatment on days 7, 10 or 14. N = 2 independent differentiations. Statistical test: Two-way ANOVA with Tukey's multiple comparisons test. Data is presented as the mean ± SEM. * $p < 0.05$, ** $p < 0.01$, *** $p < 0.001$, **** $p < 0.0001$.

α-synuclein PFFs at DIV 7, DIV 10 and DIV 17, then fixed 14 days post-seeding and stained by immunocytochemistry for the levels of pS129. Examination of the confocal microscopy images suggested that there were similar levels of pS129 seeded 14 days post-PFFs for DIV 7, 10 and 17 (Figure 15a). Quantification of key parameters such as the total spot area, relative intensity, number of spots per area of cytoplasm, spot size and the number of pS129-positive cells showed no significant difference in PFF-induced aggregation with time (Figure 15b). Knockdown of *SNCA*, which was predicted to abolish aggregation, showed no increase in pS129 aggregation in terms of intensity, size or the number of pS129-positive cells after seeding (a significant increase was noted for the total pS129 spot area between UT and PFF-treated sg*SNCA*-treated cells on DIV 17 ($p = 0.0217$), though the effect size was very small). Consequently, sg*SNCA*-expressing cells effectively served as a negative control for the assay. This is consistent with the templating of endogenous monomer by exogenous proteinopathic seeds. There was no significant change in the number of nuclei as a result of the PFF-treatment, suggesting that the PFFs and aggregation process are not toxic at the timepoints examined (Figure 15b). Overall, these data suggest that increased the increase in monomer expression over DIV 7 to 17 is associated with no substantial gains in the levels of PFF-seeded pS129-positive α-synuclein aggregation.

Previous data in dopaminergic neurons in the laboratory suggested there was an interaction between the PFF-induced aggregation of α-synuclein and the formation of the PINK1-dependent mitophagy marker pS65Ub. Staining one of the experimental replicates with an antibody targeting pS65Ub revealed a similar pattern, with levels of pS65Ub correlating with the levels of pS129 and co-localising with the pS129 puncta (Figure 15a).

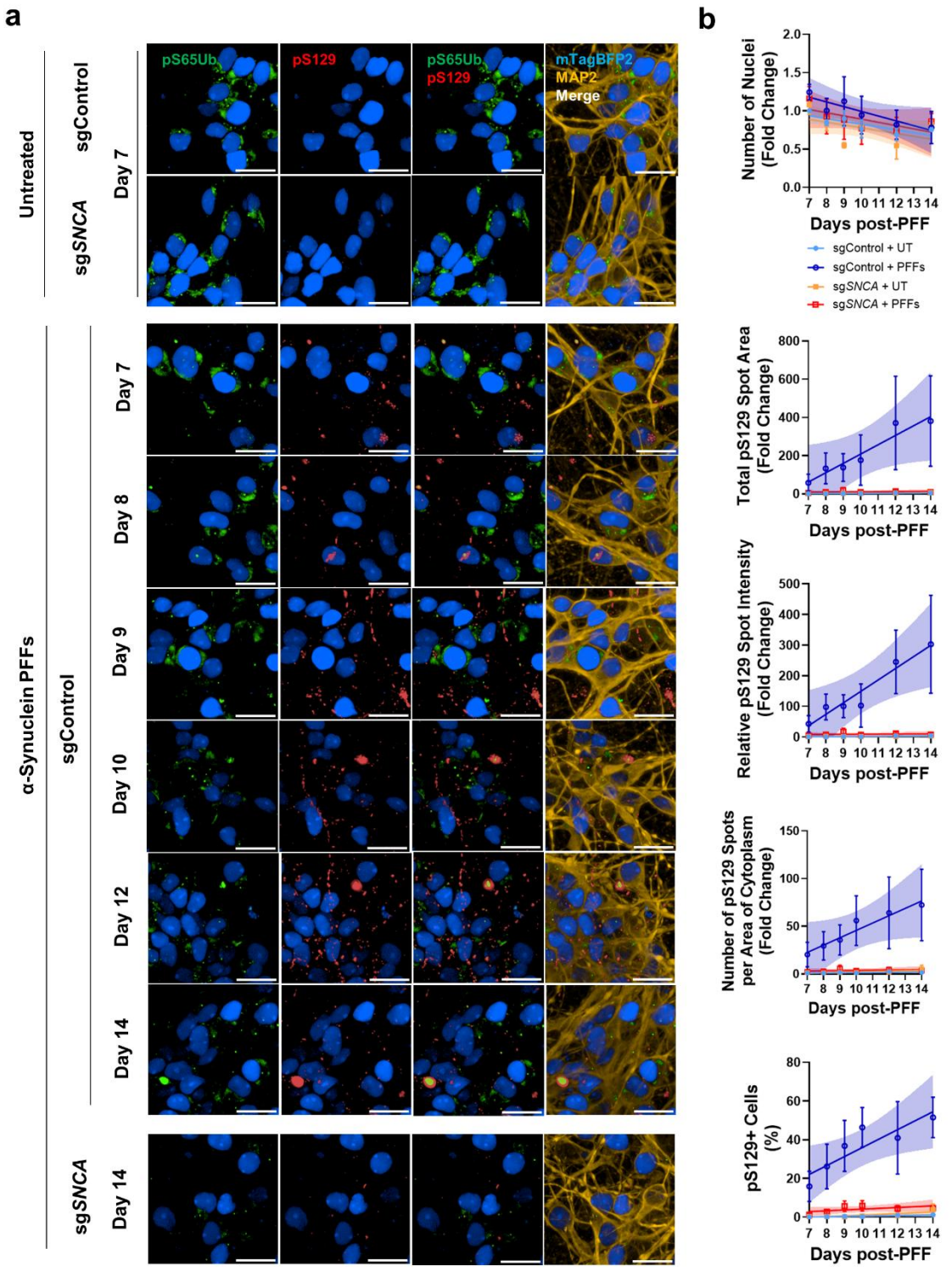


Figure 16. Time-dependent pS129 and pS65Ub accumulation over time post-seeding with PFFs.

a) Confocal microscopy images show an increase in pS129 and pS65Ub immunostaining over time after seeding with PFFs at DIV 10. Scale bars = 20 µm. 40x water immersion objective, Opera Phenix confocal microscope. b) Quantification of the immunostaining reveals a time-dependent increase in the area, intensity of pS129 immunostaining as well as the number of pS129 spots and percent of pS129-positive cells. Cells transduced with a sgRNA targeting *SNCA* have significantly reduced pS129 levels. N = 3-4 independent differentiations. Statistical test: paired mixed-effects

model with Tukey's multiple comparisons. Data is presented as the mean ± SEM. * $p < 0.05$, ** $p < 0.01$, *** $p < 0.001$, **** $p < 0.0001$.

To investigate the kinetics of pS129 and pS65Ub accumulation in i^3 neurons, the DIV 10 timepoint for PFF treatment was selected and the levels of both markers were measured by immunocytochemistry from day 7 to 14 post-seeding. Confocal microscopy images revealed an increase in pS129-positive aggregates, both in number and size, over time as well as an apparent increase in the size of the pS65Ub spots co-localising with these aggregates (Figure 16a). Quantification of the staining revealed a significant increase in the percentage of pS129-positive cells over the course of aggregation (timepoint, $p = 0.0101$, genotype and treatment, $p = 0.0016$, interaction, $p = 0.0158$) (Figure 16b). For the relative intensity, number of spots per area of cell and percentage of pS129-positive cells, there was a significant effect of genotype and treatment ($p = 0.0475$, $p = 0.0672$ and $p = 0.0016$), and knockdown of the *SNCA* gene markedly reduced the levels of pS129-positive aggregates (Figure 16a-b).

Though there was a trend towards increased total pS129 spot area, relative spot intensity and number of spots per area of cell, these measured parameters did not achieve statistical significance. It is nevertheless interesting to observe that this possible increase for most parameters is linear, suggesting that saturation was not achieved. If practical considerations allowed for evaluation of later experimental timepoints, it is possible that the process of aggregation would have continued unabated, perhaps revealing more insight into early- versus late-stage α-synuclein aggregation.

3.3.2 pS129 and pS65Ub interaction at a single-aggregate level

In the previous experiment, it was observed that both pS65Ub-positive and negative α-synuclein aggregates occurred in PFF-treated neurons, suggesting that there existed two populations, a population that co-localised with pS65Ub and a population that did not. Analysis was performed on single pS129-positive aggregates to uncover the relationship between pS65Ub and pS129. The size of pS129-positive aggregates was hypothesised to determine the interaction with pS65Ub as larger aggregates seemed to co-localise with pS65Ub to a higher degree that smaller aggregates (Figure 16a).

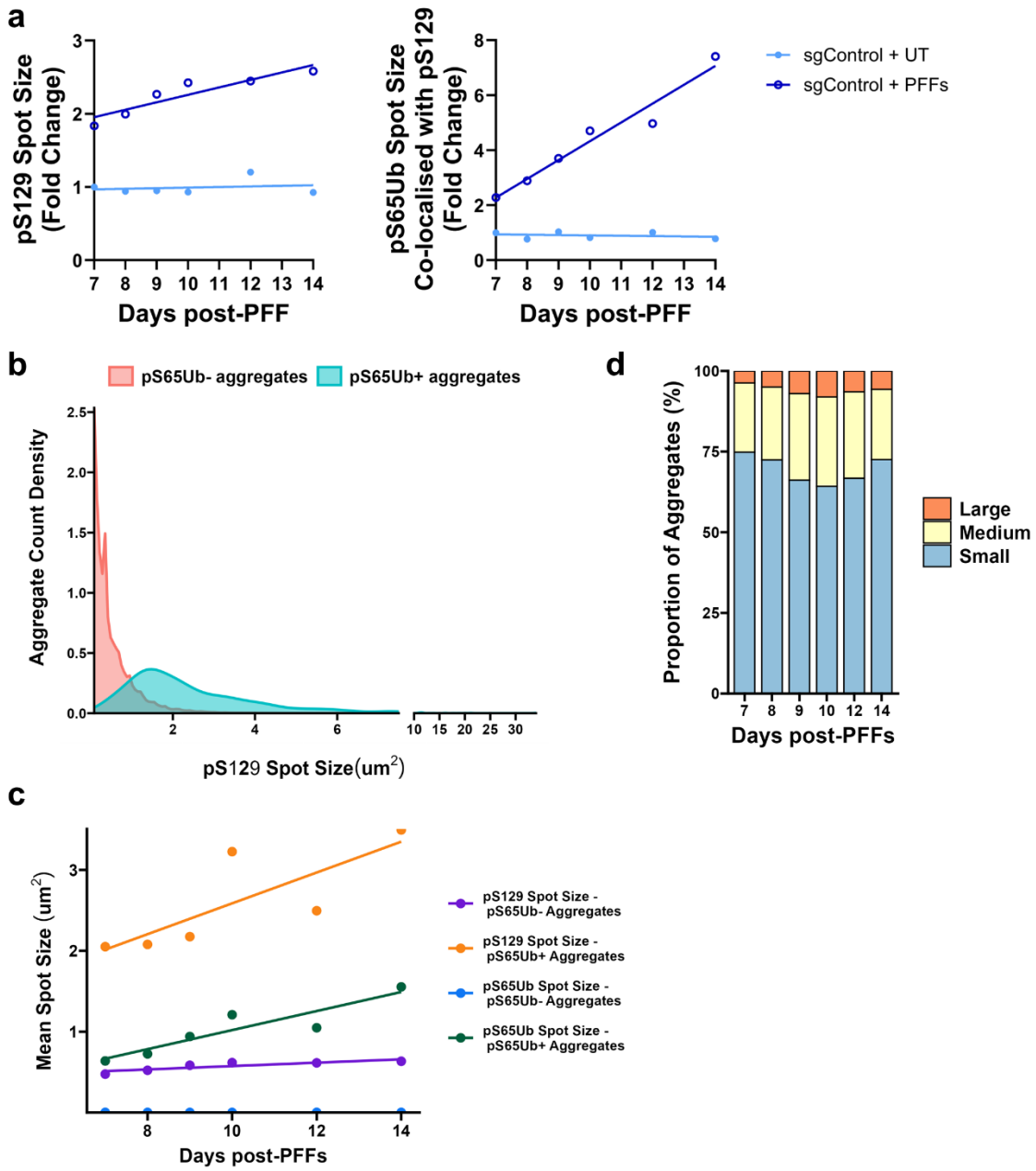


Figure 17. Relationship of pS129 and pS65Ub puncta over aggregation time course.
a) Mean pS129 and pS65Ub puncta size over days post-PFF seeding is increased linearly with time. b) Distribution density plot of the pS129 spot size, grouped based on co-localisation with pS65Ub, reveals that pS65Ub-positive aggregates are overall larger than pS65Ub-negative aggregates. c) pS129-positive aggregates were binned based on size, revealing a small increase in large aggregates and a small decrease in small aggregates over time. c) The mean spot size for pS129 and pS65Ub in pS65Ub-positive or negative pS129 aggregates shows that pS129-positive, pS65Ub-positive aggregates are larger and show increased mean size over time. N = 1 independent experiments. Data is presented as the mean.

Comparing the pS129 aggregate size over time revealed that the mean size of these puncta increases linearly (Figure 17a). Similar analysis for pS65Ub-positive puncta revealed a time-dependent increase

in colocalization of pS65Ub with pS129-positive aggregates. Furthermore, the distribution of pS129 aggregate sizes was markedly different for pS65Ub-positive and pS65Ub negative aggregates, with pS65Ub-positive aggregates being larger (Figure 17b).

The larger pS65Ub-positive pS129 spots grew in a time-dependent manner, as did the pS65Ub spots co-localised with pS129-positive aggregates (Figure 17c). In contrast, pS65Ub-negative pS129 spots were smaller in area and showed negligible growth over time. This could be indicative of a population of pS129 aggregates which show very slow aggregation kinetics and little interaction with pS65Ub. Alternatively, this could be the result of continual nucleation of pS129-positive aggregates over time, with smaller aggregates becoming larger aggregates whereupon they start accumulating pS65Ub, which are then replaced by *de novo* synthesis of small aggregates. This latter hypothesis is consistent with the linear accumulation of pS129-positive puncta in terms of area, intensity and number over time (Figure 16a-b). Classifying each aggregate into small (<0.6 um^2), medium (0.6-1.5 um^2) or large (>1.5 um^2) aggregates revealed that large aggregates increased marginally over time and small aggregates were slightly reduced between days 9 and 12 post-PFFs before returning to baseline (Figure 17d). The lack of overt trend towards reduced small aggregate and increased large aggregate proportion is also consistent with continual generation of aggregates over time.

3.3.3 PFF-induced pS65Ub formation is dependent on PINK1

To rule out non-specific antibody interactions or other confounders in the interaction between pS129-positive aggregates and pS65Ub-tagged mitochondria, CRISPRi was used to knock down *PINK1* and investigated the levels of pS65Ub after PFF seeding (Figure 18a). As expected, quantification of pS129 levels revealed a robust increase with PFF treatment, which was abolished by the knockdown of *SNCA* (Figure 18b). The levels of pS129 in *PINK1* knockdown conditions was equivalent to the control condition.

Quantification of the pS65Ub levels showed an increase in pS65Ub in control, PFF-treated conditions (Figure 18b). The increase in pS65Ub was found to be driven by pS129-positive cells. *PINK1* knockdown in neurons showed equivalent levels of pS65Ub to the untreated control in pS129-positive

cells and pS65Ub levels were significantly reduced in pS129-negative cells. Overall, these data suggest that the PFF-induced accumulation of pS65Ub is dependent on the PINK1-dependent pathway of mitophagy, and that pS129-positive aggregates are co-localised with mitochondria tagged for degradation.

3.4 Discussion

In this chapter, I have shown that i^3 neurons could be differentiated to a population of 97.4% MAP2-positive neurons, which expressed markers of neuronal progenitor cell identity during differentiation as well as markers of cortical and glutamatergic identity during differentiation and maturation. The cells acquired the capability of firing action potentials and developed a network bursting pattern of activity with increased time in culture.

To develop a robust model of α-synuclein seeding, α-synuclein monomer was aggregated *in vitro* and the resulting fibrils were shown to induce a dose-dependent increase in pS129-positive aggregates in neurons and SH-SY5Y. However, α-synuclein preparations were found to have high batch-to-batch variability. Optimisation of the aggregation protocol yielded increased consistency between preparations. Correlation of several quality control metrics with the seeding efficiency of each preparation suggested no measured parameters regarding fibril length, count, coagulation or preparation method significantly correlated with higher seeding efficiency. However, the mean fibril length showed a small inverse association and the monomer source and aggregation method showed a small positive association with pS129-positive aggregate seeding.

Optimisation of the pS129 seeded assay in i^3 neurons highlighted that α-synuclein fibril-induced aggregation was not significantly increased with seeding at later timepoints in maturation. Knockdown of *SNCA* resulted in strong inhibition of aggregation. pS129-positive aggregates were also found to co-localise with pS65Ub, a marker of mitophagy formed through the PINK1-dependent pathway. Time course analysis showed that pS129-positive aggregates increased in size with time post-seeding, as did

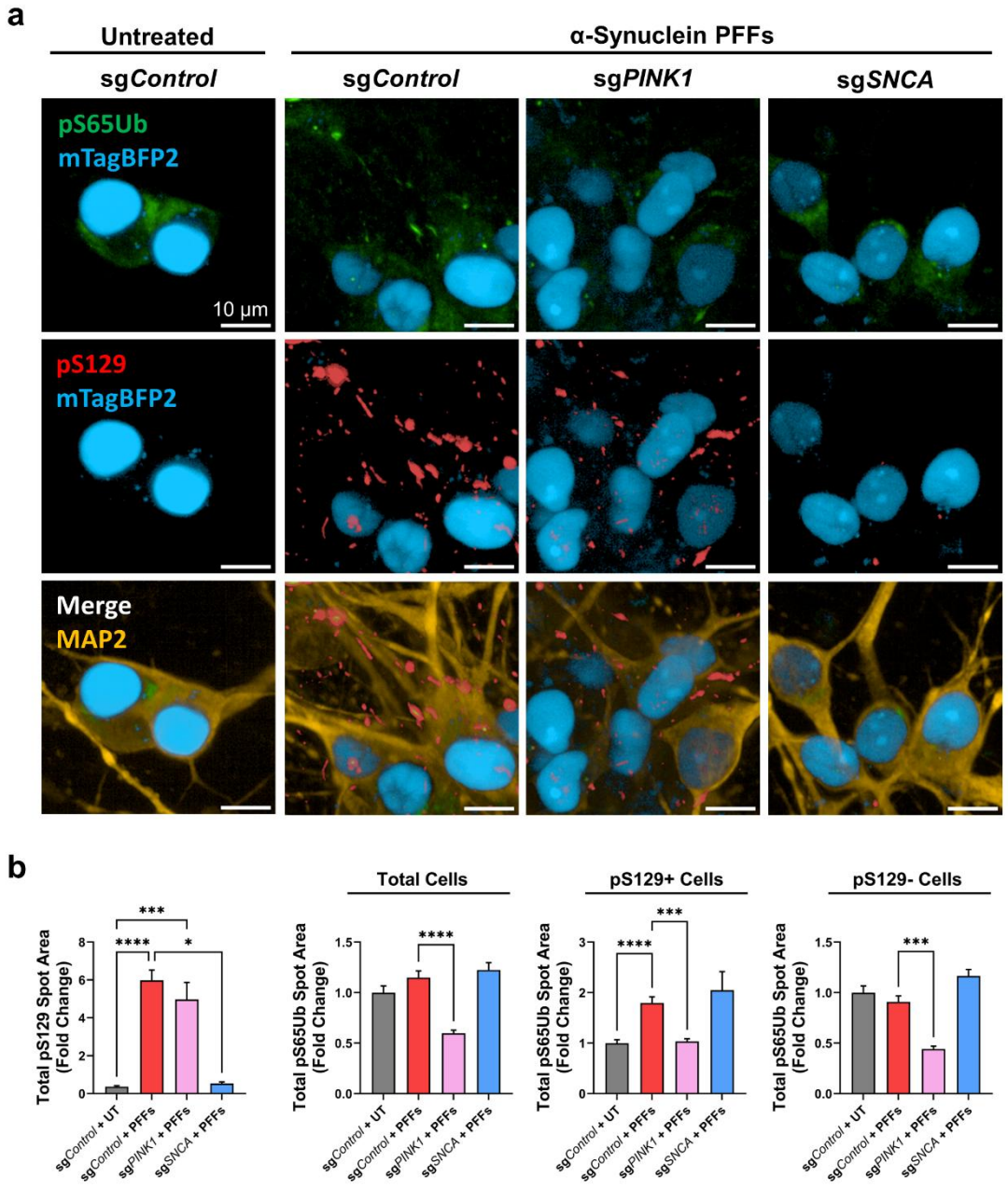


Figure 18. PFF-induced pS65Ub accumulation is dependent on the kinase PINK1.
a) Confocal microscopy images of pS65Ub and pS129 staining in cells transduced with a control sgRNA, or sgRNAs targeting *PINK1* or *SNCA*. pS129 staining is abolished with knockdown of *SNCA*, and pS65Ub immunostaining is reduced in *PINK1* knockdown conditions. b) Quantification of the pS65Ub and pS129 immunostaining in total, pS129-positive and pS129-negative cells. N = 1 independent differentiations. Statistical test: Kruskal-Wallis test with Dunn's multiple comparison test. Data is presented as the mean ± SEM. * $p < 0.05$, ** $p < 0.01$, *** $p < 0.001$, **** $p < 0.0001$.

the co-localised pS65Ub puncta. pS65Ub-positive pS129 aggregates were on average larger than their pS65Ub-negative counterparts. Knockdown of the *PINK1* gene prevented the accumulation of pS65Ub in PFF-treated conditions.

3.4.1 Maturity of iPSC-derived i^3 cortical neurons

qPCR analysis of various neuronal progenitor, neuronal, glutamatergic and cortical markers suggested that the NGN2-induced i^3 neurons express markers of neuronal progenitor cells, *PAX6* and *NES*, between DIV 3-10 and subsequently transition to a more mature, neuronal and glutamatergic profile with further maturation. Neurogenin2 is a basic helix-loop-helix transcription factor whose expression was found to be sufficient for the generation of electrophysiologically-active neurons from mouse ESCs, even in the absence of medium factors supportive of neuronal differentiation, through activation of a cascade of known developmental transcription factor expression such as *Math3, Olig2* (Thoma *et al*, 2012). Altogether, these data suggests that the forced expression of NGN2 results in activation of physiological developmental neurogenesis pathways.

It is interesting that *PAX6* was also shown to be upregulated by myself and other authors in NGN2-induced neuronal cultures (Thoma *et al.*, 2012), highlighting a reversal in the physiological cascade of transcription factors. Indeed, multiple studies have shown that in model organisms, Pax6 is an upstream neuronal progenitor factor which results in the activation of Ngn2, whose expression in turn generates a negative feedback loop where Pax6 is downregulated (Bel-Vialar *et al*, 2007; Bergström *et al*, 2016). Despite this reversal, NGN2 expression in this study was associated with generation of glutamatergic neurons expressing MAP2, TUJ1, VGLUT1 and VGLUT2, which lack *PAX6* and *NES* expression after DIV 10 and which become electrophysiologically active with further maturation from DIV 30 onwards. These data suggest that NGN2-induced neurons reproduce many of the features of physiological neurons, and thus offer a time-effective, homogeneous model of cortical excitatory neurons. However, given that the timepoints of this study were between DIV 10 and 24, my data suggests that the neurons used in these studies were still immature and did not fully recapitulate the characteristics of *in vivo* neurons, in particular the electrophysiological activity.

NGN2-induced neurons have been extensively characterised elsewhere (Zhang *et al.*, 2013; Wang *et al.*, 2017; Chen *et al.*, 2020; Rosa *et al.*, 2020; Lam *et al.*, 2024). These studies have highlighted similar advantages and disadvantages of this cell culture model. An early iteration of the NGN2-induced neuron protocol showed that NGN2-induced neurons became functional, excitatory neurons with

electrophysiological activity and features of synaptic plasticity that could integrate into mouse brains (Zhang *et al.*, 2013). However, the neurons in this study were suggested to be immature on the basis on their overall gene expression profile. Similarly, neurons differentiated from an isogenic iPSC line with stable integration of an NGN2-expressing construct expressed TUJ1, NeuN, Tau, AnkG, GluR2/3 and VGLUT1 at 4 weeks in culture. At 8 weeks, the cells were able to fire action potentials, which was inhibited by CNQX (Wang *et al.*, 2017). RNA-sequencing of i^3 neurons at timepoints over the first month of maturation showed expression of *VGLUT1*, *VGLUT2*, *ANK2*, *PAX6*, *NES*, *MAP2*, *SYN1*, *CUX2* and *CUX1* (Tian *et al.*, 2019), in line with my data. Other studies have suggested that inducible neurons cluster with foetal neurons based on gene expression profiles (Nehme *et al*, 2018), and resulted in less mature neurons than an embryoid body-based differentiation protocol, corresponding roughly to second trimester neurons (Rosa *et al.*, 2020).

3.4.2 i^3 Neurons as a model of Parkinson's disease

As discussed above, i^3 neurons provide a rapid and reproducible cell culture model that is broadly neuronal, cortical and excitatory, despite being immature. In the context of studying PD, a disease of old age, the relevance of these neurons is an appropriate question. However, iPSC-derived models have successfully replicated phenotypes found in post-mortem brains of human patients, despite iPSC-derived cells generally proving to be youthful models of *in vivo* cell types (reviewed in Cornacchia & Studer, 2017). A study of post-mortem *PARK2*-deficient patient brains and iPSC-derived cells from the same donors revealed α-synuclein aggregation in one donor's brain and iPSC-derived neurons, which was absent in the closely-related second donor's brain and iPSC-derived neurons (Imaizumi *et al*, 2012). Another comparative study highlighted deficiencies in nuclear envelope organisation, which was also found in post-mortem human brain tissue (Liu *et al*, 2012a). More broadly, studies in post-mortem brain tissues and in iPSC-derived neurons have independently identified defects in mitochondrial respiration, oxidative stress, changes in dopamine metabolism or signalling and the autophagy-lysosomal pathway as key mediators of dysfunction in PD (reviewed in Toulorge *et al*, 2016 and Tran *et al*, 2020). Overall, this provides a strong rationale for the use and study of iPSC-derived neurons to understand disease

mechanisms, especially in the context of this study where a tractable model was required to implement CRISPRi-mediated gene knockdown.

The use of NGN2-induced neurons, which adopt a cortical neuronal cell fate, allows the modelling of late-stage PD. Indeed, α-synuclein pathology in PD is thought to spread from the midbrain at early Braak stages to higher brain regions such as the cortex in later Braak stages (Braak *et al.*, 2003), though the exact primary site of α-synuclein aggregation – the midbrain or perhaps the olfactory bulb or enteric nervous system – has been controversial. However, it is well accepted that dopaminergic neurons in the substantia nigra pars compacta are particularly vulnerable to α-synuclein pathology, dysfunction and death, and it is the loss of this population of neurons that results in the motor symptoms so characteristic of the disease. As such, this study would have been well-suited to implementation in iPSC-derived dopaminergic neurons, though this was challenging on several counts.

Genetic screening on the scale required for this study is reliant on a homogeneous population of cells. Indeed, the small molecule-based differentiation protocol which is well-established in our laboratory and common in the field results in a mixed population of ~50-60% TH+ neurons (Kriks *et al*, 2011; Zambon *et al.*, 2019; Beccano-Kelly *et al.*, 2023; Cramb *et al*, 2023). This is a crucial concern as variability, replicate-to-replicate and across mixed cell populations, may obscure biological effects. This is likely to be highly compounded when the effect sizes are expected to be small. Progress is currently being made by several laboratories in creating transcription factor-induced dopaminergic iPSC lines, following the same template as NGN2-induced cortical neurons. An early iteration used a combination of Mash1, Ngn2, Sox2, Nurr1 and Pitx3 to turn fibroblasts into dopaminergic-like neurons, but showed a loss of 96-98% of cells in the process (Liu *et al*, 2012c). More recently mRNA-mediated delivery of Atoh1 and Ngn2 induced >90% of cells into TH+ neurons, but required transfection of cells with each differentiation (Xue *et al*, 2019), whereas others used a combination of ASCL1 and LMX1A (Nishimura *et al*, 2022) or ASCL1, LMX1B and NURR1 (Powell *et al*, 2023). In the latter study, no electrophysiological activity characteristic of *in vivo* dopaminergic neurons was detected. One of the most recent attempts used NGN2-induced differentiation coupled with small molecule patterning factors, and the resultant neurons synthesised dopamine and had spontaneous electrophysiological

activity reminiscent of brain dopaminergic neurons. Despite this, the population was only ~60% TH+ (Sheta *et al*, 2022). Successful generation of transcription factor-induced TH+ neurons will make feasible large-scale screening in the most vulnerable cell type in PD.

3.4.3 Methods of modelling α-synuclein aggregation in a dish

Due to the foetal nature of iPSC-derived neurons, modelling the process of α-synuclein aggregation *in vitro* has been challenging to reproduce and several different methods have been developed to trigger the process within reasonable timeframes. Indeed, iPSC-derived cells do not spontaneously develop aggregates resembling Lewy bodies or Lewy neurites in vitro, even in a genetic background containing four copies of the *SNCA* gene (Byers *et al*, 2011; Iannielli *et al*, 2022). Small, punctate aggregates appeared in a diffuse manner throughout the soma (Iannielli *et al.*, 2022), which became detectable using Thioflavin S after 5 weeks of maturation. To model α-synuclein pathology, iPSC models have been modified to use optogenetics to induce aggregation (Bérard *et al*, 2022; Kim *et al*, 2023), or bimolecular fluorescence complementation (Outeiro *et al*, 2008). Other laboratories used transduction with viral vectors to express supra-physiological levels of *SNCA* (reviewed in Delenclos *et al*, 2019). Alternatively, Volpicelli-Daley and colleagues were the first to show that recombinant α-synuclein monomer aggregated *in vitro* were able to template the aggregation of endogenous monomer expressed at physiological levels in primary neurons (Volpicelli-Daley *et al.*, 2011). This was reproducible across cell types, such as iPSC-derived neurons (Zambon *et al.*, 2019). Aggregates formed in this way reproduce many of the features of Lewy bodies and Lewy neurites *in vivo* (Mahul-Mellier *et al.*, 2020).

It should be noted that α-synuclein PFFs, by virtue of triggering the formation of α-synuclein aggregates in neurons upon uptake, are more similar to a model of disease progression than *de novo* disease initiation. α-Synuclein pathology in PD is thought to spread from lower to higher brain structures in a prion-like manner, with late-stage disease showing cortical region involvement (Del Tredici *et al*, 2016). Monomeric, oligomeric and short fibrillar species have all been found in the CSF or plasma of PD patients (Borghi *et al*, 2000; El-Agnaf *et al*, 2003; El-Agnaf *et al*, 2006; Desplats *et al*, 2009; Lobanova *et al*, 2022), exocytosed by neurons through several possible mechanisms such as extracellular vesicles or classical exocytosis (reviewed in Brás & Outeiro, 2021). In addition, many

studies have shown that these species can seed aggregation and fibril formation in seeded amplification assays (Groveman *et al*, 2018; Kang *et al*, 2019; Shahnawaz *et al*, 2020; Russo *et al*, 2021; Schaeffer *et al*, 2024; Bräuer *et al*, 2025). Several receptors have been proposed to mediate α-synuclein binding and uptake at the cell surface, in an aggregation species-dependent manner, such as LAG3 (Birol *et al*, 2019; Mao *et al*, 2016), neurexin-1β (Birol *et al*, 2019), LRP1 (Chen *et al*, 2022), or heparan sulphate proteoglycans (Birol *et al*, 2019). However, a recent study found that LAG3 was not expressed in neural stem cell-derived neurons, or human and mouse brain samples (Emmenegger *et al*, 2021), suggesting that further studies will be required to confirm uptake mechanisms of these α-synuclein species. Altogether, these data strongly suggest that α-synuclein seeds likely mediate cell-to-cell spreading over the course of the disease.

In light of this, the PFF model of α-synuclein aggregation has been widely used to model the spread of pathology *in vivo*. Injection of PFFs in mouse brains results in a transsynaptic spread of α-synuclein pathology, in a manner than is dependent on both the connectome as well as cell-intrinsic properties which confer a fertile ground for α-synuclein aggregation (Henrich *et al*, 2020), and have been widely used in the field as models of disease propagation in the brain (Desplats *et al*, 2009; Luk *et al*, 2012a; Luk *et al*, 2012b; Paumier *et al*, 2015; Abdelmotilib *et al*, 2017). In the context of this study, the combination of the α-synuclein seeding model and cortical cell model is most accurately reflecting the processes of late-stage PD, where α-synuclein pathology in cortical neurons is likely triggered by seeds produced in other brain regions.

3.4.4 Factors influencing α-synuclein PFF-induced aggregation

Since the discovery that α-synuclein aggregation could be triggered by PFFs, the model has become one of the most popular methods for modelling Parkinson's disease in cultured cells or rodents. My data showed that α-synuclein recombinant monomer can be agitated at 37°C to generate long fibrils, which are then sonicated into smaller fragments. Treatment of i^3 neurons with fragmented fibrillar α-synuclein resulted in the generation of pS129-positive α-synuclein aggregates. Whilst an early study used transduction reagents to shuttle fibrils into the cytoplasm of cultured immortalised cells (Luk *et al.*, 2009), it has since been shown on many occasions that fibrils are actively endocytosed by neurons and

other cell types and result in the generation of pS129-positive aggregates (Lee *et al*, 2008; Desplats *et al*, 2009; Volpicelli-Daley *et al.*, 2011; Luk *et al.*, 2012b; Tarutani *et al.*, 2016; Courte *et al*, 2020). In this study, initial α-synuclein preparations were characterised by high batch-to-batch variability, an aspect of the model which has been widely observed in the field (Polinski *et al.*, 2018).

There are multiple factors within the α-synuclein PFF preparation itself which have been observed to modify its seeding efficiency. The origin, quality and consistency of the α-synuclein recombinant monomer used to produce the fibrils is a strong determinant of the potency of a preparation, once aggregated. Ideally, α-synuclein monomer should be unmodified, produced at a high concentration and provided in a buffer solution containing ~100 mM NaCl with a pH of ~7.4 (Volpicelli-Daley *et al*, 2014; Polinski *et al.*, 2018; Patterson *et al*, 2019). As contaminants and other inconsistencies may affect fibrillisation, consistent monomer preparation is one of the crucial considerations in establishing a robust PFF-induced aggregation protocol (Polinski *et al*, 2018). Given that the monomer used for batches 2021_11 to 2023_02 was prepared ad hoc, this may have contributed to the stronger variability observed in these preparations. Furthermore, buffer composition was different between the monomer obtained from the Protein Production SRF (in PBS, exact composition unknown) and the monomer obtained commercially for subsequent preparations (in 20mM Tris, 100mM NaCl, pH 7.4). Whilst alterations in salt composition of buffer conditions has been shown to produce entirely different conformations of α-synuclein assembly upon aggregation (Bousset *et al*, 2013), such a marked difference in fibril architecture was not noted here. Additional considerations include the speed of agitation and length of incubation of the monomer, which was increased to 1000 rpm and decreased to 7 days, respectively, as stronger agitation has been published to buffer small changes in pH or ionic strength of the solution, increasing consistency of preparations (Narkiewicz *et al.*, 2014).

Correlation analysis of fibril length, count, coagulation and monomer source showed none of these were strong factors in influencing seeding efficiency. It should also be noted that the method of preparation of fibrils was overhauled concomitantly to the change in monomer supplier. As such, it is currently not possible to untangle the effect of the monomer preparation versus the changes in fibril incubation and agitation. Fibril length was mildly anti-correlated to the seeding efficiency score, though this was not

significant, suggesting it is possible that reduced α-synuclein fibril length is associated with increased PFF-induced aggregation. Monomer source and/or aggregation method also showed a possible effect on seeding potency. There is general support for the idea that shorter fragments may increase seeding potential. A 2016 study identified a length-dependent increase in the rate of polymerisation of fibrils as measured by ThT fluorescence kinetics, suggesting that shorter fibrils accelerate fibrillisation (Tarutani *et al*, 2016). However, dilution of sonicated fibrils replicated the kinetics of unsonicated fibrils, suggesting that the number of available seeds – and thus, presumably, nucleation points – is the determining factor (Tarutani *et al.*, 2016). This idea is further supported by other studies. For example, increased fibril concentration was found to be a stronger determinant of levels of α-synuclein pathology than the length of the fibrils injected into mouse brains. Indeed, shorter fibrils did show higher seeding activity than longer fibrils, but the effect reached a ceiling at ~100 nm in length and further fragmentation did not increase potency (Abdelmotilib *et al*, 2017). In our study, it is possible that methodological considerations are obscuring the true effect of fibril length on fibril potency. Indeed, increasing the concentration of fibrils was shown in mouse primary neurons to increase α-synuclein seeding potential but trended towards reaching a ceiling, which was attributed to attaining an equivalent concentration of exogenous PFF to the endogenous α-synuclein concentration (Abdelmotilib *et al.*, 2017). As the correlation analysis in our study was performed using the maximal values of pS129 attained – at the highest concentration of fibrils – it is possible that the effect of shorter fibril preparations may be concealed.

3.4.5 α-Synuclein fibrils template the aggregation of endogenous α-synuclein monomer

Our study showed that treatment of i^3 neurons and CMV-*SNCA*-T2A-GFP-expressing SH-SY5Y cells with α-synuclein PFFs resulted in pS129-positive α-synuclein aggregation that increased with time and was dependent on the levels of endogenous SNCA monomer. Knockdown of the *SNCA* gene using CRISPRi resulted in marked reduction of α-synuclein pathology. Several studies have established that α-synuclein PFFs are endocytosed, then escape to the cytoplasm by lysosomal rupture (Freeman *et al*, 2013) where endogenous SNCA monomer is recruited to the site of aggregation. For example, MYC-tagged fibrils have been found at the core of pS129-positive aggregates, whereas the rest of the

aggregate was devoid of the tagged α-synuclein in QBI-293 cells overexpressing *SNCA* (Luk *et al.*, 2009). Furthermore, aggregates formed in a mouse model overexpressing human A53T-mutant α-synuclein on a WT murine *SNCA* background showed incorporation of both human and mouse α-synuclein into aggregates seeded by PFFs (Luk *et al.*, 2012b). It was also established early on that seeded aggregation did not occur in SNCA KO animals and cell models, and that endogenous levels of monomer dictate the extent of aggregation (Volpicelli-Daley *et al.*, 2011; Luk *et al.*, 2012b; Courte *et al.*, 2020; Tanudjojo *et al*, 2021; Iannielli *et al.*, 2022). This is consistent with the data in this study, as SNCA expression was increased over time in culture and seeding of α-synuclein aggregation in SH-SY5Y expressing supraphysiological levels of α-synuclein resulted in rapid aggregation.

My data also shows that pS129-positive aggregates expanded and that the number of cells bearing pS129-aggregates increased over the course of time post-seeding with PFFs. Additionally, the number of pS129-positive aggregates per area of cell was increased. This suggests that α-synuclein monomer is continually being deposited into existing pS129-positive aggregates, but also that new nucleation points are generated after exogenous fibrils have triggered the generation of the first aggregates. This is consistent with a model of dynamic and continual seeding and amplification of α-synuclein monomers, oligomers and fibrils, where aggregation is energetically favoured at high monomer concentrations and/or once nucleation has occurred (Knowles *et al*, 2014; Galvagnion *et al*, 2015; Iljina *et al*, 2016; de Oliveira & Silva, 2019; Dada *et al*, 2023).

3.4.6 pS129 aggregation induces pS65Ub accumulation

We have observed that a portion of pS129-positive aggregates in PFF-seeded i^3 neurons co-localised with pS65Ub puncta, which grew in line with the growth of the α-synuclein aggregate. The accumulation of pS65Ub was dependent on the levels of the kinase PINK1. The co-occurrence of pS65Ub and α-synuclein aggregates was first described in post-mortem human brains of PD patients by Fiesel and colleagues, where it was found in the periphery of aggregates (Fiesel *et al*, 2015). These puncta were found to be co-localised with lysosomes and mitochondria. Intriguingly, pS65Ub puncta were found to be increased with ageing, and further increased in PD, but not in PINK1 or PRKN-deficient PD patients (Hou *et al.*, 2018). pS65Ub accumulation was correlated with Braak staging of α-

synuclein pathology in the substantia nigra, amygdala and the hippocampus both in patient brains from healthy controls and Lewy body disease patients, whereas similar analysis with amyloid pathology staging did not reveal a clear correlation. Further modelling revealed that the association between α-synuclein pathology and pS65Ub accumulation in the substantia nigra was the product of disease processes, rather than age. Interestingly, pS65Ub puncta colocalised with neuritic SNCA by immunocytochemistry, but not with somatic SNCA or with pS129, though they were located adjacent to Lewy bodies (Hou *et al.*, 2018). Similarly, pS65Ub staining was found in human brain tissue from 1 of 4 PD cases, and was not co-localised with α-synuclein pathology (Shiba-Fukushima *et al*, 2017). Further studies by the Springer laboratory solidified the relationship between α-synuclein aggregation and pS65Ub where *SNCA*-triplication showed increased pS65Ub compared to controls and sporadic patients. The increase in pS65Ub with increased levels of SNCA were attributed to decreased basal autophagy which resulted in higher PRKN levels (Hou *et al.*, 2023).

These data stand in contrast to the data in this study, where PFF-induced pS65Ub puncta were found to be directly co-localised with pS65Ub puncta, rather than on the outskirts. In fact, analysis of the size of each superimposed puncta showed that the pS129 area is consistently larger than the pS65Ub area for each aggregate, and the confocal images support the notion that the pS65Ub is located at the core of the aggregate, rather than on the outskirts. One of the fundamental differences between these studies is the use of patient post-mortem brain tissues, in comparison with our use of i^3 cortical neurons seeded with α-synuclein PFFs. It is possible that this results in differential maturity (early aggregate formation rather advanced-stage Lewy bodies) of α-synuclein aggregates. However, both PFF-induced α-synuclein aggregates in cell culture and Lewy bodies from post-mortem human brain show heterogeneous small vesicles and mitochondria both at the core and on the periphery of aggregates (Shahmoradian *et al.*, 2019; Mahul-Mellier *et al.*, 2020). The use of high-resolution light microscopy, able to resolve the two signals beyond the limit of diffraction of light, will be an excellent tool to precisely locate the pS65Ub and pS129 and elucidate this unresolved question.

It is also unclear if the accumulation of pS65Ub is directly a result of α-synuclein aggregation. The existence of a pS129-positive, pS65Ub-negative population of aggregates, and the fact that pS65Ub is

accumulated in a similar manner to the aggregation of pS129 post-seeding, suggests that pS65Ub is a consequence of α-synuclein aggregation. Future work should include resolving the temporal appearance of pS129 and pS65Ub in seeded cultures over time, as well as verifying by immunostaining for total α-synuclein and pS65Ub that there is no population of pS129-negative, α-synuclein-positive, pS65Ub-positive aggregates, ruling out that pS65Ub-positive mitochondria present a nucleation point for aggregation. If pS65Ub is indeed resulting from the aggregation of α-synuclein, there are two possible hypotheses. First, that pS129-positive α-synuclein aggregation produces mitochondrial stress and damage in its vicinity, either directly or indirectly, which results in activation of the PINK1-dependent pathway of mitophagy and eventual incorporation of the pS65Ub-positive mitochondria into the aggregate. Secondly, that pS129-positive aggregation causes cellular damage, leading to alterations in the autophagy-lysosomal pathway that results in the incomplete clearance and accumulation of naturally-arising pS65Ub-positive mitochondria. Further work will be required to positively rule out one or the other explanation.

4 Results: Organellar health and morphology under PD-relevant insults

Several decades of research have probed the role that mitochondria play in the cellular dysfunction and death of neurons in the substantia nigra of affected individuals and elsewhere in the brain. From this has emerged a central role of mitochondria in the pathophysiological process, both upstream and downstream of α-synuclein aggregation. It is hypothesised that the increased vulnerability of dopaminergic neurons of the midbrain may lie in their large arborisation and pacemaking activity (Guzman *et al*, 2009; Matsuda *et al*, 2009), which both contribute to high energy demands within these neurons. It is then perhaps unsurprising that mutations in the mitochondrial genes *PINK1* and *PRKN* lead to autosomal recessive, early-onset PD with or without α-synuclein aggregation, or that exposure to mitochondrial toxins such as MPTP or the pesticides rotenone or paraquat have been linked with increased risk of sporadic PD.

In cell culture models, a large number of studies have identified mitochondrial phenotypes resulting from α-synuclein overexpression or treatment with α-synuclein PFFs (Devi *et al.*, 2008; Chinta *et al.*, 2010; Cooper *et al*, 2012; Luth *et al.*, 2014; Reeve *et al.*, 2015; Di Maio *et al.*, 2016; Grassi *et al*, 2018; Little *et al*, 2018; Ludtmann *et al.*, 2018; Ryan *et al.*, 2018; Zambon *et al.*, 2019; Ryan *et al.*, 2021; Choi *et al.*, 2022; Toomey *et al*, 2022). These studies identify changes in the morphology of the mitochondrial network, as well as defects in mitochondrial respiration and turnover. However, there is little consensus on the precise mechanism by which α-synuclein may precipitate these effects at mitochondria, whether these alterations are a direct consequence of α-synuclein aggregation or the result of dysfunction in other cellular pathways, such as the lysosomal-autophagy pathway. We hypothesised that α-synuclein aggregation may be damaging mitochondria, resulting in increased mitophagy.

Consequently, the aim of this chapter was to study the impact of α-synuclein aggregation on mitochondrial and lysosomal function in human neurons. To do this, I have:

1. Identified morphological consequences of α-synuclein PFF-seeded aggregation in mitochondria and lysosomes.
2. Studied the effect of pS129-positive aggregate formation on mitochondrial membrane potential, ROS and ATP production.
3. Determined the effect of PFF treatment on lysosomal protease function.

4.1 Mitochondrial defects resulting from α-synuclein PFF treatment

4.1.1 Confocal microscopy reveals mitochondrial network changes in response to the mitochondrial toxin CCCP

The fission and fusion dynamics of mitochondria are central to preserving their function and enabling their turnover. Mitochondria fuse to buffer damage and redistribute functional protein components, and divide to allow efficient transport and engulfment by the autophagic machinery for recycling (Youle & van der Bliek, 2012). To assess the sensitivity and resolution of confocal microscopy to alterations in mitochondrial network morphology, i^3 neurons were treated with increasing concentrations of the mitochondrial toxin CCCP for 6 hours, fixed and immunostained for the mitochondrial marker TOM20 and the neuronal marker MAP2, and imaged using the Opera Phenix confocal microscope.

Examination of the microscopy images revealed circularisation of the mitochondria, as well as increased clustering in the perinuclear region (Figure 19a). Quantification supported the visual observations, showing that despite no effect of CCCP on the total area occupied by TOM20 ($p = 0.1395$), there was a significant increase in relative intensity of the TOM20 spots with treatment ($p = 0.0055$) (Figure 19b). The number of TOM20 spots per area of cell was significantly increased with 15 µM and 30 µM CCCP ($p = 0.0290$ and 0.0257) (Figure 19b). The area of individual mitochondria was overall unchanged, whereas the mean width of mitochondria was increased and

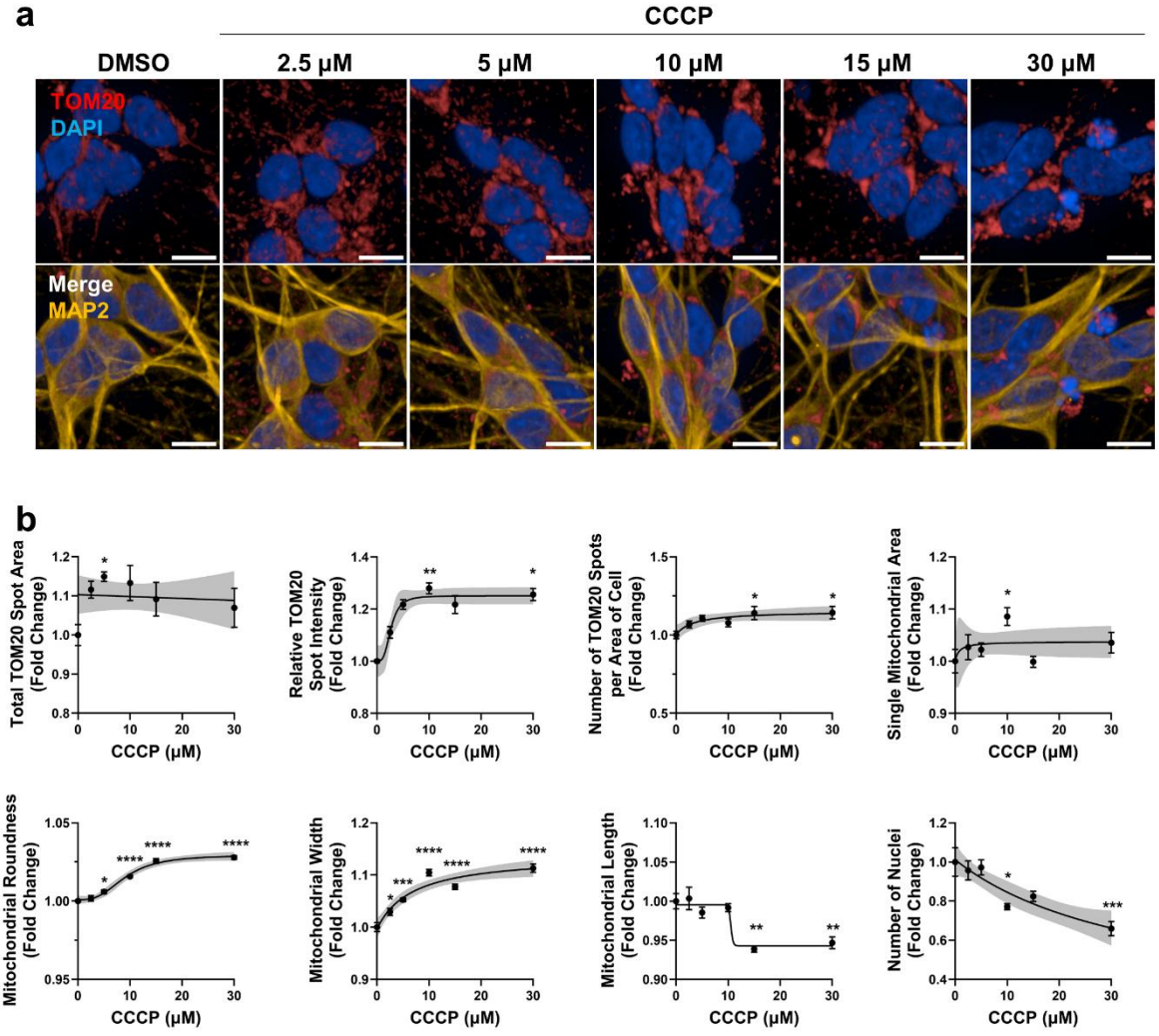


Figure 19. Mitochondrial morphology changes induced by the mitochondrial toxicant CCCP. a) Confocal microscopy images of i^3 neurons treated with increasing concentrations of the mitochondrial toxin carbonyl cyanide m-chlorophenyl hydrazone (CCCP), with mitochondria stained using an anti-TOM20 antibody. Increased doses of CCCP result in mitochondrial fragmentation and perinuclear clustering of the network. Scale bar = 10 µm. 63x water immersion objective, Opera Phenix confocal microscope. b) Quantification of mitochondrial morphology reveals an overall shift towards fragmentation and circularisation of mitochondria with CCCP treatment. N = 1 independent differentiations. Statistical test: ordinary one-way ANOVA with Dunnett's multiple comparisons test or Kruskal-Wallis test with Dunn's multiple comparisons test. Data is presented as the mean ± SEM. * $p < 0.05$, ** $p < 0.01$, *** $p < 0.001$, **** $p < 0.0001$.

the length decreased with increasing CCCP concentration ($p < 0.0001$ and $p = 0.0002$, respectively). This resulted in a highly significant change in the measured width-to-length ratio of mitochondria ($p < 0.0001$), supporting a shift in the population of mitochondria towards a shorter, rounder mitochondrial phenotype. Though these data do not directly measure mitochondrial turnover, they are consistent with induction of mitophagy by the mitochondrial toxin CCCP, resulting in fragmented mitochondria that

can be targeted to lysosomes for degradation. These data are also further supported by increases in the levels of the PINK1/PRKN-dependent mitophagy marker pS65Ub with FCCP treatment as measured by immunocytochemistry in section 5.2.1.

4.1.2 α-Synuclein aggregation induces alterations to mitochondria in neurons without aggregates

To begin understanding the effects of α-synuclein aggregation on mitochondrial health, i^3 neurons were treated with increasing concentrations of α-synuclein PFFs, fixed and stained 14 days post-seeding for the mitochondrial marker TOM20. The area, width, length, and width-to-length ratio of mitochondria were evaluated in all cells to identify morphological changes to the mitochondrial network. This analysis revealed a significant effect of treatment on the length of mitochondria in total cells ($p = 0.0389$), but other readouts were unchanged (Figure 20a-b).

To determine if this effect was dependent on α-synuclein aggregation, the analysis was performed on pS129-positive and pS129-negative cells within each condition. Mitochondrial morphology was directly compared between pS129-positive and negative cells in the same well. Aggregate-bearing neurons showed no change in any measured morphology parameter, whereas in pS129-negative neurons, the mitochondrial network showed significant changes with increased concentrations of α-syn PFFs (Figure 20b). A significant reduction in mitochondrial area was found with 50 µg/ml PFF treatment ($p = 0.0229$), as well as significantly reduced width and length of mitochondria with treatment ($p = 0.049$ and $p = 0.0113$) (Figure 20b). For both populations, the mitochondrial width-to-length ratio was unchanged. These changes suggest altered mitochondrial network morphology in the aggregate-free neurons. These results were intriguing in light of the results in section 3.3.1, which highlighted increased pS65Ub accumulation in cells bearing aggregates. As discussed above, mitochondrial damage was associated with increased mitochondrial fragmentation, to facilitate mitophagy. There being no fragmentation observable in pS129-positive neurons may support the notion that pS65Ub is accumulated in pS129-positive neurons rather than produced as a result of heightened mitophagy in these neurons.

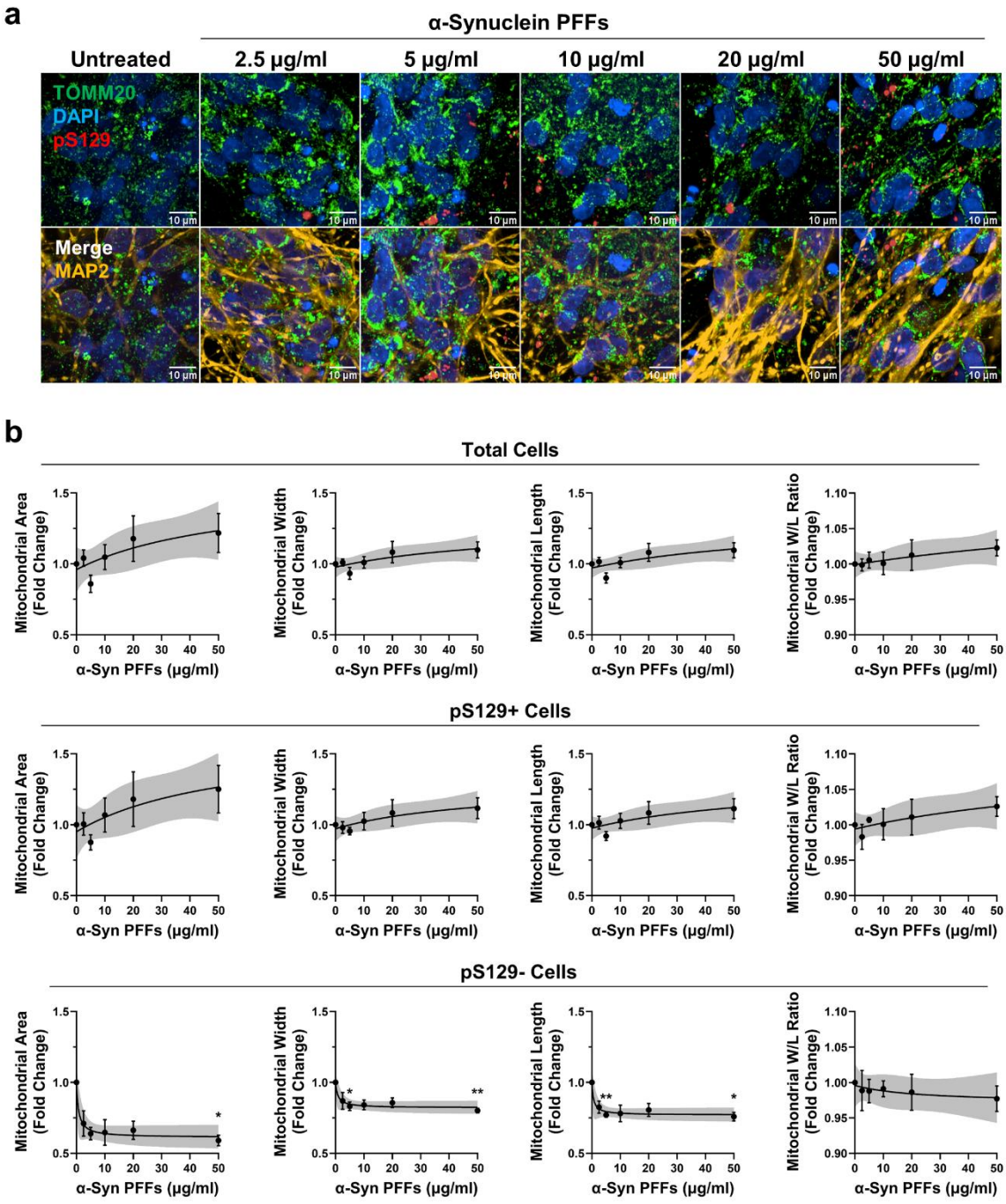


Figure 20. α-Synuclein PFF treatment induces mitochondrial network morphology alterations in pS129-negative neurons.

a) Confocal microscopy images of neurons treated with increasing concentrations of α-synuclein PFFs and immunostained for TOM20, MAP2 and pS129. Scale bar = 10 µm. 63x water immersion objective, Opera Phenix confocal microscope. **b)** Quantification of the images in a) reveals no significant effect of α-synuclein PFF treatment in total cells or pS129-positive aggregate bearing cells, but a significant reduction in area, width and length of mitochondria in aggregate-negative neurons. N = 4 independent differentiations. Statistical test: repeated measures one-way ANOVA with Dunnett's multiple comparisons test or Friedman test with Dunn's multiple comparisons test. Data is presented as the mean ± SEM. * $p < 0.05$, ** $p < 0.01$, *** $p < 0.001$, **** $p < 0.0001$.

4.1.3 Functional assays reveal altered mitochondrial respiration

Alterations of mitochondrial function have been extensively described in PD. These were investigated in our PFF-seeded model using several assays measuring mitochondrial ATP production, membrane potential and ROS generation. Dissipation of the mitochondrial membrane potential using 30 µM CCCP significantly reduced ATP production ($p = 0.0113$), JC-10 signal ($p = 0.0044$) and TMRM intensity ($p = 0.0003$), whereas treatment with 10 µM rotenone increased ROS production as measured by the MitoSOX assay ($p = 0.0250$) (Figure 21a), demonstrating that these assays identify mitochondrial functional defects.

i^3 Neurons were treated with α-synuclein PFFs and the levels of ATP were measured using the CellTiter-Glo assay 14 days post-seeding. This uncovered a trend towards decreased ATP production per cell in α-synuclein-treated cells compared to controls ($p = 0.0532$) (Figure 21b), suggesting respiration is altered in cells having received α-synuclein PFFs.

The mitochondrial membrane potential, as measured using the JC-10 potentiometric dye, was found to be unchanged with α-synuclein PFF treatment (Figure 21c). To confirm these results, a parallel experiment was performed using the imaging-based potentiometric dye tetramethylrhodamine (TMRM), which also revealed no differences between the two conditions (Figure 21d). This suggested that despite mitochondria in the α-synuclein-treated condition having difficulty with energy production, this was not due to dissipation of the membrane potential, which would have a significant impact on oxidative phosphorylation.

Prior publications have proposed that α-synuclein aggregation results in increased ROS production, which go on to damage many protein and lipid components of the cell as well as cellular processes such as dopamine metabolism and mitochondrial respiration The ROS sensor MitoSOX was used to investigate ROS levels 14 days after α-synuclein PFF treatment and showed no statistically significant change in ROS levels with α-synuclein treatment (Figure 21e). As such, this was also unlikely to explain the decrease in ATP levels observed in PFF-treated conditions. It is possible that whilst aggregate-

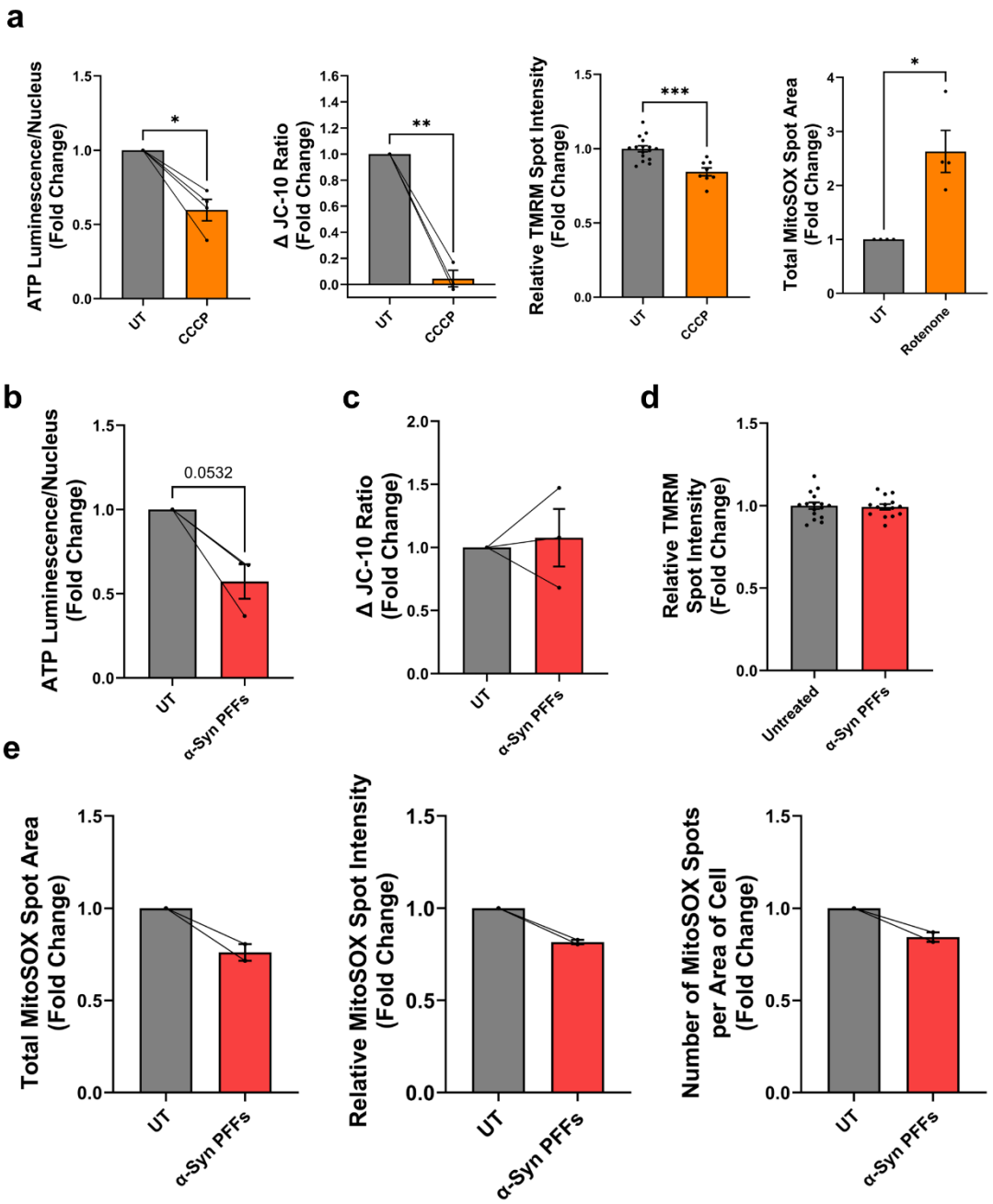


Figure 21. Mitochondrial function is altered by treatment with α-synuclein PFFs. a) i^3 Neurons were treated with CCCP to dissipate the mitochondrial membrane potential and assayed using the CellTiter Glo ATP assay, the JC-10 membrane potential assay, tetramethylrhodamine (TMRM) membrane potential assay, revealing that CCCP induces significant reductions in ATP production and membrane potential. Treatment of i3 neurons with rotenone induced significantly increased reactive oxygen species (ROS) levels as measured by the MitoSOX assay. N = 4-5 independent differentiations, each datapoint represents a biological replicate. N = 1 independent differentiations for the TMRM assay, each datapoint represents a technical replicate. Statistical test: paired t-test, Welch's t-test (TMRM data). b) ATP production trends towards a significant decrease in PFF-treated i3 neurons. N = 3 independent differentiations, each datapoint represents a biological replicate. Statistical test: paired t-test. c) Mitochondrial membrane potential as measured by the JC-10 potentiometric dye is unchanged in α-synuclein-treated conditions. N = 3 independent differentiations, each datapoint represents a biological replicate. Statistical test: paired t test. d) TMRM intensity is unchanged in PFF-treated conditions, confirming the results

obtained with JC-10. N = 1 independent differentiation, each datapoint represents a technical replicate. Statistical test: Welch's t-test. e) Mitochondrial ROS levels show no change in i3 neurons treated with α-synuclein PFFs as measured by the area, intensity and number of MitoSOX puncta. N = 2 independent differentiations, each datapoint represents a biological replicate. Statistical test: Paired t test. Data is presented as the mean ± SEM. * $p < 0.05$, ** $p < 0.01$, *** $p < 0.001$, **** $p < 0.0001$.

negative neurons were able to remodel their mitochondrial networks (Figure 20b), aggregate-bearing neurons may be unable to do so, resulting in decreased ATP generation.

4.2 Lysosomal alterations with α-synuclein PFF treatment

Impairment of the lysosomal-autophagy pathway is a consistent and characteristic feature of many neurodegenerative diseases, including PD. Indeed, it is thought that the defective clearance and recycling of proteins and other cellular components that occurs over the course of ageing may increase the likelihood of aggregation for aggregation-prone proteins, perhaps through increasing their local concentration. In turn, this aggregation may further impair the lysosomal-autophagy pathway, resulting in a highly damaging feed-forward cycle.

Lysosomal defects have been observed in several familial iPSC-derived and animal models of PD, with decreases in lysosomal activity, increases in lysosomal size or in the number of LAMP1-positive puncta being noted (Chu *et al.*, 2009; Tanik *et al.*, 2013; Boman *et al.*, 2016; Mazzulli *et al.*, 2016a). Alterations in lysosomal morphology have also been identified after α-synuclein aggregation triggered by treatment with PFFs, as α-synuclein seeds have been shown to escape the lysosome after endocytosis through lysosomal membrane rupture (Freeman *et al.*, 2013). We hypothesised that α-synuclein aggregation may be impairing mitochondrial turnover and mitochondrial function through its effects on lysosomal function.

4.2.1 Lysosomal content is reduced in aggregate-negative neurons

i^3 Neurons were treated on DIV 10 with α-synuclein PFFs, fixed and immunostained for LAMP1 and pS129 14 days post-seeding. Analysis of all neurons in the culture showed no significant changes to the area or intensity of LAMP1, nor in the number of LAMP1-positive puncta or in their size

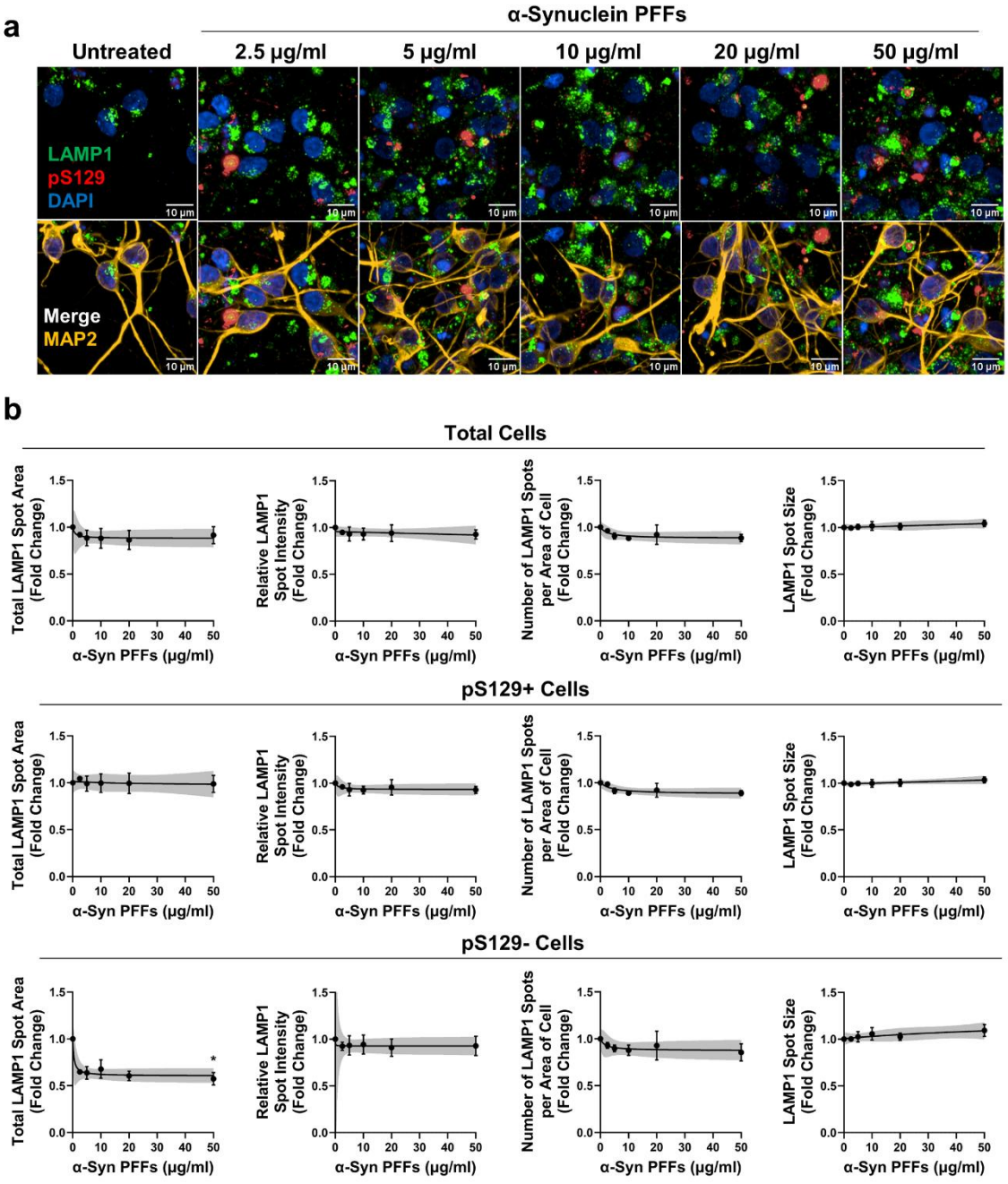


Figure 22. LAMP1-positive endolysosomal content and morphology is unchanged with α-synuclein PFF treatment.

a) Confocal microscopy images of i^3 neurons treated with α-synuclein PFFs, fixed and immunostained for LAMP1, pS129 and MAP2 14 days post-seeding. LAMP1-positive puncta are localised to the soma of neurons. Scale bar = 10 µm. 63x water immersion objective, Opera Phenix confocal microscope. b) Analysis of LAMP1 total area, relative intensity, number of puncta and size in total cells, pS129-positive aggregate-bearing cells and pS129-negative cells. A significant reduction in the number of LAMP1-positive puncta was found in pS129-negative cells with 50 µg/ml PFF treatment. N = 2 independent differentiations. Statistical test: Friedman test with Dunn's multiple comparisons test. Data is presented as the mean ± SEM. * $p < 0.05$, ** $p < 0.01$, *** $p < 0.001$, **** $p < 0.0001$.

(Figure 22a-b). Subsetting the cultures further and analysing the pS129-positive and pS129-negative populations separately showed no effect of α-synuclein PFF treatment on measured parameters in either pS129-positive or negative cells, with the exception of the LAMP1 spot area which was significantly reduced with PFF treatment ($p = 0.0292$) (Figure 22b). These data suggest that LAMP1-positive endolysosomal content is reduced specifically in the pS129-negative cells, similar to the reductions in mitochondrial contents observed above.

4.2.2 Lysosomal proteolytic activity is effectively measured by DQ-BSA imaging

Given the mitochondrial and lysosomal alterations seen in PFF-treated cells, I aimed to evaluate lysosomal function in these neurons. To establish the sensitivity and maximal signal window of the DQ-BSA lysosomal activity assay, i^3 neurons were treated at DIV 10 with increased concentrations of the lysosomal alkalising agent CQ for 48 hours. DQ-BSA relies on the endocytosis and degradation of a highly-labelled bovine serum albumin derivative, which relieves the self-quenching of the fluorophores and results in increased fluorescence in a proteolytic activity-dependent manner (ThermoFisher). DQ-BSA fluorescence was observed to be punctate and localised throughout the soma of i^3 neurons (Figure 23a). CQ treatment was found to significantly decrease the number of nuclei per well in a dose-dependent manner ($p = 0.0259$), suggesting there is strong toxicity of lysosomal inhibition with this compound (Figure 23b). Whereas treatment had no effect on the total area occupied by DQ-BSA spots or the number of puncta per area of cell, the relative intensity of DQ-BSA puncta was reduced in a dose-dependent manner ($p = 0.0053$), showing a mean 68.5% reduction in intensity at the highest dose of CQ (95% CI [-0.2211, 0.8510]). The size of individual DQ-BSA puncta was also strongly increased with CQ treatment ($p = 0.0151$). Together, these data suggest that the DQ-BSA assay can measure drug-induced changes in the proteolytic activity of lysosomes.

20 µM of CQ was identified as an effective concentration to produce strong reductions in DQ-BSA fluorescence whilst also mitigating the toxicity of the compound. At this concentration, the number of nuclei per well were reduced to 57.3% of the control (95% CI [-0.4372, 1.5584]), and the relative DQ-BSA spot intensity was decreased to 40.63% of the vehicle (H_2O) value (95% CI [-0.1690, 0.9817]). i^3

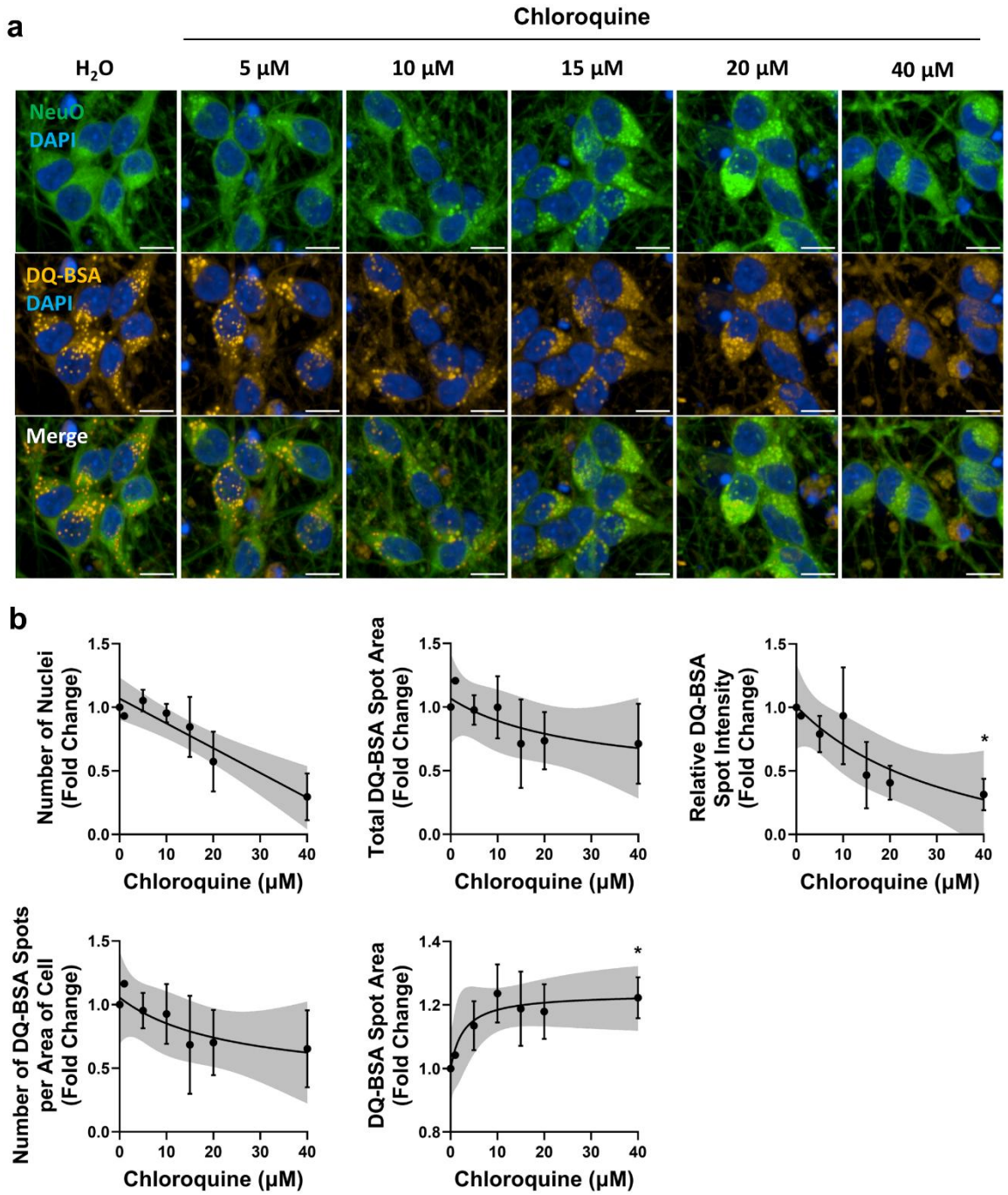


Figure 23. Lysosomal alkalising agent chloroquine reduces proteolytic activity in a dose-dependent manner.

a) Confocal microscopy images of control or chloroquine-treated i3 neurons with the lysosomal proteolytic activity reporter DQ-BSA and neuronal stain NeuO. DQ-BSA puncta have reduced intensity with increased concentration of chloroquine. Scale bar = 20 µm. 40x water immersion objective, Opera Phenix confocal microscope. b) Analysis of the number of nuclei, total DQ-BSA spot area, relative intensity, number of spots and spot size for DQ-BSA reveals a dose-dependent inhibition of lysosomal proteolytic activity and increase in endolysosomal puncta size with chloroquine treatment. N = 3 independent differentiations. Statistical test: Friedman test with Dunn's multiple comparisons test. Data is presented as the mean ± SEM. * $p < 0.05$, ** $p < 0.01$, *** $p < 0.001$, **** $p < 0.0001$.

Neurons at DIV 10 were treated for 48 hours with 20 µM CQ and incubated with DQ-BSA for 1, 2, 3, 4 or 5 hours to assess the rate of endocytosis and signal window over time. Longer incubation resulted in brighter puncta (Figure 24a), consistent with continued uptake, degradation and accumulation of the unquenched fluorophore in endosomes and lysosomes. Quantification supported this observation, with spot intensity, total area, number of puncta and size of individual puncta all showing significant increases with incubation time ($p < 0.0001$ for all readouts) (Figure 24b). Additionally, increased incubation time resulted in increased sensitivity of the assay to CQ-induced reductions in proteolytic activity measured by the background-corrected (relative) intensity of the DQ-BSA puncta.

Similarly, to assess if maximal signal window was achieved or if signal saturation was observed, titrating of the DQ-BSA concentration was performed in control and CQ-treated i^3 neurons. Significant effects of DQ-BSA dose were observed for the total area, relative intensity, and number of puncta ($p < 0.0001$ for all parameters) (Figure 24c-d). Maximal signal window between the CQ-treated and H_2O-treated condition was observed at 3 µg/ml, with the trend of the control data beginning to show saturation at 3 µg/ml. Altogether, these data suggested that 5 hours of incubation time at a concentration of 3 µg/ml DQ-BSA yielded the most sensitive assay.

4.2.3 α-Synuclein PFF treatment has no effect on lysosomal activity

i^3 Neurons were subjected to DQ-BSA imaging 14 days after PFF seeding and no effect of the treatment on any measured parameter was found (Figure 25a), suggesting that α-synuclein PFFs do not alter lysosomal proteolytic activity at this timepoint, in this cell type. To verify these observations, i^3 neurons were treated with 10 µg/ml α-synuclein PFFs using 12 and 18 technical replicates for control and PFF-treated conditions and assayed with DQ-BSA 14 days post-seeding (Figure 25b). No significant difference between the untreated and treated conditions was found for all readouts except for the size of DQ-BSA puncta, which showed a small but significant increase in the PFF-treated condition ($p = 0.0102$). Overall, these data suggest that α-synuclein PFF treatment and aggregation do not significantly impact the proteolytic activity of lysosomes in this treatment paradigm.

4.2.4 Lysosomal activity is impaired by treatment with amyloid-β

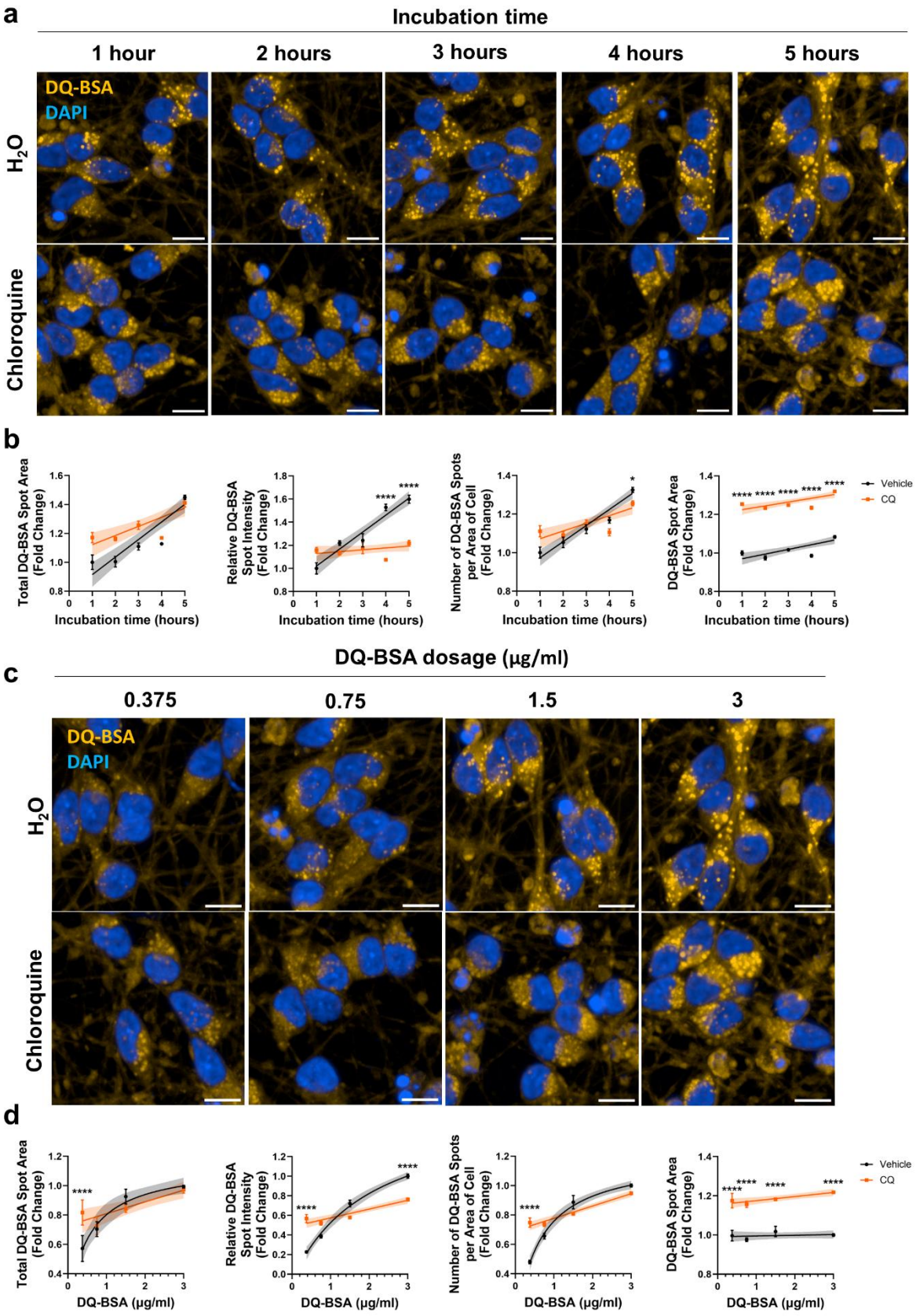


Figure 24. Optimisation of DQ-BSA incubation time and dosage in i^3 neurons. a) Confocal microscopy images show increased DQ-BSA signal intensity with incubation time, and reduced signal intensity in chloroquine-treated conditions. Scale bar = 20 µm. 40x water immersion objective,

Opera Phenix confocal microscope. b) Quantification of the DQ-BSA signal reveals significantly increased area, intensity and number of puncta with longer incubation time. c) Confocal microscopy images show increased DQ-BSA intensity with DQ-BSA concentration. Scale bar = 20 μm. 40x water immersion objective, Opera Phenix confocal microscope. N = 1 independent differentiation. Statistical test: Two-way ANOVA with Tukey's multiple comparisons test. Data is presented as the mean ± SEM. * $p < 0.05$, ** $p < 0.01$, *** $p < 0.001$, **** $p < 0.0001$.

To verify if the lack of marked lysosomal defects is specific to treatment with α-synuclein, amyloid-β oligomers were prepared and added in increasing concentrations to i^3 neuron media at DIV 10 for 5 days. No significant effect of treatment on the number of nuclei or the total area of DQ-BSA spots was observed (Figure 26a-b). The relative intensity and the number of DQ-BSA puncta was significantly reduced with increasing concentrations of amyloid-β oligomers ($p = 0.0018$ and $p = 0.0001$), and uncorrected intensity was significantly increased with 3 μM amyloid-β treatment ($p = 0.0499$), suggesting a dose-dependent impairment of lysosomal function. The size of DQ-BSA spots was not significantly altered but did trend towards a reduction with 4 μM amyloid-β treatment ($p = 0.0522$) (Figure 26b). Altogether, these data reveal that amyloid-β oligomers have deleterious effects on the function of the endolysosomal system.

4.3 High resolution microscopy for the evaluation of organellar morphology

The resolution of light microscopy is curtailed by the magnification, resolution of the confocal microscope as well as the limit of diffraction of light. In the case of mitochondria and lysosomes, morphology is most effectively visualised by techniques which circumvent the limit of diffraction of light, such as super-resolution light microscopy or electron microscopy. Whereas confocal light microscopy allows to quickly highlight the location of proteins within neurons, the data in this chapter and the previous chapter show it lacks the resolution to clearly make out sub-organellar architecture, such as the mitochondrial cristae, or the ability to precisely localise protein complexes. Electron microscopy is effective at visualisation of organellar structure and can be combined with immuno-electron approaches to pinpoint proteins within the cell but is significantly more labour intensive.

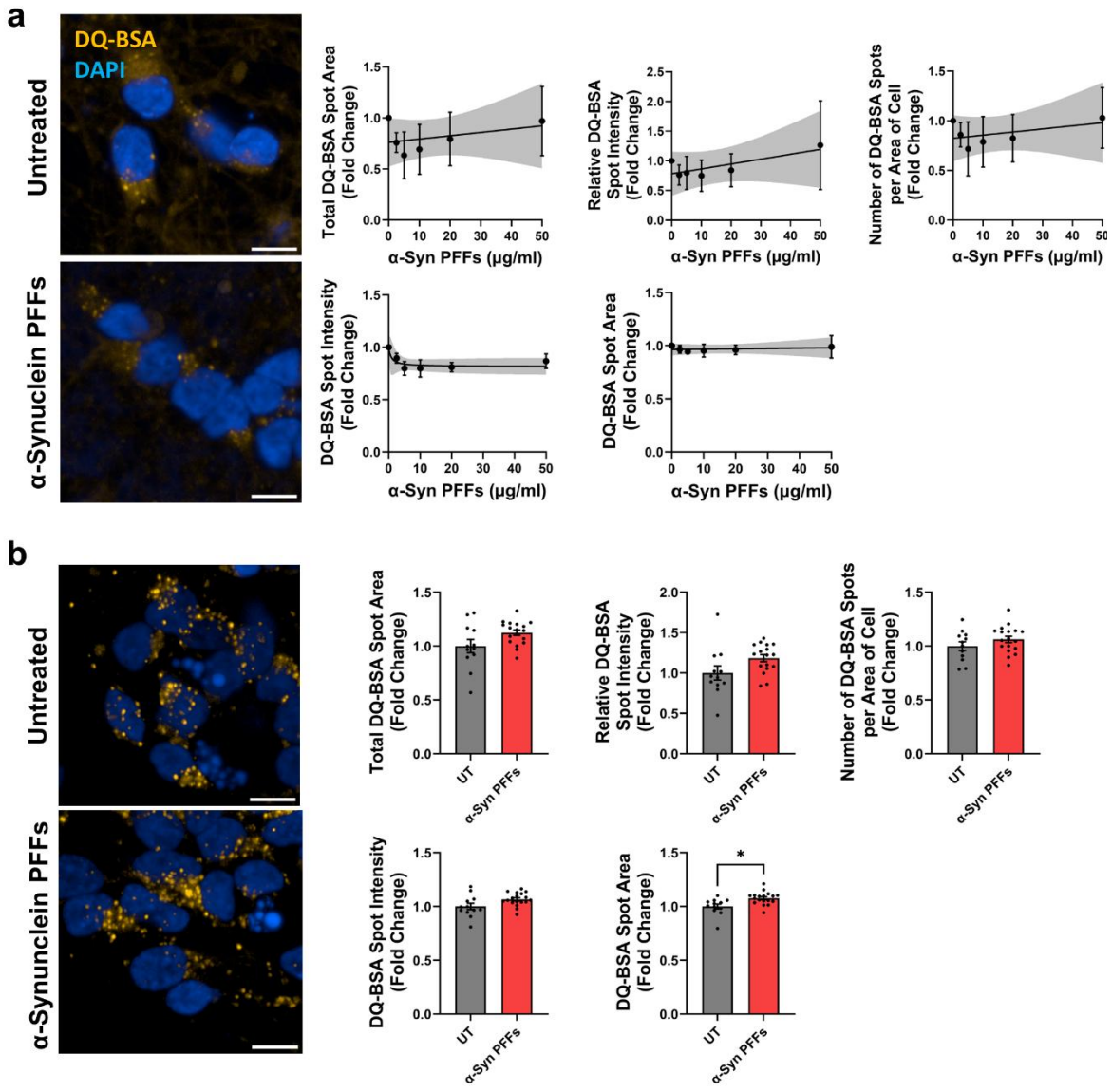


Figure 25. α-Synuclein PFF treatment has no effect on DQ-BSA signal intensity. a) Confocal microscopy images of DQ-BSA puncta in untreated and α-synuclein-treated (50 μg/ml) conditions show no differences between conditions. This is supported by quantification of the area, relative intensity, number of puncta, uncorrected intensity and individual spot size of DQ-BSA puncta with increasing PFF concentration, which shows no significant effect of treatment on any parameter measured. Scale bar = 20 μm. 40x water immersion objective, Opera Phenix confocal microscope. N = 3 independent differentiations. Statistical test: repeated-measures one-way ANOVA with Dunnett's multiple comparisons test or Friedman test with Dunn's multiple comparisons test. b) i^3 Neurons were treated with 10 μg/ml α-synuclein PFFs and DQ-BSA total area, relative intensity, number of puncta, uncorrected intensity and spot size measured 14 days post-seeding. The size of DQ-BSA puncta was found to be significantly increased in α-synuclein-treated conditions. N = 1 independent differentiation. Statistical test: Welch's t test. Data is presented as the mean ± SEM. * $p < 0.05$, ** $p < 0.01$, *** $p < 0.001$, **** $p < 0.0001$.

CLEM offers a bridge between the two techniques, for example enabling the identification of neurons bearing pS129-positive aggregates by light microscopy, and further analysis of the organellar

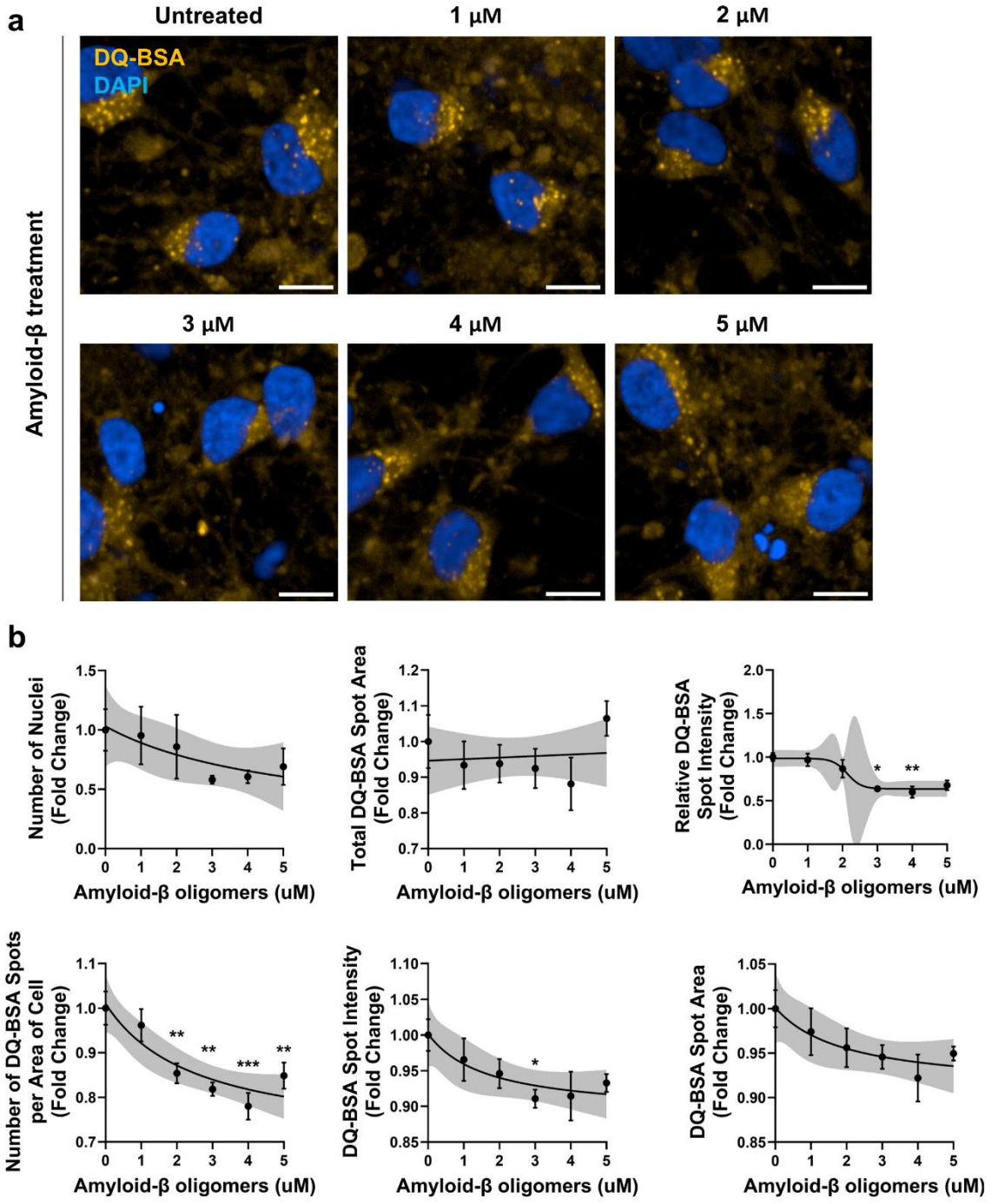


Figure 26. Amyloid-β oligomers impair lysosomal proteolytic activity in a dose-dependent manner. a) Confocal microscopy images of the DQ-BSA fluorescent reporter in i^3 neurons treated with 1 to 5 µM amyloid-β oligomers. Scale bar = 20 µm. 40x water immersion objective, Opera Phenix confocal microscope. b) Quantification revealed a statistically significant decrease in the intensity and the number of DQ-BSA puncta with increasing concentrations of amyloid-β. N = 1 independent differentiation. Statistical test: ordinary one-way ANOVA with Dunnett's multiple comparisons or Kruskal-Wallis test with Dunn's multiple comparisons test. Data is presented as the mean ± SEM. * $p < 0.05$, ** $p < 0.01$, *** $p < 0.001$, **** $p < 0.0001$.

architecture of these neurons by electron microscopy. To confirm our light microscopy findings, further analysis of mitochondrial and lysosomal morphology was attempted using CLEM to differentiate pS129-positive and negative neurons, in collaboration with Dr Camille Loiseau in the Magill laboratory.

4.3.1 Optimisation of correlative light and electron microscopy

As a preliminary trial, i^3 Neurons were cultured on alphanumerically gridded glass coverslips, treated at DIV 10 with 30 µM CCCP for 3 hours, fixed and immunostained using antibodies against pS65Ub, MAP2 and TOM20. After confocal imaging, the neurons were further fixed, stained and resin-embedded for electron microscopy analysis (Figure 27a). It soon became clear that the first challenge would be the embedding of neurons in resin, which on several occasions failed and led to neuron-shaped cutouts within the resin after sectioning (Figure 27b). To correct this, we altered the dehydration and embedding steps with step-wise dehydration in 30-100% ethanol for 10 minutes each, on ice, as well as a longer embedding step using 3:1, 1:1 and 1:3 acetone:resin solutions for 1 hour each, followed by incubation overnight in 100% resin at room temperature (see section 2.16). On the next attempt, confocal microscopy revealed clusters of MAP2-positive neurons but failed to show pS65Ub or TOM20 staining (Figure 27c, data not shown). Preparation of the electron microscopy samples resulted in correct registration of the neurons via electron microscopy, allowing for the identification of specific neurons, but the contrast on subcellular features such as the nucleus and other cell membranes was very poor (Figure 27d).

As one of the proteins of interest, pS65Ub, showed very weak signal with the sample preparation designed for CLEM, the effect of the strength of fixation reagent and incubation time on the intensity of pS65Ub, TOM20 and MAP2 staining was investigated. We hypothesised that the stronger fixation techniques used for sample preparation for CLEM were altering the conformation or availability of the epitopes for antibody binding, resulting in a loss of signal intensity. DIV 10 i^3 neurons were treated with 30 µM CCCP for 3 hours and the cells fixed using a gradient of reagent concentrations for 2 hours at room temperature. Confocal microscopy imaging demonstrated that the signal intensities for all three antibodies were strongly reduced, with pS65Ub showing the strongest reduction – the signal became diffuse and faint with concentrations of glutaraldehyde as low as 0.1% (Figure 28a). The MAP2

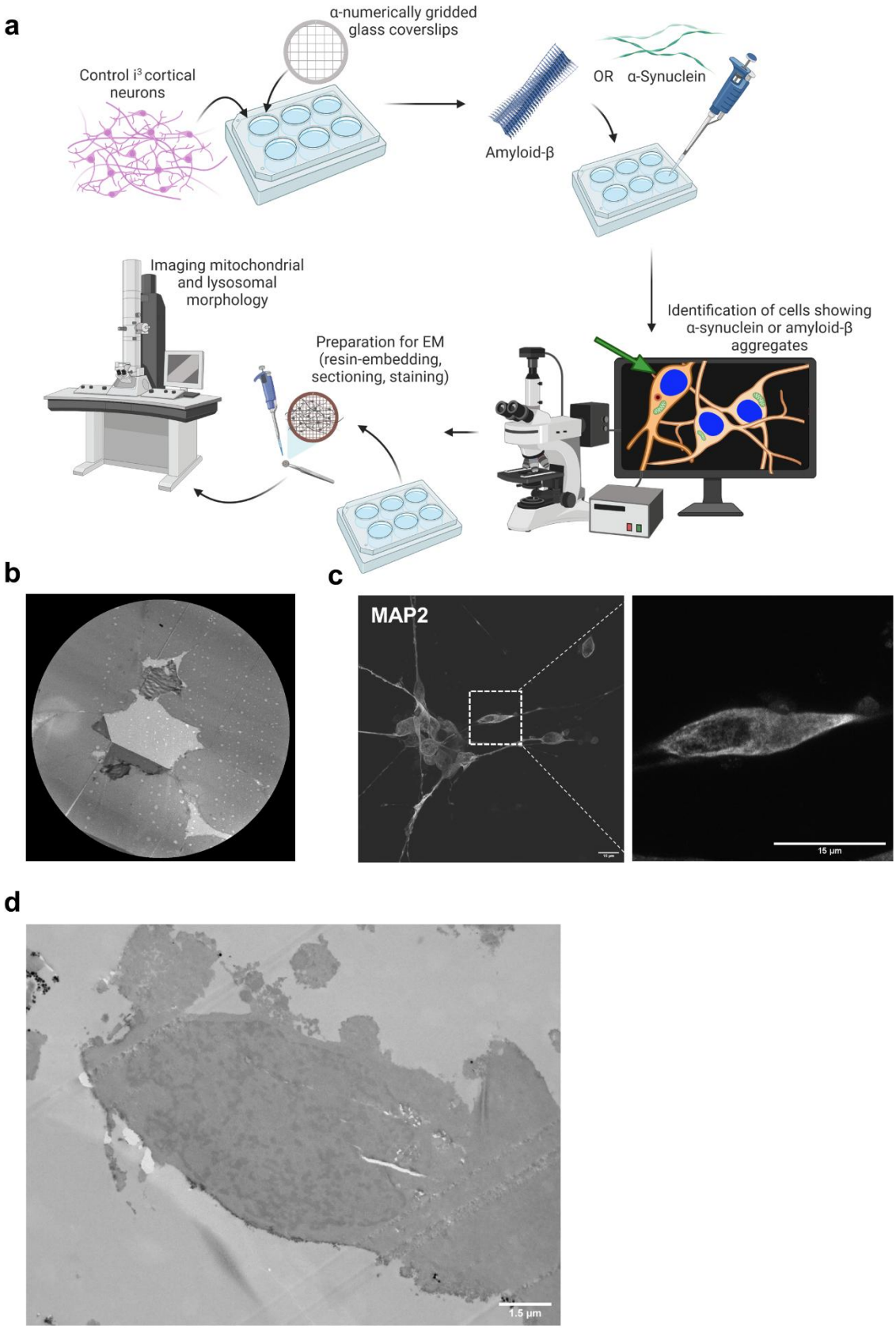


Figure 27. Optimisation of correlative light and electron microscopy in i^3 neurons. a) Schematic representation of the main steps of the correlative light and electron microscopy workflow for the identification of aggregate-positive or negative i^3 neurons and imaging of organellar morphology. b)

Initial trials of CLEM resulted in failure of resin embedding of neurons, leaving a neuron-shaped cutout in the resin. 3000x objective. c) Confocal microscopy images of a neuronal cluster and identification of a single neuron. Scale bar = 15 µm. 20x objective, Zeiss confocal microscope. Images acquired by Dr Camille Loiseau over the course of a training session. d) Electron micrograph depicting the correct embedding and registration of the neuron identified in c). Staining contrast and structural preservation of the sample, however, was very poor. Scale bar = 1.5 µm. Panel 1a created with Biorender.com.

intensity was the least affected, with unchanged staining pattern and detectable, albeit weaker, fluorescence intensity. The TOM20 staining pattern was substantially altered with increasing concentrations of glutaraldehyde, with 2% or 4% PFA with 0.1% glutaraldehyde demonstrating the most conserved mitochondrial morphology without the diffusion and clustering observed with higher concentrations of glutaraldehyde (Figure 28b). Considering that CLEM was to be used to localise pS65Ub-positive mitochondria within and without pS129-positive aggregates, these data suggested that this technique, and perhaps electron microscopy more generally, were unsuitable for this application without extensive optimisation.

4.3.2 Optimisation of structural illumination microscopy

Considering the poor performance of the pS65Ub antibody under strong fixation, an alternative technique was explored to identify and quantify changes in mitochondrial morphology. SIM uses patterned excitation of the sample to overcome the diffraction limit of light and produce super-resolution images. As a preliminary trial, SH-SY5Y cells were cultured on glass coverslips, fixed and immunostained as previously described (see section 2.2) using saponin as a permeabilisation reagent. The localisation and intensity of pS65Ub and TOM20 were observed after 30 µM CCCP or DMSO treatment for 3 hours to induce mitochondrial fragmentation and pS65Ub formation. A marked difference in the overall morphology of the mitochondrial network was observed between the two conditions, with CCCP treatment inducing fragmentation of mitochondria and formation of pS65Ub puncta and chains localised to the outside of the mitochondrial membrane (Figure 29). These data suggest that SIM enables the precise localisation and visualisation of pS65Ub at mitochondria and for evaluation of mitochondrial network morphology. However, the use of the TOM20 marker, which

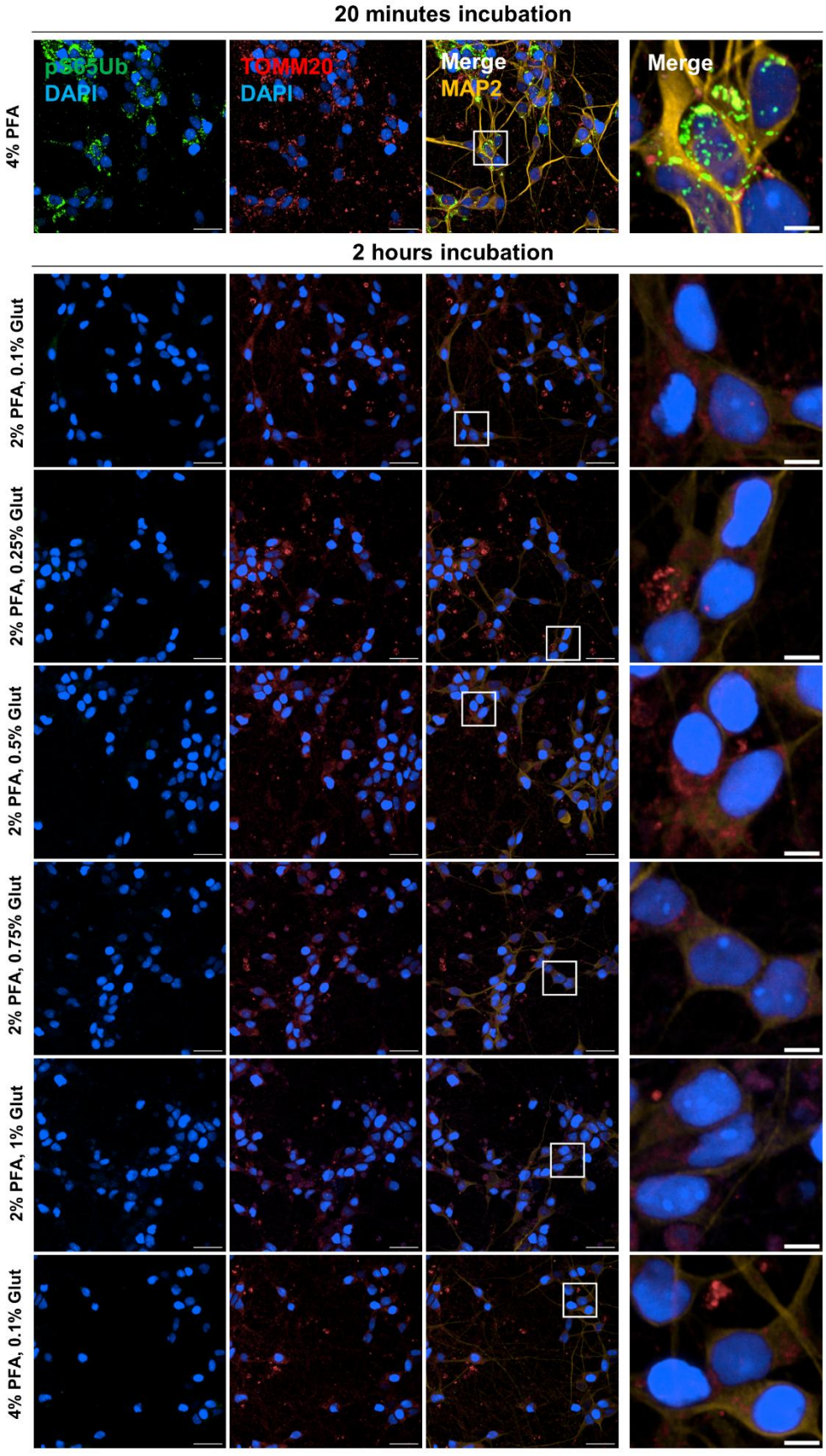


Figure 28. Comparison of fixation reagents, concentrations and incubation times and their effects on immunostaining pattern and intensity.

i^3 Neurons were treated with 30 µm CCCP for 3 hours and fixed in the standard 4% paraformaldehyde (PFA) for 20 minutes or in a stronger fixative solution containing PFA and glutaraldehyde (Glut) for 2 hours at room temperature. The neurons were subsequently immunostained using a standard protocol with antibodies against pS65Ub, MAP2 and TOM20. The staining intensity of pS65Ub was lost with the lowest concentration of glutaraldehyde and PFA with 2 hours incubation, whereas the staining pattern of TOM20 was altered and intensity lost at higher concentrations of glutaraldehyde. MAP2 intensity was reduced but the staining pattern was unchanged with any of the PFA and glutaraldehyde concentrations used with 2 hours incubation. White boxes indicate boundaries of the image inserts on the right. Scale bar for the main images = 50 µm, scale bar for the inserts = 10 µm. 40x water immersion objective, Opera Phenix confocal microscope.

highlights the outer mitochondrial membrane, may make segmentation of the mitochondria difficult for automated analysis given the complexity of segmenting membranes when mitochondria are overlapping. Better results may be obtained by using a combination of mitochondrial matrix and outer membrane markers such as TOM20 and citrate synthase.

4.4 Discussion

4.4.1 Mitochondrial uncoupling results in fragmentation of the network

Treatment of i^3 neurons with the mitochondrial uncoupler CCCP resulted in shorter, rounder mitochondria and induces the formation of pS65Ub (see Chapter 5). This phenotype is likely mitochondrial fragmentation as a result of mitophagy induction. Indeed, mitochondrial fission is initiated when mitochondria are targeted for degradation (Youle & van der Bliek, 2012) and impairing fission has been found to reduce mitophagy (Twig *et al*, 2008). Likewise, increasing fission rescued PINK1 knockout phenotypes and PINK1 overexpression led to increased fission (Yang *et al*, 2008), strengthening the bi-directional association of mitophagy with fission/fusion dynamics. Furthermore, mitochondrial depolarisation has been linked to PINK1 stabilisation and activation, recruitment of PRKN and subsequent mitophagy (Narendra *et al.*, 2008; Narendra *et al.*, 2010). However, the assertion that mitochondrial uncoupling results in true fragmentation has been challenged in recent years, with one group positing that CCCP may lead to mitochondrial rounding independent of the fission and fusion machinery, at least in the first few minutes after treatment (Miyazono *et al*, 2018). Whether this holds

true when assessing timepoints hours after treatment was not assessed. Moreover, rather than being necessary for mitophagy as has been suggested, mitochondrial fission may facilitate separation of damaged mitochondrial from the healthy network

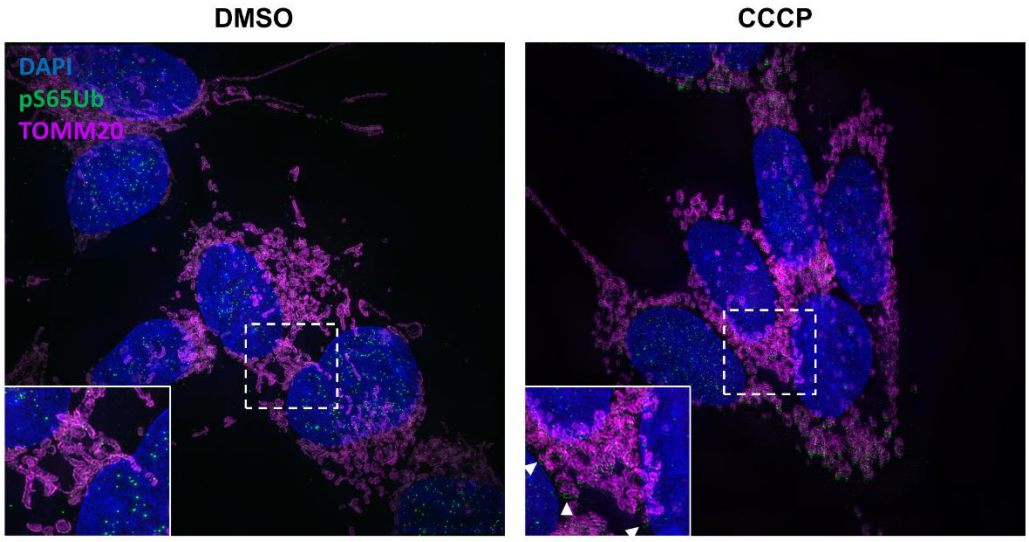


Figure 29. Preliminary trial of structure illumination microscopy (SIM) for the evaluation of mitochondrial morphology. SH-SY5Y cells were treated with 10 µM CCCP for 3 hours, fixed and immunostained as per a standard protocol, substituting the Triton X-100-based permeabilisation reagent for a saponin-based permeabilisation reagent. Antibodies against pS65Ub and TOM20 were used. The mitochondrial network showed fragmentation and formation of pS65Ub puncta and chains at the outer membrane of the mitochondria in CCCP-treated conditions. White boxes indicate the boundaries of the insert in the bottom left. White arrows indicate possible pS65Ub chains extending from the mitochondrial membrane. 60x oil immersion objective, DeltaVision OMX SR microscope, images acquired and deconvoluted by Dr Lothar Schermelleh.

for selective degradation and may not be required for the process of mitophagy to occur (Burman *et al*, 2017). The data presented in this chapter show an increased number of mitochondrial spots per area of cell, which is consistent with fragmentation. Other publications have also identified that CCCP-induced mitochondrial morphology changes are dependent on the function of fission factor DRP1 (Ishihara *et al*, 2003).

Of note, the data indicate that maximal, drug-induced morphological changes to mitochondrial networks show at most a ~10% increase in the mean width-to-length ratio. Confocal microscopy images of the network also demonstrated perinuclear clustering of mitochondria with CCCP treatment. These two

factors are likely to contribute to a lack of sensitivity, at this resolution, for subtle changes in mitochondrial morphology, suggesting that higher resolution techniques may be required.

4.4.2 Mitochondrial morphology is differentially altered in pS129-positive and negative neurons

No change in mitochondrial morphology was found in pS129-positive aggregate-bearing neurons, whereas decreased area, width and length of mitochondria were observed in pS129-negative neurons. These data suggest an α-synuclein dependent effect on mitochondrial morphology in non-aggregate-bearing neurons, an intriguing finding considering the previous observation of accumulated pS65Ub in pS129-positive cells. Mitochondrial fission has been shown to enable mitochondrial turnover, biogenesis and stress-induced apoptosis of cells, whereas fusion attenuates mitochondrial dysfunction by complementing damaged metabolic machinery (reviewed in Youle & van der Bliek, 2012).

Previous studies have shown that expression of wild-type or mutant α-synuclein in cell culture models resulted in mitochondrial fission (Kamp *et al*, 2010; Choubey *et al*, 2011; Nakamura *et al*, 2011; Plotegher *et al*, 2014) through direct membrane binding – independently of fission/fusion machinery such as DRP1 (Kamp *et al.*, 2010; Choubey *et al.*, 2011; Nakamura *et al.*, 2011). This was concomitant with reduced mitochondrial mass, reduced ATP production and increased mitophagy, whereas reversing fragmentation through a dominant-negative DRP1 or MFN2 overexpression rescued cell death in *SNCA-A53T* expressing cells (Choubey *et al.*, 2011). With expression of wild-type α-synuclein, defects in mitochondrial respiration and cell death were observed (Nakamura *et al.*, 2011).

The mechanism of action of α-synuclein contrasted with that found in *LRRK2-G2019S* models, where in primary mouse cortical neurons, HEK293T cells and PD patient fibroblasts, increased interaction between LRRK2 and DLP1 contributed to mitochondrial fragmentation (Niu *et al*, 2012; Su & Qi, 2013). This suggests that several mechanisms may be at play in causing mitochondrial alterations in PD. In support of this, in mouse primary hippocampal neurons, α-synuclein degradation products produced from degradation of PFF-seeded aggregates were found to associate with mitochondrial membranes and cause loss of membrane potential, recruit inactive acetyl-coA carboxylase 1 (pACC1)

leading to fragmentation, cytochrome c release and increased mitophagy (Grassi *et al.*, 2018). In iPSC-derived dopaminergic neurons from *SNCA* and *SNCA-A53T*-mutant PD patients, small, rounded mitochondria were associated with loss of membrane potential, impaired respiration and increased mitophagy (Little *et al.*, 2018; Ryan *et al.*, 2018; Zambon *et al.*, 2019), perhaps through inducing cardiolipin externalisation, which subsequently bound α-synuclein in a chaperone-like capacity or induced mitophagy (Ryan *et al.*, 2018).

In vivo, *SNCA*-expressing mice and PD patient brain tissues showed altered expression of mitochondrial dynamics proteins such as DRP1 and consequently, increased mitochondrial fission (Brown *et al*, 2025), whereas α-synuclein expression to human-like levels in *Drosophila* resulted in enlargement and elongation of mitochondria through mislocalised DRP1 (Ordonez *et al*, 2018). Alternatively, mitochondrial swelling has been associated with mPTP opening, which in turn impairs ATP production and induces apoptosis (reviewed in Endlicher *et al*, 2023). α-Synuclein pathology has been associated with mPTP opening (Luth *et al.*, 2014; Ludtmann *et al.*, 2018; Choi *et al.*, 2022).

These various studies and models show that modelling PD generally results in mitochondrial fragmentation. This stands in contrast with the data obtained in this study, where pS129-positive aggregate bearing cells saw no significant change in size and shape with increasing concentrations of α-synuclein, and pS129-negative cells were found to have smaller mitochondria. The current data are insufficient to make conclusions on the mechanism driving the changes to mitochondrial morphology in pS129-positive and negative neurons. Further experiments using higher resolution imaging techniques will be instrumental in confirming these observations, and CRISPRi will be a valuable tool in isolating mechanistic pathways contributing to these changes.

4.4.3 Mitochondrial function is impaired by α-synuclein PFF treatment

The data in this study suggest a decrease in ATP levels with α-synuclein PFF treatment. Mitochondrial dysfunction has been observed consistently and extensively throughout post-mortem brains, familial and sporadic models of PD, and reduced mitochondrial function may be sufficient to drive disease. Indeed, gene mutations in mitophagy genes *PINK1* and *PRKN* result in accumulation of damaged

mitochondria (Geisler *et al*, 2010b) and cause autosomal-recessive Parkinson's disease. Similarly, accidental injection of the mitochondrial toxin MPTP, which metabolised to MPP+, also results in severe parkinsonism (Langston *et al.*, 1983). Defects in mitochondrial respiration, specifically impaired complex I activity, have been found in sporadic PD patient brain tissues (Schapira *et al.*, 1990a; Schapira *et al.*, 1990b), as well as in cell culture models using α-synuclein overexpression, aggregated species-induced α-synuclein pathology, or familial PD mutations (Devi *et al.*, 2008; Chinta *et al.*, 2010; Luth *et al.*, 2014; Reeve *et al.*, 2015; Ludtmann *et al.*, 2018) suggesting that respiratory impairments are a hallmark of PD pathology. Further studies have identified reductions in oxidative phosphorylation in PD cell culture models without linking them to complex I (Cooper *et al.*, 2012; Di Maio *et al.*, 2016; Wang *et al.*, 2019; Zambon *et al.*, 2019; Choi *et al.*, 2022; Toomey *et al.*, 2022).

α-Synuclein has been implicated by several mechanisms in the repression of normal mitochondrial function. Overexpression of α-synuclein in primary human foetal dopaminergic neurons resulted in its uptake into mitochondria, where it was found to localise to inner and outer mitochondrial membranes, and was highly correlated to complex I activity reduction (Devi *et al.*, 2008). A similar overexpression model in mice showed increased A53T-mutant α-synuclein at mitochondrial membranes, resulting in complex I inhibition as well as decreased respiration and increased turnover (Chinta *et al.*, 2010). It is likely that these observations, particularly the uptake of α-synuclein into mitochondria, may be a result of artificially increasing α-synuclein expression, as endogenous monomeric α-synuclein has not been found to extensively co-localise with mitochondria unless under overexpression conditions (Parihar *et al.*, 2008; Chinta *et al.*, 2010). Oligomer or fibril-seeded aggregation, on the other hand, has been found at mitochondrial membranes, where it resulted in inhibition of protein import through direct TOM20 interaction (Di Maio *et al.*, 2016), mPTP opening through nitric oxide and cytochrome c release (Parihar *et al.*, 2008), mPTP opening through oxidation of ATP synthase (Ludtmann *et al.*, 2018) and/or inhibition of complex I (Luth *et al.*, 2014; Reeve *et al.*, 2015; Ludtmann *et al.*, 2018).

At 14 days post PFF seeding, i^3 neurons showed no reduction in mitochondrial membrane potential as measured by JC-10 and TMRM, and no change in ROS levels measured by MitoSOX. These two observations are in contrast to several studies which highlighted a loss of membrane potential or

increased levels of ROS in various PD models or PD patient brain tissues (Cooper *et al.*, 2012; Luth *et al.*, 2014; Di Maio *et al.*, 2016; Grassi *et al.*, 2018; Little *et al.*, 2018; Ryan *et al.*, 2018; Zambon *et al.*, 2019; Ryan *et al.*, 2021; Choi *et al.*, 2022; Toomey *et al.*, 2022). Considering the lack of neuron loss and the fact that aggregation saturation was not reached (see Chapter 3), it is possible that are modelling an early stage of aggregation with mild respiratory impairment prior to the advent of overt mitochondrial dysfunction. Indeed, in iPSC-derived dopaminergic neurons, mitochondrial impairment was not observed before 21 days of α-synuclein aggregation (Mahul-Mellier *et al.*, 2020).

4.4.4 α-Synuclein PFF treatment in i^3 neurons does not induce lysosomal impairment

At 14 days post-seeding, measurement of LAMP1 intensity, size and area, and of lysosomal activity using DQ-BSA in i^3 neurons demonstrated a lack of change in any measured metric relating to fluorescence intensity (a readout of proteolytic activity), number of spots or total area occupied by spots. The only exception was a very small but statistically significant increase in lysosomal size in α-synuclein-treated conditions for DQ-BSA, which was not replicated by the LAMP1 immunostaining. This was in contrast to amyloid-β-treated neurons, which showed statistically significant decreases in spot intensity and number of spots, indicating fewer and less active lysosomes. This was surprising considering well-established interactions between α-synuclein and the autophagy-lysosomal pathway in PD. In post-mortem brain tissue from PD patients, it was observed that levels of LAMP1, CTSD and HSP73 were all reduced and the effect was greatest in α-synuclein-positive neurons, an effect which was replicated in rats that overexpress α-synuclein (Chu *et al.*, 2009). PFF-treated cells formed aggregates which co-localised with p62 and LC3 but not LAMP1, implying these aggregates were flagged for degradation but never underwent autophagy, and in this study, lysosomal activity was intact (Tanik *et al.*, 2013). Similarly, culturing *SNCA*-overexpressing neurons for hundreds of days showed reduced activity of specific proteases, but not overall activity, in manner that was at least partially dependent on α-synuclein aggregation (Mazzulli *et al.*, 2016a). This implies a small effect of long-term α-synuclein aggregation on lysosomal function. However, early-stage aggregates seeded by PFFs in HEK293 cells were found to be degraded by the lysosome in a p62-dependent manner (Watanabe *et al.*, 2013). Similarly, oligomeric α-synuclein aggregates formed following rotenone exposure in

immortalised cells and neurons were effectively cleared, but larger fibrillar aggregates were not (Lee *et al.*, 2004). Considering available evidence, it is possible that lysosomal dysfunction may not be occurring in our model at this timepoint and that culturing cells with aggregates in a longer-term capacity may reveal lysosomal impairment. It is also possible that, similar to the findings of Mazzulli and colleagues, the total activity of the lysosomes may be unaffected and more specific assessment of protease activity may be key to identifying lysosomal impairments.

Interestingly, though α-synuclein may have a detrimental effect on lysosomal activity, it is well established that impairment of lysosomal autophagy pathway is a permissive cellular environment for α-synuclein aggregation. Indeed, deleterious lysosomal gene variants are overrepresented in PD patients (Robak *et al*, 2017), and increase risk of PD in areas of pesticide use (Ngo *et al.*, 2024). Similarly, mutations in ATP13A2 and Rab27b, or reduced cathepsin B activity all impair lysosomal function and lead to increased α-synuclein accumulation and aggregation, whereas increasing lysosomal function through Rab27b or cathepsin B overexpression inhibited α-synuclein aggregation (Zhang *et al*, 2022; Jones-Tabah *et al*, 2024; Scholz *et al*, 2025). Co-treatment of α-synuclein PFFs and 20 μM CQ for 48h, followed by washout of the PFFs and CQ, potentiates α-synuclein aggregation in i^3 neurons in our paradigm (Appendix Figure 48). As such, it is possible to imagine that lysosomal dysfunction in patients may pre-exist α-synuclein aggregation and subsequently be worsened in a feed-forward mechanism with increasing α-synuclein accumulation.

4.4.5 Super-resolution microscopy to confirm and extend the findings of this study

The aim of establishing CLEM was to enable the identification of neurons bearing pS129-positive aggregates and pS65Ub-tagged mitochondria within these α-synuclein aggregates, as well as allow the precise assessment of mitochondrial morphology – both of their network complexity and size and their sub-organellar architecture. This technique has been used successfully to identify pS129-positive neurons in culture and analyse the composition and location of α-synuclein aggregates within these cells, allowing the identification of multiple organelles localised within aggregates as well as posit that membranes may be nucleation sites for α-synuclein aggregates (Mahul-Mellier *et al.*, 2020; Choi *et al.*, 2022). As the pS65Ub primary antibody was highly sensitive to the strong fixation used to prepare

samples for CLEM, it became necessary to explore alternative methods. The preliminary SIM trial in SH-SY5Y revealed that the technique was compatible with our pS65Ub, MAP2 and TOM20 immunostaining technique (pS129 was not assessed due to time constraints) and revealed highly detailed mitochondrial morphology as well as precise pS65Ub localisation.

To confirm the findings in this chapter, future experiments should include computational evaluation of mitochondrial morphology in pS129-positive and pS129-negative i^3 neurons 14 days post-PFFs using immunostaining for TOM20 and pS129, by SIM. It would also be of interest to extend the findings detailed in Chapter 3 and assess the architecture of pS129-positive aggregates and the engulfment of pS65Ub-tagged mitochondria over the course of aggregation in neurons. Understanding the interactions of pS129 and pS65Ub at high resolution will allow for the development of hypotheses regarding the mechanism by which these two markers become intertwined and shed light on the process of aggregate formation.

5 Functional genomic screening identifies candidate genes modulating pS129 and pS65Ub formation

A large number of studies have been carried out on animal and cell culture models that carry familial PD mutations and from which more generalised conclusions about disease aetiology and progression have been made. In contrast to the abundance of mutation-driven models, research into sporadic models of the disease is comparatively lacking, especially in iPSC-derived neurons. Without a clear aetiological trigger for disease, iPSC lines derived from patients with idiopathic PD are the best available model. Study of sporadic PD is important considering that it is estimated that the majority of PD cases, ~85%, are idiopathic in nature, possibly triggered by a combination of environmental exposures, ageing and genetic factors.

Though not driven by any single mutation with strong effect, natural variants at a large number of loci in the genome have been shown to increase risk for PD by several genome-wide association studies (GWAS) (Edwards *et al.*, 2010; Hamza *et al.*, 2010; Do *et al.*, 2011; Nalls *et al.*, 2011; Lill *et al.*, 2012; Pihlstrøm *et al.*, 2013; Nalls *et al.*, 2019; The Global Parkinson's Genetics & Leonard, 2025). The contribution of many of these genes to the development of PD is unknown, and the study of these variants and their effects on cellular pathways and function is in its infancy. Low-throughput study of some of these genes have revealed functions and potential mechanisms by which they are implicated in PD (Dumitriu *et al*, 2011; Jinn *et al*, 2017; Diaz-Ortiz *et al*, 2022; Larbalestier *et al*, 2022; Jones-Tabah *et al.*, 2024). Considering the available evidence, we hypothesised that candidate risk genes identified by GWAS may be acting on disease relevant cell pathways that were originally identified in familial PD models, such as α-synuclein aggregation and mitochondrial dysfunction.

The most recent GWAS have identified 134 loci contributing to the risk of PD in a European population of Caucasian ancestry (The Global Parkinson's Genetics & Leonard, 2025), a marked increase from 90 loci in 2019 (Nalls *et al.*, 2019). GWAS are also being conducted in populations of differing ancestry (Satake *et al*, 2009; Foo *et al*, 2020; Rizig *et al*, 2023; Leal *et al*, 2025; Step *et al*, 2025), as disease-relevant loci can be population specific due to migration, genetic drift, natural selection and events such as population bottlenecks. Consequently, it is likely that new loci will be uncovered in the coming years, making the establishment of systematic platforms to study gene function a priority. It is expected that understanding risk gene function may identify convergent pathways and thus, therapeutic targets. As disease-associated risk variants each contribute only a small increase in the risk for disease, such mechanistic understanding may inform the calculation of polygenic risk scores. It may also lead to increased patient stratification, personalisation of medication and patient benefit.

The aim of this chapter is to identify candidate risk genes that modulate the rate of α-synuclein aggregation or the α-synuclein-induced accumulation of pS65Ub. Consequently, I have:

1. Constructed a library of CRISPRi sgRNA-expressing lentiviruses targeting candidate genes at PD GWAS risk loci.
2. Optimised and conducted an arrayed screen to identify risk genes that alter the levels of PFF-seeded pS129 and pS65Ub in iPSC-derived cortical neurons.
3. Validated pS129 and pS65Ub-modulating preliminary hits in human iPSC-derived dopaminergic neurons

5.1 Cloning and validating an arrayed CRISPRi PD GWAS candidate risk gene library

At the beginning of this project, our goal was to perform genome-wide screening for modulators of α-synuclein aggregation and pS65Ub accumulation, based on preliminary data linking the formation of these two markers. Consequently, a flow cytometry-based genome-wide screening strategy was

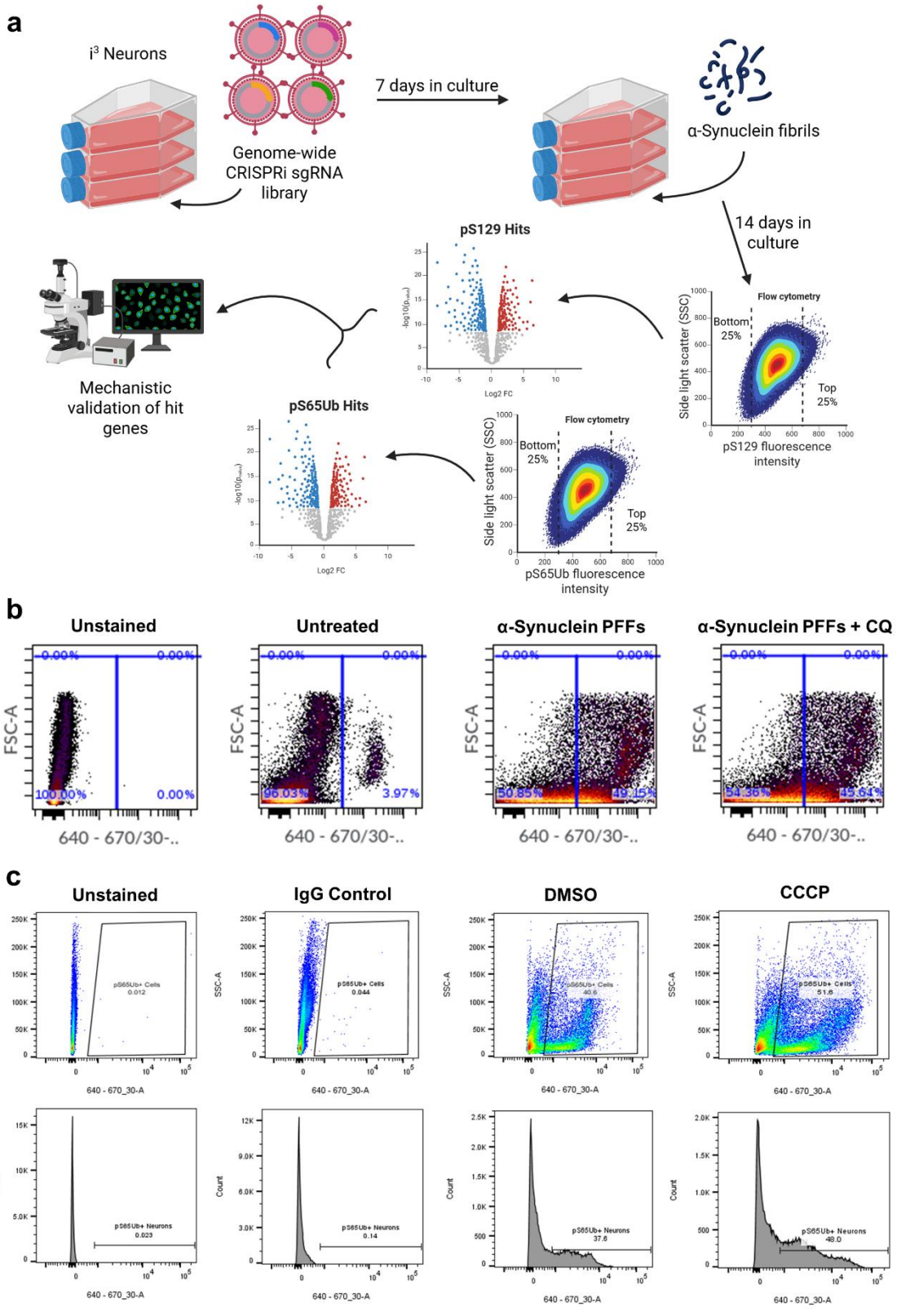


Figure 30. Flow cytometry optimisation for single-cell measurement of pS129 and pS65Ub levels.

a) Schematic representation of the pooled screening workflow. b) i^3 Neurons were lifted and immunostained in suspension using an antibody against pS129 and an Alexa-fluor 647-conjugated secondary antibody. Fluorescence intensity of pS129 was measured using a BD LSRFortessa flow cytometer with the 640 nm laser line and 670/30 emission filter. Aggregation-positive neurons were

gated based on the intensity of the untreated, stained population. PFF treatment increased the number of cells in the aggregation-positive gate from 3.97% to 49.15%. Treatment with PFFs and chloroquine resulted in a very similar population shift, with the number of cells entering the pS129-positive gate achieving 45.64%. c) i^3 Neurons were immunostained in suspension for pS65Ub and the single-cell fluorescence intensity measured on the BD Fortessa flow cytometer using a 640 nm laser line and 670/30 emission filter. pS65Ub-positive cells were found to increase from 37.8% to 48.0% in CCCP-treated conditions compared to DMSO. Histograms of the population distribution do not indicate the presence of two distinct and separated populations for pS65Ub-negative and pS65Ub-positive neurons. For all flow cytometry experiments, neurons were gated based on SSC and FSC to identify single whole cells and eliminate debris, doublets or clumps, then gated on viability using Live/Dead NIR staining before gating for pS129 or pS65Ub positivity. Representative data from N = 1 independent differentiation, each datapoint represents a single event. Panel 1a created with Biorender.com.

initially devised, leveraging the α-synuclein PFF model in i^3 neurons (Figure 30a). Co-treatment of α-synuclein fibrils with the lysosomal alkalinising agent CQ for 48 hours was shown to increase the percentage of cells bearing aggregates from 73.4% (95% CI [68.58, 78.17]) to 84.1% (95% CI [73.01, 95.12]) (Appendix Figure 48) and significantly increased the total pS129 area, relative pS129 intensity and number of pS129 spots per area of cytoplasm in PFFs + CQ conditions compared to PFF treatment alone ($p < 0.0001$ for all readouts). However, when optimising immunostaining in solution for flow cytometry, no distinction between the PFF-treated and PFF + CQ treated conditions was found (Figure 30b). Similarly, a shift of only 11% in the number of events occurring in the pS65Ub-positive gate was found when comparing cells treated with 30 µM CCCP versus DMSO (40.6% to 51.6%) (Figure 30c). Consequently, after several months of optimisation, these techniques were determined to be of insufficient sensitivity

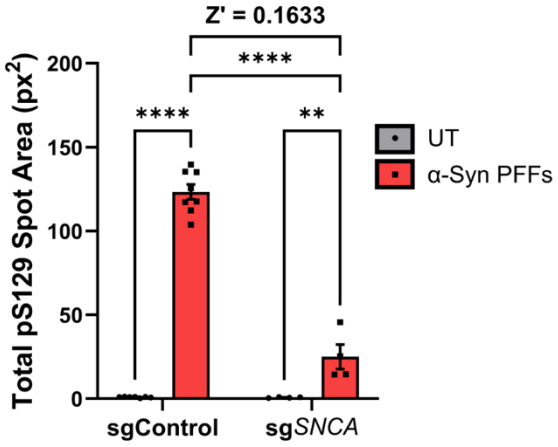


Figure 31. Sensitivity of the pS129 immunocytochemical assay.
i^3 Neurons stably-expressing a control sgRNA or a sgRNA targeting *SNCA* were treated with α-synuclein PFFs on DIV 10, fixed and immunostained 14 days post-seeding for levels of pS129. *SNCA* knockdown significantly reduced the levels of pS129 produced, and comparison of the two conditions determined a Z' value of 0.1633. N = 1 independent differentiations, each datapoint represents a technical replicate. Statistical test: two-way ANOVA with Tukey's multiple comparisons test. Data is presented as the mean ± SEM. * $p < 0.05$, ** $p < 0.01$, *** $p < 0.001$, **** $p < 0.0001$.

to support screening and a new strategy was devised based on the well-characterised immunocytochemistry assays for both markers.

Arrayed screens sacrifice the high throughput of pooled screens but generate information-rich datasets which can provide multi-parametric readouts (Franks *et al.*, 2024). The images produced by these screens lend themselves to further analysis which may yield insight into biological questions linked to the screen paradigm. As discussed in Chapter 3, in cell lines stably expressing a sgRNA targeting *SNCA*, pS129 levels were found to be reduced compared to controls at DIV 24 following PFF-seeding, indicating that reducing *SNCA* expression levels effectively abolished the aggregation of α-synuclein. Indeed, the Z prime (Z') value calculated from comparing the control condition to a *SNCA* knockdown condition was 0.1633 (Figure 31), which was acceptable given the smaller scale of the arrayed screen and cell-based aggregation model.

5.1.1 Library design and candidate risk gene selection

In 2022, the largest existing GWAS meta-analysis was conducted by Nalls and colleagues and identified 90 loci across the genome which increased risk for Parkinson's disease (Nalls *et al.*, 2019) (Figure 32a). Using the web-based iPDGC locus browser, the top 2 candidate genes at each locus, as ranked by Grenn and colleagues, were retained (Grenn *et al.*, 2020). In the absence of clear candidates, the nearest gene was selected. These selected candidates were subsequently filtered using a publicly-available RNA-sequencing dataset (Tian *et al.*, 2019) for expression in i^3 neurons and two sgRNAs targeting each of the remaining genes were selected from the hCRISPRv.2 library on the basis of their *in silico* score (Horlbeck *et al*, 2016). These sgRNA oligonucleotides were subsequently cloned into a lentiviral vector, sequence verified and packaged into lentiviral particles to enable transduction into neurons and subsequent screening (Figure 32b).

The library was composed of 71 genes retained from the GWAS meta-analyses and was supplemented with 4 familial PD genes not represented in the GWAS (*PINK1*, *PRKN*, *PARK7*, *VPS35*), 9 non-targeting controls and 13 hit genes from a proteomics study in our laboratory in PFF-treated dopaminergic neurons (data by Helle Bogetofte-Barnkob, unpublished) (Table 23), for a total of 181

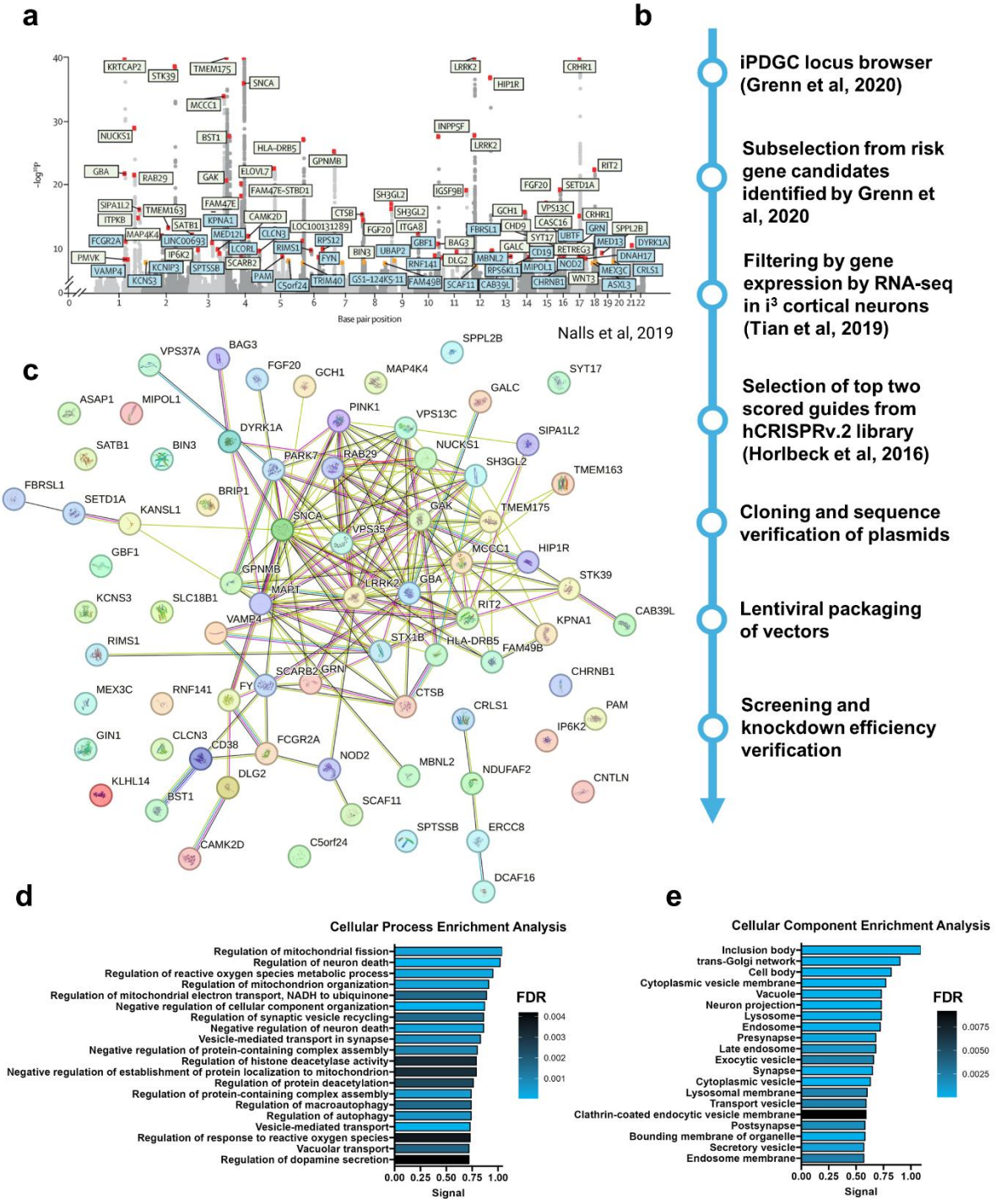


Figure 32. Design of the arrayed PD GWAS candidate risk gene CRISPRi screening library. a) Candidate risk genes were identified from the 2019 meta-analysis by Nalls and colleagues which identified 90 loci associated with increased risk of Parkinson's disease (Figure adapted from Nalls et al, 2019). b) Library design and screening workflow. c) Candidate risk genes selected for the library were inputted to STRING DB (Szklarczyk *et al.*, 2025) to assess their network connectivity, revealing one large cluster with associated offshoots, and one smaller cluster encapsulating proteins CRLS1, NDUFAF2, ERCC8 and DCAF16. The remaining protein-coding genes either have yet to be functionally connected or are functionally disparate to the other candidate risk genes in the library. d) Gene ontology evaluation performed using STRING DB reveals enrichment of terms related to cellular processes such as mitochondrial dynamics and function, as well as neuronal death and

synaptic function. Statistical test: hypergeometric test with Benjamini-Hochberg multiple comparisons test. e) Terms relating to cellular components revealed an enrichment in inclusion bodies, the trans-Golgi network, the soma, neuronal projections, the endolysosomal system and synapses. Statistical test: hypergeometric test with Benjamini-Hochberg multiple comparisons test. Data is presented as signal enrichment values and coloured according to false discovery rate.

lentiviral vectors (2 sgRNAs/gene). Network analysis of the selected candidate genes identified one main cluster composed of endolysosomal, synapto-vesicular and mitochondrial genes as well as many standalone genes which were either unlinked to the other genes, indirectly linked or whose connectivity has not yet been established (Figure 32c). Analysing the cell processes enriched in the GWAS and familial gene library revealed an enrichment (signal > 0.75, FDR < 0.001) of genes involved in mitochondrial fission, such as *LRRK2*, *VPS35*, *MAPT*, *PINK1*, and *FAM49B*, as well as genes involved in neuronal death regulation, and mitochondrial architecture and metabolism (Figure 32d). Analysis of the enrichment of cellular components in the library showed terms related to inclusion bodies, relating to the genes *CLCN3*, *TMEM163*, *LRRK2* and *SNCA*, as well as terms relating to the trans-Golgi network, cell body, cytoplasmic vesicles, neuronal projections and synapses, as well as the endolysosomal system (Figure 32e).

5.1.2 sgRNA cloning and lentiviral packaging

Of 181 vectors, 146 sgRNAs required cloning into a lentiviral vector which encodes ampicillin resistance and EF1α-driven puromycin resistance, as well as a nuclear-localised mTagBFP2 reporter (Figure 33a). 41 sgRNAs had already been cloned by Dr Stewart Humble and Peter Holderrieth (Table 23). The integration of the sgRNA into the lentiviral backbone was enabled by double enzymatic restriction digestion at the BstXI and BlpI restriction sites, and ligation of the sgRNA oligonucleotides using T4 ligase-mediated DNA ligation. Whereas the steps up to and including ligation and bacterial transformation could be performed in a 96-well format, transformants were individually streaked onto ampicillin-containing LB agar petri dishes and colonies were individually picked for vector amplification, purification and sequence verification (Figure 33b). Sequence verification of these clonal vectors was performed using commercial next-generation Sanger sequencing and yielded a majority (~60%) of vectors with the correct insert and a minority which retained the sgRNA sequence of the

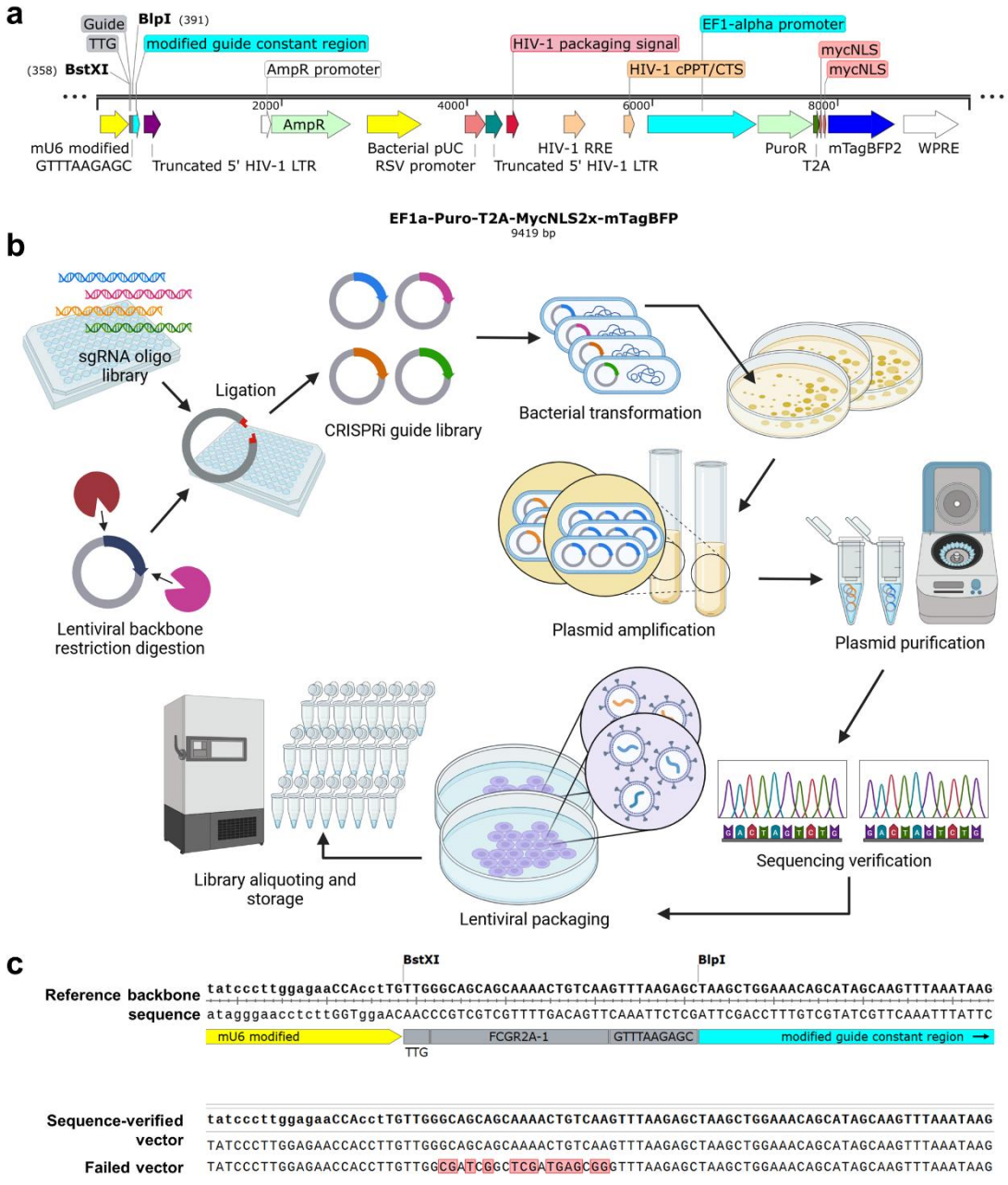


Figure 33. Cloning CRISPRi sgRNAs into lentiviral vectors at scale.
a) Lentiviral CRISPRi vector with an ampicillin resistance selection marker and an EF1α-driven puromycin resistance construct and nuclear-localised mTagBFP2. The guide construct is driven off a modified mU6 promoter and sgRNA sequences are inserted via double enzymatic digestion at the BstXI and BlpI restriction sites. b) Schematic of the process of cloning the sgRNA oligonucleotides into the lentiviral vector backbone using double-enzymatic digestion and ligation and packaging the vectors into lentiviral particles using bacterial amplification of the plasmid, plasmid purification and transfection into virus-producing cells. c) Sequence verification of picked and amplified colonies. Panel 1b created with Biorender.com.

original backbone (Figure 33c). The process was repeated iteratively until all sgRNA vectors were sequence verified. Each vector underwent lentivirus packaging and concentration by transfection into HEK-293T cells along with co-transfection of packaging vectors.

The lentiviral library underwent functional titration by treating i^3 neurons with increasing volumes of lentivirus and observing the percentage of mTagBFP2-positive nuclei in the culture. A far-red nuclear dye highlighted all nuclei in the culture, allowing for nuclear and cytoplasmic segmentation (Figure 34a). mTagBFP2 reporter fluorescence intensity was measured, and mTagBFP2-positive cells were identified, allowing the calculation of the percentage of mTagBFP2-positive cells on a well-by-well basis. Almost all vectors showed a dose-dependent increase in the percentage of reporter-positive neurons in the culture, with the average vector achieving the target transduction rate of 70% at ~700 nl (Figure 34b). 20 sgRNA-expressing lentiviruses failed to achieve the 70% transduction rate threshold and for these sgRNAs the maximum volume of 1500 nl was used in the final screen due to limits in the practicality and logistics of dispensing larger volumes with the ECHO nanodispenser. Furthermore, the average vector saw no decrease in the number of nuclei at the highest volume of lentivirus used, suggesting there is no general toxicity associated with dispensing increasing volumes or increased concentrations of the sgRNA-expressing lentiviruses (Figure 34c). A small number of sgRNA-expressing lentiviruses showed a reduction in the number of nuclei at the highest volume dispensed (1500 nl), highlighting the necessity of identifying the lowest lentivirus volume that transduced ~70% of neurons.

5.2 Optimisation of arrayed CRISPRi screening

One of the main considerations in the implementation of an arrayed CRISPRi screen was assay sensitivity, which would determine the feasibility of detecting subtle changes in phenotypes resulting from incomplete gene silencing. In iPSC-derived neuronal models, there existed the additional complication that we and others have observed silencing of the sgRNA or dCas9 machinery expression over the course of dopaminergic neuron maturation. To address these challenges, optimisation of the

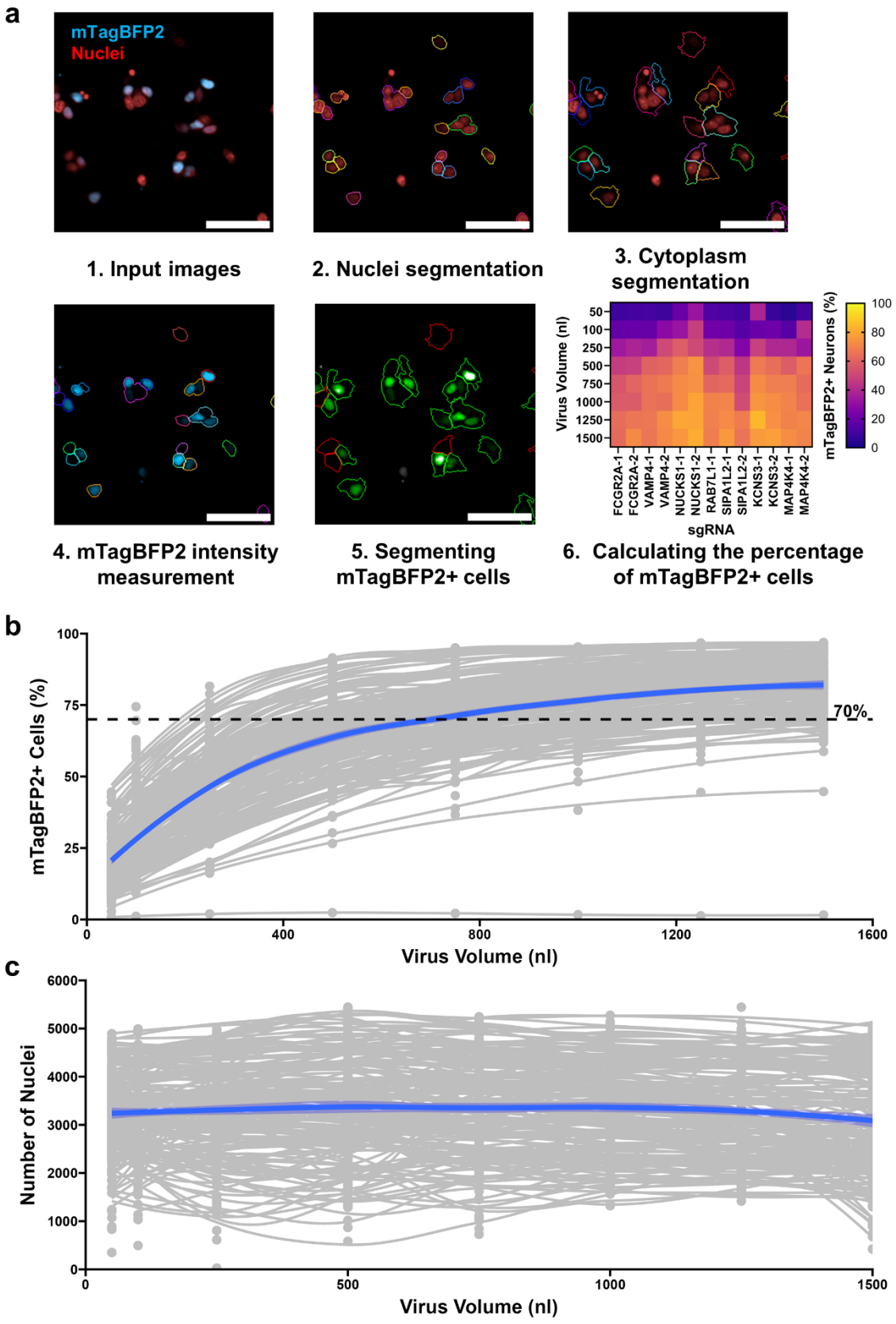


Figure 34. Lentiviral library functional titration in i^3 neurons. a) Main steps of the analysis pipeline for the functional titration of sgRNA-expressing lentiviruses. Nuclear and cytoplasmic segmentation was performed on the total nuclear population highlighted by HCS NuclearMask Far

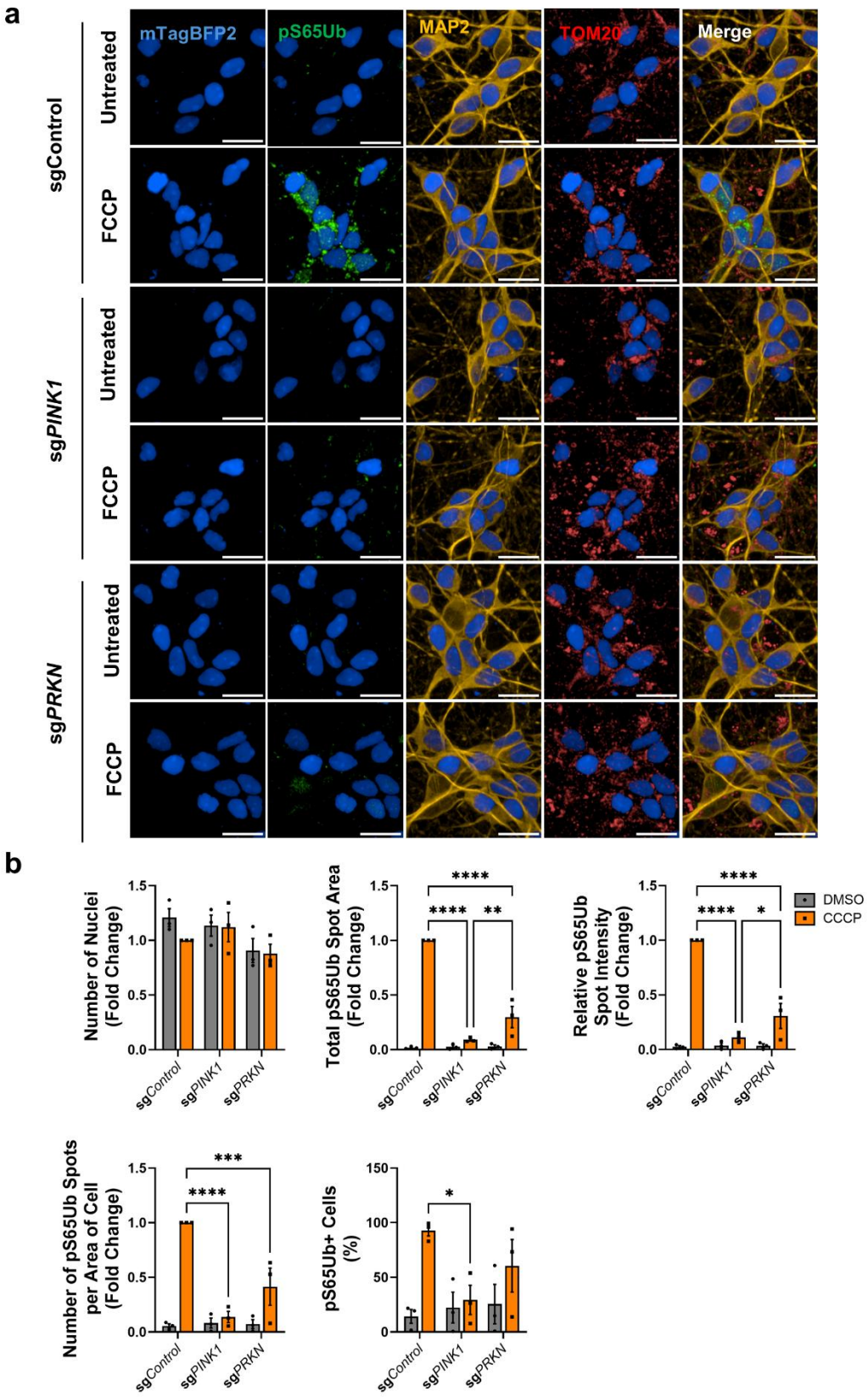
Red. The intensity of mTagBFP2 was measured in the nuclear region on a per cell basis and a threshold approach used to identify sgRNA-positive cells. Scale bar = 50 µm. 20x water immersion objective, Opera Phenix confocal microscope. b) Titration curves of all vectors in the library. The dashed line represents the target 70% transduction rate. c) Quantification of the number of nuclei by volume of lentivirus dispensed, to assess toxicity. For both b) and c), the mean curve is plotted in blue and the 95% confidence interval is represented by the shaded area around the curve. Data is presented as the mean, each datapoint represents a biological replicate.

functional effect of sgRNAs over the course of i^3 neuron maturation, of the screening workflow and of the analysis pipeline was conducted.

5.2.1 sgRNAs and dCas9 machinery are not silenced over maturation

To determine the functionality of CRISPRi silencing over the course of neuronal maturation, i^3 neurons stably expressing a sgRNA targeted to *PINK1* or *PRKN*, or expressing a control sgRNA, were treated at DIV 10 and DIV 31 with 30 µM FCCP to induce the formation of pS65Ub. The neurons were subsequently fixed and stained for the levels of pS65Ub and TOM20 by immunocytochemistry. Confocal microscopy revealed a marked decrease in the levels of pS65Ub in *PINK1* and *PRKN* knockdown conditions compared to control at both DIV 10 (Figure 35a) and DIV 31 (Figure 35c). Quantification of the pS65Ub levels showed a significant decrease of pS65Ub total spot area, relative spot intensity and number of spots per area of cell in *PINK1* and *PRKN* knockdown conditions at DIV 10 (Figure 35b) and DIV 31 (Figure 35d) ($p < 0.0001$ for all readouts, except for the number of pS65Ub spots per area of cell at DIV 10, where sgControl vs sg*PRKN* $p = 0.0005$). This suggests that the CRISPRi machinery is continuously expressed and functional until DIV 31, a timepoint beyond the endpoint of the PFF-induced pS129 accumulation paradigm.

Intriguingly, though there is a statistically significant difference between the total spot area and relative spot intensity of pS65Ub in *PINK1* versus *PRKN* knockdown conditions at DIV 10 ($p = 0.0093$ and $p = 0.0387$, respectively), this difference is no longer observed at DIV 31. Moreover, the fluorescence intensity of pS65Ub is lower overall in control conditions at DIV 31 versus DIV 10, perhaps suggesting lower capacity for mitophagy in more mature neurons. Nevertheless, iPSC-derived i^3 neurons generated pS65Ub in the presence of FCCP at DIV 31 in culture and retained functional CRISPRi silencing at this timepoint.


a
mTagBFP2
pS65Ub
MAP2
TOM20
Merge
sgControl
sgPINK1
sgPRKN
Untreated
FCCP
b
Number of Nuclei (Fold Change)
Total pS65Ub Spot Area (Fold Change)
Relative pS65Ub Spot Intensity (Fold Change)
DMSO
CCCP
Number of pS65Ub Spots per Area of Cell (Fold Change)
pS65Ub+ Cells (%)
sgControl
sgPINK1
sgPRKN

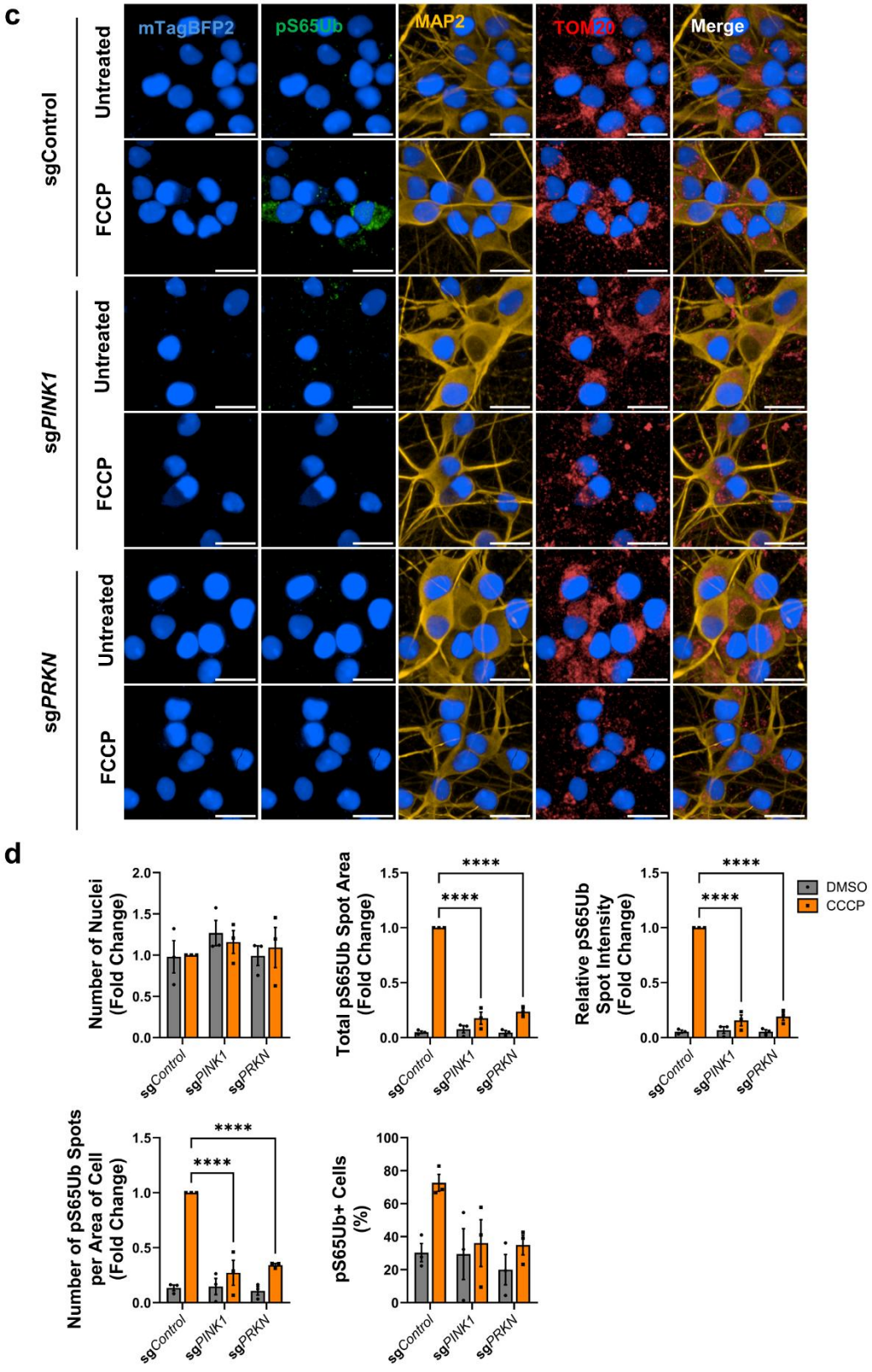


Figure 35. Functional characterisation of CRISPRi silencing at DIV 10 and 31. a) Representative confocal microscopy images of i^3 neurons stably-expressing a control sgRNA or sgRNAs against *PINK1* and *PRKN* treated with 30 µM FCCP at a) DIV 10 and c) DIV 31. The neurons were fixed and

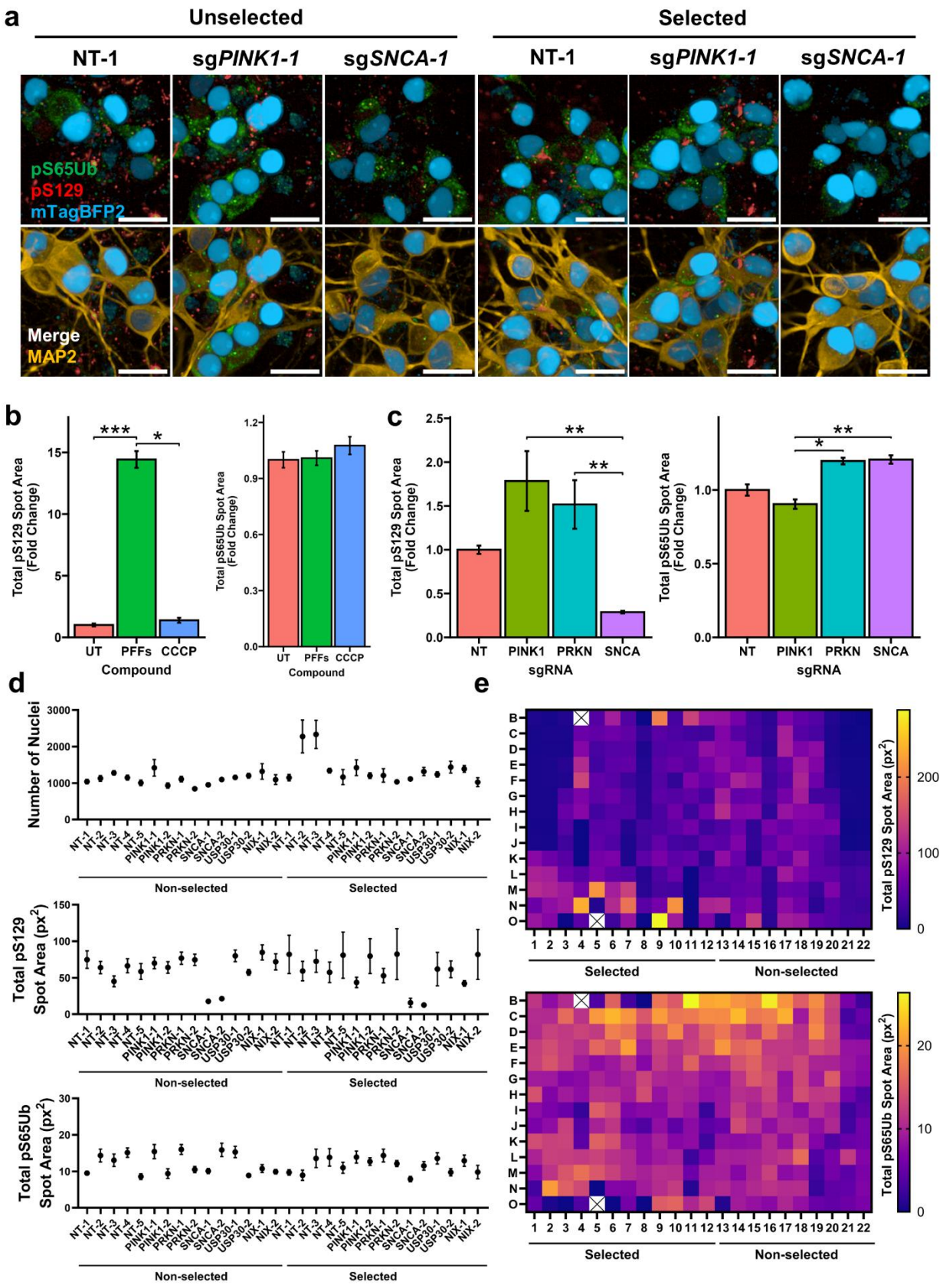
immunostained for pS65Ub , MAP2 and TOMM20. Scale bar = 20 µm. 40x water immersion objective, Opera Phenix confocal microscope. Quantification of the microscopy images reveals significant decreases in levels of pS65Ub in both *PINK1* and *PRKN* knockdown conditions at b) DIV 10 and d) DIV 31. N = 3 independent differentiations, each datapoint represents a biological replicate. Statistical test: two-way repeated measures ANOVA with Tukey's multiple comparisons test. Data is presented as the mean ± SEM. * $p < 0.05$, ** $p < 0.01$, *** $p < 0.001$, **** $p < 0.0001$.

5.2.2 Optimisation of screening workflow and analysis

To evaluate the feasibility, scale and variability of the arrayed CRISPRi screening workflow and its readouts, a small-scale pilot screen was performed. The aims of this pilot were threefold:

1. To perform the arrayed screening workflow from start to finish and detect any unforeseen issues arising from use of robotics for high-throughput plate handling, specifically in regards to dispensing sgRNA-expressing lentiviral vectors and identifying spatial and systemic effects from media changes and treatments.
2. To assess the sensitivity and variability of the readouts related to pS129 and pS65Ub, and consequently determine the feasibility of arrayed screening.
3. To evaluate the use of puromycin selection to purify the sgRNA-positive population in each well and increase assay sensitivity.

i^3 Neurons were transduced with lentiviruses expressing 5 non-targeting sgRNAs serving as controls for plate-by-plate normalisation and sgRNAs targeting *PINK1*, *PRKN*, *SNCA*, *USP30*, and *NIX*. These genes were chosen as *PINK1* and *PRKN* are important for the formation of pS65Ub and the presence of SNCA monomer is required for the aggregation of α-synuclein. The deubiquitylase USP30 is a negative regulator of pS65Ub formation and silencing its expression was expected to increase pS65Ub formation. NIX is involved in PINK1-independent mitophagy, and was hypothesised to have no effect on pS65Ub or pS129 levels. The neurons were either treated with 15 µg/ml of puromycin to select for sgRNA-positive cells or untreated prior to DIV 10, at which time the cells were treated with α-synuclein PFFs. At 14 days post-seeding, the cells were fixed and immunostained for pS65Ub, MAP2 and pS129.


a
Unselected
Selected
NT-1
sgPINK1-1
sgSNCA-1
NT-1
sgPINK1-1
sgSNCA-1
pS65Ub
pS129
mTagBFP2
Merge
MAP2
b
Total pS129 Spot Area (Fold Change)
***
*
UT
PFFs
CCCP
Compound
Total pS65Ub Spot Area (Fold Change)
UT
PFFs
CCCP
Compound
c
Total pS129 Spot Area (Fold Change)
**
**
NT
PINK1
PRKN
SNCA
sgRNA
Total pS65Ub Spot Area (Fold Change)
**
*
NT
PINK1
PRKN
SNCA
sgRNA
d
Number of Nuclei
Non-selected
Selected
Total pS129 Spot Area (px²)
Non-selected
Selected
Total pS65Ub Spot Area (px²)
Non-selected
Selected
e
Total pS129 Spot Area (px²)
Selected
Non-selected
Total pS65Ub Spot Area (px²)
Selected
Non-selected

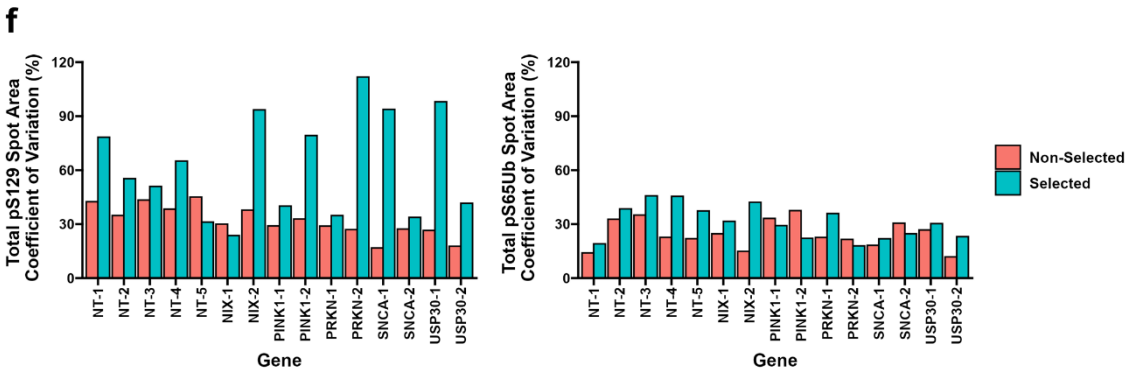


Figure 36. Preliminary screening to optimise arrayed screening workflow. a) Representative confocal microscopy images of i^3 neurons transduced on day 3 with sgRNAs targeting *PINK1* or *SNCA*, or a control sgRNA. From DIV 6 to DIV 10, the cells were selected by refreshing the medium and adding puromycin at 15 µg/ml and the neurons were treated with α-synuclein PFFs on DIV 10. At 14 days post-seeding, the cells were fixed and immunostained for pS65Ub and pS129. b) Quantification revealed the expected increase in pS129 in PFF-treated conditions, but only no significant difference for the area of pS65Ub in CCCP-treated conditions. c) Knockdown of the *SNCA* or *PINK1* genes showed no significant differences with controls in pS129 or pS65Ub levels, but were significantly reduced compared to other cell types. d) Quantification of the above images revealed no change in the number of mTagBFP2-positive nuclei being detected by the analysis pipeline, increased variability in the total pS129 spot area for neurons having undergone puromycin selection and possible positional effects regarding pS65Ub immunostaining. e) Heatmaps highlight systemic spatial effects in the pS65Ub immunostaining, but not the pS129 immunostaining. f) Coefficients of variation of the total pS129 and pS65Ub spot area in selected and unselected conditions. N = 1 independent differentiations, each datapoint represents a biological replicate. Statistical test: Kruskal-Wallis test with Dunn's multiple comparisons test. Data is presented as the mean ± SEM. * $p < 0.05$, ** $p < 0.01$, *** $p < 0.001$, **** $p < 0.0001$.

Confocal microscopy imaging revealed no alterations to overall morphology or levels of pS129 and pS65Ub in the unselected or selected cells (Figure 36a). Assay controls included untreated, PFF-treated and CCCP-treated NT control neurons to verify the effect of α-synuclein PFFs on pS129-positive aggregate formation, as well as PFF-treated NT control, *PINK1*, *PRKN* and *SNCA* knockdown neurons to confirm that depletion of *PINK1* and *SNCA* result in reduced pS129 and pS65Ub levels, respectively. pS129 levels were found to be significantly increased in PFF-treated conditions ($p = 0.00017$) compared to the untreated control, but no significant difference was found for the area of pS65Ub when cells were treated with CCCP (Figure 36b). In PFF-treated cells, the effect of genotype was statistically significant for the total area of pS129 ($p = 0.00154$), though post-hoc comparison testing showed no significant difference between sg*SNCA*-treated cells and controls (Figure 36c).

The total pS65Ub spot area was not significantly different between sg*PINK1*-treated cells and controls in preliminary screening (Figure 36c). Measurement of other parameters for pS65Ub, such as intensity, showed a significant increase in CCCP-treated conditions (Appendix Figure 50). Comparing selected and unselected cells revealed no change in the number of nuclei detected by the analysis pipeline, which was expected as sgRNA-negative cells were unlabelled and thus excluded from analysis (Figure 36b). *SNCA* knockdown using both *SNCA*-targeted sgRNAs showed a strong reduction in pS129-positive aggregation, but *PINK1*-targeted sgRNAs failed to significantly reduce the levels of PFF-induced pS65Ub. Plotting heatmaps of the pS129 and pS65Ub total area highlighted systemic spatial effects in the pS65Ub data which were absent in the pS129 data, confirming that correction of spatial effects would be necessary on a per-readout basis (Figure 36c). To account for the possibility these systemic effects were induced by the manual dispensing the primary antibody solution to a source plate for robotic liquid handling, in subsequent experiments this step was performed in a randomised, column-by-column manner.

Interestingly, treatment of cells with puromycin appeared to increase the variability of technical replicates for pS129 immunostaining but not pS65Ub immunostaining, and this was confirmed by an increase in the coefficient of variation in selected conditions for pS129 but not pS65Ub (Figure 36d).

5.2.3 Optimisation of the analysis pipeline

To determine the maximal signal window achievable, settings spanning 0.1 to 1.0 for the key pS129 detection sensitivity parameter were tested on the first replicate of primary screening using the Z-score of the *SNCA*-targeted sgRNA. Setting the detection sensitivity parameter to 0.1, 0.2 or 0.3 resulted in a larger number of pS129 puncta being detected by the software at a sensitivity setting of 0.3, particularly in the untreated condition, suggesting that higher sensitivity identifies more background fluorescence as pS129-positive puncta (Appendix Figure 51a). Plotting the Z-score of wells treated with the *SNCA*-targeted sgRNA-expressing lentivirus showed that for most readouts, the Z-score was lowest with a detection sensitivity of 0.1, suggesting that restricting the identification of pS129-positive puncta to the brightest spots increased the discrimination of the analysis pipeline between the positive and negative control (Appendix Figure 51b). Plotting the proportion of pS129-positive neurons also demonstrated

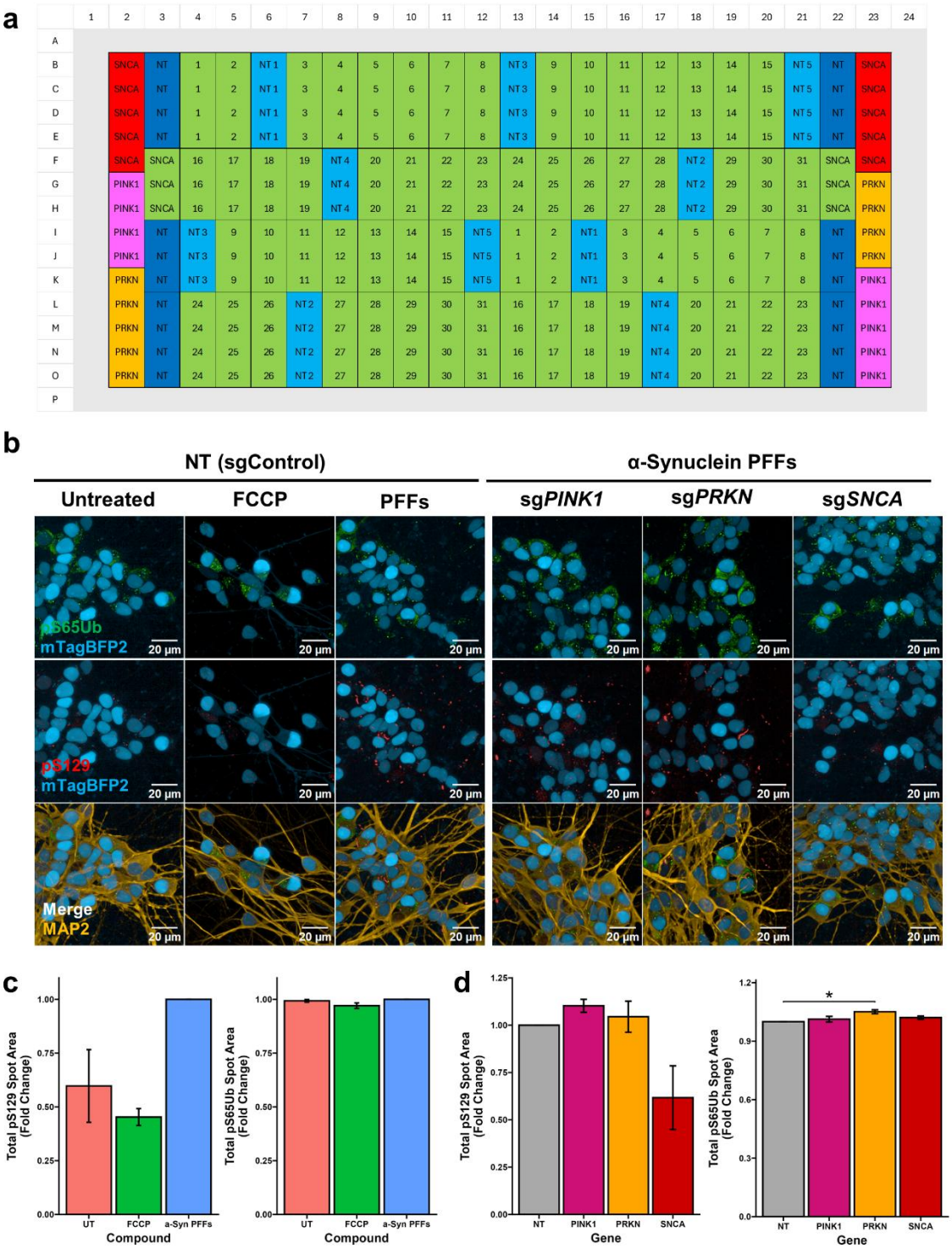


Figure 37. Screen plate design and controls.

a) Example screening plate layouts, with 31 sgRNAs/plate targeting PD GWAS genes in green, plate-to-plate normalisation control sgRNAs (non-targeting controls, NT) in blue and assay negative and positive controls in columns 2, 3, 22, and 23. b) Representative images of assay control neurons stably expressing a non-targeting sgRNA, or sgRNAs towards *PINK1*, *PRKN*, and *SNCA*, showing an increase in pS129 in PFF-treated conditions, and a reduction in pS129 levels with expression of a *SNCA*-targeted sgRNA. Scale bar = 20 µm. 40x water immersion objective, Opera Phenix confocal microscope. c) Quantification of the pS129 and pS65Ub total spot area in assay control, non-targeting sgRNA-expressing neurons shows the expected increase in pS129 levels with

α-synuclein PFF treatment, but the expected increase in pS65Ub area with FCCP treatment was not observed. d) Quantification of the pS65Ub and pS129 total spot area in PFF-treated i^3 neurons stably expressing sgRNAs targeting *PINK1*, *PRKN*, or *SNCA* or a control, non-targeting sgRNA revealed reduced pS129 levels in *SNCA*-targeting cells, but the expected decrease in pS65Ub with *PINK1*-targeting sgRNA expression was not observed. N = 3 independent differentiations. Statistical test: Kruskal-Wallis test with Dunn's multiple comparisons test. Data is presented as the mean ± SEM. * $p < 0.05$, ** $p < 0.01$, *** $p < 0.001$, **** $p < 0.0001$.

that higher sensitivity settings for this parameter increased the number of cells classed as pS129-positive, until the analysis software could no longer discriminate between pS129-positive and negative neurons. With this evidence, the detection sensitivity was set to 0.1 for subsequent screening analysis.

5.3 Primary screening of PD GWAS risk candidate genes

Primary screening of all 181 vectors was conducted in i^3 neurons in a 384-well format. sgRNA-expressing lentiviruses were dispensed to neurons on DIV 3 using acoustic nanodispensing, and the cells treated with α-synuclein PFFs on DIV 10. 14 days post-seeding, the neurons were fixed and stained by immunocytochemistry for pS129, MAP2 and pS65Ub. Three replicates of primary screening were conducted to mitigate variability in the effect of sgRNAs. The well location of sgRNAs were randomised for each experimental replicate to account for systemic spatial effects and plate-to-plate effects.

5.3.1 Screen plate design and controls

To account for systemic spatial effects, sgRNA technical replicates were spatially separated within the plate, with one group distributed centrally and one peripherally, as well as across the left and right edges (Figure 37a). Five non-targeting sgRNAs were selected and dispensed in the same positions on each of the screening plates, allowing for plate-by-plate normalisation of the data. Assay controls were positioned in columns 2, 3, 22 and 23. *SNCA*-targeted sgRNA-expressing neurons were expected to show a reduction in pS129-positive aggregation levels, and *PINK1*-targeted sgRNA-expressing neurons were expected to show a decrease in pS65Ub levels. *PRKN*-targeted sgRNAs, on the other hand, were expected to show a mild increase in pS129-positive aggregation levels, as this had been previously observed for smaller scale experiments and preliminary screening and subsequently published (Schmidt

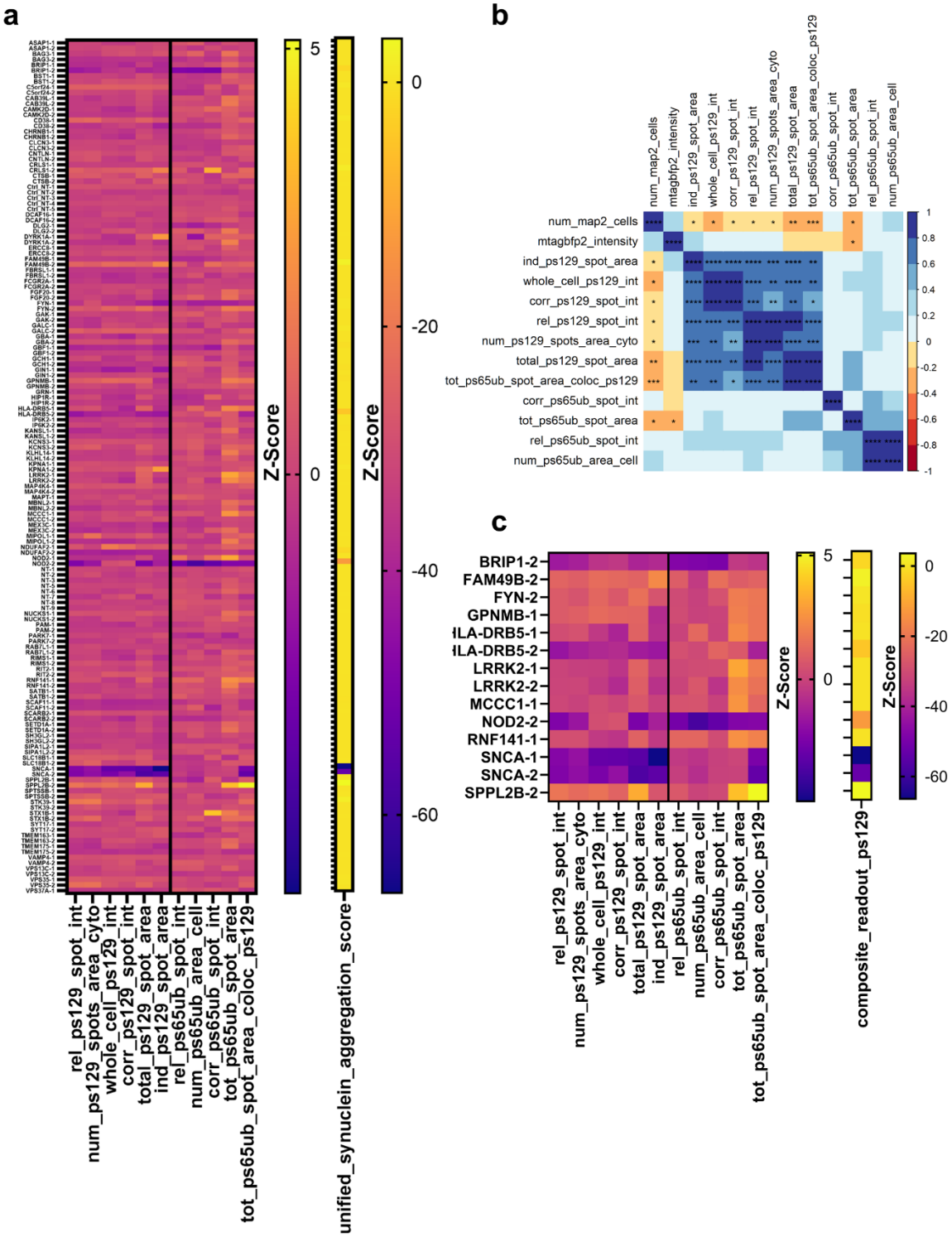


Figure 38. Correlation of screening readouts and composite readouts.
a) Heatmap of the Z-score of all readouts and genes and of the Z-score associated with the composite pS129 readout. b) Correlogram of the screening readouts arranged by hierarchal clustering, showing strong correlation of all the pS129-associated readouts and more moderate correlation of the pS65Ub readouts. Data is presented as mean Spearmann's ρ. c) Heatmap of the Z-score for all readouts and a subset of hit genes. N = 3 independent differentiations. Statistical test: Pearson's correlation. Data is presented as the mean z-score. * $p < 0.05$, ** $p < 0.01$, *** $p < 0.001$, **** $p < 0.0001$.

et al., 2025). Non-targeting sgRNA-expressing neurons were also left untreated, or treated with FCCP (FCCP induced a strong pS65Ub response in cortical neurons) and α-synuclein PFFs to increase pS65Ub and pS129 levels, respectively.

Confocal microscopy imaging and analysis of the screening controls across all experimental replicates revealed the expected effect of treating non-targeting sgRNA-expressing neurons with α-synuclein PFFs in increasing the area of pS129-positive aggregation, though the effect was not significant (Figure 37b-c). However, treatment of i^3 neurons with FCCP did not produce a significant increase in the levels of pS65Ub, a surprising finding considering that multiple previous experiments supported the effect of this toxin on pS65Ub formation. Likewise, levels of pS129-positive aggregation were trended towards reduction in *SNCA*-targeted sgRNA-expressing neurons, as expected, but the levels of pS129 were not increased in *PRKN*-targeted sgRNA-expressing neurons (Figure 37b-d). This was likely due to the small effect size of *PRKN* silencing on pS129-positive aggregation, which was identified in smaller scale experiments with >12 technical replicates. With larger-scale experiments, the use of nine technical replicates per plate, reduced by loss of some wells due to low cell adherence, may have resulted in insufficient power to identify this increase. The levels of pS65Ub were unchanged in neurons expressing a *PINK1*-targeted sgRNA. Together, these data support the effect of *SNCA* knockdown on reducing pS129 levels and increased confidence in the interpretation of sgRNAs modulating pS129, but cautioned the interpretation of the pS65Ub data.

Table 17. Screening Harmony pipeline readouts and interpretation

Readout name in Harmony	Readout code	Interpretation
Live MAP2+ Cells - Number of Objects	num_map2_cells	Number if MAP2-positive cells in culture (count)
Live MAP2+ Cells - Nuclear mTagBFP2 Intensity Mean - Mean per Well	mtagbfp2_intensity	Intensity of nuclear mTagBFP2 reporter (arbitrary units)
Live MAP2+ Cells - Relative Spot Intensity - Mean per Well	rel_ps129_spot_int	Integrated pS129 signal (signal being spot intensity minus the spot

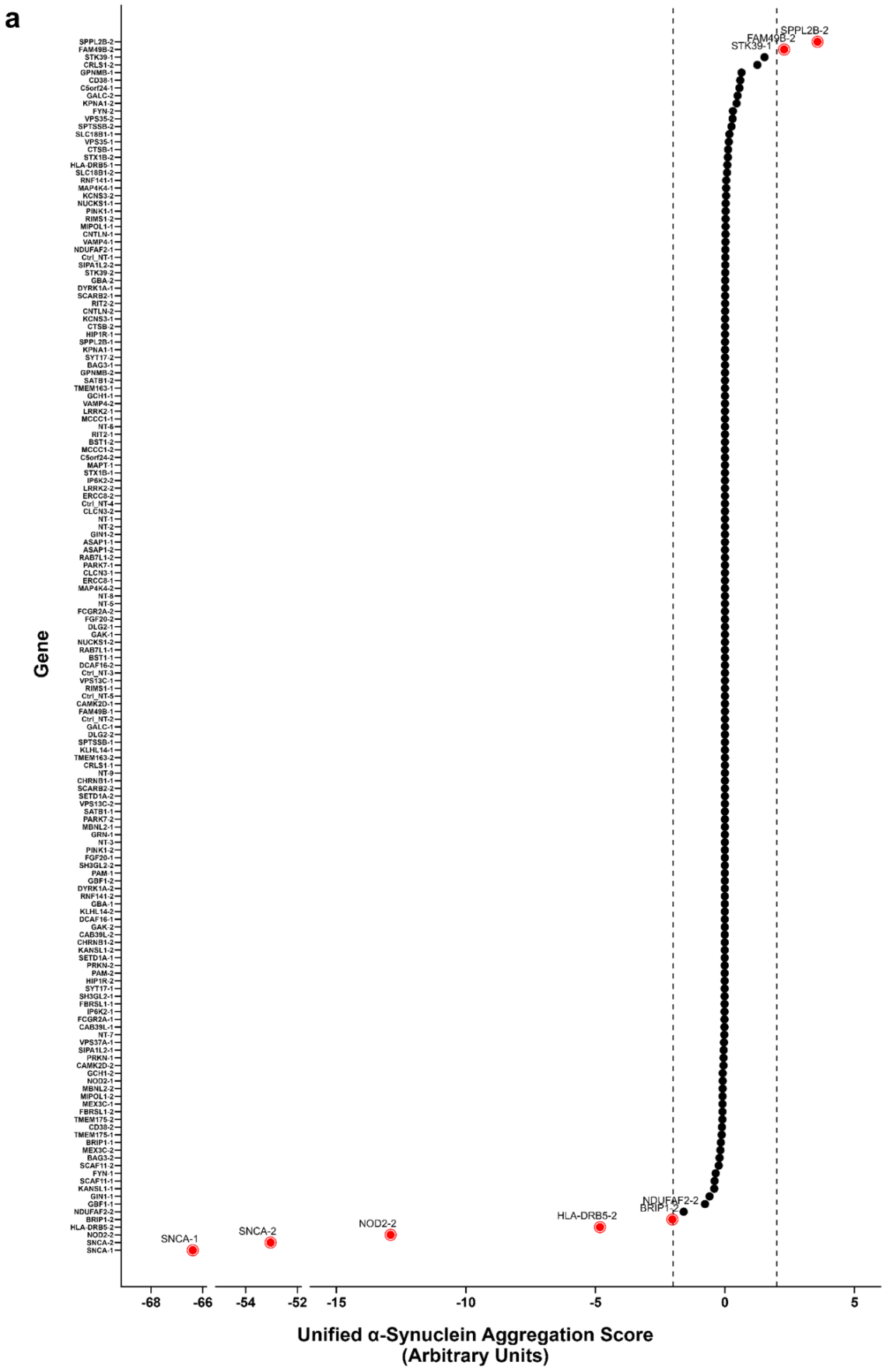
		background intensity) divided by the integrated intensity of pS129 across the cell (arbitrary units)
Live MAP2+ Cells - Number of Spots per Area of Cytoplasm - Mean per Well	num_ps129_spots_area_cyto	Number of pS129 spots divided by the area of the cytoplasm (count/px^2)
Live MAP2+ Cells - Whole Cell - Synuclein Intensity Mean - Mean per Well	whole_cell_ps129_int	Mean intensity of pS129 across all pixels of the cell (arbitrary units)
Live MAP2+ Cells - Corrected Spot Intensity- Mean Live MAP2+ Cells - All pS129 Spots - Mean per Well	corr_ps129_spot_int	Mean intensity of the pS129 spot peak minus the intensity of the background (arbitrary units)
Live MAP2+ Cells - Spot Area [px²]- Sum Live MAP2+ Cells - All pS129 Spots - Mean per Well	total_ps129_spot_area	Sum of the area of all pS129 spots identified in the cell (px^2)
Live MAP2+ Cells - All pS129 Spots Morphology Area [µm²]- Mean Live MAP2+ Cells - All pS129 Spots - Mean per Well	ind_ps129_spot_area	Mean of the areas of single pS129 spots in the cell, also known as spot size (px^2)
Live MAP2+ Cells - Relative Spot Intensity (2) - Mean per Well	rel_ps65ub_spot_int	Integrated pS65Ub signal (signal being spot intensity minus the spot background intensity) divided by the integrated intensity of pS65Ub across the cell (arbitrary units)
Live MAP2+ Cells - Number of Spots per Area of Cell - Mean per Well	num_ps65ub_spots_area_cell	Number of pS65Ub spots divided by the area of the cytoplasm (count/px^2)
Live MAP2+ Cells - Corrected Spot Intensity- Mean Live MAP2+ Cells -All pS65Ub Spots - Mean per Well	corr_ps65ub_spot_int	Mean intensity of the pS65Ub spot peak minus the intensity of the background (arbitrary units)
Live MAP2+ Cells - Spot Area [px²]- Sum Live MAP2+ Cells - All pS65Ub Spots - Mean per Well	tot_ps65ub_spot_area	Sum of the area of all pS65Ub spots identified in the cell (px^2)

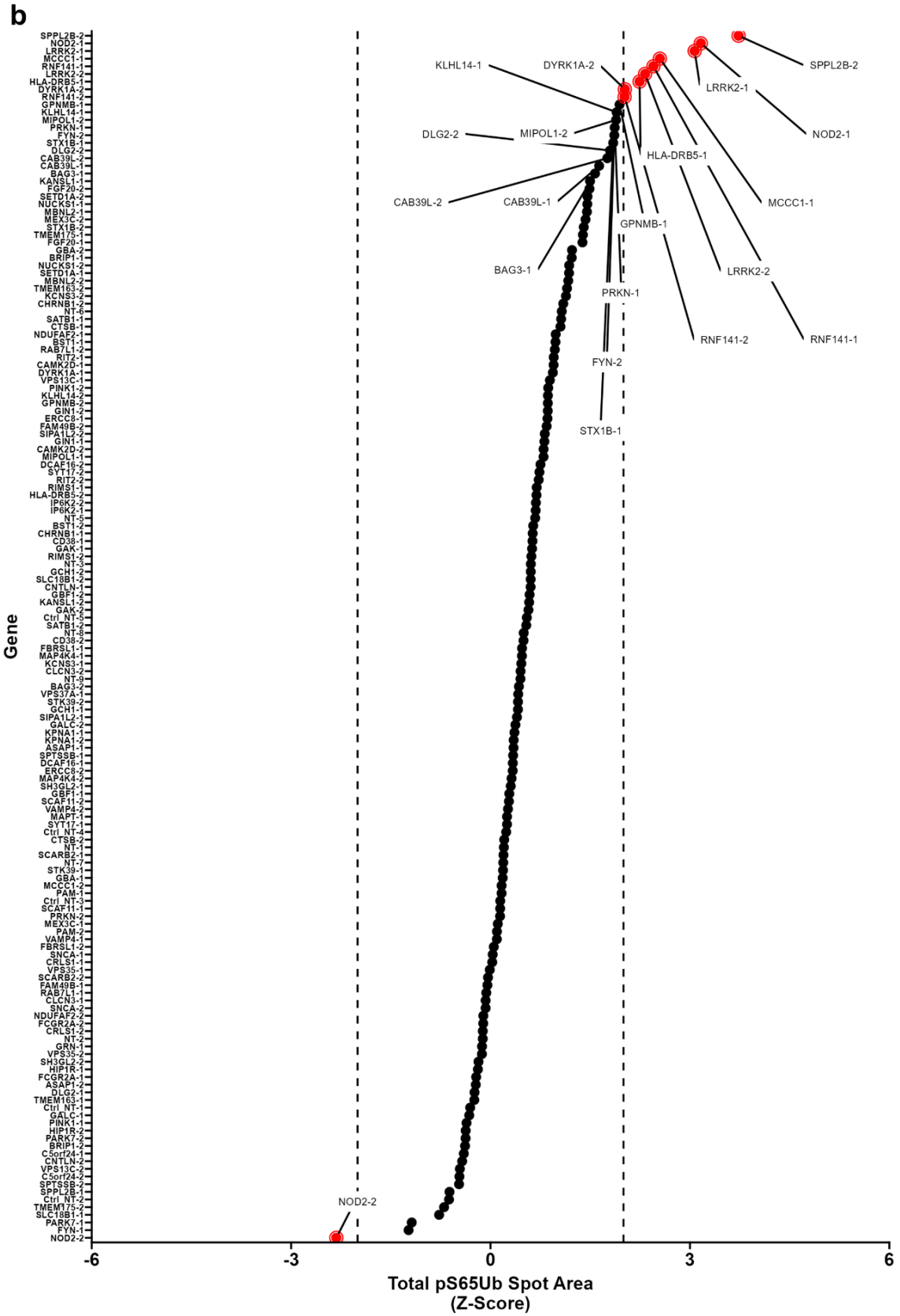
Live MAP2+ Cells - Spot Area [px²]- Sum Live MAP2+ Cells - pS65Ub Spots Co-localised with pS129 Spots - Mean per Well	tot_ps65ub_spot_area_coloc_ps129	Sum of the areas of pS65Ub spots co-localising with pS129 (determined through thresholding the pS129 intensity within the pS65Ub spot) (px^2)

5.3.2 Readout correlation and unified scoring

Arrayed CRISPRi screens generate large amounts of data stemming from the information-rich image dataset acquired, which poses a significant challenge in the identification of candidate risk genes to pursue for mechanistic validation. The readouts produced by the Harmony analysis software were selected on the basis of their biological interpretation and provide complementary information on the levels of pS129 or pS65Ub in each knockdown condition (Table 17). To better prioritise candidate hit genes, the Z-score of each screened sgRNA for each readout was plotted as a heatmap to enable comparison of Z-score values between outputs (Figure 38a). This revealed strong correspondence of Z-score values for all pS129 readouts, though the relative pS129 spot intensity, number of spots per area of cytoplasm, and total spot area were most similar.

The five pS65Ub readouts were overall less similar. These conclusions were supported by correlation analysis of the readouts, where hierarchal clustering demonstrated that all pS129-associated readouts were significantly correlated, including the total pS65Ub area colocalised with pS129 (Figure 38b). However, pS65Ub readouts clustered separately. The only significant correlation between pS65Ub readouts arose between the relative pS65Ub spot intensity and the number of pS65Ub spots per area of cell. Subsetting the dataset by identifying preliminary hit genes yielded additional information on the readouts contributing most to hit gene identification (Figure 38c). As a means of reducing data dimensionality and identifying the strongest candidate hit genes, a unified pS129 score was generated for pS129-associated readouts, produced by the multiplication of the Z-scores for the pS129 relative spot intensity, total spot area, number of spots per area of cell and individual spot area. This composite


a
Gene
SPPL2B-2
FAM49B-2
STK39-1
SNCA-1
SNCA-2
NOD2-2
HLA-DRB5-2
NDUFAF2-2
BRIP1-2
-68
-66
-54
-52
-15
-10
-5
0
5
Unified α-Synuclein Aggregation Score
(Arbitrary Units)


b
Gene
Total pS65Ub Spot Area
(Z-Score)
-6
-3
0
3
6
SPPL2B-2
KLHL14-1
DYRK1A-2
LRRK2-1
DLG2-2
MIPOL1-2
NOD2-1
HLA-DRB5-1
CAB39L-2
CAB39L-1
MCCC1-1
GPNMB-1
BAG3-1
LRRK2-2
PRKN-1
RNF141-2
RNF141-1
FYN-2
STX1B-1
NOD2-2

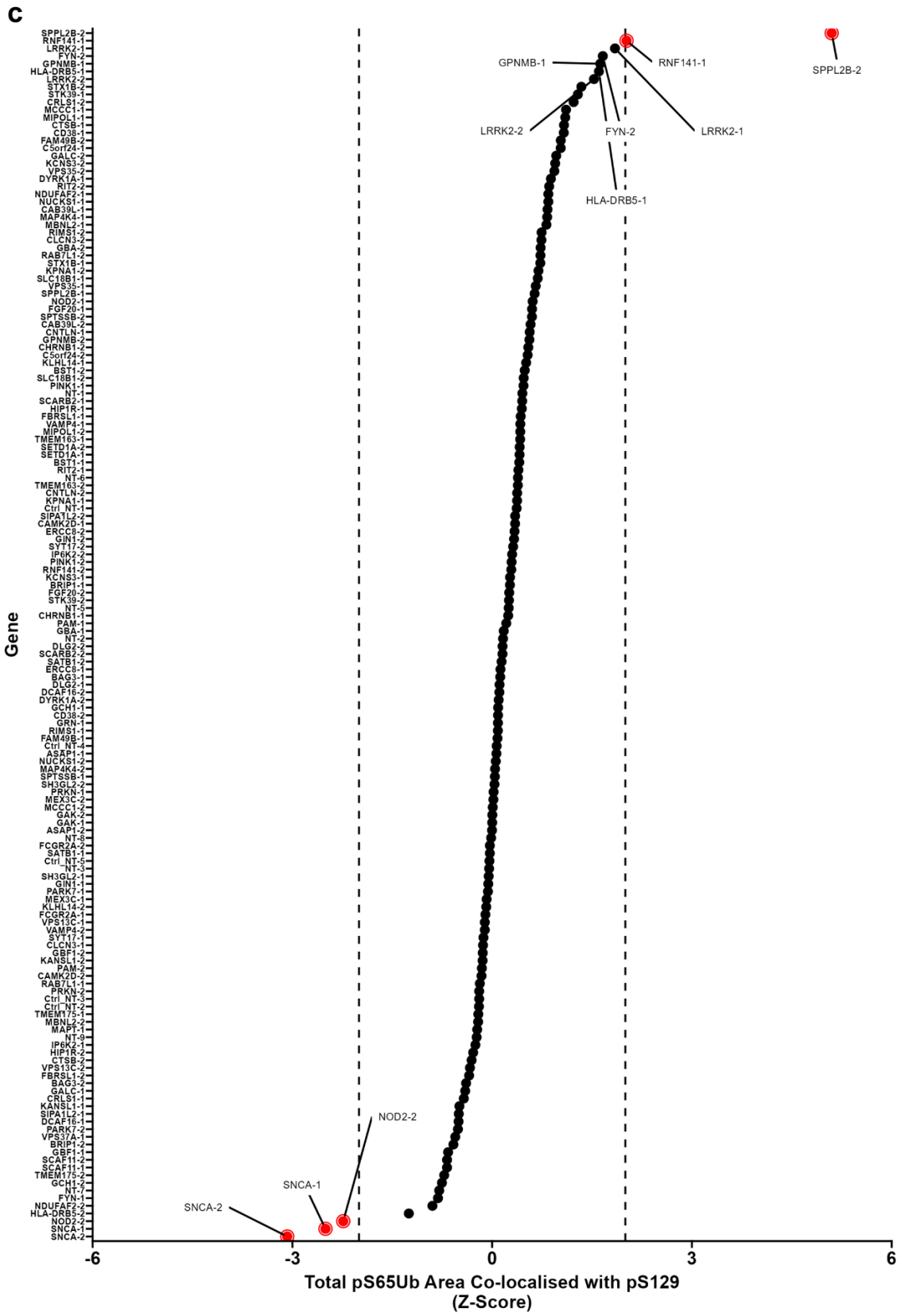

c
Gene
GPNMB-1
RNF141-1
SPPL2B-2
LRRK2-2
FYN-2
LRRK2-1
HLA-DRB5-1
NOD2-2
SNCA-1
SNCA-2
-6
-3
0
3
6
Total pS65Ub Area Co-localised with pS129
(Z-Score)

Figure 39. Primary GWAS candidate risk gene screening. a) Quantification of the primary screen results based on the unified aggregation score for pS129, a composite readout produced by the multiplication of the Z-scores of 4 pS129-associated readouts. Knockdown of *SPPL2B* and *FAM49B* showed upregulation of pS129 levels, whereas knockdown of *BRIP1*, *HLA-DRB5*, *NOD2* and *SNCA* resulted in decreased pS129 aggregation. b) Quantification of the screen results using the z-score for the readouts total pS65Ub spot area and c) total pS65Ub spot area co-localised with pS129. Dashed lines identify the cutoff used to classify hit or non-hit genes, at score = ±2 and hit genes are labelled in red. N = 3 independent differentiations. Data is presented as the mean unified pS129 score or as the mean z-score.

readout was subsequently used to prioritise hit genes for further validation and mechanistic study. Due to the weaker correlation between the pS65Ub readouts, a composite score was not calculated for this readout and instead the total pS65Ub spot area, co-localised or not with pS129, were used as primary readouts.

5.3.3 Identification of putative modulators of pS129-positive aggregate formation and α-synuclein PFF-induced pS65Ub

Images from all 181 sgRNA-mediated knockdown conditions and assay controls were acquired, analysed, and processed with custom analysis pipelines. The data was cleaned by first filtering out wells with abnormally low or high numbers of neurons, then log transforming the data and adjusting for systemic spatial effects using linear regression over rows and columns. The log-transformed data was further normalised by calculating the Z-score of each sgRNA in relation to the mean of 5 non-targeting controls on a plate-by-plate basis. A Z-score threshold of ±2 was used to identify candidate hit genes. Once the data was combined into a unified pS129 score and pS65Ub readouts, this resulted in 7 pS129-associated hit sgRNAs (Figure 39a) (6 genes) and 9 pS65Ub-associated hit sgRNAs (8 genes) (Figure 39b), representing 3.86% and 4.97% of vectors screened, respectively. These values are similar to the percentage of hit sgRNAs which might be expected by chance.

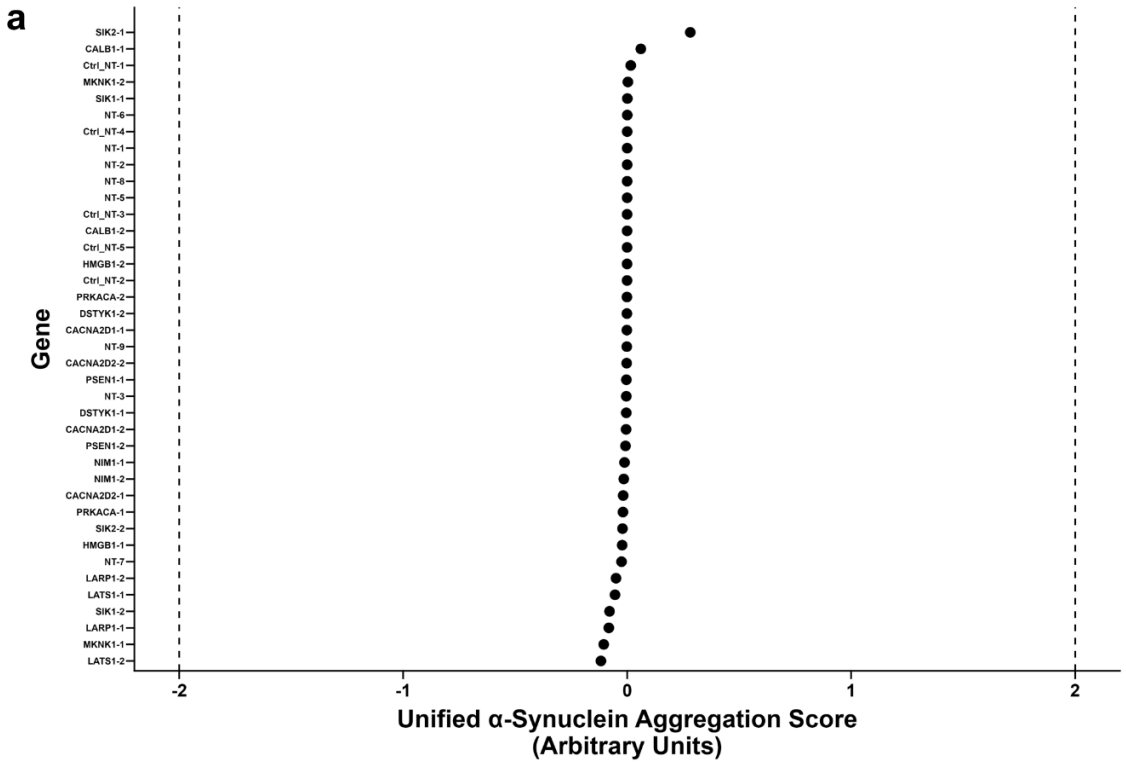
Table 18. Top upregulating sgRNAs ranked by readout score in the primary screen

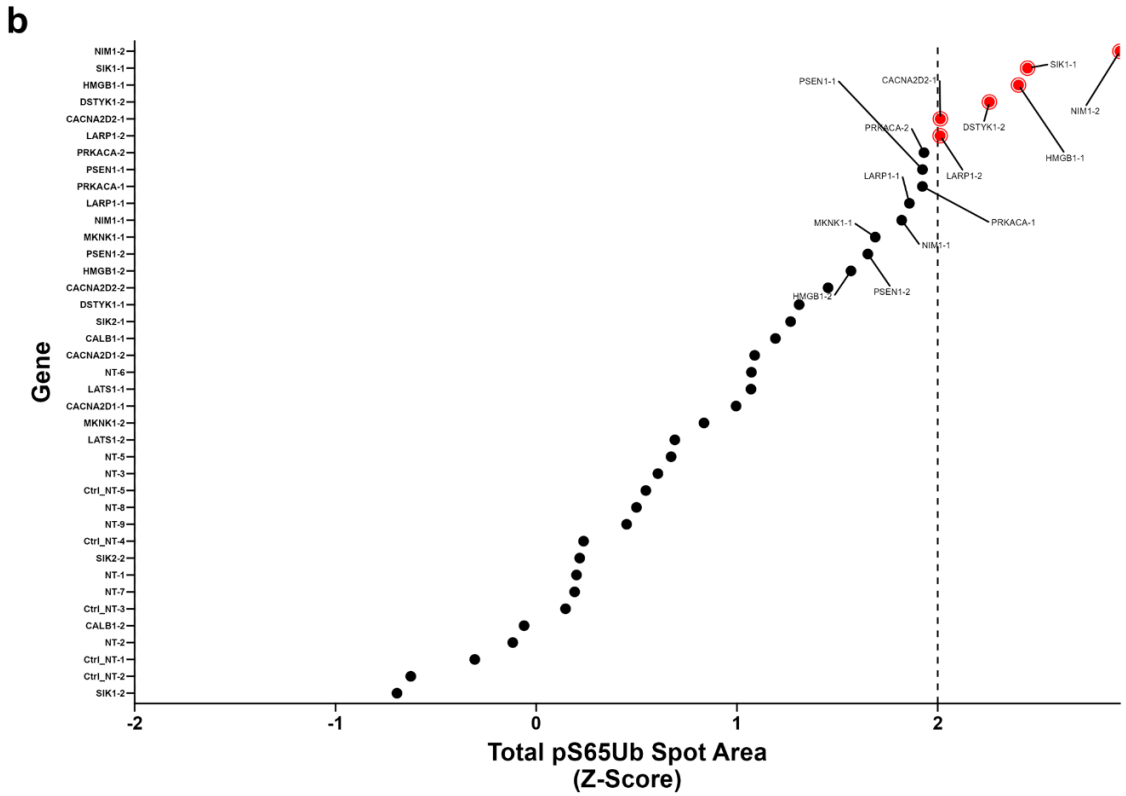
GWAS dataset				Proteomics dataset			
pS129		**pS65Ub**		**pS129**		**pS65Ub**	
sgRNA	Score	sgRNA	Z-score	sgRNA	Score	sgRNA	Z-score
SPPL2B-2	3.57	SPPL2B-2	3.73	SIK2-1	0.28	NIM1-2	2.91
FAM49B-2	2.28	NOD2-1	3.16	CALB1-1	0.06	SIK1-1	2.45
STK39-1	1.53	LRRK2-1	3.07	Ctrl_NT-1	0.02	HMGB1-1	2.40
CRLS1-2	1.25	MCCC1-1	2.55	MKNK1-2	0.00	DSTYK1-2	2.26
GPNMB-1	0.64	RNF141-1	2.45	SIK1-1	0.00	CACNA2D2-1	2.01
CD38-1	0.59	LRRK2-2	2.32	NT-6	0.00	LARP1-2	2.01
C5orf24-1	0.56	HLA-DRB5-1	2.24	Ctrl_NT-4	0.00	PRKACA-2	1.93
GALC-2	0.49	DYRK1A-2	2.02	NT-1	0.00	PSEN1-1	1.92
KPNA1-2	0.45	RNF141-2	2.02	NT-2	0.00	PRKACA-1	1.92
FYN-2	0.31	GPNMB-1	1.94	NT-8	0.00	LARP1-1	1.86

Table 19. Top downregulating sgRNAs ranked by readout score in the primary screen

GWAS dataset				Proteomics dataset			
pS129		**pS65Ub**		**pS129**		**pS65Ub**	
sgRNA	Score	sgRNA	Z-score	sgRNA	Score	sgRNA	Z-score
SNCA-1	-66.39	NOD2-2	-2.32	LATS1-2	-0.12	SIK1-2	-0.69
SNCA-2	-53.04	FYN-1	-1.23	MKNK1-1	-0.10	Ctrl_NT-2	-0.62
NOD2-2	-12.91	PARK7-1	-1.19	LARP1-1	-0.08	Ctrl_NT-1	-0.31
HLA-DRB5-2	-4.82	SLC18B1-1	-0.77	SIK1-2	-0.08	NT-2	-0.12
BRIP1-2	-2.03	TMEM175-2	-0.70	LATS1-1	-0.05	CALB1-2	-0.06

The top-ranked preliminary hit sgRNAs by pS129 or pS65Ub score that showed increased pS129 aggregation were SPPL2B-2 and FAM49B-2 (unified score = 3.57 and 2.28, respectively). Two more sgRNAs, STK39-1 and CRLS1-2 (pS129 unified score = 1.53 and 1.25, respectively), trended towards


a
Gene
SIK2-1
CALB1-1
Ctrl_NT-1
MKNK1-2
SIK1-1
NT-6
Ctrl_NT-4
NT-1
NT-2
NT-8
NT-5
Ctrl_NT-3
CALB1-2
Ctrl_NT-5
HMGB1-2
Ctrl_NT-2
PRKACA-2
DSTYK1-2
CACNA2D1-1
NT-9
CACNA2D2-2
PSEN1-1
NT-3
DSTYK1-1
CACNA2D1-2
PSEN1-2
NIM1-1
NIM1-2
CACNA2D2-1
PRKACA-1
SIK2-2
HMGB1-1
NT-7
LARP1-2
LATS1-1
SIK1-2
LARP1-1
MKNK1-1
LATS1-2
-2
-1
0
1
2
Unified α-Synuclein Aggregation Score
(Arbitrary Units)


b
Gene
NIM1-2
SIK1-1
HMGB1-1
DSTYK1-2
CACNA2D2-1
LARP1-2
PRKACA-2
PSEN1-1
PRKACA-1
LARP1-1
NIM1-1
MKNK1-1
PSEN1-2
HMGB1-2
CACNA2D2-2
DSTYK1-1
SIK2-1
CALB1-1
CACNA2D1-2
NT-6
LATS1-1
CACNA2D1-1
MKNK1-2
LATS1-2
NT-5
NT-3
Ctrl_NT-5
NT-8
NT-9
Ctrl_NT-4
SIK2-2
NT-1
NT-7
Ctrl_NT-3
CALB1-2
NT-2
Ctrl_NT-1
Ctrl_NT-2
SIK1-2
PSEN1-1
CACNA2D2-1
SIK1-1
NIM1-2
PRKACA-2
DSTYK1-2
HMGB1-1
LARP1-1
LARP1-2
PRKACA-1
MKNK1-1
NIM1-1
HMGB1-2
PSEN1-2
-2
-1
0
1
2
Total pS65Ub Spot Area
(Z-Score)

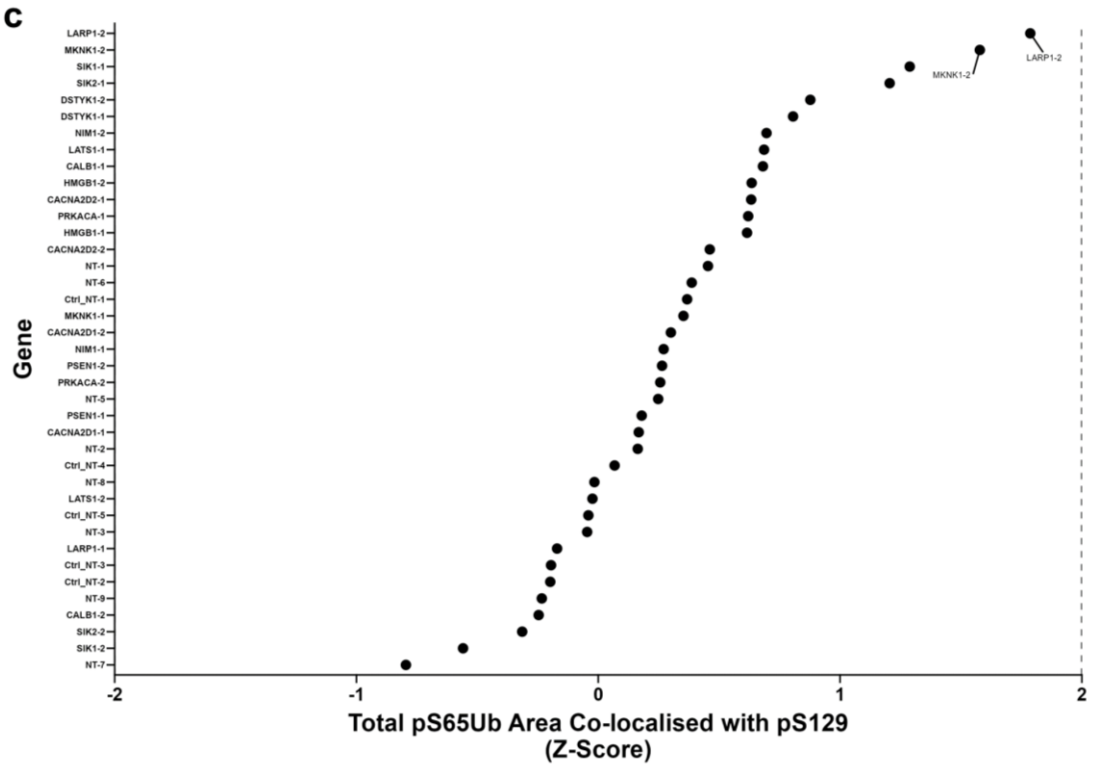


Figure 40. Primary screening of sgRNAs targeting proteomics hit genes.
a) sgRNAs targeting genes identified by proteomics in PFF-treated or untreated dopaminergic neurons (data by Helle Bogetofte-Barnkob, unpublished) were screened in the same manner as PD GWAS candidate gene-targeting sgRNAs. Analysis of the unified α-synuclein aggregation score showed no sgRNAs effected change on pS129 aggregation levels in i^3 neurons. b) Quantification of the total pS65Ub spot area z-score revealed several sgRNAs which upregulate pS65Ub levels in cortical neurons. c) Quantification of the total pS65Ub co-localised with pS129 revealed no sgRNAs that achieved the threshold to be classed as hits. Dashed lines identify the cutoff used to classify hit or non-hit genes, at unified score = ±2 and hit genes are labelled in red. N = 3 independent differentiations. Data is presented as the mean unified pS129 score or as the mean z-score.

upregulation of pS129 aggregation but did not achieve the threshold, suggesting hit genes of low effect size. The strongest sgRNAs associated with decreased pS129 aggregation were both sgRNAs targeting *SNCA* (unified score = -66.38 and -53.03, respectively). sgRNAs NOD2-2, HLA-DRB5-2, BRIP1-2 all exceeded the threshold for hit identification with unified pS129 scores of -12.90, -4.82 and -2.02, whereas the sgRNA NDUFAF2-2, with a score of -1.59, trended towards downregulation of pS129-positive aggregation but did not achieve the cutoff (Figure 39a).

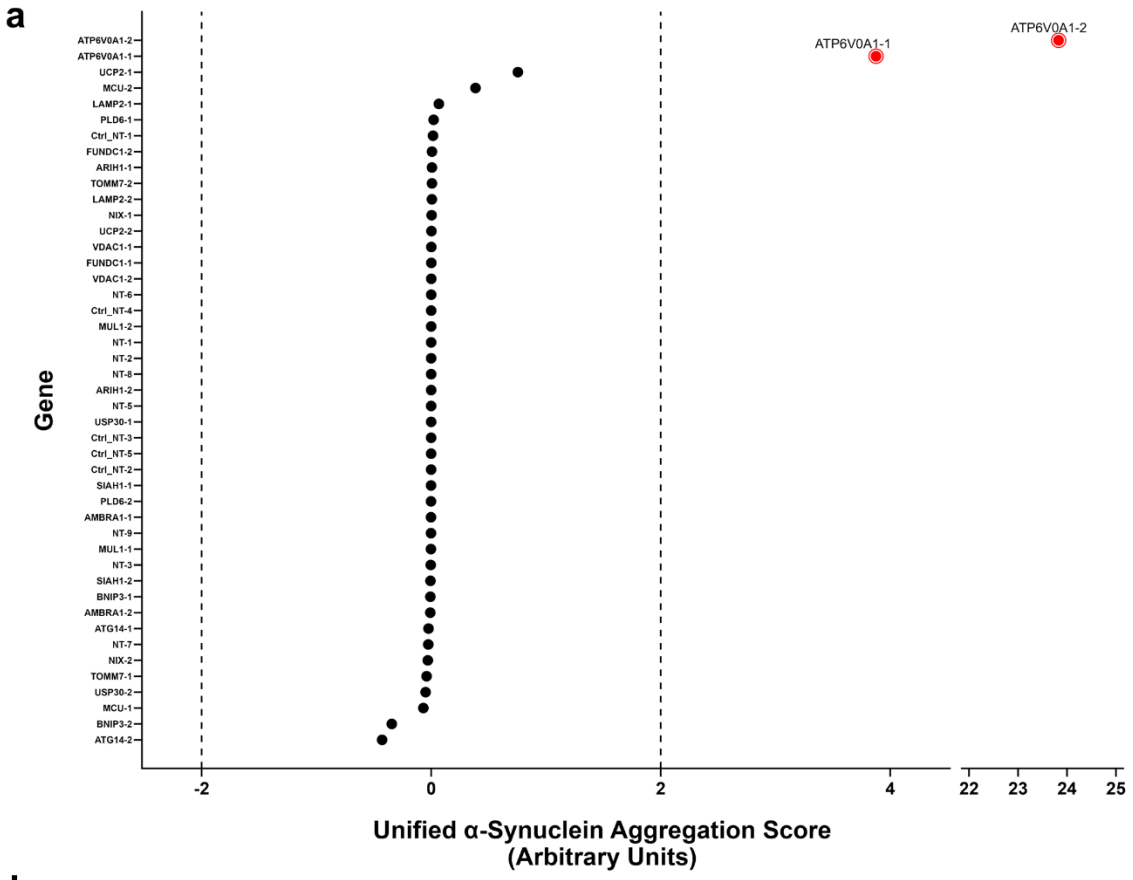
sgRNAs SPPL2B-2, NOD2-1, LRRK2-1 and LRRK2-2, MCCC1-1, RNF141-1, HLA-DRB5-1, DYRK1A-2 and RNF141-2 were identified as preliminary hits on the basis of their total pS65Ub spot area Z-score (3.73, 3.16, 3.07 and 2.32, 2.54, 2.45, 2.24 and 2.02 respectively) (Figure 39b). sgRNAs

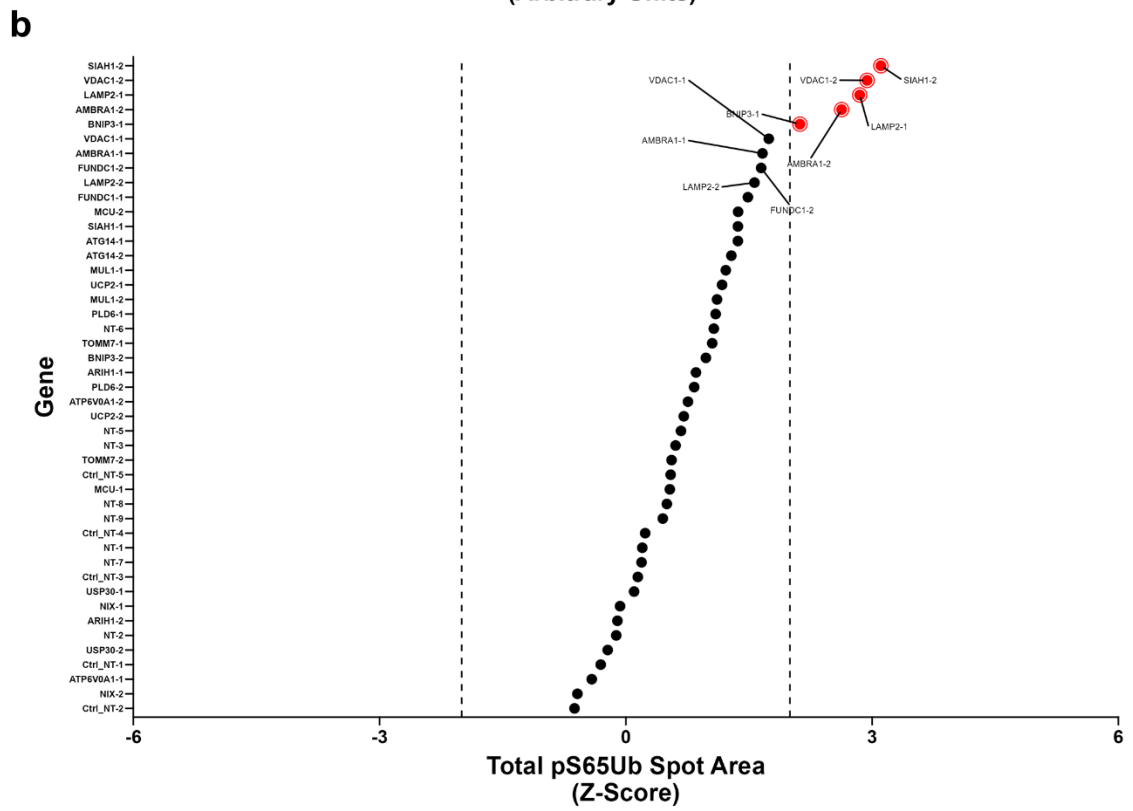
GPNMB-1 and KLHL14 achieved scores of 1.94 and 1.89 respectively and were not classified as preliminary hit genes. Only one sgRNA was found to downregulate pS65Ub. NOD2-2 achieved a Z-score of -2.32. Interestingly, comparing this readout to the total pS65Ub spot area co-localised with pS129 highlighted pS65Ub formation in different subcellular contexts – most sgRNAs identified did not show an increase in pS65Ub area co-localised with pS129, indicating that this may be independent of pS129 formation (Figure 39c). However, both RNF141-1 and SPPL2B-2 (Z-scores 5.10 and 2.01) were also identified to increase pS65Ub co-localised with pS129, suggesting that they increase pS65Ub spot area in a pS129-dependent manner.

sgRNAs targeting genes identified in a proteomics analysis of PFF-treated and untreated *SNCA*-triplication dopaminergic neuronal cultures were analysed in the same manner as PD GWAS genes, but none were found to modulate the levels of pS129 (Figure 40a). Intriguingly, several were found to increase the levels of pS65Ub, with sgRNAs NIM1-2, SIK1-1, HMGB1-1, DSTYK1-2, CACNA2D2 and LARP1 achieving Z-scores of 2.90, 2.45, 2.40, 2.25, 2.01 and 2.01 (Figure 40b).

5.3.4 Cellular pathways underlying pS129 and pS65Ub regulation

To identify major cellular pathways underlying the regulation of pS129 and pS65Ub, sgRNAs targeting an array of genes related to mitochondria and mitophagy, the endolysosomal and autophagy pathways were screened for their effects on pS129 and pS65Ub levels. Both sgRNAs targeting the lysosomal ATPase subunit-encoding gene *ATP6V0A1*, a subunit of the lysosomal proton pump responsible for acidifying lysosomes, showed strong increases in pS129 aggregation (unified pS129 score = 3.88 and 23.82 for ATP6V0A1-1 and ATP6V0A1-2, respectively) (Figure 41a), in line with the results of increased α-synuclein aggregation with co-treatment of PFFs and the lysosomal alkalising agent CQ. As expected, several mitochondrial-targeted sgRNAs upregulated pS65Ub levels, but the sgRNA with the strongest effect targeted *SIAH1* (Z-score 3.10) (Figure 41b). Furthermore, VDAC1-2, LAMP2-1, AMBRA1-2 and BNIP3-1 achieved scores of 2.93, 2.84, 2.62, and 2.12 respectively. VDAC1-1, AMBRA1-1, FUNDC1-2, and LAMP2-2 also trended towards increasing pS65Ub area (Z-scores 1.74,


a
Gene
ATP6V0A1-2
ATP6V0A1-1
UCP2-1
MCU-2
LAMP2-1
PLD6-1
Ctrl_NT-1
FUNDC1-2
ARIH1-1
TOMM7-2
LAMP2-2
NIX-1
UCP2-2
VDAC1-1
FUNDC1-1
VDAC1-2
NT-6
Ctrl_NT-4
MUL1-2
NT-1
NT-2
NT-8
ARIH1-2
NT-5
USP30-1
Ctrl_NT-3
Ctrl_NT-5
Ctrl_NT-2
SIAH1-1
PLD6-2
AMBRA1-1
NT-9
MUL1-1
NT-3
SIAH1-2
BNIP3-1
AMBRA1-2
ATG14-1
NT-7
NIX-2
TOMM7-1
USP30-2
MCU-1
BNIP3-2
ATG14-2
ATP6V0A1-2
ATP6V0A1-1
-2
0
2
4
22
23
24
25
Unified α-Synuclein Aggregation Score
(Arbitrary Units)


b
Gene
SIAH1-2
VDAC1-2
LAMP2-1
AMBRA1-2
BNIP3-1
VDAC1-1
AMBRA1-1
FUNDC1-2
LAMP2-2
FUNDC1-1
MCU-2
SIAH1-1
ATG14-1
ATG14-2
MUL1-1
UCP2-1
MUL1-2
PLD6-1
NT-6
TOMM7-1
BNIP3-2
ARIH1-1
PLD6-2
ATP6V0A1-2
UCP2-2
NT-5
NT-3
TOMM7-2
Ctrl_NT-5
MCU-1
NT-8
NT-9
Ctrl_NT-4
NT-1
NT-7
Ctrl_NT-3
USP30-1
NIX-1
ARIH1-2
NT-2
USP30-2
Ctrl_NT-1
ATP6V0A1-1
NIX-2
Ctrl_NT-2
VDAC1-1
VDAC1-2
SIAH1-2
BNIP3-1
LAMP2-1
AMBRA1-1
AMBRA1-2
LAMP2-2
FUNDC1-2
-6
-3
0
3
6
Total pS65Ub Spot Area
(Z-Score)

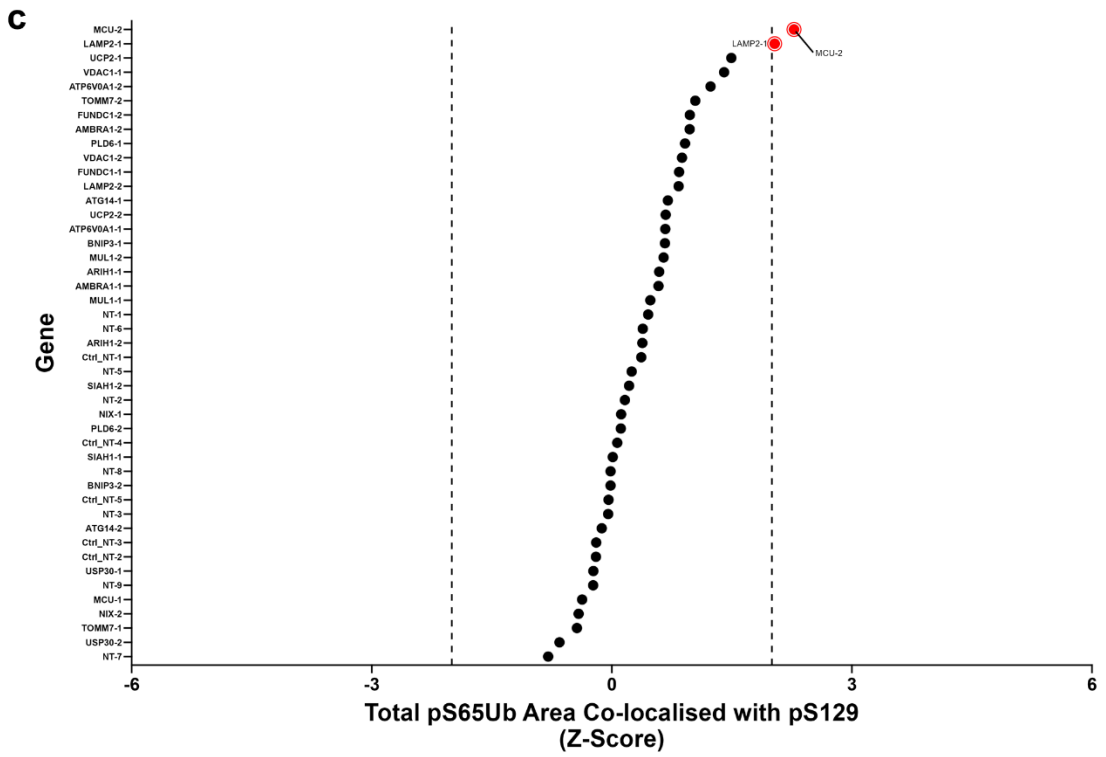


Figure 41. Identification of cellular pathways and processes underlying pS129 and pS65Ub accumulation. a) sgRNAs targeting genes relating to mitochondrial function, mitophagy, the endolysosomal and autophagy pathways were screened alongside PD GWAS candidate risk gene-targeting sgRNAs in i^3 neurons. Quantification of the unified pS129 aggregation score highlighted the lysosomal proton V-ATPase as a strong modulator of PFF-induced pS129 aggregation. b) Quantification of the pS65Ub total spot area z-score identified lysosomal and mitochondrial-targeted sgRNAs as modulators of pS65Ub accumulation. c) Quantification of the total pS65Ub spot area co-localised with pS129 z-score revealed only two sgRNAs which achieved the cutoff. Dashed lines identify the cutoff used to classify hit or non-hit genes, at score = ±2 and hit genes are labelled in red. N = 2 independent differentiations. Data is presented as the mean unified pS129 score or as the mean z-score.

1.66, 1.64 and 1.56). MCU-2 and LAMP2-1 (Z-score 2.28 and 2.03), on the other hand, were found to upregulate pS65Ub levels co-localised with pS129 (Figure 41). Altogether, these data implicate lysosomes in the regulation of pS129 levels and mitochondria, autophagosomes and lysosomes in the regulation of pS65Ub levels.

5.3.5 Correlation of pS129 and pS65Ub levels in screening data

Previous data discussed in this thesis demonstrated an accumulation of pS65Ub as a result of PFF treatment in i^3 neurons (see section 3.3.1). Consequently, commonalities between hit genes modulating the pathways were expected. Comparison of pS65Ub and pS129 readouts between sgRNA-mediated knockdown conditions allowed the identification of several groups: pS129 and pS65Ub up and

downregulators, pS129-specific up and downregulators and pS65Ub-specific up and downregulators (Figure 42a). There were few pS129 and pS65Ub regulators with only *SPPL2B* and *LAMP2* exerting an effect on levels of both proteins. pS129 modulators included *ATP6V0A1*, *MCU*, as well as, of course, *SNCA*, whereas pS65Ub modulators included *LRRK2*, *VDAC1*, *RNF141*, *LARP1*, *SIK1*, *NIM1*, *DYRK1A*, *RNF141*, *AMBRA1*, *DSTYK1*, *SIAH1*, and *MCCC1*. Guides to *HLA-DRB5* were found to both specifically upregulate pS65Ub or specifically downregulate pS129, possibly suggesting off-target effects.

Despite the scarcity of genes shown to regulate both pS129 and pS65Ub in the combined screening data, on a well-to-well basis, correlating the pS65Ub and pS129 total spot area data from all three screening replicates showed a weak correlation (R^2 = 0.19), suggesting indirect regulation of pS65Ub by pS129 (or possibly vice-versa) (Figure 42b). Furthermore, statistical testing using Spearman's rank correlation coefficient also demonstrated a weak but statistically significant correlation ($\rho = 0.331$, $p < 0.0001$) between these two variables, further confirming that pS129 and pS65Ub are co-regulated.

5.4 Validation screening in iPSC-derived dopaminergic neurons

iPSC-derived cortical neurons provide a model of cortical involvement in the late stages of PD and represent a population of neurons that shows neurodegeneration in advanced disease. To identify possible disease-relevant cell-type-specific differences in the genetic regulation of PFF-induced pS129 seeding and pS65Ub accumulation, control and *SNCA*-triplication human iPSC lines were differentiated to dopaminergic neurons. At DIV 35, 69.3 and 62.8% of cells from healthy control lines 156 and 856 (both expressing dCas9) were MAP2-positive, and 35.0 and 28.7% were tyrosine hydroxylase (TH)-positive (Figure 43a). TH-positive cells represented 50.1 and 44.4% of the MAP2-positive cells in culture.

The differentiation efficiency was markedly lower for the 831-1 and 831-3 *SNCA*-triplication lines, with 9.3 and 14.3% of cells showing MAP2 positivity and 2.1 and 7.0% showing TH-positivity (Figure 43b). Due to the low differentiation efficiency, the data from these lines is not shown in this thesis.

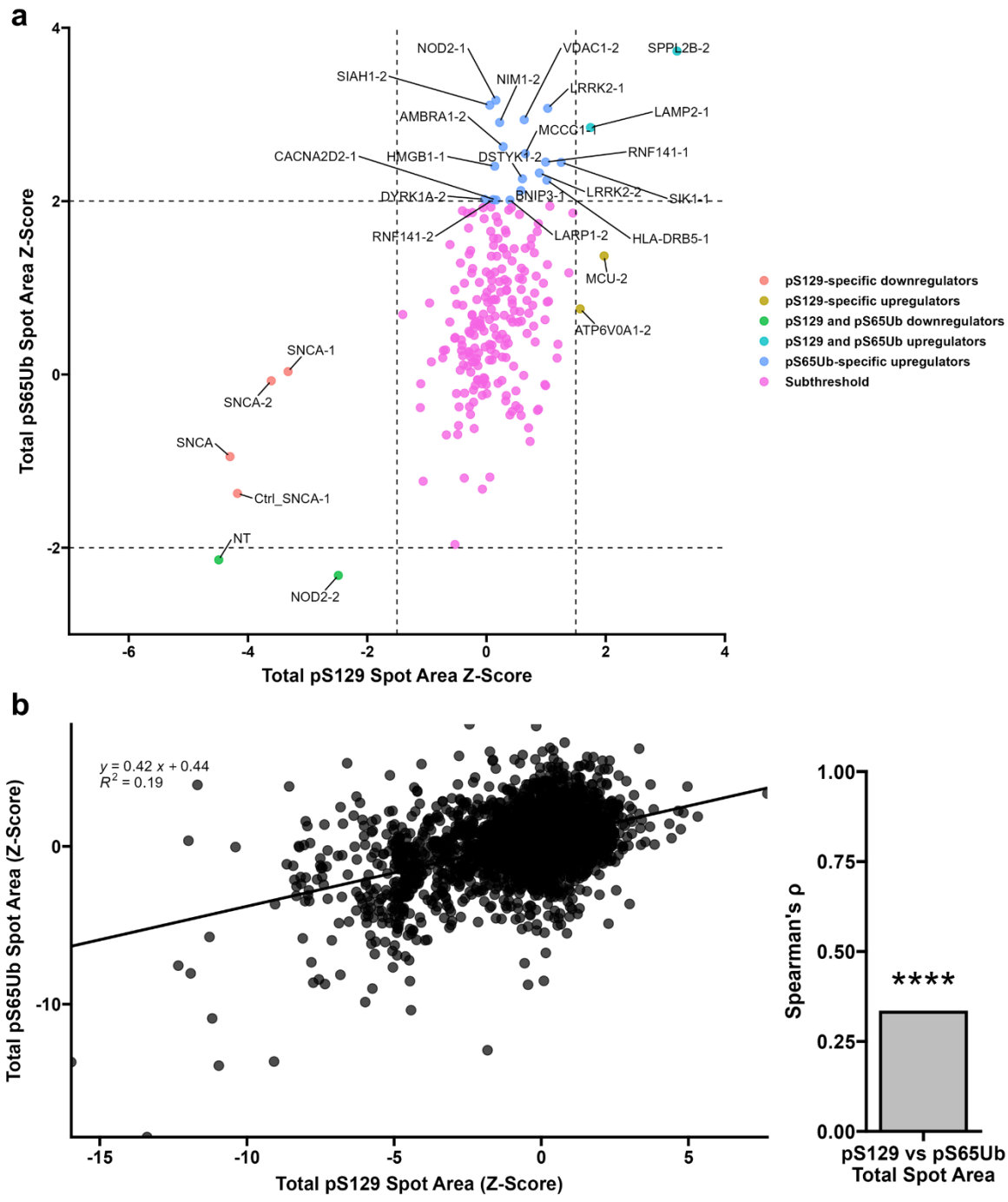


Figure 42. Regulation of pS129 and pS65Ub is largely independent.
a) Comparing the pS129 and pS65Ub total spot areas identifies up and downregulators of pS129, pS65Ub or both. *SNCA*, *ATP6V0A1*, and *MCU* are identified as specific modulators of pS129 levels, whereas several genes such as *LRRK2*, *LARP1*, *FYN*, *VDAC1*, *AMBRA*, *SIK1*, and *MCCC1* depletion was associated with pS65Ub upregulation. Knockdown of *SPPL2B* and *NOD2* are identified as up- and downregulating both pS129 and pS65Ub, respectively. Dashed lines identify cutoffs used to classify hit or non-hit genes, at Z-score score = ±1.5 for pS129 and Z-score = ±2 for pS65Ub. b) Combining the well-average data from all three screening replicates and comparing the total pS129 and pS65Ub area Z-scores on a well-by-well basis identifies a weak correlation between pS129 and pS65Ub. Quantification of correlation using Spearman's method achieves a highly significant correlation with $\rho = 0.331$. N = 3 independent differentiations. Data is presented as the mean z-score. Statistical test: Spearman's correlation test. * $p < 0.05$, ** $p < 0.01$, *** $p < 0.001$, **** $p < 0.0001$.

iPSC-derived dopaminergic neurons were transduced with lentiviral vectors on DIV16 and treated with α-synuclein PFFs on DIV35. The cells were subsequently fixed, stained and imaged 14 days post-PFFs. Treatment of dopaminergic neurons with CCCP resulted in a statistically significant increase in pS65Ub spot area in the first replicate of validation screening but had no effect in the second ($p = 0.0003$ and $p = 0.11$). The mean of both replicates combined is shown in Figure 44. Likewise, α-synuclein PFFs induced a statistically significant increase in pS129 levels compared to untreated cells in the second replicate of validation but not the first ($p = 0.087$ and $p = 0.00004$). *PINK1*-expressing cells did not show a reduction in pS65Ub for either replicate (Figure 44), but pS129 levels were decreased for *SNCA*-knockdown cells only in the second validation replicate ($p = 0.36$ and $p = 0.00003$).

Table 20. Top upregulating sgRNAs ranked by readout score in the validation screen

GWAS dataset				**Proteomics dataset**			
pS129		**pS65Ub**		**pS129**		**pS65Ub**	
sgRNA	Score	sgRNA	Z-score	sgRNA	Score	sgRNA	Z-score
VPS35-2	1.16	SPPL2B-1	0.61	Ctrl_NT-3	0.01	MKNK1-1	0.50
VPS35-1	1.02	SPPL2B-2	0.55	Ctrl_NT-5	0.00	Ctrl_NT-3	0.44
SPPL2B-2	0.07	STK39-1	0.51	SIK2-1	0.00	MKNK1-2	0.15
FAM49B-2	0.05	GPNMB-1	0.49	Ctrl_NT-4	0.00	Ctrl_NT-5	0.07
STK39-2	0.04	DYRK1A-1	0.48	Ctrl_NT-1	0.00	Ctrl_NT-4	0.02
FAM49B-1	0.03	HLA-DRB5-1	0.47				
SPPL2B-1	0.02	Ctrl_NT-3	0.44				
CRLS1-1	0.01	FAM49B-1	0.39				
Ctrl_NT-3	0.01	NOD2-2	0.33				
DYRK1A-1	0.01	PRKN-2	0.28				

Table 21. Top downregulating sgRNAs ranked by readout score in the validation screen

GWAS dataset				Proteomics dataset			
pS129		**pS65Ub**		**pS129**		**pS65Ub**	
SNCA-2	-0.48	PINK1-2	-0.75	SIK1-2	-0.13	SIK1-2	-0.38
SNCA-1	-0.44	PRKN-1	-0.67	SIK1-1	-0.03	Ctrl_NT-1	-0.34
STK39-1	-0.04	VPS35-2	-0.50	Ctrl_NT-2	0.00	SIK1-1	-0.31
GPNMB-2	-0.01	FYN-1	-0.40	SIK2-2	0.00	Ctrl_NT-2	-0.15
NDUFAF2-2	-0.01	SNCA-2	-0.39	MKNK1-2	0.00	SIK2-1	-0.07

The screening data showed a similarly muted effect size for sgRNAs expected to strongly disrupt pS129 or pS65Ub formation (Figure 45). Line 856 dCas9 showed very low levels of pS129-positive aggregate formation after PFF treatment and no effect of *SNCA* knockdown on any measured parameter of aggregation, and consequently was excluded from the study. For control line 156 dCas9, both sgRNAs towards *SNCA* showing a trend towards reducing pS129 levels using the unified α-synuclein aggregation score but only achieved scores of -0.44 and -0.48 (Figure 45a). There was also an upwards trend of both sgRNAs towards *VPS35* in increasing the levels of pS129 (score = 1.02 and 1.16). This contrasts with the data in cortical neurons, where sgRNAs towards VPS35 were not amongst the top-ranked sgRNAs. sgRNAs targeting *PINK1* and *PRKN* (PINK1-2 and PRKN-1) were the top ranked sgRNAs decreasing the area of pS65Ub (Z-scores = -0.75 and -0.67), with both sgRNAs against *SPPL2B* taking the top ranks for sgRNAs upregulating pS65Ub levels (Z-scores = 0.61 and 0.55) (Figure 45b). From the proteomics dataset, no sgRNA showed a convincing effect on the modulation of pS129 (Figure 45d), but an *MKNK1*-targeting guide was the best-ranked towards upregulating pS65Ub levels (Z-score = 0.50) (Figure 45d). Consequently, these data suggest there may be commonalities as well as cell-type-specific differences (specifically regarding pS129-modulation by VPS35) in regulation of pS129 induced by PFFs, but additional validation of these hits will be required.

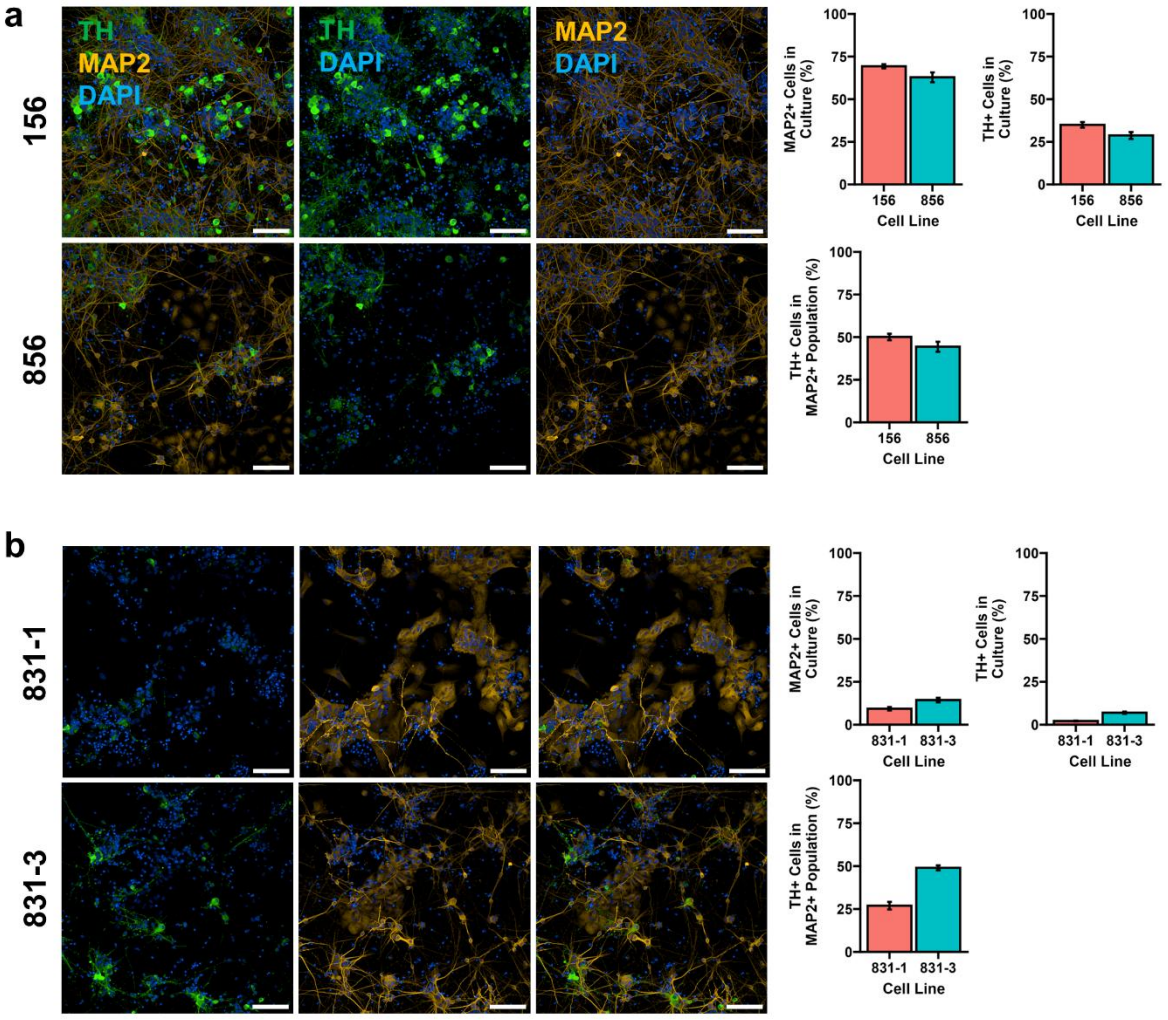


Figure 43. Differentiation efficiency of iPSC-derived dopaminergic neurons.
a) Healthy control dCas9-expressing iPSC lines 156 and 856 were differentiated to dopaminergic neurons using a small-molecule differentiation protocol, fixed and stained on DIV 35 for TH and MAP2. Quantification of the number of TH-positive and MAP2-positive cells in culture demonstrated both lines achieved a differentiation efficiency of above 60% for MAP2-positivity and ~30% for TH-positivity. b) *SNCA*-triplication dCas9-expressing lines 831-1 and 831-3 had much poorer differentiation efficiency, achieving only <15% MAP2-positive cells and only 2 and 7% TH-positivity. These lines were excluded from further analysis. Scale bar = 100 μm. N = 1 independent differentiations. Data is presented as the mean ± SEM. * $p < 0.05$, ** $p < 0.01$, *** $p < 0.001$, **** $p < 0.0001$.

5.5 Prioritisation of hit genes for mechanistic follow-up

Though the effect size for several of the validation screen replicates in both i^3 neurons and dopaminergic neurons was small, it is interesting to note that several sgRNAs and gene targets were ranked in the top 5 or 10 based on their pS129 unified score or total pS65Ub spot area Z-score. Small effect sizes were

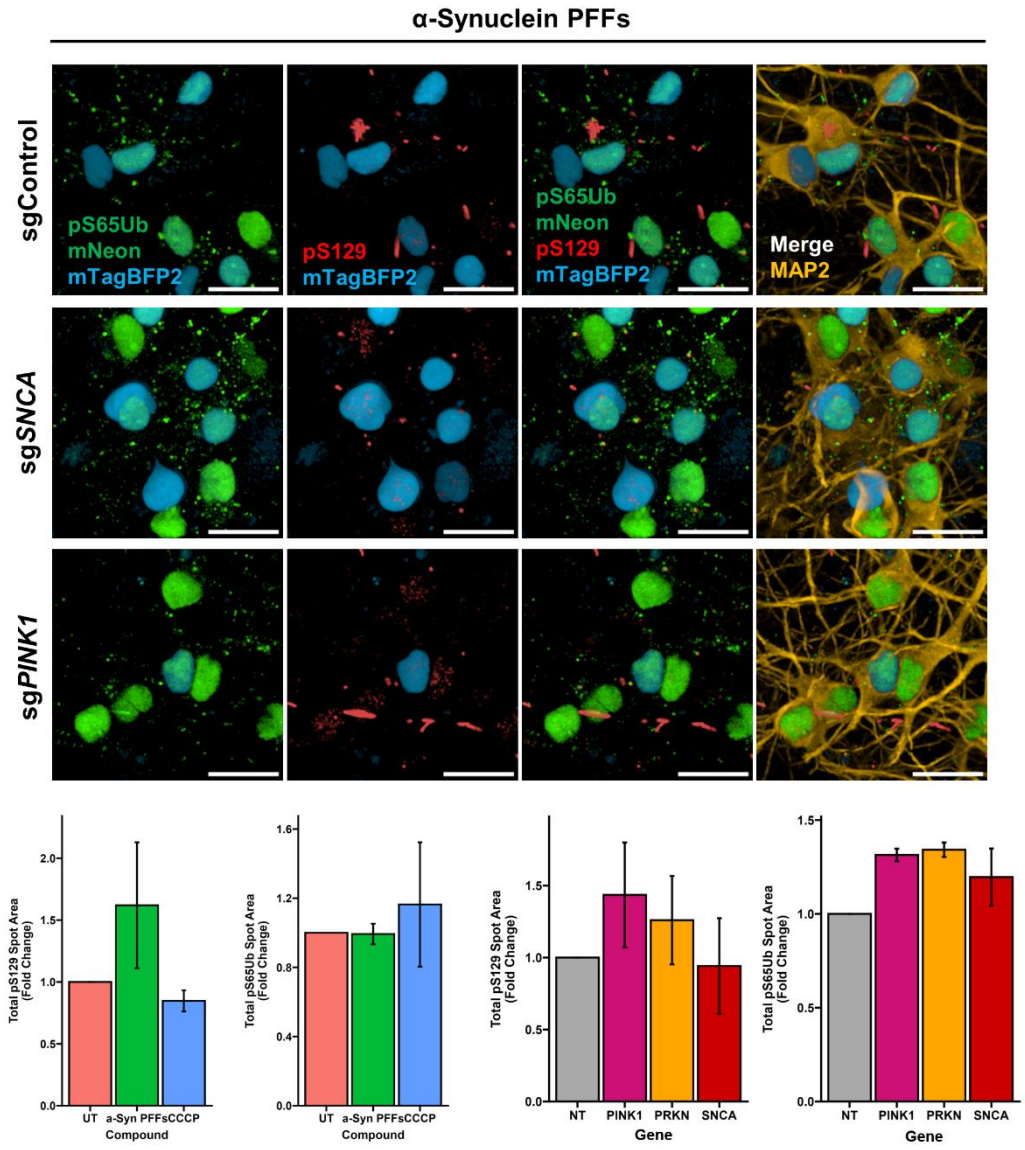
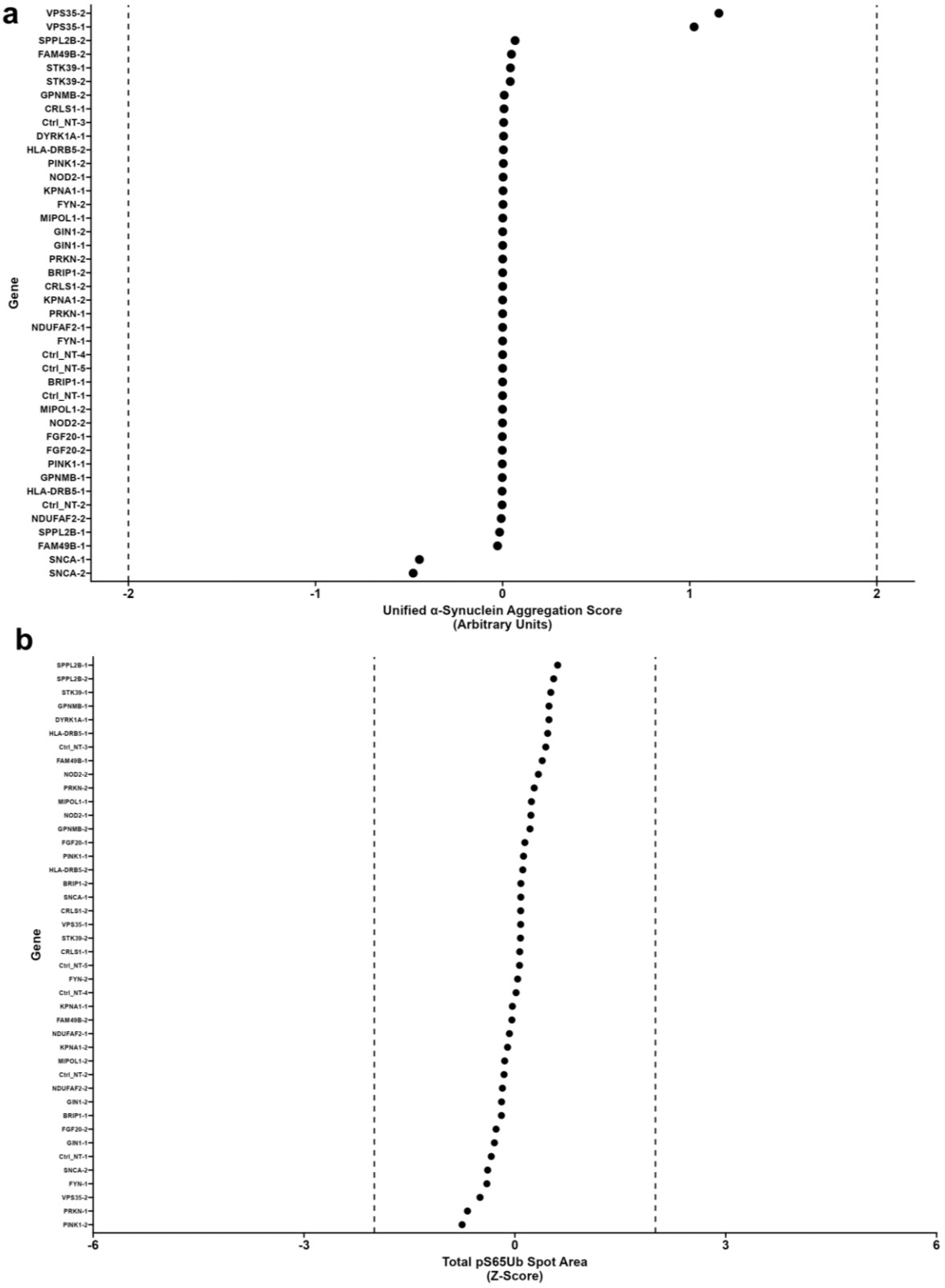


Figure 44. Quantification of internal assay controls in iPSC-derived dopaminergic validation screening.

Dopaminergic neurons were treated with α-synuclein on DIV 35, fixed and immunostained for pS129 and pS65Ub 14 days post-seeding. dCas9-expressing cells are marked by nuclear mNeon Green signal, and sgRNA-expressing cells are marked by nuclear mTagBFP2. Quantification reveals a trend towards increased levels of pS129 in PFF-treated conditions, as well as lower levels of pS129 in *SNCA* knockdown cells for one replicate of validation screening though not the other. N = 2 independent differentiations. Statistical test: Kruskal-Wallis test with Dunn's multiple comparisons. Data is presented as the mean ± SEM. * $p < 0.05$, ** $p < 0.01$, *** $p < 0.001$, **** $p < 0.0001$.

expected, considering that it is well established that risk variants provide a small increase in disease risk. Table 22 details the genes for which one or both sgRNAs were found amongst the top 5 or 10 ranked sgRNAs by readout score in both the primary screen and validation screen in dopaminergic neurons. This list prioritises genes for follow-up, such as those which are common to both pS129 and

pS65Ub-related readouts. For example, *FAM49B* and *CRLS1* knockdown was found to upregulate pS129 in both screens, but did not always achieve the threshold. Similarly, *SPPL2B* and *DYRK1A* were common upregulators of pS65Ub across both screens. *LRRK2* had a very strong effect in primary



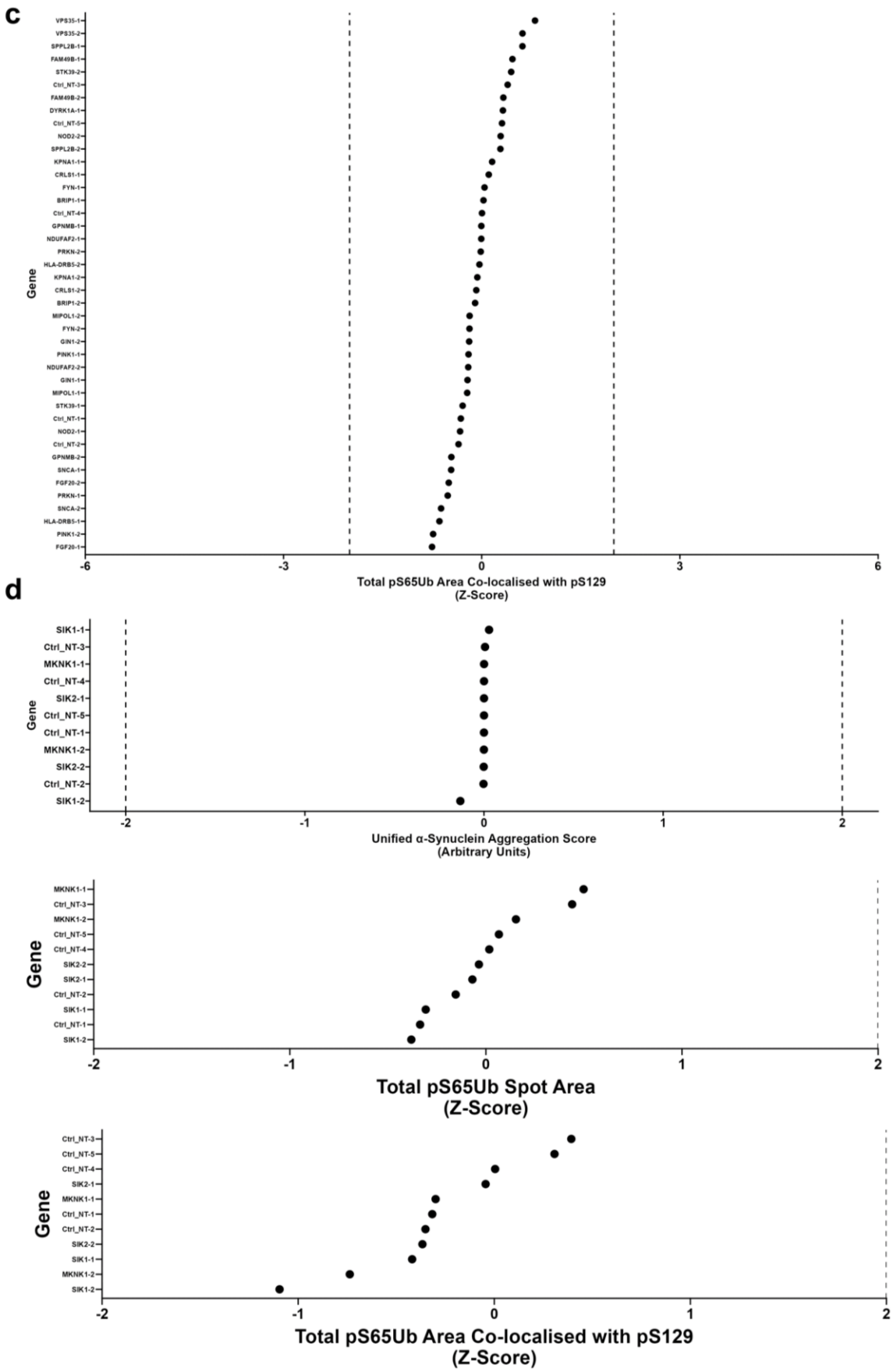


Figure 45. Validation screening in iPSC-derived dopaminergic neurons. a) The top-ranked hits from secondary screening in i^3 neurons were retained for screening in dopaminergic neurons. Though

the effect size for each sgRNA was very low, including both sgRNA targeting *SNCA*, the top-ranked genes included *VPS35, SPPL2B* and *FAM49B.* The *SNCA*-targeted sgRNAs both showed a trend towards reducing pS129, as measured by the unified α-synuclein aggregation score. b) sgRNAs targeting *PINK1* and *PRKN* were best-ranked for their effect in downregulating pS65Ub spot area, and both sgRNAs targeting *SPPL2B* were found to increase the levels of pS65Ub, though they did not achieve the cut-off at ±2. c) *VPS35*, *SPPL2B*, *FAM49B* and *STK39* were the top-ranked genes targeted by sgRNAs for pS129-associated pS65Ub area, though the effect sizes were very low. Conversely, *FGF20*, *PINK1* and *HLA-DRB5* showed the strongest downregulatory effects. d) Due to throughput for the validation in dopaminergic neurons, a limited number of genes were assessed from the proteomics dataset in this experiment. No genes were found to modulate the levels of pS129 and MKNK1 was the best-ranked gene modulating the levels of pS65Ub. N = 1-2 independent differentiations. Dashed lines identify the cutoff used to classify hit or non-hit genes, at score = ±2 and hit genes are labelled in red. Data is presented as the mean unified pS129 score or as the mean z-score.

screening and was mistakenly omitted from dopaminergic neuron screening, but will be prioritised for further follow-up as its role in pS65Ub is supported by previous study (Williamson *et al.*, 2023). Most of the prioritised genes were found to form a main interaction cluster (Figure 46).

Though some may prove to be spurious, further analysis using 96-well format, which has provided increased sensitivity over 384-well format in previous experiments, will be necessary to confirm the effect of these genes on the readouts assessed in this study. Likewise, 96-well studies should identify the top 2 genes to pursue for further mechanistic study.

Table 22. Genes targeted by the top-ranked up or downregulating sgRNAs in both primary and validation screening

pS129 ↑	pS129 ↓	pS65Ub ↑	pS65Ub ↓
FAM49B	SNCA	SPPL2B	SIK1
CRLS1		DYRK1A	
SPPL2B		NOD2	
VPS35		HLA-DRB5	
		GPNMB	

5.5.1 Future directions

A crucial aspect to interpretation of the prioritised hit genes will be the evaluation of gene knockdown by qPCR for each sgRNA. This experiment could not be completed as planned prior to the submission

of this thesis but will inform the interpretation of the results of the screens. The next step will be the confirmation of the results in 384-well high-throughput experiments in a 96-well format. To follow up on the genes prioritised for their effect on pS129, thorough characterisation of all steps of the PFF-seeding process will be required. qPCR for the levels of the *SNCA* gene will determine if α-synuclein PFFs might be resulting in increased pS129 through higher concentration and availability of monomer for seeding. Treatment of sgRNA-expressing cells with fluorescently-labelled PFFs and timelapse imaging of their uptake into cells will allow to determine uptake levels and kinetics. DQ-BSA and LysopH assays will be required to verify if defective proteolytic degradation may contribute to the pS129 phenotype. For genes prioritised for their effect on pS65Ub levels, a similar process will involve determining if sgRNA-expressing cells may reduce mitochondrial membrane potential, induce PRKN relocalisation to mitochondria or increase pS65Ub at baseline, in the presence of PFFs and in the presence of CCCP. Similarly, examination of the co-localisation of mitochondria with LC3b and LAMP1 will allow to determine if clearance of damaged mitochondria is defective.

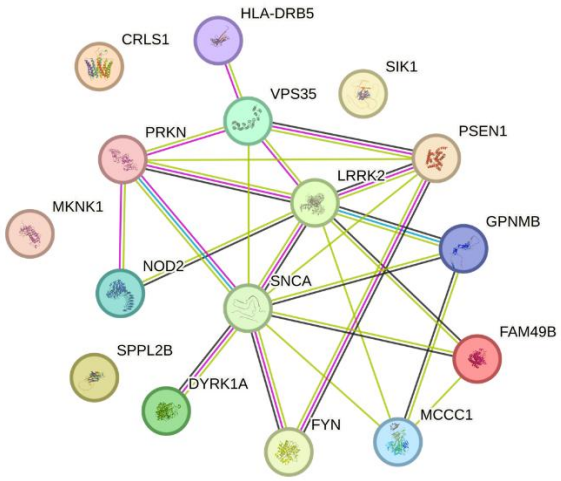


Figure 46. Interaction network of prioritised genes for mechanistic follow-up.
Comparison of best-ranked genes using STRING DB (Szklarczyk *et al.*, 2025) for the regulation of pS129 and pS65Ub across 2 screens or more yielded a shortlist of genes for mechanistic follow-up. Interaction analysis reveals a main cluster of interconnected genes, and several genes which do not directly interact with any others, such as *CRLS1*, *MKNK1*, *SIK1*, and *SPPL2B*.

5.6 Discussion

In this chapter, a CRISPRi library of 181 vectors to 75 PD-related genes and 13 genes identified by proteomics was cloned and packaged into lentiviral vectors. These genes are components of several cellular processes such as regulation of mitochondrial fission and architecture, neuronal death, metabolism, synapse function and autophagy. Measurement of pS65Ub levels in *PINK1* and *PRKN* knockdown conditions revealed functional knockdown of proteins using CRISPRi over the course of maturation. Preliminary screening enabled testing of the screening workflow, liquid handling robotics and analysis pipelines. Puromycin selection did not increase the sensitivity of the screen and increased the variance of pS129-related readouts. Preliminary screens also identified spatial systemic effects that required experimental and computational correction. Primary screening of all library genes identified several candidates, which were retained for secondary screening in iPSC-derived dopaminergic neurons. Following screening, sgRNAs modulating pS129, pS65Ub or both were ranked and prioritised for mechanistic follow-up, including *FAM49B*, *CRLS1*, *SPPL2B*, *LRRK2*, *DYRK1A*, *VPS35*, *NOD2*, *GPNMB*, *HLA-DRB5*, and *SIK1*.

5.6.1 Targeted arrayed screening provides a rich and complex dataset

This study was first designed as a genome-wide screen using flow cytometry to identify sgRNAs which regulate the levels of pS129 and pS65Ub post-seeding. This approach would have been advantageous for its ability to identify strong modulators of pS129 in an unbiased, hypothesis-free and systematic manner. Yet, this approach would have been less specific and relevant to PD, and would not have identified perturbations causing low effects, making it unsuitable for the study of candidate risk genes identified by GWAS. Due to the difficulty of optimising a flow cytometry-based staining technique in iPSC-derived neurons, an arrayed approach was instead devised, based on well-characterised immunocytochemistry assays. With a Z' value of 0.16, pS129-positive aggregation by immunostaining was a rational candidate for hypothesis-driven, systematic analysis of the function of PD risk genes.

Arrayed screening also had the advantage of enabling the observation and quantification of the entire genetically-perturbed population, as opposed to flow cytometry-enabled genome-wide screening which,

due to screen design, relies on sequencing the top and bottom quantiles of the pooled population and identification of over-represented sgRNAs. In the case of the pS129 assay, this is highly advantageous as the process of α-synuclein is highly stochastic, with a proportion of cells not responding, a proportion responding moderately and a proportion responding strongly to the PFF insult. Single-cell output of the well data identified a large spread of the population for each sgRNA, consequently, flow cytometry based only on high or low-intensity cells may have lacked sufficient information. The dimensionality reduction and representation of the single-cell data that can be extracted from the arrayed screen is an area of current investigation.

Unlike flow cytometry-based genome-wide screens, which rely on single, simple readouts such as the intensity of pS129 or pS65Ub fluorescence, arrayed screens allow for multiple, complex readouts. From the current dataset, readouts based on the number, size, and intensity of pS129 aggregates, as well as spatial information such as their location within the cell (somatic or neuritic) and their morphology (round vs elongated) were all extracted for future analysis. Having information-rich microscopy images and multi-parametric readouts allows the data gathered in this study to be mined in future to answer complementary biological questions. As it stands, this dataset has already provided the necessary data for analysis of pS65Ub levels in different subcellular compartments.

5.6.2 Screening design

The plate layouts for screening were designed to account for systemic spatial variation, enable computational correction of spatial effects, and allow for plate-to-plate normalisation of the data. Consequently, each screening plate had assigned internal assay controls, to provide positive and negative controls for the pS129 and pS65Ub assays, and five non-targeting controls distributed throughout the plates for normalisation. Seven technical replicates per guide were chosen to provide enough sensitivity to identify sgRNA candidates. Power calculations using preliminary screening data to determine the sample size necessary for a statistical power of 0.8 with 180 groups (ANOVA, $\alpha = 0.05$) were attempted but predicted a statistical power of 1.0 for all values of sample size, perhaps due to a low number of groups (six) in the preliminary screen design (data not shown).

In preliminary screens, *SNCA* knockdown cells showed strong downregulation of pS129, whereas pS65Ub levels showed systemic variation that required changes to staining technique – notably, the randomised distribution of antibody solution to source plates for liquid handling to reduce bias in staining intensity.

Composite readouts for pS129 were calculated in a bid to increase the sensitivity to sgRNAs of moderate effect size. As pS129 readouts are highly positively correlated, by using a multiplicative model, the effects of small changes are compounded whilst sgRNAs of very low or inconsistent effect size are reduced. However, this approach has several caveats. Whilst useful in reducing the dimensionality of the data and prioritising genes based on their cumulative effects on multiple readouts, composite readouts do not capture which readouts are producing most of the effect size, and the multiplicative model is inadequate for screen readouts where one or two parameters may be conferring a large effect, and other parameters are near zero. In this study, readouts related to pS65Ub were different to each other and were not correlated. Utilising several individual readouts to prioritise genes or exploring an additive model for composite readout calculation may be more advantageous.

The use of lines stably expressing sgRNAs targeted to *SNCA*, *PINK1*, and *PRKN* was motivated by the need to reduce the large amount of these control lentiviruses that would be required to provide internal controls on each plate, enabling the use of fewer resources per screen. In preliminary screening, primary screening and validation screening, these lines functioned as intended to provide proof of the effect of α-synuclein PFFs and of *SNCA* knockdown on the formation of pS129-positive aggregates. However, the effect of sg*PINK1*-expressing cells and CCCP and FCCP on the levels of pS65Ub were more variable, despite both the *PINK1* knockdown line and both these drugs having been tested on i^3 neurons prior to application in screening. There are several possibilities that will require further investigation. First, it is possible that the FCCP and CCCP used in these experiments may have degraded, despite having been aliquoted and stored at -80°C under optimal conditions. CCCP is light sensitive as well as prone to degradation after freeze-thawing (Nag *et al*, 2023), indicating low stability. It is possible that over time and temperature fluctuations that the compounds used in this study had become ineffective. However, fresh FCCP was made for the second replicate of primary screening and showed no effect on

the sgControl-expressing cells in this screen. Furthermore, the *PINK1* knockdown line did not show the previously validated and expected decrease in pS65Ub levels for both primary and validation screening.

Plating of the same stable-expression sgControl, sg*PRKN* and sg*PINK1*-expressing lines as was used for the first and second replicates of validation screening in a 96-well format for a final replicate of the experiment in Figure 35 revealed a strong response to FCCP in the sgControl line, and a strongly reduced response in *PINK1* and *PRKN* knockdown cells using a different antibody (Cell Signalling, Cat #62802), suggesting that neither the line nor the drug explains the behaviour of the screening controls. Though the same batch number of the direct-conjugate pS65Ub antibody (Millipore, Cat#ABS1513-I-AF488) was used for both the preliminary screening and subsequent screens, new vials of the antibody were ordered to accommodate the large antibody use requirements of the primary screens. It is possible that small differences in antibody storage or shipment may have reduced the affinity of the antibody for pS65Ub, which compounded with high background, resulted in reduced sensitivity.

5.6.3 Prioritised genes reflect mostly mitochondrial and lysosomal biology

Though the considerations discussed above caution the interpretation of the pS65Ub data, it should also be noted that the primary screen identified *LRRK2* as a modulator of pS65Ub, which has been previously published to be a modulator of mitophagy by several laboratories, including ours. *LRRK2 G2019S* and *LRRK2 R1441C* mutations, which potentially increase the kinase activity of the protein, have been shown to impair basal and induced mitophagy in mouse and human cell models (Hsieh *et al.*, 2016; Bonello *et al*, 2019; Wauters *et al*, 2020; Singh *et al*, 2021; Williamson *et al.*, 2023). Several publications have linked this phenotype to the kinase activity of LRRK2, either through inhibition of mitochondrial fission (Bonello *et al.*, 2019), through impaired degradation of MIRO1 (Hsieh *et al.*, 2016; Hsieh *et al*, 2019) (or without direct evidence of kinase involvement (Williamson *et al.*, 2023)), through reduced optineurin recruitment due to RAB10 phosphorylation (Wauters *et al.*, 2020). As α-synuclein aggregation has also been linked to defective MIRO1 degradation (Shaltouki *et al.*, 2018), examining the links between pS129 formation, LRRK2 activity and pS65Ub accumulation will be of interest for the field.

Similarly, a panel of mechanistic sgRNAs showed *VDAC1*, *LAMP2*, and *AMBRA1* knockdown increases the levels of pS65Ub. This has mechanistic basis as AMBRA1 has been shown to modulate mitophagy through binding LC3b at the outer mitochondrial membrane and driving PRKN-dependent and independent mitophagy, with *AMBRA1*-deficient embryos showing increased numbers of damaged mitochondria (Strappazzon *et al*, 2015). VDAC1 may also be involved in mitophagy, with *VDAC1* silencing in HeLa cells slightly delaying the recruitment of PRKN to mitochondria after depolarisation but also reducing mitochondrial clearance after depolarisation (Geisler *et al.*, 2010a). The role of LAMP2 in mitophagy is less clearly defined, with controversy regarding its role in the PINK1/PRKN-dependent pathway. A study in HeLa cells showed no effect of LAMP2 knockdown on the clearance of mitochondria following oligomycin/antimycin or CCCP-induced mitophagy (Liu *et al*, 2020), though a study in iPSC-derived cardiomyocytes from *LAMP2*-mutant patients and in *Lamp2* knockout mice noted impaired clearance of mitochondria and the accumulation of damaged mitochondria (Hashem *et al*, 2017); a cell-type specific effect of LAMP2 cannot be ruled out. It is possible that LAMP2 may have a role in mitophagy by regulating autophagosome-to-lysosome fusion (Chi *et al*, 2019), or alternatively, LAMP2 deficiency may lead to impaired trafficking of lysosomal enzymes (Eskelinen *et al*, 2002).

Identification of *SNCA* in all three screens as the main gene downregulating pS129 levels strengthens the validity of the assay. Interestingly, there were no sgRNAs identified to consistently and robustly downregulate pS129 – other genes prioritised for mechanistic follow-up on the basis of their effect on pS129 upregulated levels of this protein. *FAM49B* is a protein that may localise to mitochondria and regulate mitochondrial fission and metabolism (Chattaragada *et al*, 2018), though it has also been implicated in actin polymerisation through RAC1 signalling (Yuki *et al*, 2019), and in immunity via RAB10 and TLR4 (Li *et al*, 2021). To our knowledge, this is the first study linking FAM49B to the formation of pS129-positive aggregates, but it is possible that its role in downregulating macropinocytosis and phagocytosis (Yuki *et al.*, 2019) may regulate α-synuclein PFF uptake. *CRLS1* encodes a mitochondrial enzyme which catalyses the conversion of phosphatidyl glycerol to cardiolipin. Bi-allelic *CRLS1* deficiency in humans has been linked to a multisystem degenerative disease with primary fibroblasts demonstrating fragmented mitochondrial networks and altered mitochondrial

architecture, as well as ER and mitochondrial stress (Lee *et al*, 2022). Cardiolipin has also been implicated in the aggregation of α-synuclein, by interacting with monomers and accelerating the rate of fibrillisation at mitochondrial membranes (Choi *et al.*, 2022) or by acting as a chaperone to remove monomers from fibrils and re-fold them (Ryan *et al.*, 2018). In this thesis, *CRLS1* knockdown increased pS129 levels, suggesting that increased levels of cardiolipin may reduce pS129-positive aggregation.

SPPL2B knockdown was found to upregulate both pS129 and pS65Ub. This is intriguing considering this protein is an aspartyl protease which cleaves intramembrane-regions of proteins, generating an intracellular domain fragment. SPPL2b cleaves type II transmembrane proteins (reviewed in Badman *et al*, 2025). SPPL2b is localised to the plasma membrane and late endosomes/lysosomes and is highly expressed in the brain, where it is thought to act on immune signalling and synaptic function through cleavage of substrates such as TNFα, VAMP1-4 and TMEM106B (Badman *et al.*, 2025). It is possible that SPPL2b's role in increasing pS65Ub and pS129 may be the result of its role in intramembrane cleavage of proteins, suggesting action on a common signalling pathway. Alternatively, SPPL2b has been shown to modulate the levels of amyloid-β (Maccioni *et al*, 2024) and amyloid-β increases the rate of α-synuclein aggregation (Köppen *et al*, 2020; Röntgen *et al*, 2025). Further characterisation of the mechanism of SPPL2b may provide further insight into the mechanistic convergence of Alzheimer's and Parkinson's disease.

The increased effect of *VPS35* knockdown on pS129-positive aggregation in dopaminergic neurons compared to cortical neurons was an interesting discovery and suggests that there may be commonalities as well as differences in the effect size of predisposing genes in different neuronal cell types. VPS35 is an integral part of the retromer complex, which serves to recycle target receptors, transporters, enzymes and other cargo back to the trans-Golgi network or the plasma membrane, enabling them to escape lysosomal degradation (reviewed in Rowlands & Moore, 2024). As VPS35 is involved in the sorting and recycling of many cargo proteins, it is possible that *VPS35* silencing may increase α-synuclein aggregation through alterations in autophagy, such as ATG9A mislocalisation, and/or alterations in lysosomal proteolysis and chaperone-mediated autophagy due to impaired sorting of cathepsin D or LAMP2a (Rowlands & Moore, 2024). As α-synuclein has been shown to be degraded by chaperone-

mediated autophagy (Cuervo *et al.*, 2004), this could explain the increase in α-synuclein following silencing of *VPS35*. However, the mechanism by which the effect of reduced VPS35 should be higher in dopaminergic neurons compared to cortical neurons is unclear.

5.6.4 A PD-centred approach to α-synuclein biology

To our knowledge, this is the first high-throughput study to leverage the identification of PD risk loci and uncover modulators of α-synuclein aggregation in human neurons. An approach very similar to the one used in this study, using RNAi, was successfully applied to screening prioritised GWAS candidates for their effect on oligomycin/antimycin-induced pS65Ub formation, identifying KAT8 and KANSL1 as regulators of stress-induced mitophagy (Soutar *et al*, 2022). This study highlighted the potential of these types of high-throughput experiments in identifying the function of genes, with modulation of *KANSL1* rather than *MAPT* showing a biological effect in this paradigm despite overlapping GWAS signals. Previous studies have either studied the function of single GWAS-identified risk genes (Dumitriu *et al.*, 2011; Jinn *et al.*, 2017; Diaz-Ortiz *et al.*, 2022; Larbalestier *et al.*, 2022; Jones-Tabah *et al.*, 2024), or targeted a larger and/or less specific library of genes, such as the druggable genome (Rousseaux *et al*, 2018), lysosomal storage disorder genes (Yu *et al*, 2023) or a curated library of genes associated with mitochondrial biology, cellular trafficking and cytoskeleton (Neupane *et al*, 2025). Other studies utilised compound libraries to screen for small-molecule modifiers of α-synuclein levels or aggregation *in vitro* or in cell models (Pujols *et al*, 2017; Staats *et al*, 2020; Svanbergsson *et al*, 2021; Casalino *et al*, 2022).

Screening for modulators of α-synuclein aggregation in HEK cells identified inhibitors of p38 MAPK and PKC which conferred their effect through increasing the number of lysosomes by blocking their permeabilisation by fibrils (Svanbergsson *et al.*, 2021). Recent screens using α-synuclein PFFs to trigger α-synuclein pathology have identified modulators of PFF uptake such as heparan sulphate proteoglycan genes as well as v-ATPase subunits which acidify phagosomes and *VPS35* (Vanderperre *et al*, 2024), in addition to mitochondrial gene *OXR1* and endoplasmic reticulum gene *EMC4* (Neupane *et al.*, 2025). These screens highlight diverging as well as converging mechanisms to screens that assess the levels of α-synuclein monomer or aggregation by overexpression. For example, a genome-wide

screen using the levels of endogenous, fluorescently-linked SNCA as a readout identified the NatB complex as a regulator of α-synuclein stability (Santhosh Kumar *et al.*, 2024). Genome-wide screening in LUHMES cells identified a retromer complex subunit, SNX5, as protective against the toxicity of α-synuclein overexpression (Höllerhage *et al*, 2025), whereas a genome-wide screen using bi-molecular complementation to monitor α-synuclein oligomerisation identified three RAB proteins and five phosphotransferases (Gonçalves *et al*, 2016).

These different biological paradigms have identified modulators of differing aspects of α-synuclein biology. This is useful in understanding underlying pathways that may be important in the regulation of α-synuclein levels and aggregation, but it is intriguing that many of these studies have not identified more PD-related genes. The exception is the study by Yu and colleagues in Drosophila which identified many lysosomal storage disorder genes that affect α-synuclein pathology – a more targeted library, enriched in genes that have been linked to PD by GWAS. Our approach using a PD-centred library may thus be advantageous in identifying disease-relevant biology that may, for one reason or another, be more subtle than the modulators that are identified at larger scale, using less specific libraries. Until the full network of risk genes, their functions and their interactions are known (and whether they converge on genes identified in the screens conducted to date), we may learn more about PD from smaller-scale screening of relevant libraries than from genome-wide-scale experiments.

6 Discussion

I have shown that aggregates of α-synuclein were seeded in human iPSC-derived cortical neurons by addition of *in vitro*-aggregated α-synuclein PFFs. Optimisation of fibril generation and treatment paradigms in cultured cells enabled robust and reproducible seeding. pS129-positive PFF-seeded aggregates in human iPSC-derived neurons showed co-localisation and correlation with the mitophagy marker pS65Ub, with pS129, pS65Ub-positive aggregates increasing in size and intensity over time. Furthermore, pS65Ub co-localisation was associated with increased size of pS129-positive aggregates.

Moreover, treatment of cortical neurons with α-synuclein PFFs impacted the function of mitochondria by reducing ATP production in the absence of mitochondrial membrane potential dissipation or increased ROS generation. The proteolytic activity of lysosomes was unchanged. A library of 181 vectors targeting 71 candidate risk genes at 90 risk loci identified novel and previously-published modulators of pS129-positive aggregate formation and pS129-induced pS65Ub accumulation. Validation of screening hits in cortical neurons and dopaminergic neurons highlighted cell-type specific differences in genetic modulation of both markers.

6.1 pS129-positive aggregate formation is linked with PINK1-dependent mitophagy in PFF-treated conditions

The data presented here suggest but do not prove that formation of pS129-positive aggregates alters the process of PINK1-dependent mitophagy prior to the degradation of pS65Ub-tagged mitochondria at the lysosome, either by inducing mitophagy through mitochondrial damage or disrupting naturally-occurring mitophagy. Measurement of mitochondrial membrane potential using the potentiometric dye JC-10 showed no dissipation of mitochondrial membrane potential, despite there being a significant decrease in ATP production. This argues against the possibility of PINK1/PRKN-activating

mitochondrial damage mediated by seeded α-synuclein aggregation. However, it is also possible that bulk measurement of mitochondrial membrane potential using the JC-10 dye lacks the sensitivity to detect subtle alterations of the potential in the mitochondrial network or disruption of the potential of a subset of mitochondria within the population. This could mask mitochondrial damage induced by α-synuclein aggregation which may trigger excess PINK1/PRKN-dependent mitophagy. Moreover, these assays were performed at 14 days post-seeding, at a timepoint after the initial nucleation of α-synuclein aggregates and prior to loss of neurons. Measurement of membrane potential earlier or later timepoints may reveal the damaging effects of α-synuclein entry and nucleation, as well as the point where α-synuclein aggregation overwhelms the cell's capacity to buffer the damage.

Furthermore, measurement of total lysosomal proteolytic activity showed no change, suggesting that a potential lack of clearance of pS65Ub-tagged mitochondria is not due to a general reduction in lysosomal protease activity. This does not preclude that deficiency of specific enzymes, such as glucocerebrosidase (GCase, the product of PD gene *GBA*) or cathepsin B (CTSB, the product of PD gene *CTSB*), may exist. Indeed, several studies have established circumstantial and direct evidence of an interaction between α-synuclein and GCase or CTSB in disease conditions.

Lysosomal GCase deficiency has been found in substantia nigra samples from sporadic and *GBA* mutation-carrying PD patients (Gegg *et al*, 2012). There is evidence that α-synuclein may interact directly with GCase (Yap *et al*, 2011) or with glucosylceramide (Mazzulli *et al*, 2011) at acidic pH, with overexpression of α-synuclein resulting in a deficiency in GCase activity and protein levels (Gegg *et al.*, 2012). α-Synuclein and GCase interaction may establish a negative feedback loop that increases α-synuclein levels and aggregation at further expense to GCase activity (Mazzulli *et al.*, 2011; Mazzulli *et al*, 2016b). Furthermore, the cysteine protease CTSB has been implicated in α-synuclein monomer and fibril degradation – altering the aggregation rate of α-synuclein – as well as in modulation of GCase activity (McGlinchey & Lee, 2015; Tsujimura *et al*, 2015; Jones-Tabah *et al.*, 2024), providing an alternative mechanism by which α-synuclein aggregation could lead to impaired degradation of mitochondria targeted for mitophagy. Reduced GCase activity has been associated with impaired clearance of mitophagosomes and increased mitochondrial dysfunction (Li *et al*, 2019a). Altogether,

these data provide evidence towards the possibility that α-synuclein may modulate specific lysosomal enzymes rather than result in a general reduction in lysosomal degradative capacity.

To further elucidate the mechanism of pS65Ub accumulation, several considerations need to be addressed. The most fundamental is establishing certainty over the causal link between pS65Ub accumulation and pS129-positive aggregation. To address this, evaluating the sequence of appearance of pS129 and pS65Ub by immunocytochemistry over the course of early aggregation (from days 0 to 7 following PFF addition) will be essential in determining the sequence of events. Likewise, staining for total α-synuclein, pS129, TOM20 and pS65Ub will determine whether α-synuclein aggregation could be seeded at mitochondrial membranes, as has been recently suggested (Choi *et al.*, 2022). The presence of pS65Ub-positive or TOM20-positive, α-synuclein-positive puncta would be evidence towards mitochondrial membranes being an early site of α-synuclein aggregation, prior to pS65Ub and pS129 formation. Performing aggregation experiments in the presence and absence of subthreshold concentrations of the mitochondrial toxin CCCP or an autophagy inhibitor, such as SAR405 or 3-methyladenine, may also provide insights into the underlying mechanism. However, we should be mindful that interventions increasing the aggregation of α-synuclein will make it difficult to untangle the link between the two markers, so pharmaceutical interventions should occur after the PFFs have been internalised by cells and escaped to the cytoplasm.

6.2 Functional characterisation of candidate risk genes at PD risk loci to enable aetiological stratification of patients

One of the main aims of this study was the identification of PD candidate risk genes which regulate the process of pathological α-synuclein aggregation or the PINK1/PRKN-dependent turnover of mitochondria. α-Synuclein aggregation and mitochondrial dysfunction are pillars of PD pathology that have been extensively studied, with multiple lines of evidence – from post-mortem human brain samples to animal and cell culture models – implicating them in the process of neurodegeneration. In this study, these two aspects of disease pathology formed the basis for screening PD-associated risk

genes, providing disease-relevant insight. One of the major contributions of this study to the field is the identification of several candidate risk genes (*FAM49B*, *CRLS1*, *SPPL2B*, and *VPS35*) which alter the rate of α-synuclein aggregation in both cortical and dopaminergic human neurons. The data presented here also provide further evidence towards the involvement of LRRK2 in regulating mitophagy, linking two important aspects of PD pathophysiology. This study enabled the creation of a rich and multi-parametric dataset that may be mined for other types of information – for example, neuronal morphology and aggregate location. Future studies will confirm and extend the findings presented here, confirming the role of these genes in the processes of pS129-positive aggregate formation and pS65Ub accumulation as well as providing insight into the underlying mechanisms.

This project was designed to address a key question which underlies fundamental advancement in the understanding of Parkinson disease(s). The function and contribution of PD candidate risk genes in disease pathogenesis is currently a major area of research, with past studies having typically selected a single candidate for in depth analysis (Jinn *et al.*, 2017; Diaz-Ortiz *et al.*, 2022; Jones-Tabah *et al.*, 2024), or performed high-throughput screens without a specific focus on PD candidate risk genes (Neupane *et al.*, 2025). One of the strengths of this study was the combination of high-content biology with a PD-centric gene library, highlighting pathogenic pathways which are likely of high importance in PD pathogenesis. Whilst the aggregation of α-synuclein and mitochondrial toxin-induced pS65Ub have individually been extensively studied, the combination of α-synuclein aggregation and pS65Ub in the context of genetic perturbation of GWAS loci is novel.

Understanding the convergence or divergence of these risk genes on cell processes and pathways such as α-synuclein aggregation or mitochondrial dysfunction – and how this relates to disease onset, symptoms, and progression – is likely to enable progress in identifying disease-modifying therapies. Polygenic risk scores have already been associated with clinical outcomes such as the progression of motor symptoms, the age-at-onset as well as non-motor symptoms (Paul *et al*, 2018; Iwaki *et al*, 2019). Disease-modifying therapies based on genetic risk profiles are currently in clinical trials for GCase or LRRK2-targeted therapeutics. LRRK2 inhibitors are being tested for patients carrying mutations that enhance the kinase activity of the protein (reviewed in Ding & Ren, 2020). Several classes of

compounds are in clinical trials for treatment of PD with *GBA* mutations, such as small molecule chaperones or GCase activators, which may need to be tailored to individual mutations (reviewed in Smith & Schapira, 2022). Targeting a selected and biologically-defined population in this manner with therapeutics informed by biological pathogenesis may increase the number of successful outcomes at clinical trials (Pagano *et al*, 2024).

Using CRISPRi to identify genes modulating PD-associated phenotypes resulted in the identification, in this study, of 10 genes which alter α-synuclein aggregation and/or mitophagy upon downregulation of their expression. *FAM49B, CRLS1, SPPL2B, LRRK2, DYRK1A, VPS35, NOD2, GPNMB, HLA-DRB5*, and *SIK1* show associations with mitochondria, metabolism, the endo-lysosomal system, and immunity. Silencing of *SPPL2B, FAM49B* and *VPS35* increased the rate of α-synuclein aggregation, suggesting that their physiological function may decrease disease risk, as α-synuclein aggregation has been linked with dysfunction and neurodegeneration in several (Desplats *et al*, 2009; Volpicelli-Daley *et al*, 2011; Abdelmotilib *et al*, 2017; Berard *et al*, 2022), though interestingly, not all (Tanaka *et al*, 2004; reviewed in Jellinger *et al*, 2009; Hatton *et al*, 2020; Chu *et al*, 2024) studies. Downregulation of genes which altered pS65Ub levels without altering pS129-positive aggregation formation, such as *LRRK2*, may instead be protective. Indeed, mitophagy enhancement has been proposed as a therapeutic strategy in PD (Fang *et al*, 2023). Further studies, preferably in an *in vivo* model, will be necessary to confirm the effect of modulating these genes on the course of the disease.

With growing appreciation for the heterogeneity of genetic and aetiological factors contributing to development of PD, this increased interest in precision medicine is driving research that enables patient stratification based on biology. By establishing the involvement of PD candidate risk genes in α-synuclein aggregation or PFF-induced pS65Ub accumulation, we hope that the data presented in this study will contribute towards the biological definition of disease aetiology and subtyping. Indeed, it has been posited that PD may not be a single disease, but rather a collection of related entities with distinct biological underpinnings and that this heterogeneity may be confounding clinical trials (Farrow *et al.*, 2022a). Furthermore, two frameworks have been proposed to overhaul the diagnosis and classification of PD patients, based on biological biomarkers rather than clinical signs and symptoms. Both utilise the

presence of pathological α-synuclein in patient cerebrospinal fluid or tissues, as determined by seed amplification assay, and neurodegeneration, as determined by clinical imaging, to provide a diagnosis of PD (Höglinger *et al*, 2024; Simuni *et al*, 2024). However, only one framework, the SynNeurGe framework, also takes genetic risk from fully penetrant or moderately penetrant loci into account and patients with risk variants that do not confer strong predisposition are not currently classified (Höglinger *et al.*, 2024). As research enables better understanding of genetic risk and its impact on PD development and progression, this may allow further refinement of these frameworks for disease-mechanism-based subclassification.

There are also several caveats to the study's design as well as considerations in regards to interpretation of this data in the context of clinical application. Identification of risk gene function and integration of this information into polygenic risk scores may be informative for pinpointing major pathways of disease pathogenesis in patient subgroups and allowing therapeutic targeting of these pathways but is unlikely to be useful for predicting the progression of individuals to PD. Indeed, they provide information at a population level (Koch *et al*, 2021) and make for poor screening tools with low detection rates and high false-positive rates (Wald & Old, 2019). This is due to individual SNPs generally having low effect sizes, though some, such as those linked to *SNCA*, may have increased odds ratios compared to other loci. Furthermore, additional studies will be required to validate and expand upon the data presented here prior to clinical application.

Moreover, it is possible that an unknown proportion of the candidate risk genes selected for screening in this study may not be the genes causing the risk signal at these loci. Identification of the true causative genes at risk loci is a complex task. Risk variants may regulate several genes in cis and trans (Farrow *et al*, 2022b), precluding the identification of single genes at all loci. Risk variants may also alter gene splicing rather than function or expression (Li *et al*, 2016; Tan *et al*, 2021). SNPs associated with risk signals identified by GWAS are often in linkage disequilibrium with several other variants, further confounding candidate gene identification. Correlation of risk loci with eQTLs (Grenn *et al.*, 2020), fine-mapping, integration with epigenetic marker datasets or transcriptomics in health and disease (Li *et al.*, 2019c), and case-by-case study of gene function may all be necessary to confirm a candidate

gene's effect on PD risk. Several different techniques have been applied to this issue to date. In a recent study, transcriptomic and epigenetic data was used to identify *GPNMB*, *RAB29*, and *TMEM163* as candidate risk genes at their respective loci, whereas the genes *ZRANB3*, *PCGF3*, *NEK1*, *NUPL2*, *GALC* and *CTSB* were significantly associated with splicing variants (Kia *et al*, 2021). Another study performed a transcriptome-wide association study (TWAS), highlighting several genes previously studied in the context of PD, such as *SNCA*, *LRRK2*, *CTSB*, *CRHR1*, *DYRK1A*, *TMEM163*, *KANSL1*, *GPNMB*, *CTSB* and *TMEM175* (Li *et al*, 2023). Several other genes such as *MMRN1*, *DND1P1*, *PLEKHM1*, amongst others, were also prioritised. Further functional validation of TWAS-prioritised genes in a *Drosophila* PD model found that 58.8% of the 80 genes screened in this model showed modulation of motor phenotypes, suggesting that this analysis identified variants that may be relevant to PD pathology (Li *et al*, 2023). It is likely that through the integration of multiple data types and analyses, increased confidence in candidate risk gene identification could be achieved.

The uncertainty surrounding the identity of disease-causing genes at GWAS-identified loci is a fundamental challenge to the aforementioned identification of disease-causing mechanisms and patient stratification. Erroneous prioritisation of candidate risk genes may confound pathway analysis, highlighting pathways that do not strongly influence disease initiation or progression, or alternatively failing to identify important disease-modulating pathways. GWAS provide an incomplete picture of the genetic variation contributing to disease by focussing on common genetic variation, as well as being generally conducted with a few of many models of analysis (e.g. autosomal additive, or recessive) (reviewed in Tam *et al*, 2019). Finally, PD is highly influenced by environmental conditions, as discussed in section 1.1, which may act on pathways that drive disease in absence of a genetic predisposition, though it should be noted that several pesticides and chemicals associated with PD, such as rotenone, paraquat or trichloroethylene, have been linked to mitochondrial and endolysosomal defects (Dorsey *et al*, 2025), two pathways that have been implicated in genetic forms of PD. The involvement of many of the genes prioritised in this thesis with mitochondrial and endo-lysosomal pathways reflects two of the major cellular processes that have been implicated both in monogenic PD as well as in candidate risk genes identified from GWAS loci (Billingsley *et al*, 2019; Bandres-Ciga *et*

al, 2020; Dehestani *et al*, 2022; reviewed in Bhore *et al*, 2024; Doostparast Torshizi *et al*, 2024), though other pathways such as protein misfolding, synaptic transmission, immune response and post-translational modification, amongst others, have also been implication (Bandres-Ciga *et al*, 2020).

The exclusive use of CRISPRi to screen candidate risk genes is another limitation of the study, as it is well established that risk loci may up or downregulate gene expression, function or alter gene splicing. For example, the risk-associated SNP rs1293298 in *CTSB* has a protective allele (A) which has been associated with upregulated *CTSB* expression in brain tissues (Blauwendraat *et al*, 2020), and another variant has been associated with alternative splicing (Kia *et al*, 2021). On the other hand, several SNPs associated with the *SNCA* gene increase risk for PD (Mohammadi *et al*, 2025), likely through increased gene expression (Cronin *et al*, 2009). Gene expression enrichment analysis has also identified that several of these genes, despite being enriched in brain tissues (Nalls *et al*, 2019), may be enriched in glia (Kia *et al*, 2021). Consequently, the finding in this study that the majority of the candidate genes evaluated do not alter α-synuclein aggregation or mitophagy in cortical neurons does not preclude that some of these genes may alter these phenotypes upon upregulation of function or expression, in a different cell type, or may have other effects, such as splicing. As such, a natural extension of this study is to conduct this screen with CRISPRa to provide a complementary dataset. Similarly, this study does not address the combinatorial and interactive nature of risk genes. Disease genes have been found to interact with each other in networks converging on pathological pathways (Barabási *et al*, 2011). An individual's combination of risk is expected to be different than would be predicted by the addition or multiplication of the effects of individual risk genes, which may be particularly relevant in the context of polygenic risk scores. However, genetic interaction screens are difficult to perform with large numbers of genes, as combinatorial testing exponentially scales. Consequently, the study of genetic interactions is outside of the scope of this study.

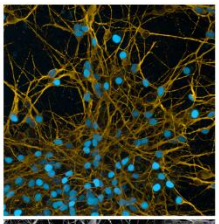
Despite these limitations, this study establishes a modular platform for the study of GWAS-identified candidate risk genes, where screening can be extended to include confirmed risk genes as well as new candidates identified through the study of more diverse populations. Indeed, as risk loci are to some extent ancestry specific (Satake *et al.*, 2009; Simón-Sánchez *et al*, 2009; Foo *et al.*, 2020), it will be

crucial to perform large-scale GWAS to identify and functionally validate additional risk loci that may inform personalised medicine for all ancestries.

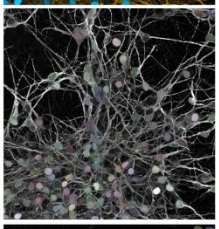
6.3 Conclusions

In summary, this study identified a correlation between the aggregation of α-synuclein and the levels of mitophagy marker pS65Ub in human neurons. The potency of α-synuclein PFFs was influenced by the monomeric α-synuclein source and preparation method, as well as unknown factors. PFF-induced aggregation was associated with functional changes at mitochondria in the absence of detectable membrane potential dissipation or ROS generation whereas lysosomal degradative capacity was unaffected in conditions of PFF-seeded aggregation. Screening of candidate genes at PD-associated risk loci identified *FAM49B*, *CRLS1*, *SPPL2B* and *VPS35* as potential modulators of α-synuclein aggregation and *LRRK2* as a modulator of pS65Ub levels. Future studies will be focussed on uncovering the mechanisms underlying the interaction of pS129 and pS65Ub as well as how hit genes identified in screening contribute to regulation of both markers. The data in this study is expected to contribute to the field's understanding of the function of PD candidate risk genes and the mechanisms and pathways underpinning disease aetiology, which we hope will enable better patient stratification and reduced confounding heterogeneity in clinical trials.

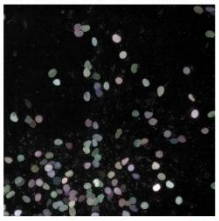
Appendix



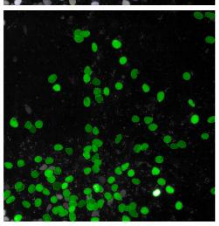
1. Maximal projection of image z-stacks



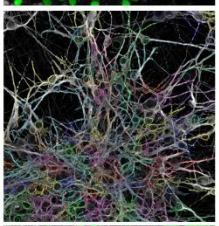
2. Segmentation of nuclei based on mTagBFP2 nuclear intensity



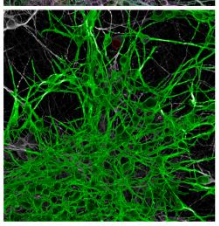
3. Measurement of nuclear intensity, morphology and texture properties



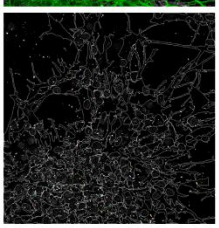
4. Selection of live nuclei based on intensity, morphology and texture properties



5. Segmentation of cytoplasm based on MAP2-stained region



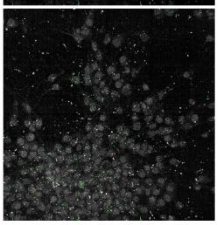
6. Selection of MAP2-positive cells based on MAP2 intensity



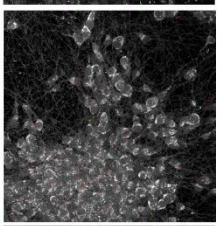
7. Segmentation of pS129-positive spots



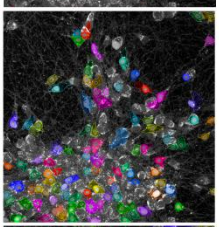
8. Calculation of pS129 intensity and morphology properties



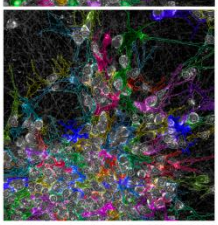
9. Selection of circular pS129 spots on the basis of morphology properties (roundness)



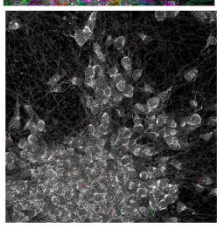
10. Selection of elongated pS129 spots on the basis of morphology properties (roundness)



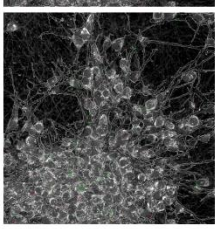
11. Defining the neuronal somatic region by expanding the perinuclear ring region.



12. Defining the neuritic region by excluding the somatic region from the cytoplasm ROI



13. Selection of pS129 spots within the somatic region and calculating their morphological properties



14. Selection of pS129 spots within the neuritic region and calculating their morphological properties

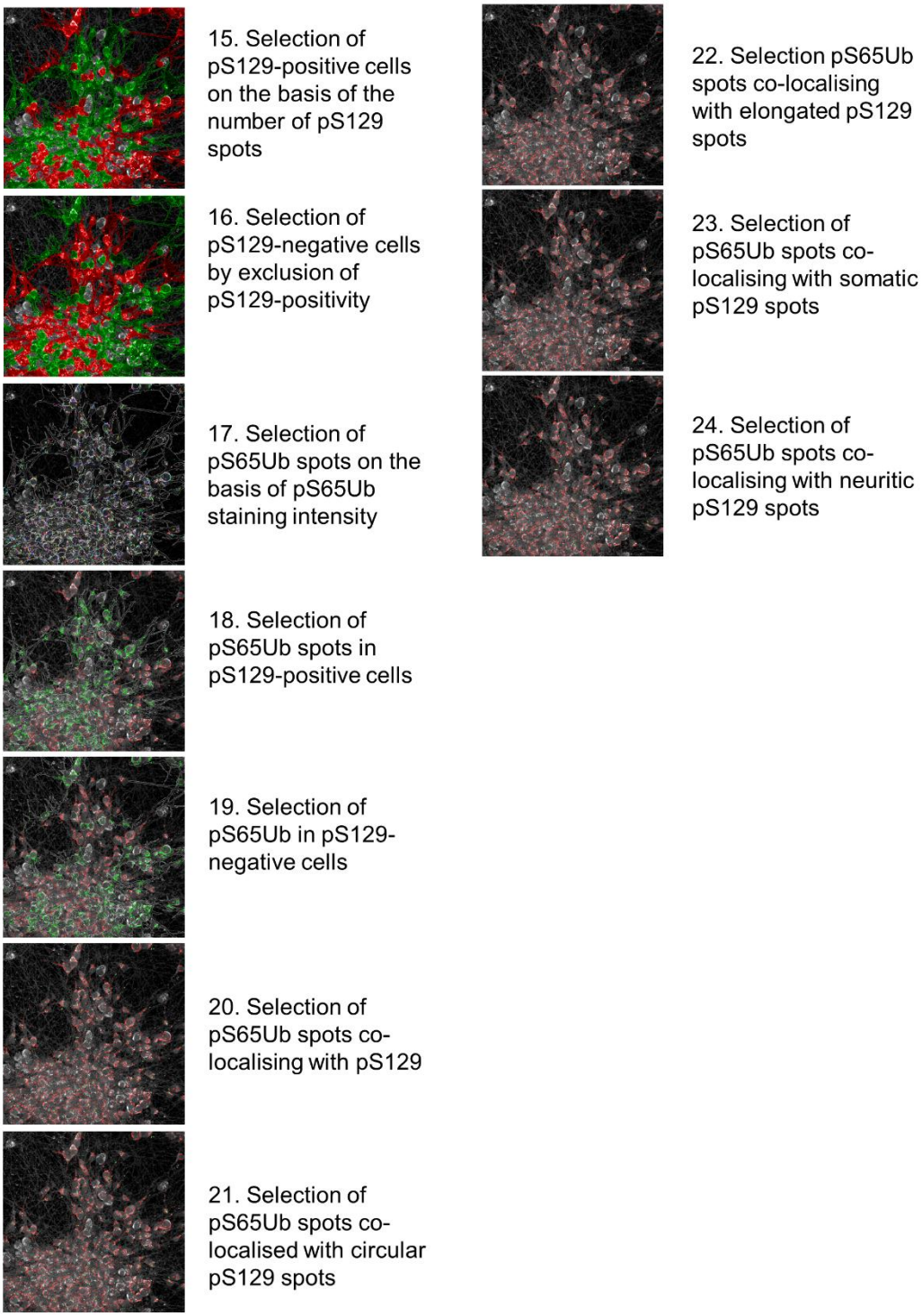


Figure 47. Automated analysis pipeline in Harmony for the analysis of arrayed CRISPRi screens measuring pS129 and pS65Ub.
Steps for the segmentation and selection of MAP2-positive neurons, followed by the identification of pS129-positive aggregates in the soma and neurites. pS65Ub spots were identified in all cells, pS129-positive or pS129-negative cells. pS65Ub spots were also co-localised with round, elongated or all pS129 spots. The readouts used in this study are detailed in section 5.3.1. Images were taken on the 40x water immersion objective of the Opera Phenix confocal microscope.

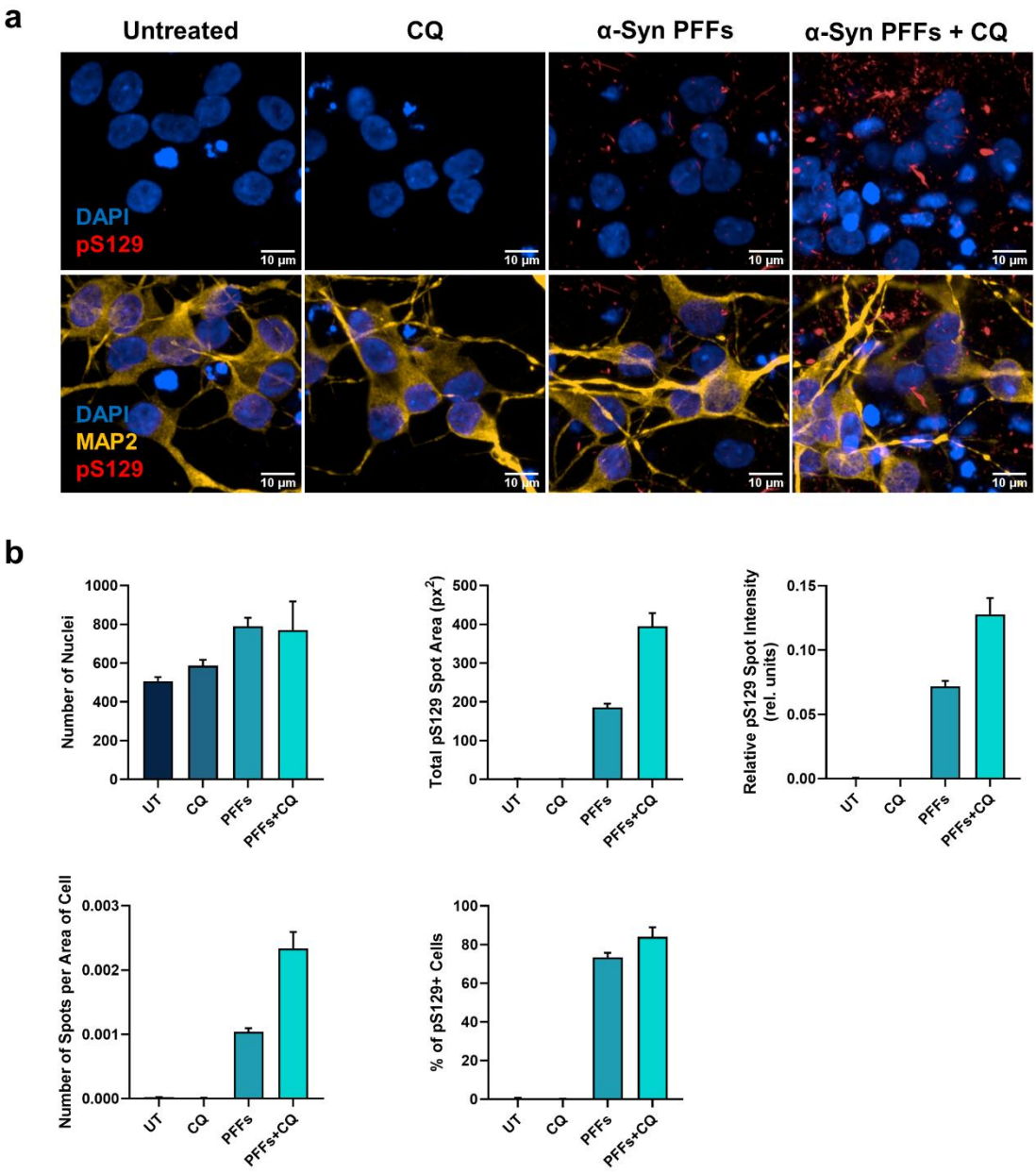


Figure 48. Lysosomal alkalinising agent chloroquine (CQ) potentiates pS129-positive aggregation. a) Confocal microscopy images of i^3 neurons treated on DIV 10 with 10 µg/ml α-synuclein PFFs or co-treated with 20 µM CQ and 10 µg/ml α-synuclein PFFs. Plates were fixed on DIV 24 and immunostained for aggregated α-synuclein marker pS129. Scale bar = 10 µm. 63x water immersion objective on the Opera Phenix confocal microscope. b) Quantification revealed increased levels of pS129-positive aggregation with co-treatment of PFFs and CQ compared to PFFs only. N = 1 independent differentiations. Data is presented as the mean ± SEM.

Table 23. Details of CRISPRi sgRNAs used in this study

sgRNA	Category	Gene	Kampmann Reference Number	In Silico Score	Sequence	Code	Origin
FCGR2A-1	GWAS	FCGR2A	FCGR2A_+_161475317.23-P1P2	0.799	GGCAGCAGCAAAACTGTCAA	A 1A	This study
FCGR2A-2	GWAS		FCGR2A_+_161475683.23-P1P2	0.786	GATGCTGGGGAGGTGAGCTT	A 1B	This study
VAMP4-1	GWAS	VAMP4	VAMP4_+_171711193.23-P1P2	0.970	GCGATCGGCTCGATGAGCGG	A 1C	This study
VAMP4-2	GWAS		VAMP4_+_171711196.23-P1P2	0.891	GCGCCGATCGGCTCGATGAG	A 1D	This study
NUCKS1-1	GWAS	NUCKS1	NUCKS1_-_205718968.23-P1P2	0.878	GGTGCGCGCGGGCCCCGAAA	A 1E	This study
NUCKS1-2	GWAS		NUCKS1_-_205719091.23-P1P2	0.767	GGACTCCGCACTGACCTGAC	A 1F	This study
RAB7L1-1	GWAS	RAB7L1	RAB7L1_+_205744193.23-P1P2	0.954	GGCCCAGACAGGCGGTGGGT	A 1G	This study
RAB7L1-2	GWAS		RAB7L1_-_205744188.23-P1P2	0.917	GCCCTCTTCAAACTGAAGTG	A 1H	This study
SIPA1L2-1	GWAS	SIPA1L2	SIPA1L2_-_232650285.23-P1P2	0.785	GCTGTCTCTCCCCATCAGGA	A 2A	This study
SIPA1L2-2	GWAS		SIPA1L2_+_232650129.23-P1P2	0.769	GAGGAGAGCCGACTGGAGAG	A 2B	This study
KCNS3-1	GWAS	KCNS3	KCNS3_+_18060165.23-P1P2	0.959	GCCTGGACCACAGGAGACTG	A 2C	This study
KCNS3-2	GWAS		KCNS3_-_18059939.23-P1P2	0.903	GGCGGGACCGACGGACAGAC	A 2D	This study
MAP4K4-1	GWAS	MAP4K4	MAP4K4_+_102314194.23-P1P2	0.782	GAGGACGGGCCCGGAGCGTG	A 2E	This study
MAP4K4-2	GWAS		MAP4K4_+_102314209.23-P1P2	0.767	GGCGCCGCGCGCCTCGAGGA	A 2F	This study
TMEM163-1	GWAS	TMEM163	TMEM163_-_135476142.23-P1P2	1.014	GGTGCCGGCCGCAGAAGGTG	A 2G	This study
TMEM163-2	GWAS		TMEM163_+_135476146.23-P1P2	1.007	GGAACGCCGCTAGCCGAGAG	A 2H	This study
STK39-1	GWAS	STK39	STK39_-_169104097.23-P1P2	1.029	GCGCCGAAGCCAGCTAGGAG	A 3A	This study
STK39-2	GWAS		STK39_+_169104017.23-P1P2	0.885	GGCCGGCCGAGAGGTGTCGG	A 3B	This study
SATB1-1	GWAS	SATB1	SATB1_-_18466360.23-P1	1.064	GCCCCGGGCAGGATAGAGGG	A 3C	This study
SATB1-2	GWAS		SATB1_-_18466357.23-P1	0.950	GGGCCCCCGGGCAGGATAGA	A 3D	This study
IP6K2-1	GWAS	IP6K2	IP6K2_+_48754592.23-P1P2	1.075	GCCGAGGAACCCGGCTGAGG	A 3E	This study
IP6K2-2	GWAS		IP6K2_+_48754601.23-P1P2	1.011	GACGGAAACGCCGAGGAACC	A 3F	This study
KPNA1-1	GWAS	KPNA1	KPNA1_+_122233801.23-P1	1.564	GCGCGCGTAGGCGCTCGGGC	A 3G	This study
KPNA1-2	GWAS		KPNA1_+_122233737.23-P1	0.917	GCTCGCTGCTCGGTGCGAGG	A 3H	This study
GAK-1	GWAS	GAK	GAK_+_926062.23-P1P2	0.903	GAGATGGTGCACCTCCGGGC	A 4A	This study
GAK-2	GWAS		GAK_+_926066.23-P1P2	0.891	GCGGAAGATGGTGCACCTCC	A 4B	This study
DCAF16-1	GWAS	DCAF16	DCAF16_+_17812291.23-P1P2	0.918	GTAGGCCTGGCTGGGTCGTG	A 4C	This study
DCAF16-2	GWAS		DCAF16_+_17812328.23-P1P2	0.915	GAGTGGCCTTGCCACCGGAG	A 4D	This study
CAMK2D-1	GWAS	CAMK2D	CAMK2D_-_114682878.23-P1P2	0.982	GAGCCCGCGCGGCTTCAAGA	A 4E	This study
CAMK2D-2	GWAS		CAMK2D_-_114682323.23-P1P2	0.924	GCCCGCGGCGCTGTCACCCA	A 4F	This study

CLCN3-1	GWAS	CLCN3	CLCN3_+_170541739.23-P1P2	1.170	GCCGGACCGGCCCTGACCCA	A 4G	This study
CLCN3-2	GWAS		CLCN3_+_170541734.23-P1P2	1.101	GCCGGCCCTGACCCACGGAA	A 4H	This study
ERCC8-1	GWAS	ERCC8	ERCC8_-_60240852.23-P1P2	0.984	GGCATATCGTGTCCTCACAC	A 5A	This study
ERCC8-2	GWAS		ERCC8_+_60240826.23-P1P2	0.855	GGTGAGGACACGATATGCTG	A 5B	This study
NDUFAF2-1	GWAS	NDUFAF2	NDUFAF2_-_60240946.23-P1P2	1.091	GCGGTGATATATCCGGCCAA	A 5C	This study
NDUFAF2-2	GWAS		NDUFAF2_-_60241076.23-P1P2	0.955	GGGCAGCGCTGGAAACTGGG	A 5D	This study
GIN1-1	GWAS	GIN1	GIN1_+_102455804.23-P1P2	0.998	GGCGCGAGATAAATCACGAG	A 5E	This study
GIN1-2	GWAS		GIN1_-_102455774.23-P1P2	0.976	GGAACGACCACTCACCGAGG	A 5F	This study
PAM-1	GWAS	PAM	PAM_+_102201705.23-ENST00000438793.3	1.019	GGAGGCGTCTCGGTCACGAG	A 5G	This study
PAM-2	GWAS		PAM_+_102201571.23-ENST00000304400.7	0.988	GTATGACTCCGGAATGACAG	A 5H	This study
C5orf24-1	GWAS	C5orf24	C5orf24_-_134181671.23-P1P2	1.000	GCGCCTCTAACACTACAGGG	A 6A	This study
C5orf24-2	GWAS		C5orf24_+_134181678.23-P1P2	0.975	GCCCCGGACGCAGTACGAAG	A 6B	This study
RIMS1-1	GWAS	RIMS1	RIMS1_-_72596682.23-P1P2	0.966	GTGCTGGGCGTGCATCCGAA	A 6C	This study
RIMS1-2	GWAS		RIMS1_-_72596645.23-P1P2	0.840	GCTAGGGCTCCGCTGTGAGG	A 6D	This study
FYN-1	GWAS	FYN	FYN_+_112194611.23-P1P2	0.965	GCGAGCAGCCGCGCTGGTGG	A 6E	This study
FYN-2	GWAS		FYN_-_112194589.23-P1P2	0.953	GCGGCTCCGCTCCTGACAGA	A 6F	This study
SLC18B1-1	GWAS	SLC18B1	SLC18B1_+_133119637.23-P1P2	0.893	GGAGGTCGAGTCCAAGGACG	A 6G	This study
SLC18B1-2	GWAS		SLC18B1_+_133119412.23-P1P2	0.883	GGGGCCTGATCGTGGGGTTC	A 6H	This study
VPS37A-1	GWAS	VPS37A	VPS37A_+_17104482.23-P1P2	0.854	GCGCCCAAACCGGCCAGCCA	A 7A	This study
VPS37A-2	GWAS		VPS37A_-_17104916.23-P1P2	0.845	GCTCCACCGGAGGAAAAAGT	A 7B	This study
BIN3-1	GWAS	BIN3	BIN3_-_22526419.23-P1P2	0.972	GCACCGAGGGAACGACCCTA	A 7C	This study
BIN3-2	GWAS		BIN3_+_22526573.23-P1P2	0.885	GGGACCCCGGCGGCAGACGC	A 7D	This study
FAM49B-1	GWAS	FAM49B	FAM49B_-_130952029.23-P1	1.062	GAGAGCCGCGACAAGCCAGG	A 7E	This study
FAM49B-2	GWAS		FAM49B_+_131028535.23-P2	1.043	GATCCGATTTGCCCCCGGAG	A 7F	This study
ASAP1-1	GWAS	ASAP1	ASAP1_-_131455906.23-P1P2	0.807	GCCGAGCGCGGCGCAGGAAG	A 7G	This study
ASAP1-2	GWAS		ASAP1_-_131455861.23-P1P2	0.785	GCAGTGCTCGCCCGCGGCAG	A 7H	This study
SH3GL2-1	GWAS	SH3GL2	SH3GL2_-_17579147.23-P1P2	1.108	GCCGGCGGCGGCACGACCAG	A 8A	This study
SH3GL2-2	GWAS		SH3GL2_-_17579132.23-P1P2	1.055	GCTCGCGCCCATAGCCCCGG	A 8B	This study
CNTLN-1	GWAS	CNTLN	CNTLN_+_17135087.23-P1P2	0.907	GGCGCTGGGGGCGAAGGGTG	B 1A	This study
CNTLN-2	GWAS		CNTLN_+_17135503.23-P1P2	0.902	GCTGGGCGGGGTAGGTCCCA	B 1B	This study
GBF1-1	GWAS	GBF1	GBF1_+_104005322.23-P1P2	1.031	GCCGGGACGGGCAGTAGAGC	B 1C	This study
GBF1-2	GWAS		GBF1_-_104005285.23-P1P2	1.020	GCAGGCAGCGGGCTAGACTG	B 1D	This study
BAG3-1	GWAS	BAG3	BAG3_+_121411323.23-P1P2	0.898	GCGCGGGTCGTTCCACGTAG	B 1E	This study
BAG3-2	GWAS		BAG3_-_121411132.23-P1P2	0.837	GGGCGGCCCGGCCAGAGACT	B 1F	This study
RNF141-1	GWAS	RNF141	RNF141_-_10562561.23-P1P2	1.838	GGGCTAGGCCTGTCTCCCCG	B 1G	This study
RNF141-2	GWAS		RNF141_-_10562697.23-P1P2	1.049	GCAAGGCATCGCGCACCCTG	B 1H	This study

DLG2-1	GWAS	DLG2	DLG2_-_84027894.23-P1P2	0.959	GTGGGCTGAACCAACCATGT	B 2A	This study
DLG2-2	GWAS		DLG2_-_84028346.23-P1P2	0.875	GCAGTGCATCGTGGGAGCAG	B 2B	This study
SCAF11-1	GWAS	SCAF11	SCAF11_+_46384075.23-P1P2	1.229	GCAGCTGTCTGGGAGAGACG	B 2C	This study
SCAF11-2	GWAS		SCAF11_+_46384171.23-P1P2	0.889	GGACCTGGGAACCTACTGTG	B 2D	This study
HIP1R-1	GWAS	HIP1R	HIP1R_+_123320035.23-P1P2	1.660	GGACTCACAGCCTCACGGTC	B 2E	This study
HIP1R-2	GWAS		HIP1R_-_123320047.23-P1P2	0.796	GCTGGGGCTGCCGGACCGTG	B 2F	This study
FBRSL1-1	GWAS	FBRSL1	FBRSL1_+_133066769.23-P1P2	0.857	GCCTGGGCACCGGGCTCGTG	B 2G	This study
FBRSL1-2	GWAS		FBRSL1_+_133066766.23-P1P2	0.805	GGGGCACCGGGCTCGTGAGG	B 2H	This study
CAB39L-1	GWAS	CAB39L	CAB39L_-_50018126.23-P1	1.053	GGCAGCCTCACACCTACCGG	B 3A	This study
CAB39L-2	GWAS		CAB39L_-_50018123.23-P1	1.046	GATGGCAGCCTCACACCTAC	B 3B	This study
MBNL2-1	GWAS	MBNL2	MBNL2_-_97874785.23-P1P2	0.889	GGGACAGGCAGAGCTAAACA	B 3C	This study
MBNL2-2	GWAS		MBNL2_+_97874974.23-P1P2	0.779	GTTGCCTCACCCCAAACAGG	B 3D	This study
MIPOL1-1	GWAS	MIPOL1	MIPOL1_+_37667657.23-P1P2	0.993	GTGGGCACAGAGTCGATCAG	B 3E	This study
MIPOL1-2	GWAS		MIPOL1_+_37667282.23-P1P2	0.900	GATGCGCCTGGCATAGACCG	B 3F	This study
SYT17-1	GWAS	SYT17	SYT17_+_19179623.23-P1P2	1.011	GCGCCTGGGCAAGCAGCCCG	B 3G	This study
SYT17-2	GWAS		SYT17_+_19179645.23-P1P2	0.937	GCCAGGCTGGAATAAGGCCG	B 3H	This study
SETD1A-1	GWAS	SETD1A	SETD1A_+_30969392.23-P1P2	0.895	GACCTCGCGCGGCACCTCAG	B 4A	This study
SETD1A-2	GWAS		SETD1A_-_30969773.23-P1P2	0.835	GCTTGCTCCGAGGCCAAGTG	B 4B	This study
STX1B-1	GWAS	STX1B	STX1B_-_31021964.23-P1P2	1.038	GCGGCACAGGGTAGGATGGA	B 4C	This study
STX1B-2	GWAS		STX1B_-_31021956.23-P1P2	0.963	GTGCGGCTGCGGCACAGGGT	B 4D	This study
CHRNB1-1	GWAS	CHRNB1	CHRNB1_-_7348458.23-P1P2	1.113	GCGCCAGGCTATGACCCCAG	B 4E	This study
CHRNB1-2	GWAS		CHRNB1_-_7348409.23-P1P2	0.986	GCCTGTGCTGGCGGTCCCAG	B 4F	This study
KANSL1-1	GWAS	KANSL1	KANSL1_+_44270352.23-P1P2	0.981	GCCCCCCGCCCGGAAAGTCA	B 4G	This study
KANSL1-2	GWAS		KANSL1_-_44270669.23-P1P2	0.965	GCCGCCGCGGCGAGACGAGT	B 4H	This study
KLHL14-1	GWAS	KLHL14	KLHL14_-_30349866.23-P1P2	0.991	GCCAGCTCCGACTCCACGGG	B 5A	This study
KLHL14-2	GWAS		KLHL14_-_30350225.23-P1P2	0.984	GGTCAGCAGCTTGTCGTCGG	B 5B	This study
MEX3C-1	GWAS	MEX3C	MEX3C_-_48723919.23-P1P2	0.895	GGGTAGGTAACTAGGTGGGT	B 5C	This study
MEX3C-2	GWAS		MEX3C_-_48723915.23-P1P2	0.854	GCAGAGGTAGGTAACTAGGT	B 5D	This study
SPPL2B-1	GWAS	SPPL2B	SPPL2B_-_2328912.23-P1P2	1.756	GTCCGCCGTCCCCGCGTTGT	B 5E	This study
SPPL2B-2	GWAS		SPPL2B_+_2328680.23-P1P2	1.123	GCGGTGCCCGCCGCAACCAA	B 5F	This study
DYRK1A-1	GWAS	DYRK1A	DYRK1A_-_38792743.23-ENST00000398960.2	0.647	GAAGAGAATGTGGGAATCGA	B 5G	This study
DYRK1A-2	GWAS		DYRK1A_-_38793111.23-ENST00000398960.2	0.559	GGATATTATACCCATACATA	B 5H	This study
SPTSSB-1	GWAS	SPTSSB	SPTSSB_+_161089261.23-P1P2	0.823	GTGGGGAGGAGCCAAAGCCT	B 6A	This study
SPTSSB-2	GWAS		SPTSSB_-_161088856.23-P1P2	0.816	GGGGCAGAGAGGGATTGTAT	B 6B	This study
CD38-1	GWAS	CD38	CD38_+_15779997.23-P1P2	0.997	GGGCTGGGCGAAGATGAGGC	B 6C	This study
CD38-2	GWAS		CD38_-_15780419.23-P1P2	0.993	GGTGCTGAGTAGGGAGTCCC	B 6D	This study

BST1-1	GWAS	BST1	BST1_-_15704748.23-P1P2	0.961	GAGTGGAGGAAGCACGGGAC	B 6E	This study
BST1-2	GWAS		BST1_-_15704751.23-P1P2	0.916	GGGAGGAAGCACGGGACTGG	B 6F	This study
HLA-DRB5-1	GWAS	HLA-DRB5	HLA-DRB5_-_32497983.23-P1P2	0.831	GTGCCATGTAGGAACCTCCA	B 6G	This study
HLA-DRB5-2	GWAS		HLA-DRB5_+_32497964.23-P1P2	0.661	GCTCCCTGGAGGTTCCTACA	B 6H	This study
GPNMB-1	GWAS	GPNMB	GPNMB_-_23286430.23-P1	0.953	GTCTTGGTGGACGGGCCCAG	B 7A	This study
GPNMB-2	GWAS		GPNMB_+_23286445.23-P1	0.925	GTCACGGACGCAGGCACTCA	B 7B	This study
FGF20-1	GWAS	FGF20	FGF20_-_16859809.23-P1P2	0.944	GGCTGCCAATACTAGGACTA	B 7C	This study
FGF20-2	GWAS		FGF20_-_16859438.23-P1P2	0.919	GTCCTGCGCTCGCCCAGCAG	B 7D	This study
LRRK2-1	GWAS	LRRK2	LRRK2_+_40618865.23-P1P2	0.979	GCTGCTCAGGGAACCGGCAG	B 7E	This study
LRRK2-2	GWAS		LRRK2_+_40618843.23-P1P2	0.926	GCGCCGGCCACAGCTCCCCG	B 7F	This study
NOD2-1	GWAS	NOD2	NOD2_-_50727543.23-P1P2	1.006	GGGGAGTCGTGGCCCGGAGT	B 7G	This study
NOD2-2	GWAS		NOD2_+_50727533.23-P1P2	0.968	GCGACTCCAAGGCCCACTCC	B 7H	This study
BRIP1-1	GWAS	BRIP1	BRIP1_+_59940616.23-P1P2	1.075	GCGGAGGGAAGTCCACGGAA	B 8A	This study
BRIP1-2	GWAS		BRIP1_+_59940838.23-P1P2	1.013	GTGAGGGGTCTGGTGGGTCG	B 8B	This study
RIT2-1	GWAS	RIT2	RIT2_+_40695276.23-P1P2	0.862	GTGCTGTTAGAGGTGAACTG	B 8C	This study
RIT2-2	GWAS		RIT2_-_40695615.23-P1P2	0.792	GGGTAAGAACCATCAGCGTC	B 8D	This study
GBA-3	GWAS	GBA	GBA_-_155214386.23-P2	0.876	GCTGGGCGGGACTGGAGACT	A 8C	This study
GBA-4	GWAS		GBA_-_155214372.23-P2	0.871	GGCCTGCAAAGGCGCCTGGG	A 8D	This study
CALB1-1	Proteomics	CALB1	CALB1_+_91094600.23-P1P2	0.808	GTCAGCGTGTGCGCGAGTCA	A 9A	This study
CALB1-2	Proteomics		CALB1_+_91095021.23-P1P2	0.863	GTTCCAGGAACGGTAATGGT	A 9B	This study
CACNA2D1-1	Proteomics	CACNA2D1	CACNA2D1_-_82073246.23-P1P2	0.928	GAGAGACTTGTGGAAGCGAG	A 9C	This study
CACNA2D1-2	Proteomics		CACNA2D1_-_82073236.23-P1P2	0.906	GTGGCAGGCAGAGAGACTTG	A 9D	This study
CACNA2D2-1	Proteomics	CACNA2D2	CACNA2D2_-_50540709.23-P1P2	0.926	GCGGCGAGCAGCGGTAGAAG	A 9E	This study
CACNA2D2-2	Proteomics		CACNA2D2_-_50540593.23-P1P2	0.901	GAAGGAGTAGCGCGGACCGG	A 9F	This study
SIK1-1	Proteomics	SIK1	SIK1_+_44847002.23-P1P2	0.901	GGCGGCTCCGGGCTGACATG	B 9A	This study
SIK1-2	Proteomics		SIK1_+_44846607.23-P1P2	0.887	GGACCGCGGGCGGAGATACC	B 9B	This study
SIK2-1	Proteomics	SIK2	SIK2_-_111473540.23-P1P2	0.940	GCGAGAGGCCGCCTCACTGG	B 9C	This study
SIK2-2	Proteomics		SIK2_-_111473134.23-P1P2	0.791	GTGACGTCGGCGCACGTCAG	B 9D	This study
NIM1-1	Proteomics	NIM1	NIM1_+_43192363.23-P1P2	1.125	GAGGCTCCCGGAGCTGTCAG	B 9E	This study
NIM1-2	Proteomics		NIM1_-_43192399.23-P1P2	0.993	GGGAGCCTCAAGCGCGACAG	B 9F	This study
PRKACA-1	Proteomics	PRKACA	PRKACA_+_14228563.23-P1P2	1.055	GGCGGGGGCGTCACAGACAG	B 9G	This study
PRKACA-2	Proteomics		PRKACA_+_14228550.23-P1P2	1.037	GAGACAGCGGCAGAGATCTT	B 9H	This study
PSEN1-1	Proteomics	PSEN1	PSEN1_+_73603670.23-P1P2	0.906	GCTGGACAAGGACACACCCG	B 10A	This study
PSEN1-2	Proteomics		PSEN1_-_73603461.23-P1P2	0.870	GCCGTGTGGGAAACCAGGAG	B 10B	This study

MKNK1-1	Proteomics	MKNK1	MKNK1_-_47082123.23-P2	1.137	GGGAAGGTCGTAGGACCCAG	B 10C	This study
MKNK1-2	Proteomics		MKNK1_+_47082452.23-P2	0.988	GGGCTGACAGGAGAGAGAAC	B 10D	This study
LARP1-1	Proteomics	LARP1	LARP1_-_154092586.23-ENST00000336314.4	0.825	GCTGCCCTGGCAGACTCCCA	B 10E	This study
LARP1-2	Proteomics		LARP1_+_154092615.23-ENST00000336314.4	0.797	GCCTGTGGGCTCCTTCCTCG	B 10F	This study
HMGB1-1	Proteomics	HMGB1	HMGB1_-_31191681.23-P2	0.873	GACCACGCTCGCGCGGACCA	B 10G	This study
HMGB1-2	Proteomics		HMGB1_-_31191644.23-P2	0.861	GCACCTCCGCGGGTCACCCC	B 10H	This study
DSTYK1-1	Proteomics	DSTYK	DSTYK_+_205180672.23-P1P2	1.145	GCCGAGCCGCAAAGACAGAG	B 11A	This study
DSTYK1-2	Proteomics		DSTYK_+_205180408.23-P1P2	0.988	GAGGCGATGTCGCCGAAACC	B 11B	This study
LATS1-1	Proteomics	LATS1	LATS1_+_150039161.23-P1P2	0.901	GGCGGTGGCCTGGTGTTAAG	B 11C	This study
LATS1-2	Proteomics		LATS1_-_150038761.23-P1P2	0.865	GTCCGAGGCCGAAAAGCCTG	B 11D	This study
NIX-1	Mechanistic	NIX	BNIP3L_+_26240600.23-P1P2	1.016	GGCAGCAGCAGGACCGTCTC	m-C1	Humble et al, unpublished
NIX-2	Mechanistic		BNIP3L_-_26240851.23-P1P2	0.874	GGGAGGAGAAGGCAGCTCAT	m-D1	Humble et al, unpublished
USP30-1	Mechanistic	USP30	USP30_+_109490408.23-P1P2	1.101	GGCCGGACCGAGGGATACGA	m-E3	Humble et al, unpublished
USP30-2	Mechanistic		USP30_-_109490609.23-P1P2	1.088	GTGCCGAAGAGGCCGGGACC	m-F3	Humble et al, unpublished
PRKN-1	Familial	PRKN	PARK2_+_163148768.23-P1P2	0.998	GACCCAGGAGAGCCGCTGGT	S 1E	Humble et al, unpublished
PRKN-2	Familial		PARK2_-_163148753.23-P1P2	0.945	GAACAGGCCCATGCGCGCAG	S 1F	Humble et al, unpublished
PINK1-1	Familial	PINK1	PINK1_-_20960047.23-P1P2	0.858	GGGCCGCGGCGCCACCATGG	S 1C	Humble et al, unpublished
PINK1-2	Familial		PINK1_+_20960036.23-P1P2	0.806	GGCCTGTCGCACCGCCATGG	S 1D	Humble et al, unpublished
MCCC1-1	GWAS	MCCC1	MCCC1_-_182817269.23-P1P2	1.145	GCCGTGACTCCCCAGTACAG	S A 3E	Humble et al, unpublished
MCCC1-2	GWAS		MCCC1_+_182817301.23-P1P2	1.039	GGGGTCACGAGGCTTCGTAG	S A 3F	Humble et al, unpublished
TMEM175-1	GWAS	TMEM175	TMEM175_-_926289.23-P1P2	1.000	GCCGGCCGGGCTGACTCAAG	S 4C	Humble et al, unpublished
TMEM175-2	GWAS		TMEM175_-_926717.23-P1P2	0.873	GTGGGGCAGTGACCAGTAGT	S 4D	Humble et al, unpublished
SCARB2-1	GWAS	SCARB2	SCARB2_+_77134573.23-P1P2	0.821	GCCAGAGTATCGAGAAGGTG	S A 3A	Humble et al, unpublished

SCARB2-2	GWAS		SCARB2_-_77134528.23-P1P2	0.784	GAAGATGTAGCAGCAGGGAT	S A 3B	Humble et al, unpublished
SNCA-1	GWAS	SNCA	SNCA_+_90758294.23-P1P2	0.965	GGGACGGCGACGACCAGAAG	S 2A	Humble et al, unpublished
SNCA-2	GWAS		SNCA_+_90758283.23-P1P2	0.924	GACCAGAAGGGGCCCAAGAG	S 2B	Humble et al, unpublished
CTSB-1	GWAS	CTSB	CTSB_+_11725568.23-P1P2	1.018	GAGGGCTCCGGCAACCGCTC	S 4E	Humble et al, unpublished
CTSB-2	GWAS		CTSB_-_11725558.23-P1P2	1.000	GCAGCCTGCGCGCAGCGGAG	S 4F	Humble et al, unpublished
GCH1-1	GWAS	GCH1	GCH1_-_55369491.23-P1P2	0.957	GCTGTGGCCGGAGTCACCTG	S 4A	Humble et al, unpublished
GCH1-2	GWAS		GCH1_-_55369495.23-P1P2	0.950	GGGCCGGAGTCACCTGAGGA	S 4B	Humble et al, unpublished
GALC-1	GWAS	GALC	GALC_+_88459060.23-P1P2	0.950	GCCGGAGGTCCAGAGAGTAT	S A 3C	Humble et al, unpublished
GALC-2	GWAS		GALC_+_88459496.23-P1P2	0.931	GGACCCACACAATGGCTGAG	S A 3D	Humble et al, unpublished
VPS13C-1	GWAS	VPS13C	VPS13C_-_62352597.23-P1P2	1.014	GGGCGCTGAGGCACAAGGAG	S 3G	Humble et al, unpublished
VPS13C-2	GWAS		VPS13C_-_62352585.23-P1P2	0.888	GCAGCACCATGGTGGCGCTG	S 3H	Humble et al, unpublished
GRN-1	GWAS	GRN	GRN_-_42422695.23-P1P2	0.998	GTGCCCAAGGACCGCGGAGT	S 7A	Humble et al, unpublished
MAPT-1	GWAS	MAPT	MAPT_+_43971932.23-P1P2	0.922	GTGTTGGTGCCGGAGCTGGT	S 8H	Humble et al, unpublished
CRLS1-1	GWAS	CRLS1	CRLS1_+_5986787.23-P1P2	1.085	GCGGCAACCACTCAGACACT	S A 3G	Humble et al, unpublished
CRSL1-2	GWAS		CRLS1_-_5986783.23-P1P2	0.814	GTAAAGTAGTATGGAGGCAG	S A 3H	Humble et al, unpublished
PARK7-1	GWAS	PARK7	PARK7_+_8022079.23-P1P2	0.909	GTCCATGCCGGCGAGAGGTT	S 1G	Humble et al, unpublished
PARK7-2	GWAS		PARK7_+_8021784.23-P1P2	0.903	GGTACCACTCACCCCACACC	S 1H	Humble et al, unpublished
VPS35-1	GWAS	VPS35	VPS35_+_46723041.23-P1P2	0.991	GAGGCTCTGGGGAGTCGCCA	S 2E	Humble et al, unpublished
VPS35-2	GWAS		VPS35_+_46723052.23-P1P2	0.948	GCTGCTTGCTGCAGGCTCTG	S 2F	Humble et al, unpublished

3179	Controls	3179	non-targeting_00243_i1	non-targeting_00243	-	GACCCGAGACTGCTTCCCGG	S 11A	Humble et al, unpublished
3180	Controls	3180	non-targeting_00242_i1	non-targeting_00242	-	GAGACGAGGACATGTGTAGC	S 11B	Humble et al, unpublished
3181	Controls	3181	non-targeting_00239_i1	non-targeting_00239	-	GTACCACCCAAACGATAACG	S 11C	Humble et al, unpublished
3083	Controls	3083	non-targeting_00249_i1	non-targeting_00249	-	GCAGGCCCGTTTGCTTACGA	S 11E	Humble et al, unpublished
3084	Controls	3084	non-targeting_00248_i1	non-targeting_00248	-	GAGTCTGGGGAGGACATTGT	S 11F	Humble et al, unpublished
3085	Controls	3085	non-targeting_00247_i1	non-targeting_00247	-	GCAGGCCAGAGGCCCCGTGC	S 11G	Humble et al, unpublished
3086	Controls	3086	non-targeting_00244_i1	non-targeting_00244	-	GACTCACGTAGCAGTGGAAA	S 11H	Humble et al, unpublished
1872	Controls	1872	0_i25	negative_control-10010	-	GTCCACCCTTATCTAGGCTA	S 12A	Humble et al, unpublished
1873	Controls	1873	0_i26	negative_control-10016	-	GGACTAAGCGCAAGCACCTA	S 12B	Humble et al, unpublished

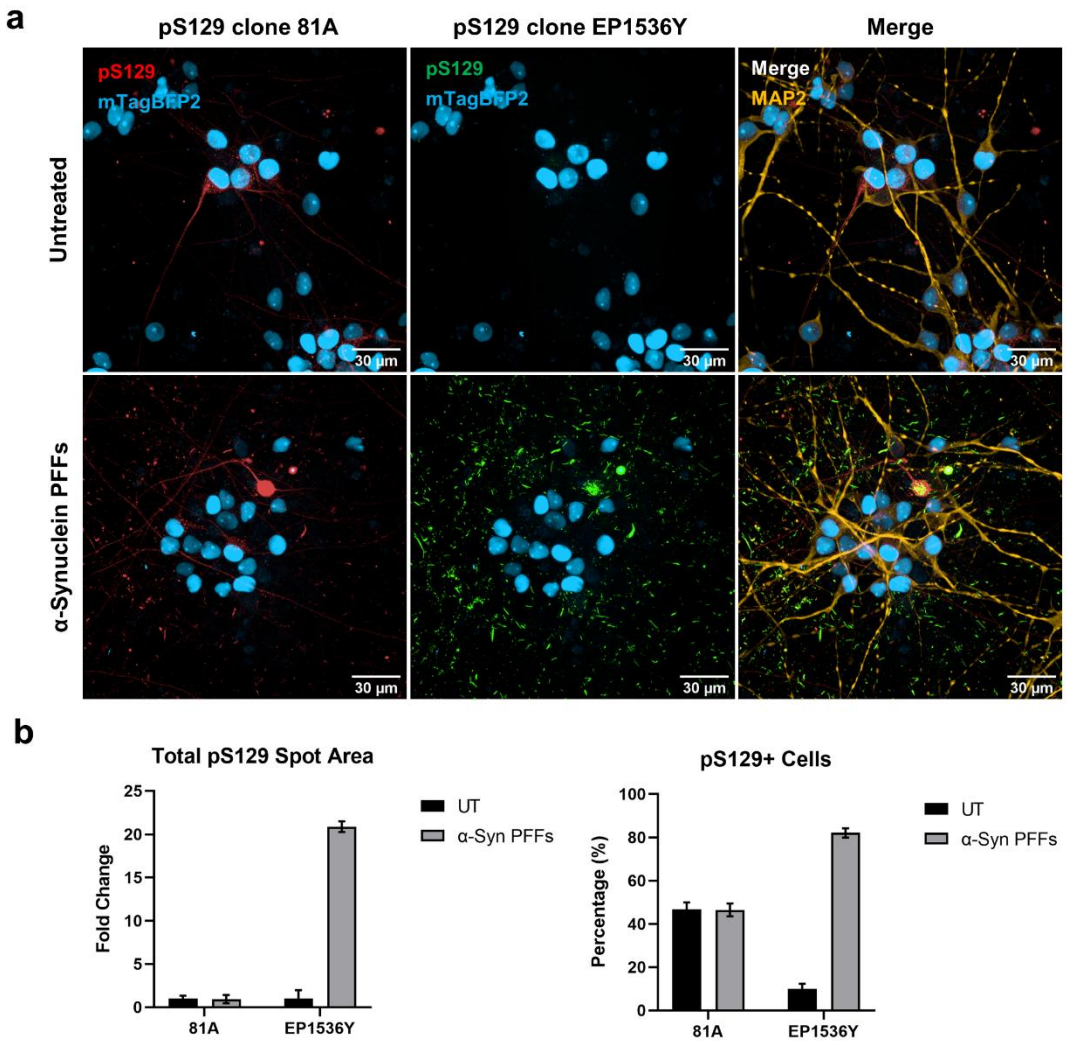


Figure 49. Comparison of pS129 antibodies in PFF-treated i^3 neurons. a) i^3 Cortical neurons were treated on DIV 10 with 10 µg/ml α-synuclein PFFs, fixed and immunostained 14 days post-PFFs with two different pS129 antibodies, clone 81A (Abcam, ab184674) or EP1536Y (Abcam, ab51253). 81A demonstrated strong unspecific staining even at 1:40,000 dilution in the untreated condition, whereas EP1536Y was highly specific. Scale bar = 30 µM. 40x water immersion objective on the Opera Phenix confocal microscope. b) Quantification of the staining demonstrated that the 81A antibody showed no difference between basal and treated conditions, resulting in no increased fold change in PFF-treated wells. EP1536Y discriminated well between untreated and treated conditions. Data is presented as the mean ± SEM.

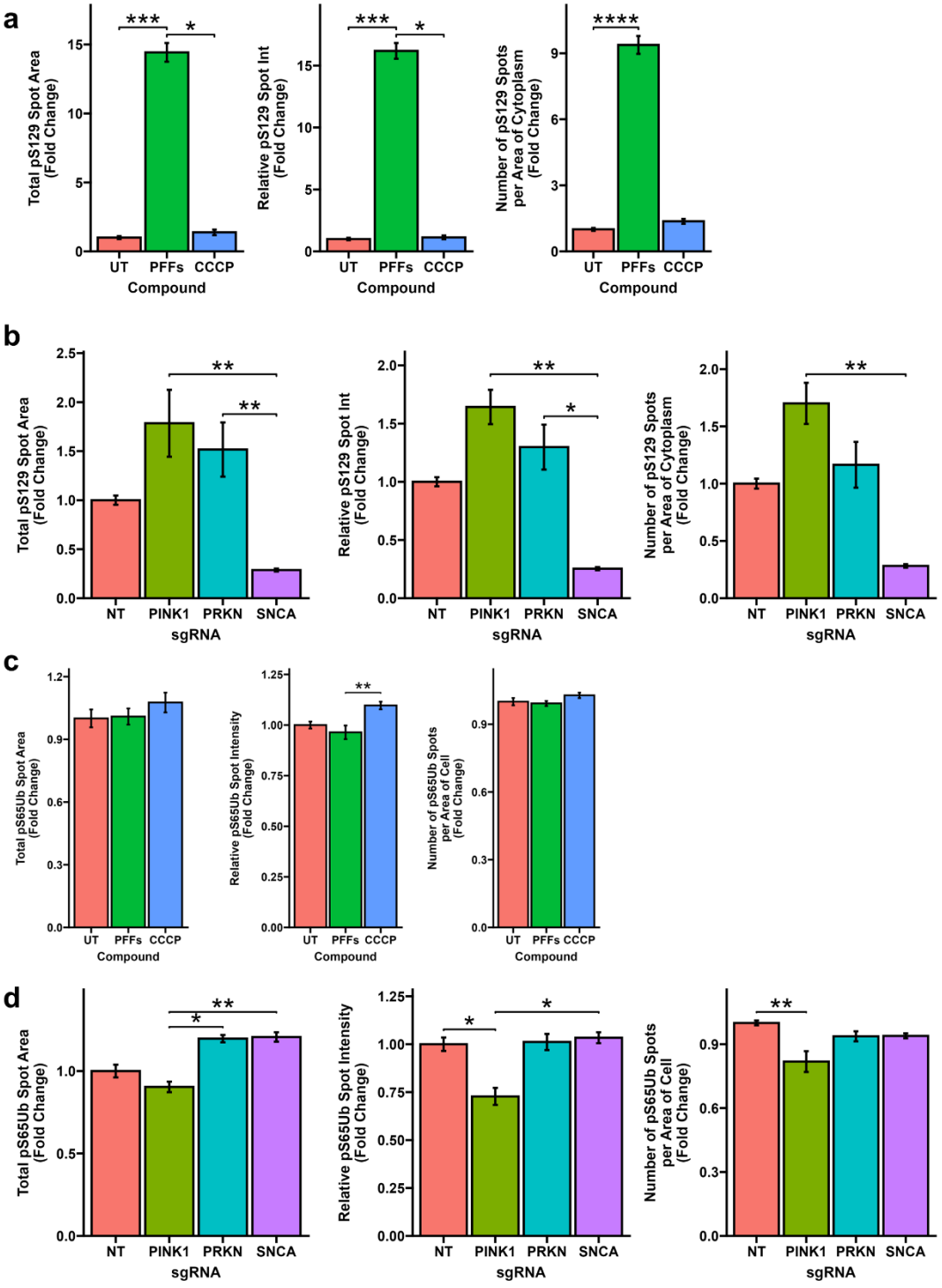
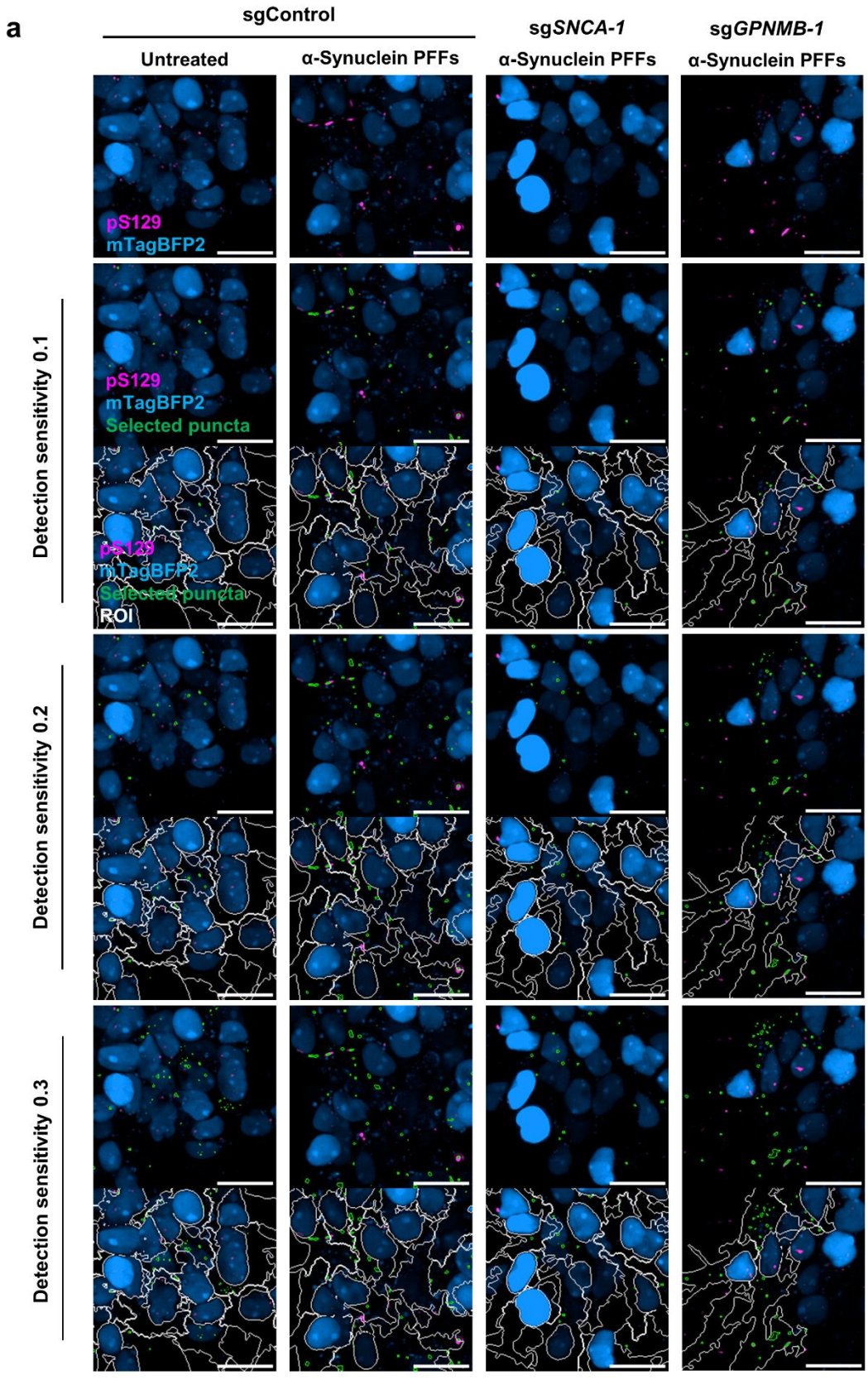


Figure 50. Preliminary screening internal controls. a) α-Synuclein PFF-treatment shows increased pS129 area, intensity and number of spots per area of cell. b) PFF-treated cells show a decrease of pS129 in *SNCA* knockdown conditions compared to *PINK1* and *PRKN* knockdown cells, but not sgControl-expressing cells. c) CCCP treatment increases the intensity of pS65Ub when compared to PFF-treated cells, but not control cells. d) *PINK1* knockdown cells show reduced pS65Ub spot intensity and number compared to controls. N = 1 independent differentiation. Statistical test: Kruskal-Wallis test with Dunn's multiple comparisons test. Data is presented as the mean ± SEM. * $p < 0.05$, ** $p < 0.01$, *** $p < 0.001$, **** $p < 0.0001$.


a
sgControl
sgSNCA-1
sgGPNMB-1
Untreated
α-Synuclein PFFs
α-Synuclein PFFs
α-Synuclein PFFs
pS129
mTagBFP2
Detection sensitivity 0.1
pS129
mTagBFP2
Selected puncta
pS129
mTagBFP2
Selected puncta
ROI
Detection sensitivity 0.2
Detection sensitivity 0.3

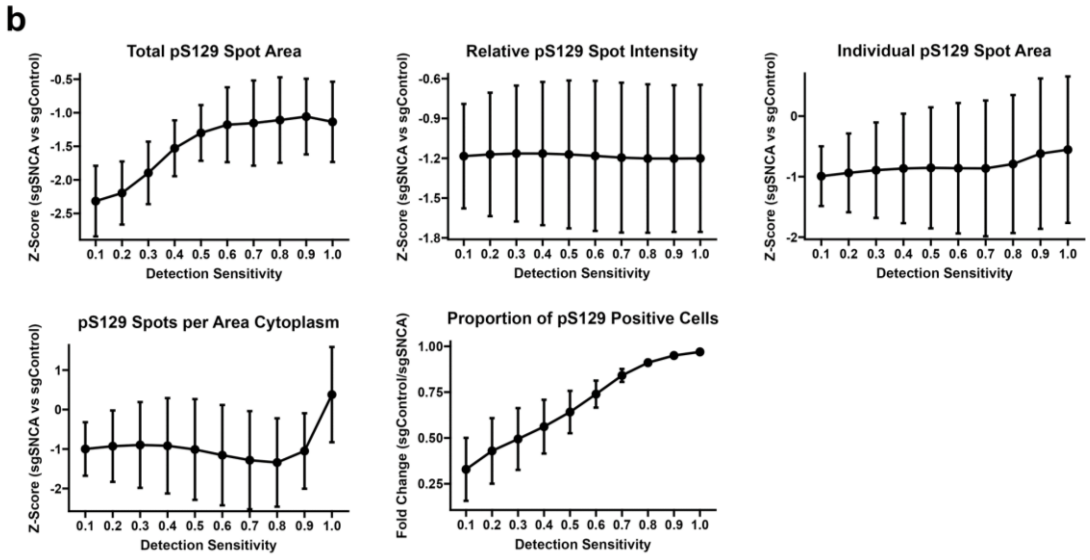
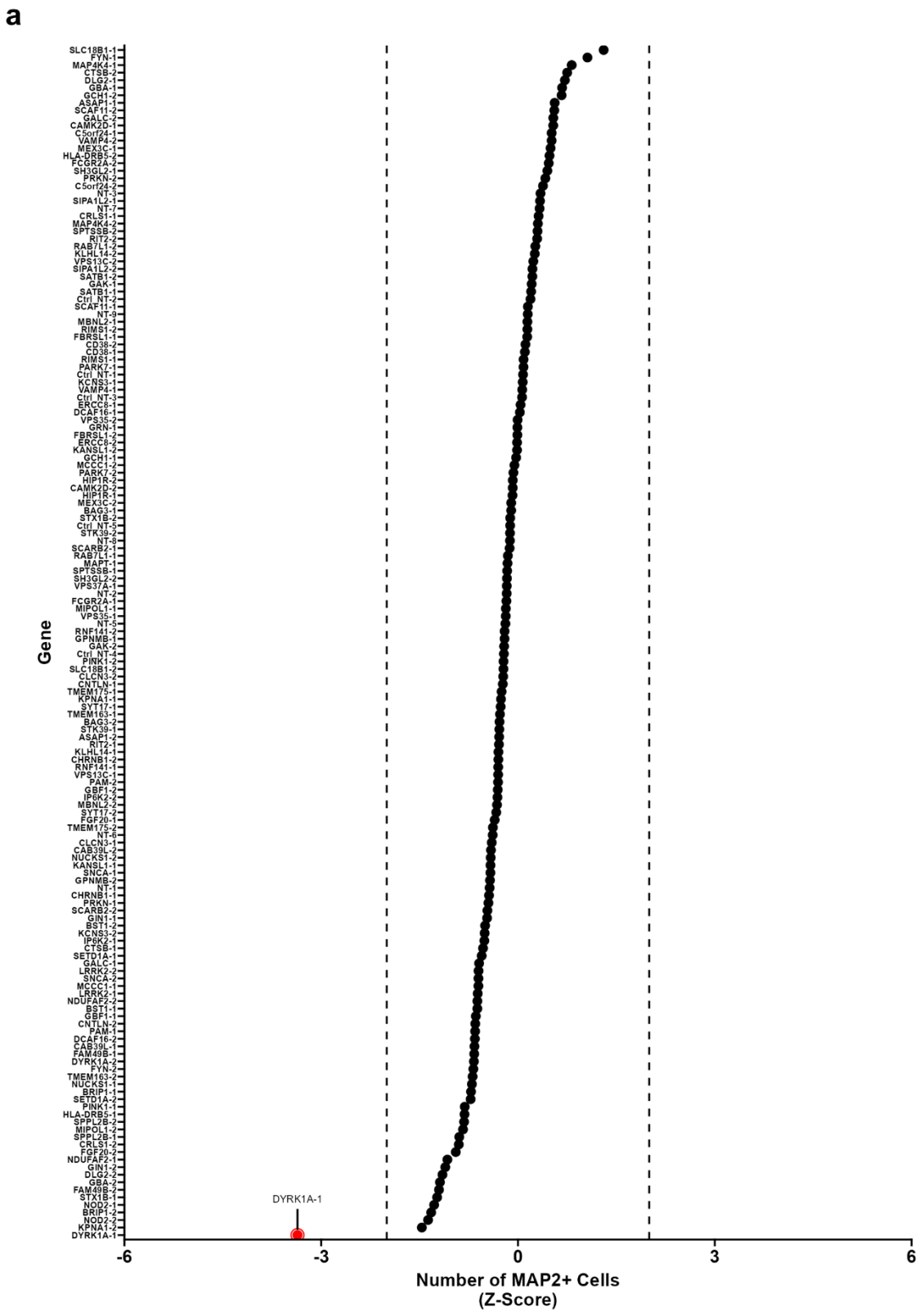
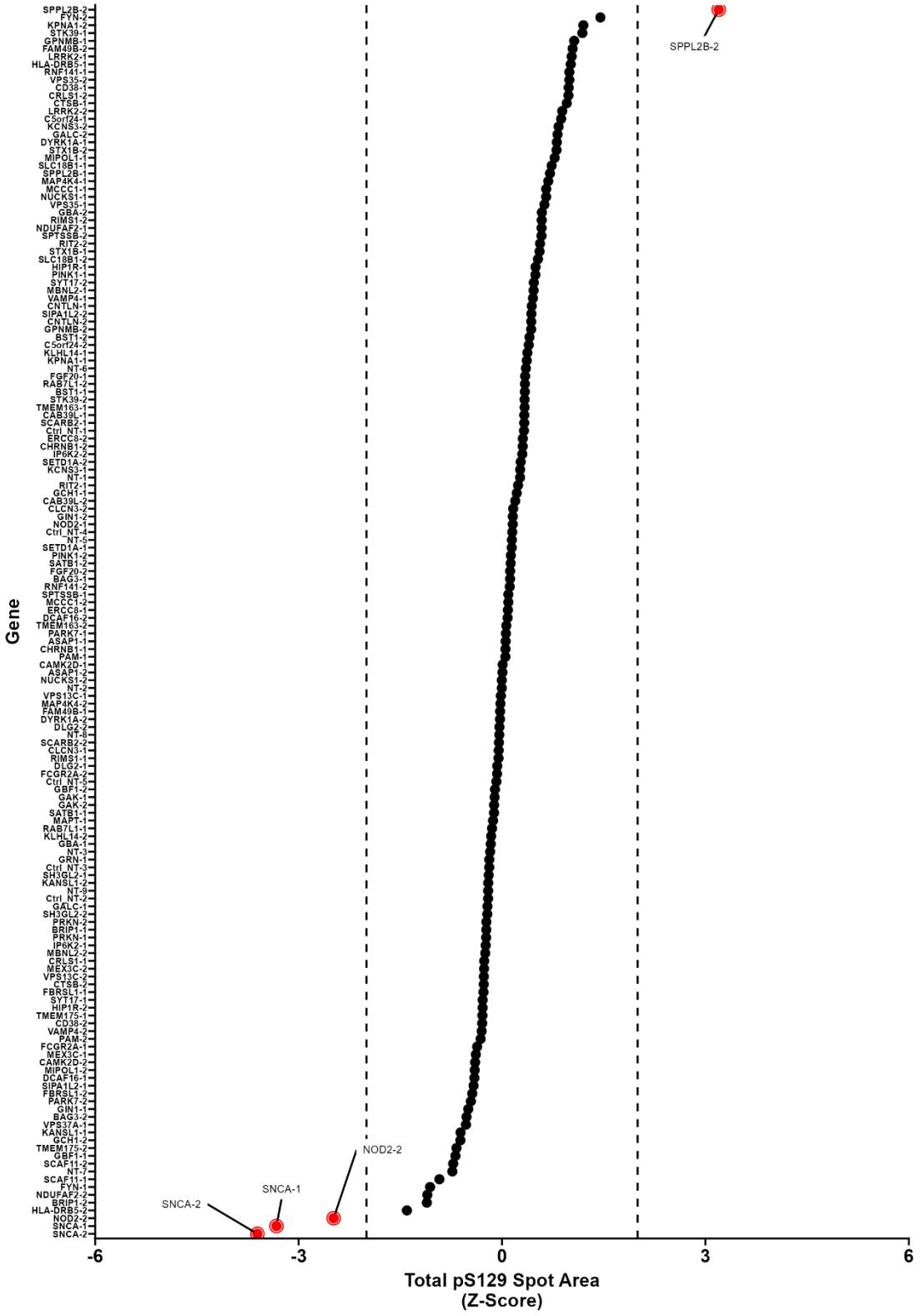
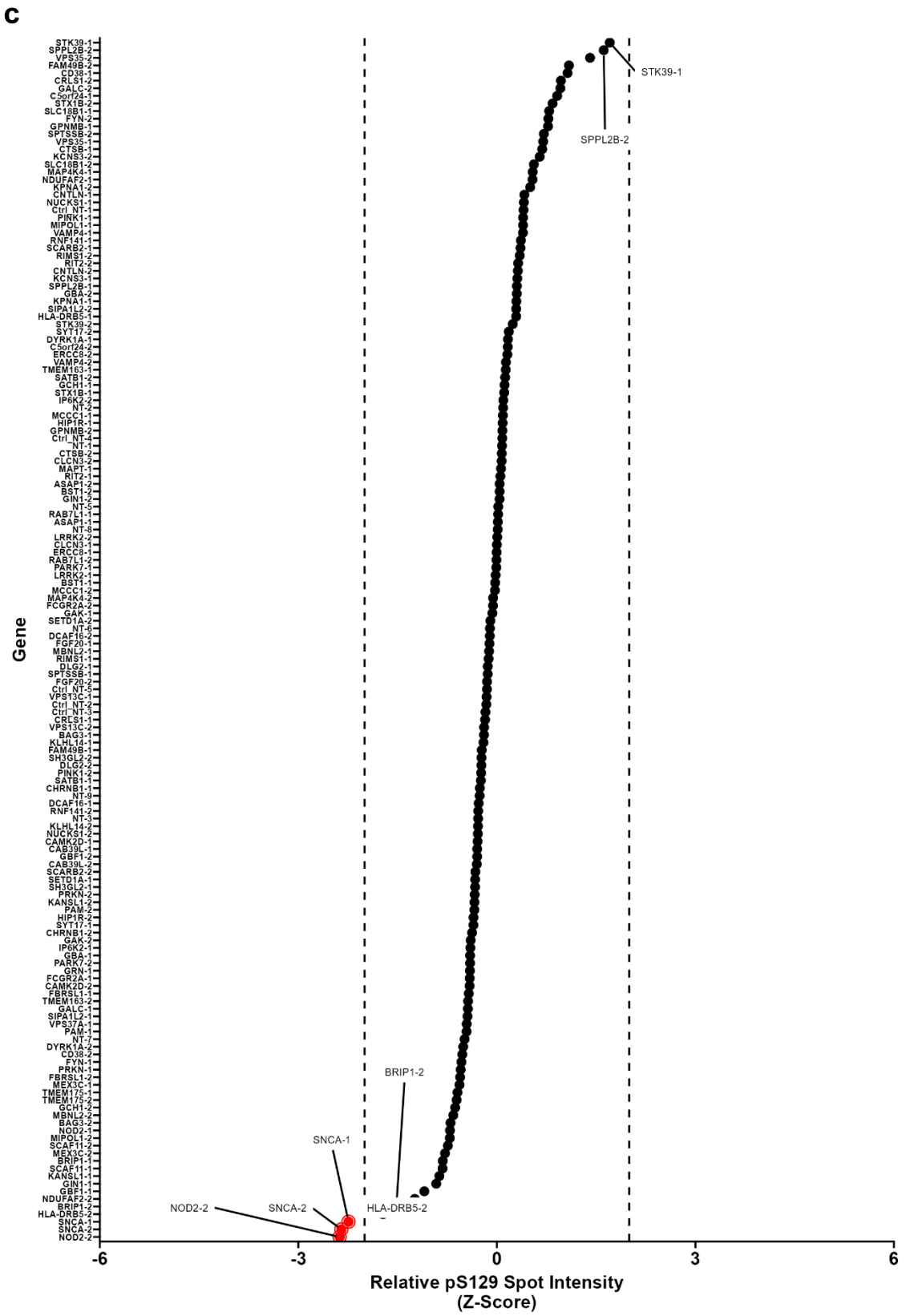


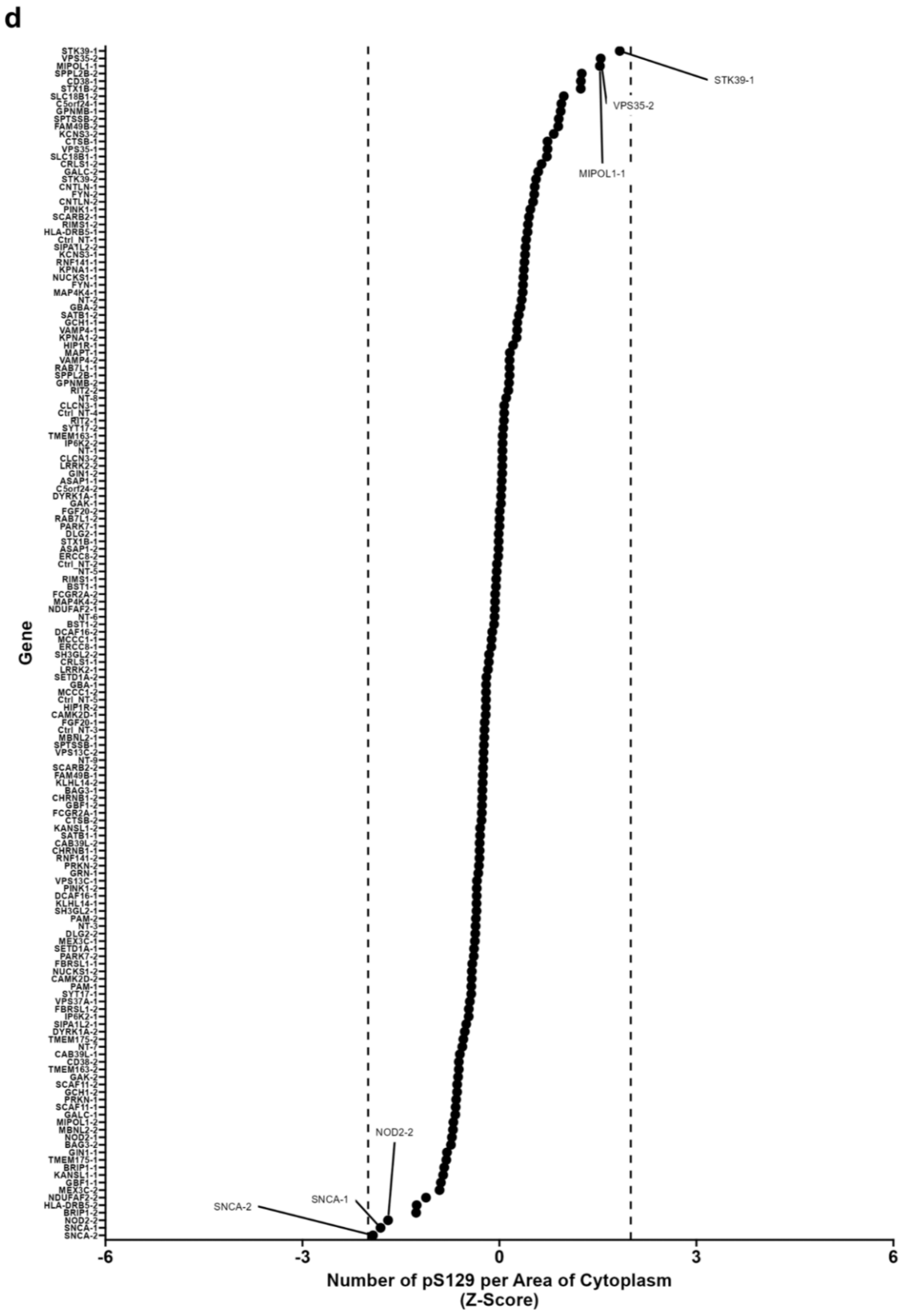
Figure 51. Harmony analysis pipeline optimisation. a) Confocal microscopy images of *SNCA* and *GPNMB*-targeted or control sgRNA-expressing i^3 neurons from the first replicate of primary screening, treated with PFFs at DIV 10 and fixed, stained and imaged 14 days post-seeding. The Harmony software analysis was optimised to detect bright pS129 puncta and disregard background fluorescence – the puncta highlighted green are detected by the algorithm, within the region of interested delineated in white. Scale bar = 20 µm. 40x water immersion objective, Opera Phenix confocal microscope. b) Detection sensitivity parameters from 0.1 to 1.0 were tested to determine the setting with the largest assay window as assessed by the *SNCA*-targeted guide's Z-score, in comparison to control sgRNA-expressing neurons. Low detection sensitivity settings (sensitivity = 0.1) showed the largest Z-score for *SNCA* knockdown conditions and were retained for analysis of this and further replicates of the primary screen. With increasing detection sensitivity, higher background was observed which contributed to a greater proportion of cells classed as pS129-positive.

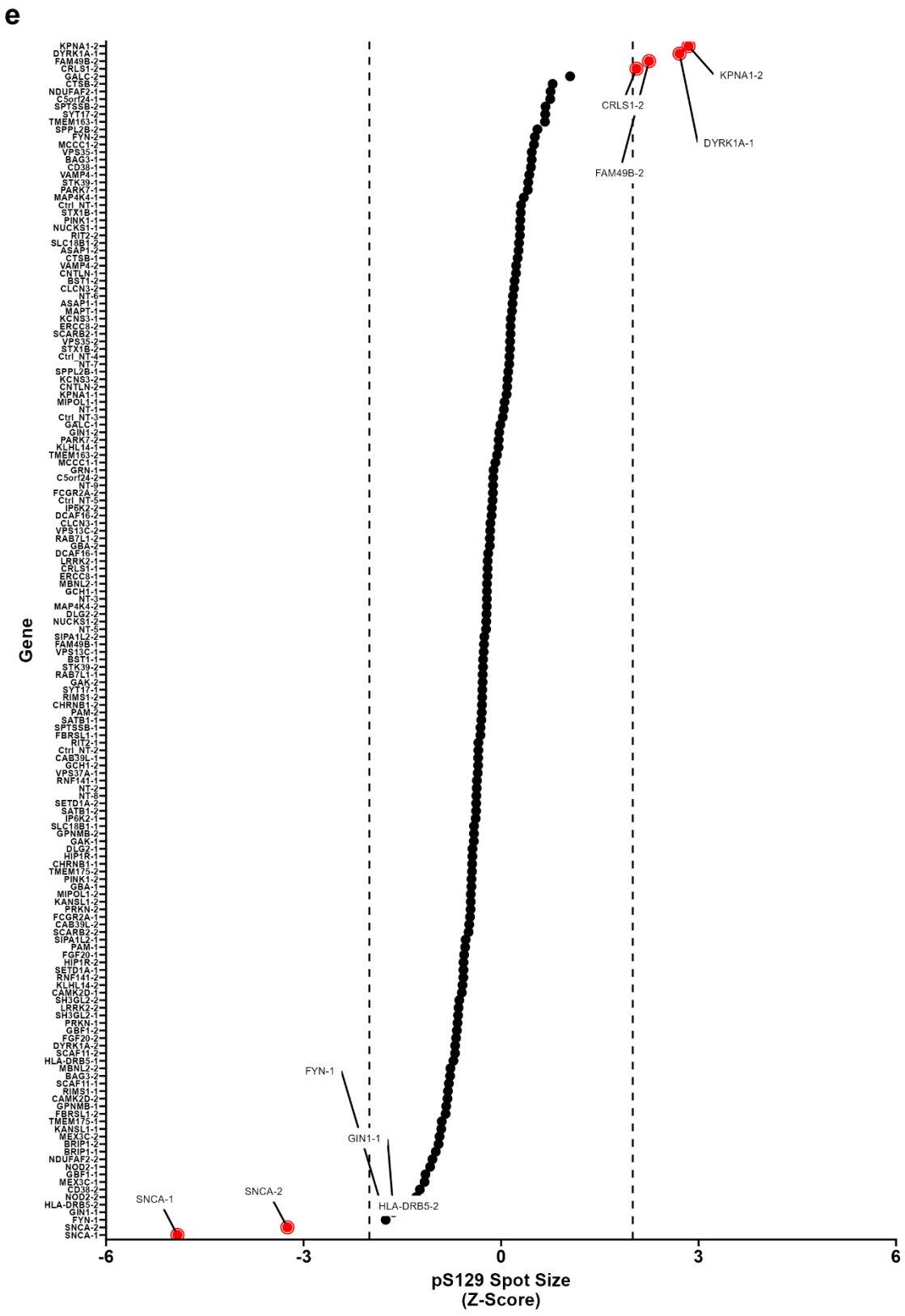

a
Gene
DYRK1A-1
-6
-3
0
3
6
Number of MAP2+ Cells
(Z-Score)

b

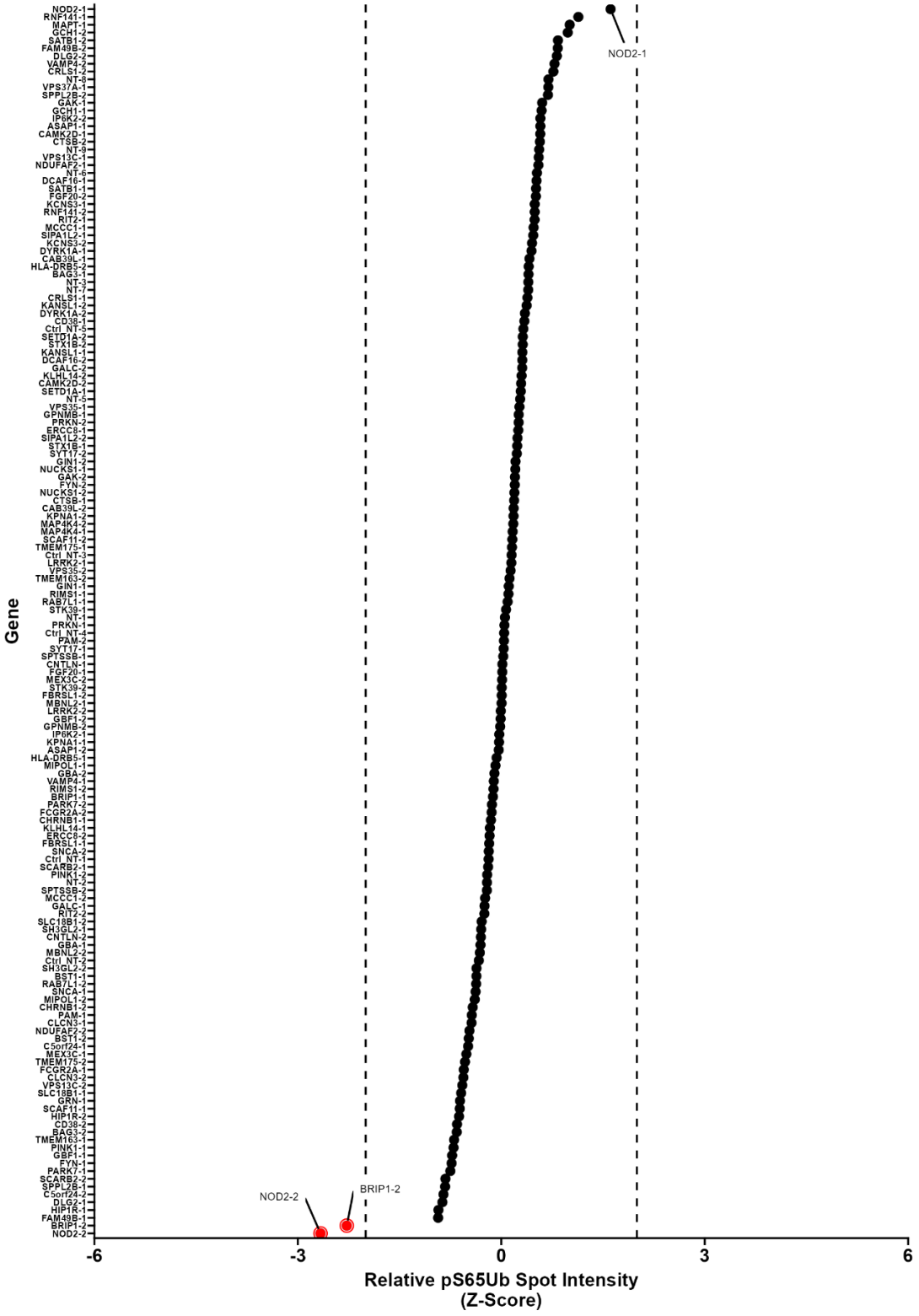

Gene
SPPL2B-2
NOD2-2
SNCA-1
SNCA-2
-6
-3
0
3
6
Total pS129 Spot Area
(Z-Score)


c
Gene
STK39-1
SPPL2B-2
BRIP1-2
SNCA-1
NOD2-2
SNCA-2
HLA-DRB5-2
-6
-3
0
3
6
Relative pS129 Spot Intensity
(Z-Score)


d
Gene
STK39-1
VPS35-2
MIPOL1-1
NOD2-2
SNCA-1
SNCA-2
-6
-3
0
3
6
Number of pS129 per Area of Cytoplasm
(Z-Score)


e
Gene
pS129 Spot Size
(Z-Score)
-6
-3
0
3
6
KPNA1-2
CRLS1-2
DYRK1A-1
FAM49B-2
FYN-1
GIN1-1
HLA-DRB5-2
SNCA-1
SNCA-2

f


Gene
NOD2-1
NOD2-2
BRIP1-2
-6
-3
0
3
6
Relative pS65Ub Spot Intensity
(Z-Score)

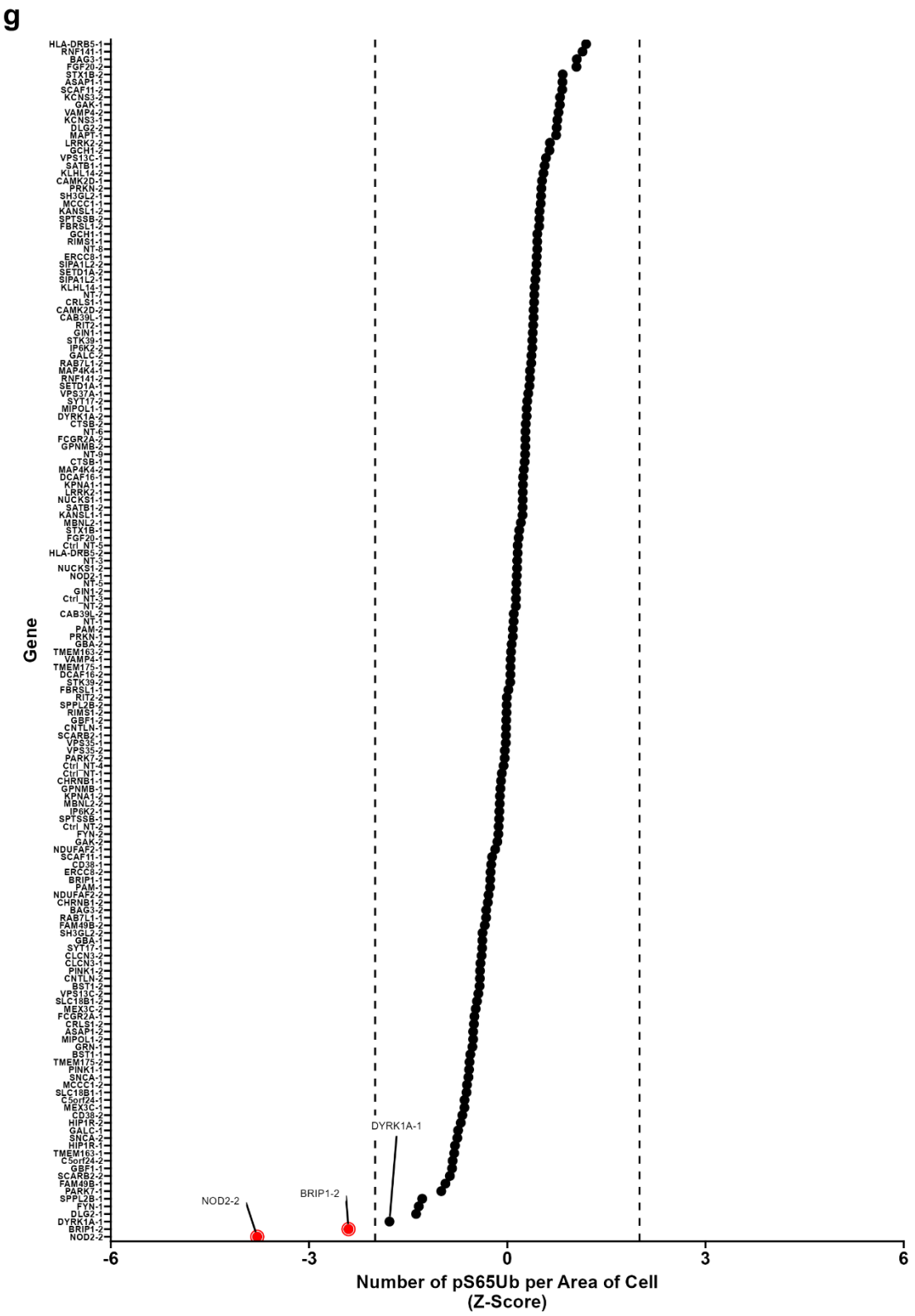
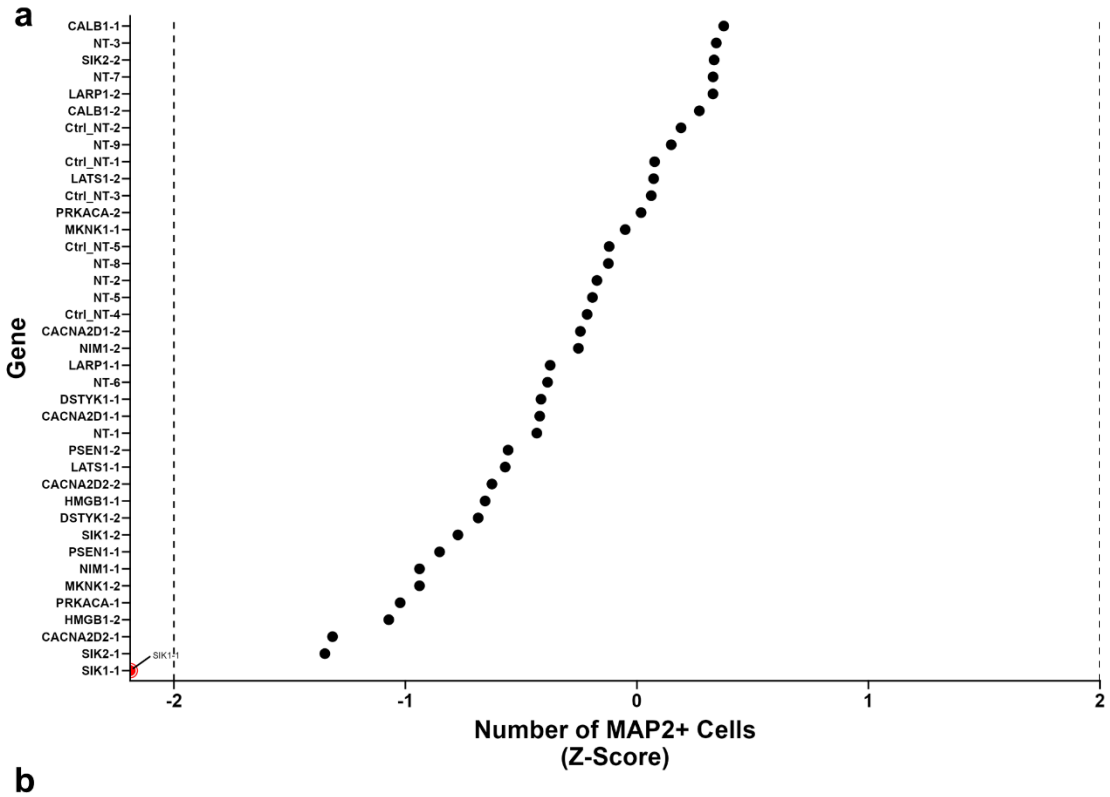
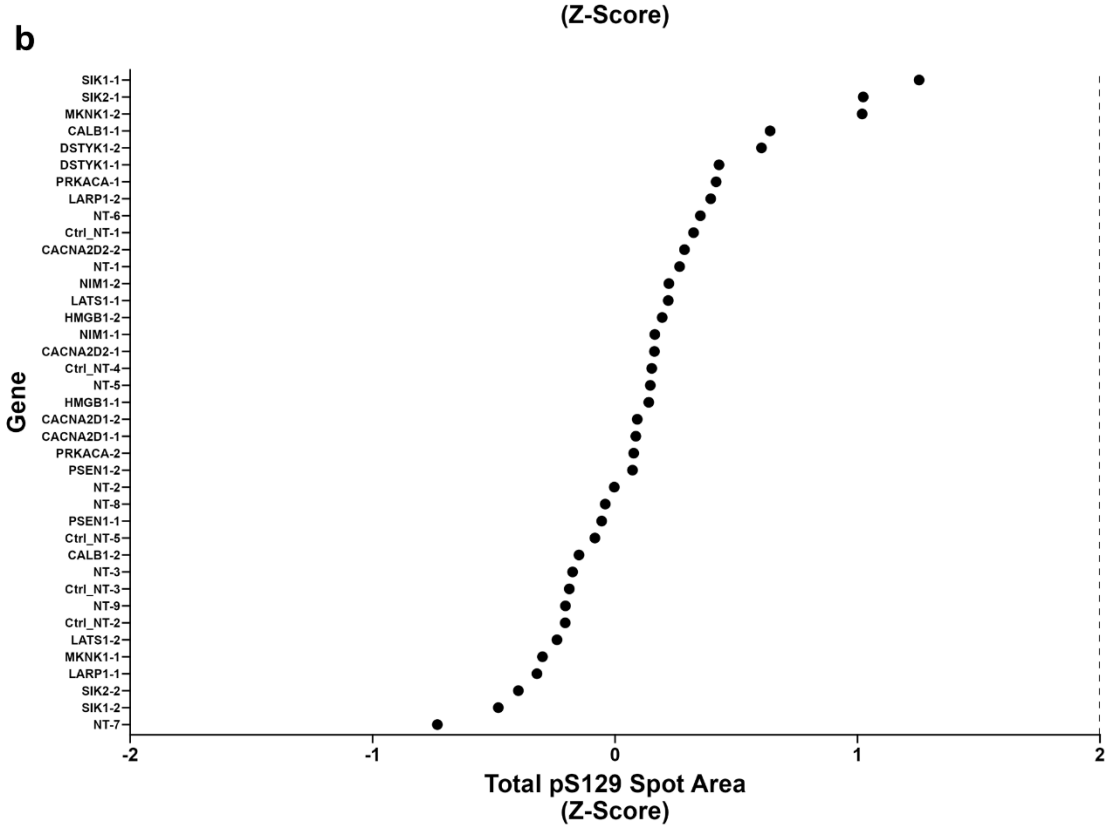
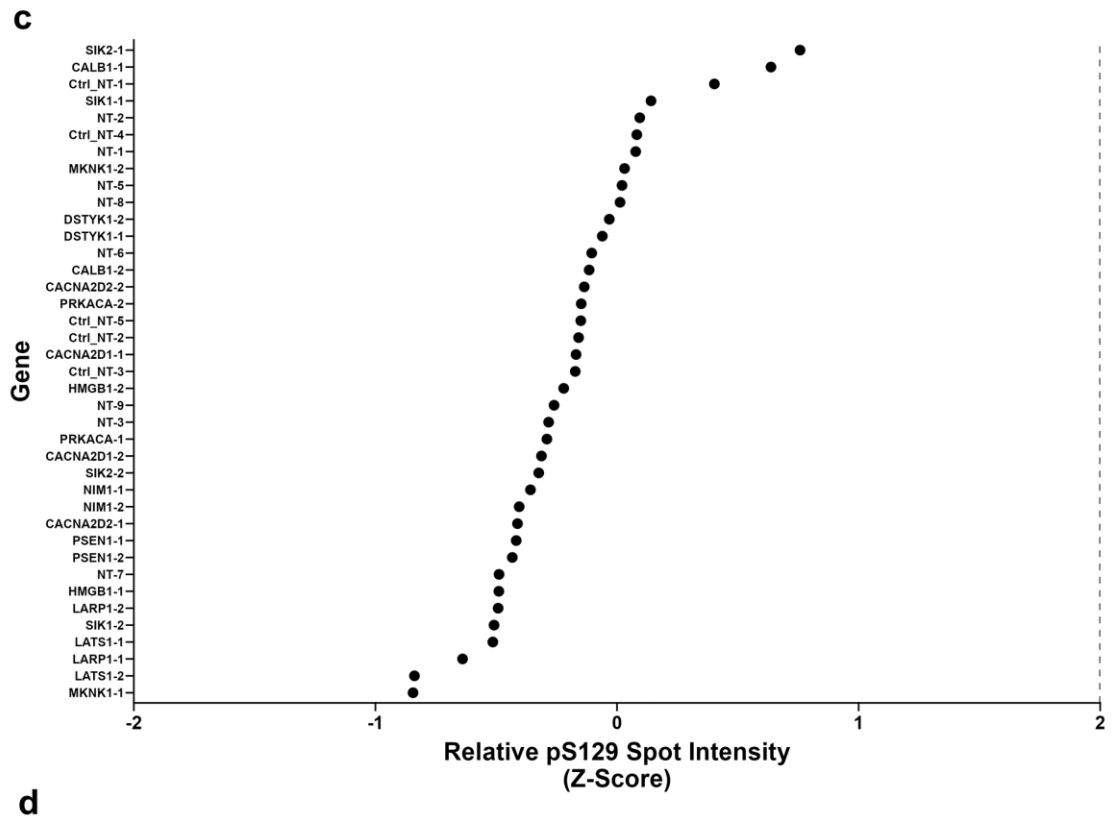
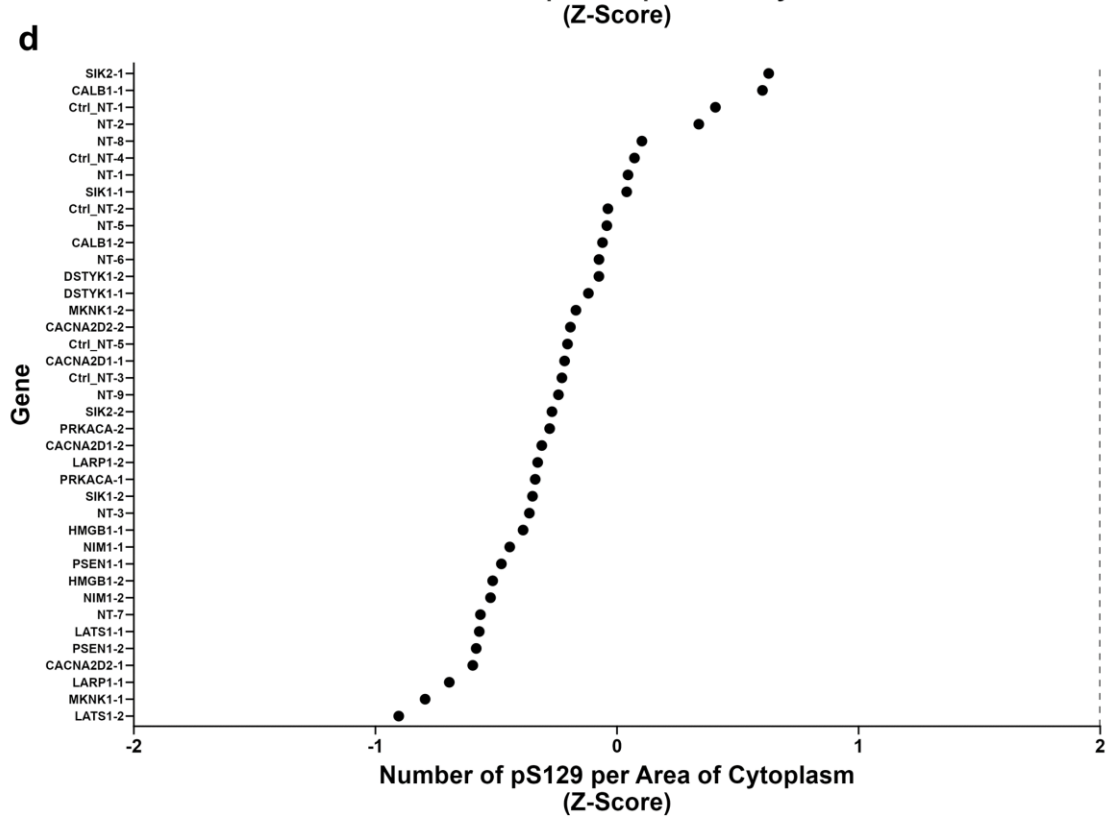


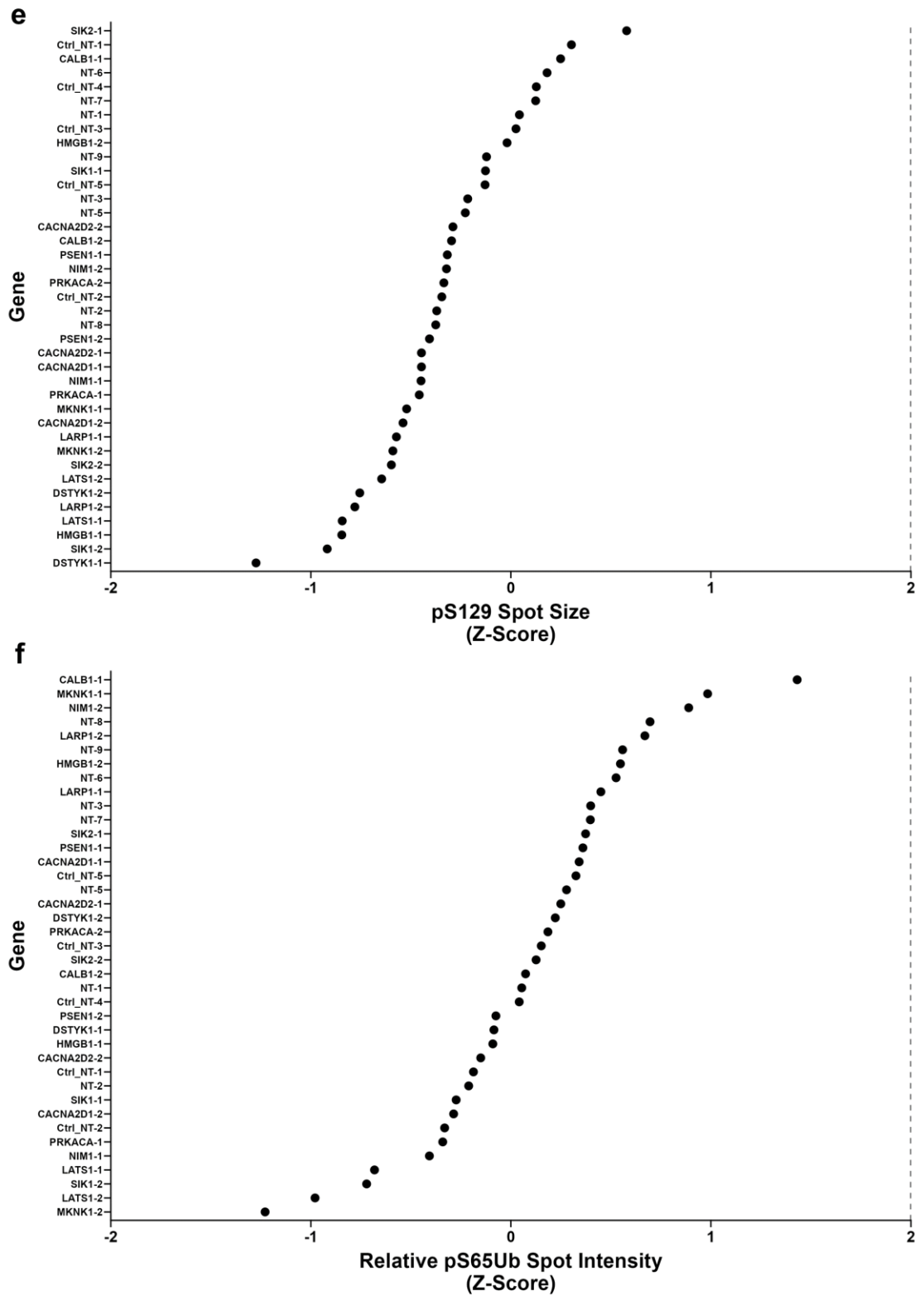
Figure 52. Primary screening readouts in cortical neurons. a) to f) Quantification of readouts from the primary screen from cortical neurons. Dashed lines identify the cutoff used to classify hit or non-hit genes, at score = ±2 and hit genes are labelled in red. N = 3 independent differentiations.


a
Gene
CALB1-1
NT-3
SIK2-2
NT-7
LARP1-2
CALB1-2
Ctrl_NT-2
NT-9
Ctrl_NT-1
LATS1-2
Ctrl_NT-3
PRKACA-2
MKNK1-1
Ctrl_NT-5
NT-8
NT-2
NT-5
Ctrl_NT-4
CACNA2D1-2
NIM1-2
LARP1-1
NT-6
DSTYK1-1
CACNA2D1-1
NT-1
PSEN1-2
LATS1-1
CACNA2D2-2
HMGB1-1
DSTYK1-2
SIK1-2
PSEN1-1
NIM1-1
MKNK1-2
PRKACA-1
HMGB1-2
CACNA2D2-1
SIK2-1
SIK1-1
SIK1-1
-2
-1
0
1
2
Number of MAP2+ Cells
(Z-Score)


b
Gene
SIK1-1
SIK2-1
MKNK1-2
CALB1-1
DSTYK1-2
DSTYK1-1
PRKACA-1
LARP1-2
NT-6
Ctrl_NT-1
CACNA2D2-2
NT-1
NIM1-2
LATS1-1
HMGB1-2
NIM1-1
CACNA2D2-1
Ctrl_NT-4
NT-5
HMGB1-1
CACNA2D1-2
CACNA2D1-1
PRKACA-2
PSEN1-2
NT-2
NT-8
PSEN1-1
Ctrl_NT-5
CALB1-2
NT-3
Ctrl_NT-3
NT-9
Ctrl_NT-2
LATS1-2
MKNK1-1
LARP1-1
SIK2-2
SIK1-2
NT-7
-2
-1
0
1
2
Total pS129 Spot Area
(Z-Score)


c
Gene
SIK2-1
CALB1-1
Ctrl_NT-1
SIK1-1
NT-2
Ctrl_NT-4
NT-1
MKNK1-2
NT-5
NT-8
DSTYK1-2
DSTYK1-1
NT-6
CALB1-2
CACNA2D2-2
PRKACA-2
Ctrl_NT-5
Ctrl_NT-2
CACNA2D1-1
Ctrl_NT-3
HMGB1-2
NT-9
NT-3
PRKACA-1
CACNA2D1-2
SIK2-2
NIM1-1
NIM1-2
CACNA2D2-1
PSEN1-1
PSEN1-2
NT-7
HMGB1-1
LARP1-2
SIK1-2
LATS1-1
LARP1-1
LATS1-2
MKNK1-1
-2
-1
0
1
2
Relative pS129 Spot Intensity
(Z-Score)


d
Gene
SIK2-1
CALB1-1
Ctrl_NT-1
NT-2
NT-8
Ctrl_NT-4
NT-1
SIK1-1
Ctrl_NT-2
NT-5
CALB1-2
NT-6
DSTYK1-2
DSTYK1-1
MKNK1-2
CACNA2D2-2
Ctrl_NT-5
CACNA2D1-1
Ctrl_NT-3
NT-9
SIK2-2
PRKACA-2
CACNA2D1-2
LARP1-2
PRKACA-1
SIK1-2
NT-3
HMGB1-1
NIM1-1
PSEN1-1
HMGB1-2
NIM1-2
NT-7
LATS1-1
PSEN1-2
CACNA2D2-1
LARP1-1
MKNK1-1
LATS1-2
-2
-1
0
1
2
Number of pS129 per Area of Cytoplasm
(Z-Score)


e
Gene
SIK2-1
Ctrl_NT-1
CALB1-1
NT-6
Ctrl_NT-4
NT-7
NT-1
Ctrl_NT-3
HMGB1-2
NT-9
SIK1-1
Ctrl_NT-5
NT-3
NT-5
CACNA2D2-2
CALB1-2
PSEN1-1
NIM1-2
PRKACA-2
Ctrl_NT-2
NT-2
NT-8
PSEN1-2
CACNA2D2-1
CACNA2D1-1
NIM1-1
PRKACA-1
MKNK1-1
CACNA2D1-2
LARP1-1
MKNK1-2
SIK2-2
LATS1-2
DSTYK1-2
LARP1-2
LATS1-1
HMGB1-1
SIK1-2
DSTYK1-1
-2
-1
0
1
2
pS129 Spot Size
(Z-Score)
f
Gene
CALB1-1
MKNK1-1
NIM1-2
NT-8
LARP1-2
NT-9
HMGB1-2
NT-6
LARP1-1
NT-3
NT-7
SIK2-1
PSEN1-1
CACNA2D1-1
Ctrl_NT-5
NT-5
CACNA2D2-1
DSTYK1-2
PRKACA-2
Ctrl_NT-3
SIK2-2
CALB1-2
NT-1
Ctrl_NT-4
PSEN1-2
DSTYK1-1
HMGB1-1
CACNA2D2-2
Ctrl_NT-1
NT-2
SIK1-1
CACNA2D1-2
Ctrl_NT-2
PRKACA-1
NIM1-1
LATS1-1
SIK1-2
LATS1-2
MKNK1-2
-2
-1
0
1
2
Relative pS65Ub Spot Intensity
(Z-Score)

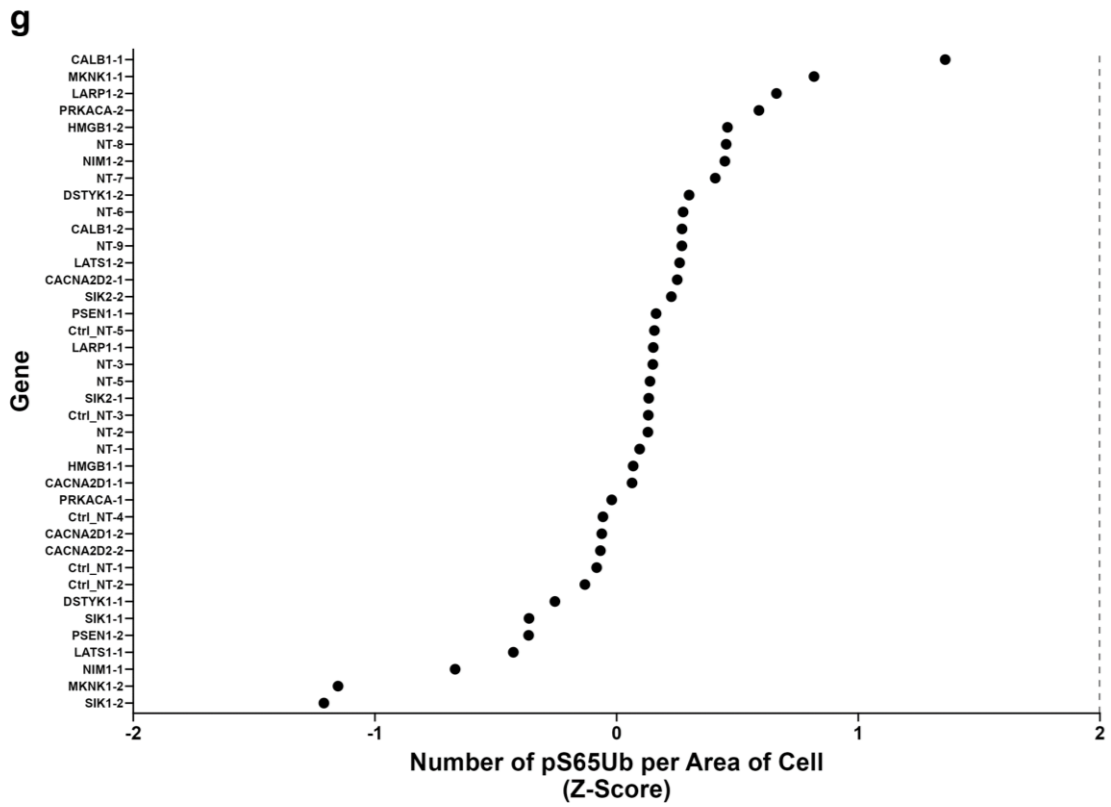
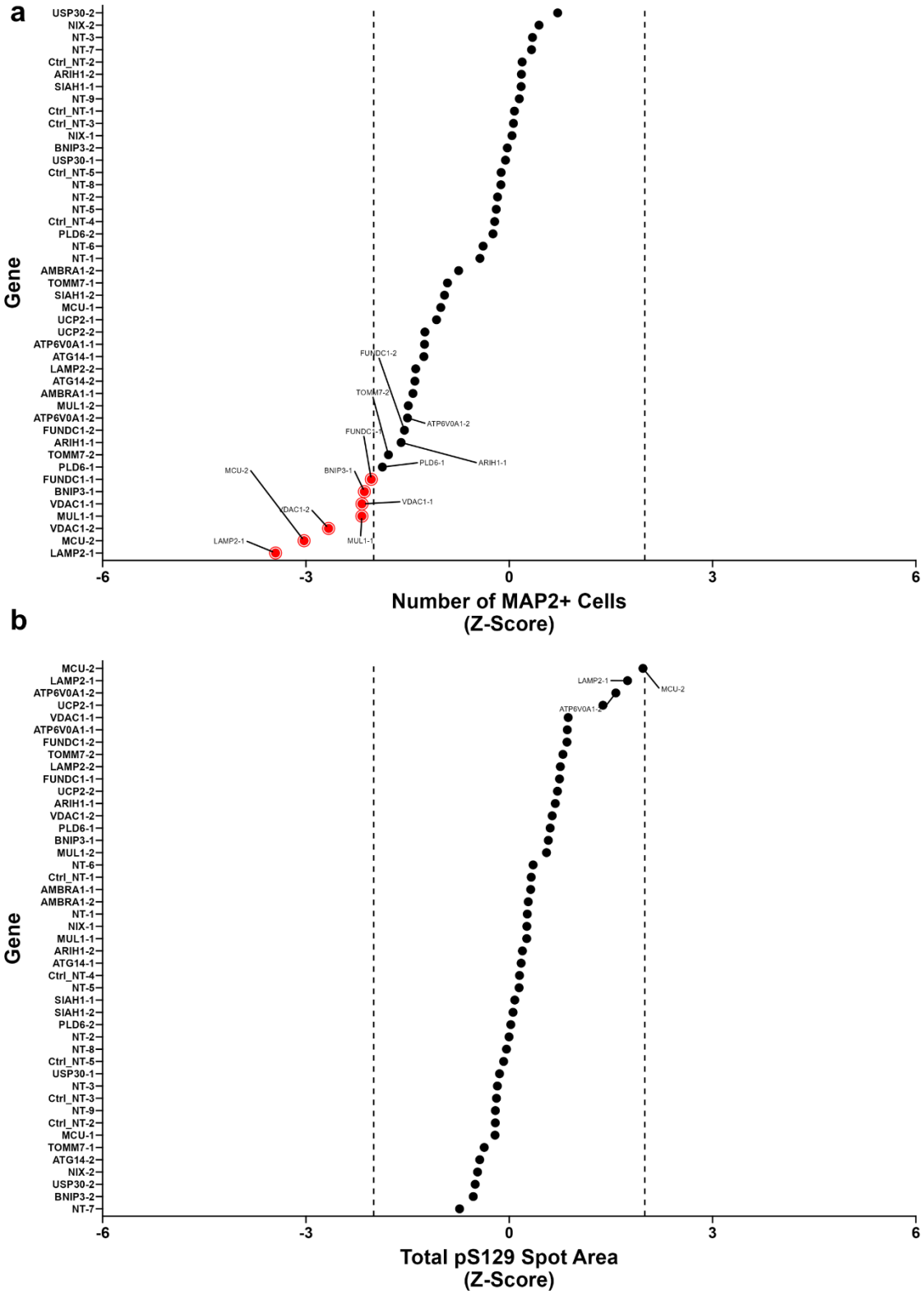
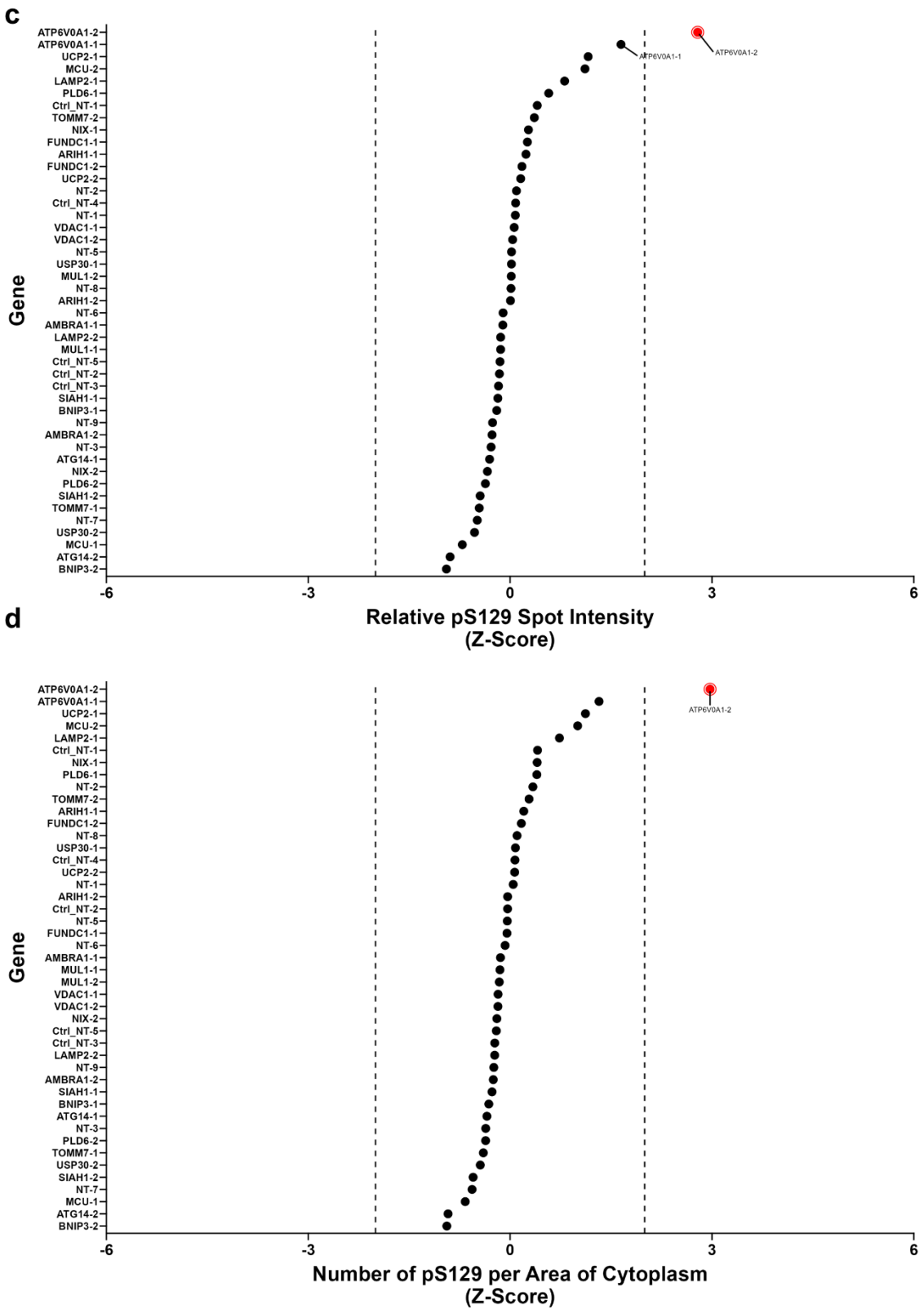
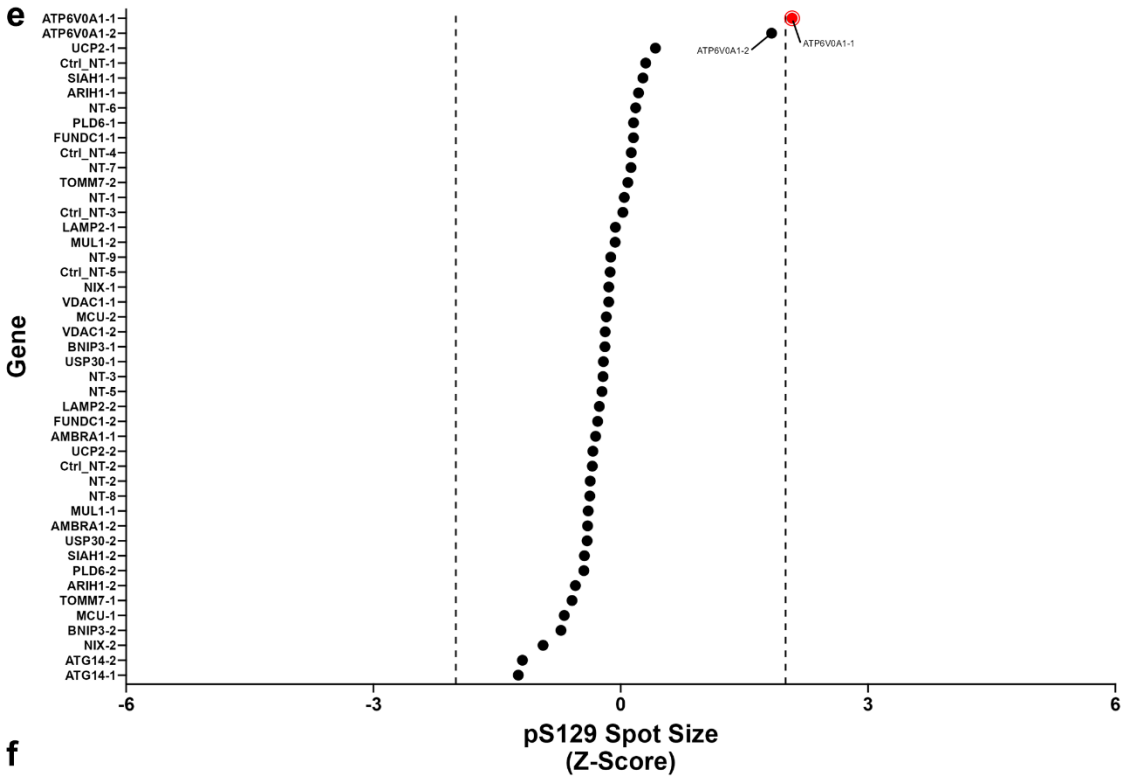
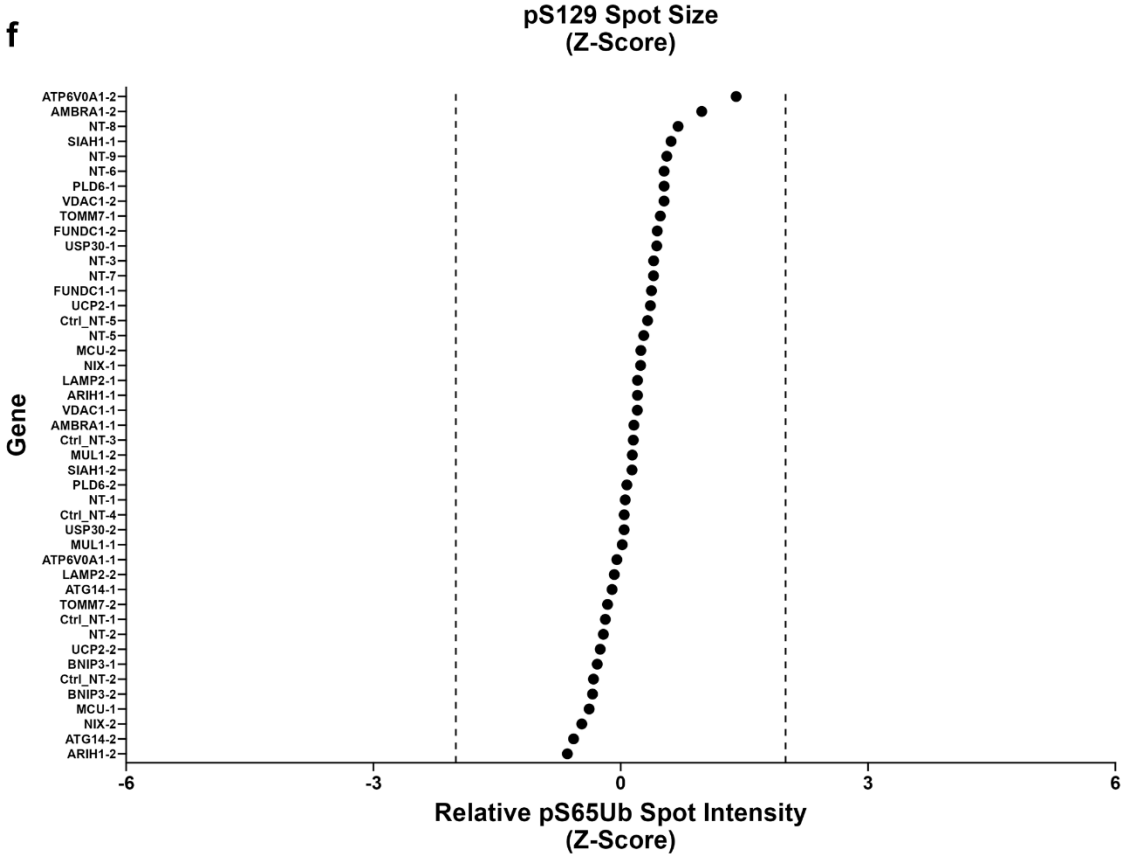


Figure 53. Primary screening readouts for genes in the proteomics datasets in cortical neurons. a) to g) Quantification of readouts from the primary screen of proteomics genes-targeting sgRNAs. Dashed lines identify the cutoff used to classify hit or non-hit genes, at score = ±2 and hit genes are labelled in red. N = 3 independent differentiations. Data is presented as the mean z-score.


a
Gene
USP30-2
NIX-2
NT-3
NT-7
Ctrl_NT-2
ARIH1-2
SIAH1-1
NT-9
Ctrl_NT-1
Ctrl_NT-3
NIX-1
BNIP3-2
USP30-1
Ctrl_NT-5
NT-8
NT-2
NT-5
Ctrl_NT-4
PLD6-2
NT-6
NT-1
AMBRA1-2
TOMM7-1
SIAH1-2
MCU-1
UCP2-1
UCP2-2
ATP6V0A1-1
ATG14-1
LAMP2-2
ATG14-2
AMBRA1-1
MUL1-2
ATP6V0A1-2
FUNDC1-2
ARIH1-1
TOMM7-2
PLD6-1
FUNDC1-1
BNIP3-1
VDAC1-1
MUL1-1
VDAC1-2
MCU-2
LAMP2-1
FUNDC1-2
TOMM7-2
ATP6V0A1-2
FUNDC1-1
ARIH1-1
PLD6-1
MCU-2
BNIP3-1
VDAC1-1
VDAC1-2
MUL1-1
LAMP2-1
-6
-3
0
3
6
Number of MAP2+ Cells
(Z-Score)
b
Gene
MCU-2
LAMP2-1
ATP6V0A1-2
UCP2-1
VDAC1-1
ATP6V0A1-1
FUNDC1-2
TOMM7-2
LAMP2-2
FUNDC1-1
UCP2-2
ARIH1-1
VDAC1-2
PLD6-1
BNIP3-1
MUL1-2
NT-6
Ctrl_NT-1
AMBRA1-1
AMBRA1-2
NT-1
NIX-1
MUL1-1
ARIH1-2
ATG14-1
Ctrl_NT-4
NT-5
SIAH1-1
SIAH1-2
PLD6-2
NT-2
NT-8
Ctrl_NT-5
USP30-1
NT-3
Ctrl_NT-3
NT-9
Ctrl_NT-2
MCU-1
TOMM7-1
ATG14-2
NIX-2
USP30-2
BNIP3-2
NT-7
LAMP2-1
MCU-2
ATP6V0A1-2
-6
-3
0
3
6
Total pS129 Spot Area
(Z-Score)


c
Gene
ATP6V0A1-2
ATP6V0A1-1
UCP2-1
MCU-2
LAMP2-1
PLD6-1
Ctrl_NT-1
TOMM7-2
NIX-1
FUNDC1-1
ARIH1-1
FUNDC1-2
UCP2-2
NT-2
Ctrl_NT-4
NT-1
VDAC1-1
VDAC1-2
NT-5
USP30-1
MUL1-2
NT-8
ARIH1-2
NT-6
AMBRA1-1
LAMP2-2
MUL1-1
Ctrl_NT-5
Ctrl_NT-2
Ctrl_NT-3
SIAH1-1
BNIP3-1
NT-9
AMBRA1-2
NT-3
ATG14-1
NIX-2
PLD6-2
SIAH1-2
TOMM7-1
NT-7
USP30-2
MCU-1
ATG14-2
BNIP3-2
-6
-3
0
3
6
Relative pS129 Spot Intensity
(Z-Score)
d
Gene
ATP6V0A1-2
ATP6V0A1-1
UCP2-1
MCU-2
LAMP2-1
Ctrl_NT-1
NIX-1
PLD6-1
NT-2
TOMM7-2
ARIH1-1
FUNDC1-2
NT-8
USP30-1
Ctrl_NT-4
UCP2-2
NT-1
ARIH1-2
Ctrl_NT-2
NT-5
FUNDC1-1
NT-6
AMBRA1-1
MUL1-1
MUL1-2
VDAC1-1
VDAC1-2
NIX-2
Ctrl_NT-5
Ctrl_NT-3
LAMP2-2
NT-9
AMBRA1-2
SIAH1-1
BNIP3-1
ATG14-1
NT-3
PLD6-2
TOMM7-1
USP30-2
SIAH1-2
NT-7
MCU-1
ATG14-2
BNIP3-2
-6
-3
0
3
6
Number of pS129 per Area of Cytoplasm
(Z-Score)


e
Gene
ATP6V0A1-1
ATP6V0A1-2
UCP2-1
Ctrl_NT-1
SIAH1-1
ARIH1-1
NT-6
PLD6-1
FUNDC1-1
Ctrl_NT-4
NT-7
TOMM7-2
NT-1
Ctrl_NT-3
LAMP2-1
MUL1-2
NT-9
Ctrl_NT-5
NIX-1
VDAC1-1
MCU-2
VDAC1-2
BNIP3-1
USP30-1
NT-3
NT-5
LAMP2-2
FUNDC1-2
AMBRA1-1
UCP2-2
Ctrl_NT-2
NT-2
NT-8
MUL1-1
AMBRA1-2
USP30-2
SIAH1-2
PLD6-2
ARIH1-2
TOMM7-1
MCU-1
BNIP3-2
NIX-2
ATG14-2
ATG14-1
ATP6V0A1-2
ATP6V0A1-1
-6
-3
0
3
6
pS129 Spot Size
(Z-Score)


f
Gene
ATP6V0A1-2
AMBRA1-2
NT-8
SIAH1-1
NT-9
NT-6
PLD6-1
VDAC1-2
TOMM7-1
FUNDC1-2
USP30-1
NT-3
NT-7
FUNDC1-1
UCP2-1
Ctrl_NT-5
NT-5
MCU-2
NIX-1
LAMP2-1
ARIH1-1
VDAC1-1
AMBRA1-1
Ctrl_NT-3
MUL1-2
SIAH1-2
PLD6-2
NT-1
Ctrl_NT-4
USP30-2
MUL1-1
ATP6V0A1-1
LAMP2-2
ATG14-1
TOMM7-2
Ctrl_NT-1
NT-2
UCP2-2
BNIP3-1
Ctrl_NT-2
BNIP3-2
MCU-1
NIX-2
ATG14-2
ARIH1-2
-6
-3
0
3
6
Relative pS65Ub Spot Intensity
(Z-Score)

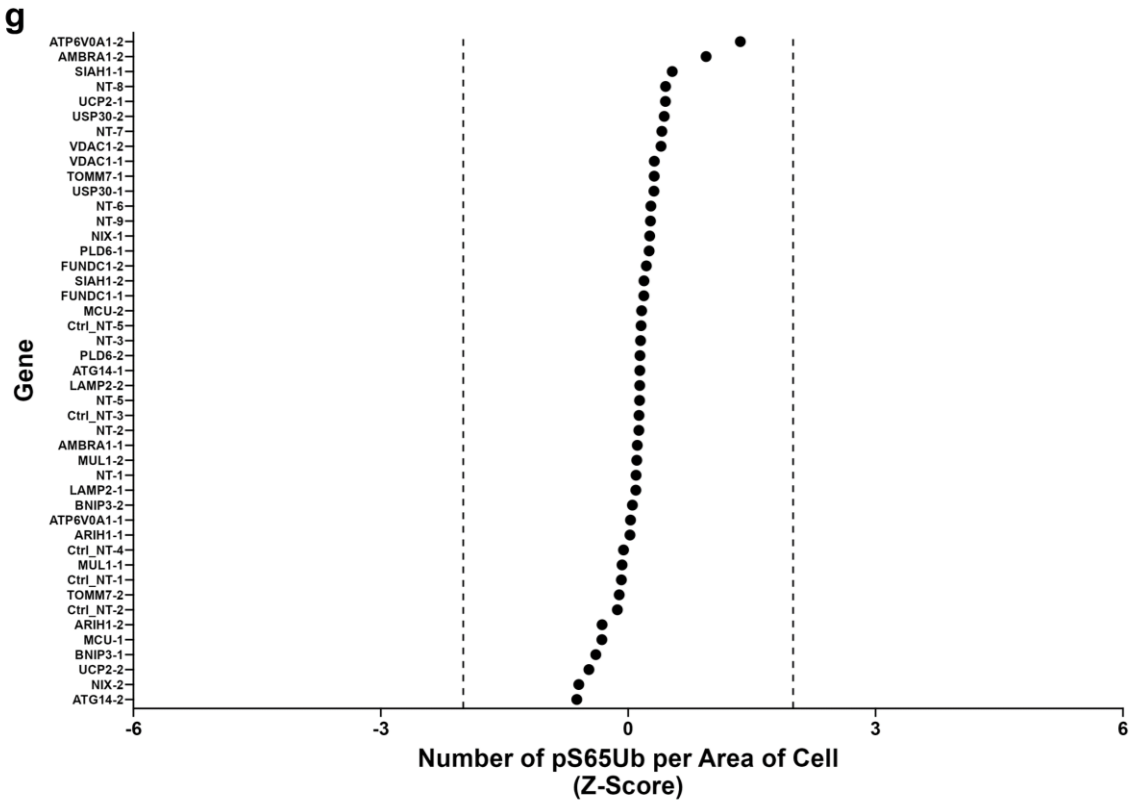


Figure 54. Screening readouts for the mechanistic library of genes targeting mitochondria, lysosomes and autophagy. a) to g) Quantification of readouts from the screen of mechanistic genes. Dashed lines identify the cutoff used to classify hit or non-hit genes, at score = ±2 and hit genes are labelled in red. N = 3 independent differentiations. Data is presented as the mean z-score.

References

Abdelmotilib H, Maltbie T, Delic V, Liu Z, Hu X, Fraser KB, Moehle MS, Stoyka L, Anabtawi N, Krendelchtchikova V *et al* (2017) α-Synuclein fibril-induced inclusion spread in rats and mice correlates with dopaminergic Neurodegeneration. *Neurobiol Dis* 105: 84–98

Adriaenssens E, Schaar S, Cook ASI, Stuke JFM, Sawa-Makarska J, Nguyen TN, Ren X, Schuschnig M, Romanov J, Khuu G *et al* (2025) Reconstitution of BNIP3/NIX-mitophagy initiation reveals hierarchical flexibility of the autophagy machinery. *Nat Cell Biol* 27: 1272–1287

Aguirre AJ, Meyers RM, Weir BA, Vazquez F, Zhang CZ, Ben-David U, Cook A, Ha G, Harrington WF, Doshi MB *et al* (2016) Genomic Copy Number Dictates a Gene-Independent Cell Response to CRISPR/Cas9 Targeting. *Cancer Discov* 6: 914–929

Aharon-Peretz J, Rosenbaum H, Gershoni-Baruch R Mutations in the Glucocerebrosidase Gene and Parkinson's Disease in Ashkenazi Jews. *New Engl J Med* 351: 1972–1977

Alam P, Bousset L, Melki R, Otzen DE (2019) α-synuclein oligomers and fibrils: a spectrum of species, a spectrum of toxicities. *J Neurochem* 150: 522–534

Alerasool N, Segal D, Lee H, Taipale M (2020) An efficient KRAB domain for CRISPRi applications in human cells. *Nat Methods* 17: 1093–1096

Alvarez-Erviti L, Rodriguez-Oroz MC, Cooper JM, Caballero C, Ferrer I, Obeso JA, Schapira AH (2010) Chaperone-mediated autophagy markers in Parkinson disease brains. *Arch Neurol* 67: 1464–1472

Baden P, Perez MJ, Raji H, Bertoli F, Kalb S, Illescas M, Spanos F, Giuliano C, Calogero AM, Oldrati M *et al* (2023) Glucocerebrosidase is imported into mitochondria and preserves complex I integrity and energy metabolism. *Nat Commun* 14: 1930

Badman J, Parracino A, Kumar R, Tambaro S (2025) Insights into the intramembrane protease SPPL2b and its substrates: Functions and disease implications. *Sci Signal* 18: eadt2272

Bandres-Ciga S, Saez-Atienzar S, Kim JJ, Makarious MB, Faghri F, Diez-Fairen M, Iwaki H, Leonard H, Botia J, Ryten M, *et al* (2020) Large-scale pathway specific polygenic risk and transcriptomic community network analysis identifies novel functional pathways in Parkinson disease. *Acta Neuropathol* 140: 341–358

Barabási A-L, Gulbahce N, Loscalzo J (2011) Network medicine: a network-based approach to human disease. *Nat Rev Genet* 12: 56–68

Beccano-Kelly DA, Cherubini M, Mousba Y, Cramb KML, Giussani S, Caiazza MC, Rai P, Vingill S, Bengoa-Vergniory N, Ng B *et al* (2023) Calcium dysregulation combined with mitochondrial failure and electrophysiological maturity converge in Parkinson's iPSC-dopamine neurons. *iScience* 26: 107044

Bel-Vialar S, Medevielle F, Pituello F (2007) The on/off of Pax6 controls the tempo of neuronal differentiation in the developing spinal cord. *Dev Biol* 305: 659–673

Bellucci A, Navarria L, Zaltieri M, Falarti E, Bodei S, Sigala S, Battistin L, Spillantini M, Missale C, Spano P (2011) Induction of the unfolded protein response by α-synuclein in experimental models of Parkinson's disease. *J Neurochem* 116: 588–605

Bengoa-Vergniory N, Faggiani E, Ramos-Gonzalez P, Kirkiz E, Connor-Robson N, Brown LV, Siddique I, Li Z, Vingill S, Cioroch M *et al* (2020) CLR01 protects dopaminergic neurons in vitro and in mouse models of Parkinson's disease. *Nat Commun* 11: 4885

Bérard M, Sheta R, Malvaut S, Rodriguez-Aller R, Teixeira M, Idi W, Turmel R, Alpaugh M, Dubois M, Dahmene M *et al* (2022) A light-inducible protein clustering system for in vivo analysis of α-synuclein aggregation in Parkinson disease. *PLOS Biol* 20: e3001578

Bergström P, Agholme L, Nazir FH, Satir TM, Toombs J, Wellington H, Strandberg J, Bontell TO, Kvartsberg H, Holmström M *et al* (2016) Amyloid precursor protein expression and processing are differentially regulated during cortical neuron differentiation. *Sci Rep* 6: 29200

Betarbet R, Sherer TB, MacKenzie G, Garcia-Osuna M, Panov AV, Greenamyre JT (2000) Chronic systemic pesticide exposure reproduces features of Parkinson's disease. *Nat Neurosci* 3: 1301–1306

Betzer C, Lassen LB, Olsen A, Kofoed RH, Reimer L, Gregersen E, Zheng J, Calì T, Gai WP, Chen T *et al* (2018) Alpha-synuclein aggregates activate calcium pump SERCA leading to calcium dysregulation. *EMBO Rep* 19

Bhore N, Bogacki EC, O'Callaghan B, Plun-Favreau H, Lewis PA & Herbst S (2024) Common genetic risk for Parkinson's disease and dysfunction of the endo-lysosomal system. *Philos Trans R Soc Lond B Biol Sci* 379: 20220517

Bhujabal Z, Birgisdottir Å B, Sjøttem E, Brenne HB, Øvervatn A, Habisov S, Kirkin V, Lamark T, Johansen T (2017) FKBP8 recruits LC3A to mediate Parkin-independent mitophagy. *EMBO Rep* 18: 947–961

Billingsley KJ, Barbosa IA, Bandrés-Ciga S, Quinn JP, Bubb VJ, Deshpande C, Botia JA, Reynolds RH, Zhang D, Simpson MA, *et al* (2019) Mitochondria function associated genes contribute to Parkinson's Disease risk and later age at onset. *NPJ Parkinsons Dis* 5: 8

Bingol B, Tea JS, Phu L, Reichelt M, Bakalarski CE, Song Q, Foreman O, Kirkpatrick DS, Sheng M (2014) The mitochondrial deubiquitinase USP30 opposes parkin-mediated mitophagy. *Nature* 510: 370–375

Birol M, Wojcik SP, Miranker AD & Rhoades E (2019) Identification of N-linked glycans as specific mediators of neuronal uptake of acetylated α-Synuclein. *PLOS Biol* 17: e3000318

Blauwendraat C, Heilbron K, Vallerga CL, Bandres-Ciga S, von Coelln R, Pihlstrøm L, Simón-Sánchez J, Schulte C, Sharma M, Krohn L, *et al* (2019) Parkinson's disease age at onset genome-wide association study: Defining heritability, genetic loci, and α-synuclein mechanisms. *Mov Disord* 34: 866–875

Blauwendraat C, Reed X, Krohn L, Heilbron K, Bandres-Ciga S, Tan M, Gibbs JR, Hernandez DG, Kumaran R, Langston R *et al* (2020) Genetic modifiers of risk and age at onset in GBA associated Parkinson's disease and Lewy body dementia. *Brain* 143: 234–248

Bloem BR, Okun MS, Klein C (2021) Parkinson's disease. *Lancet* 397: 2284–2303

Boman A, Svensson S, Boxer A, Rojas JC, Seeley WW, Karydas A, Miller B, Kågedal K, Svenningsson P (2016) Distinct Lysosomal Network Protein Profiles in Parkinsonian Syndrome Cerebrospinal Fluid. *J Parkinsons Dis* 6: 307–315

Bonello F, Hassoun S-M, Mouton-Liger F, Shin YS, Muscat A, Tesson C, Lesage S, Beart PM, Brice A, Krupp J *et al* (2019) LRRK2 impairs PINK1/Parkin-dependent mitophagy via its kinase activity: pathologic insights into Parkinson's disease. *Hum Mol Genet* 28: 1645–1660

Bonifati V, Rizzu P, van Baren MJ, Schaap O, Breedveld GJ, Krieger E, Dekker MCJ, Squitieri F, Ibanez P, Joosse M *et al* (2003) Mutations in the DJ-1 Gene Associated with Autosomal Recessive Early-Onset Parkinsonism. *Science* 299: 256–259

Book A, Guella I, Candido T, Brice A, Hattori N, Jeon B, Farrer MJ (2018) A Meta-Analysis of α-Synuclein Multiplication in Familial Parkinsonism. *Front Neurol* 9: 1021

Borghi R, Marchese R, Negro A, Marinelli L, Forloni G, Zaccheo D, Abbruzzese G & Tabaton M (2000) Full length α-synuclein is present in cerebrospinal fluid from Parkinson's disease and normal subjects. *Neurosci Lett* 287: 65–67

Bousset L, Pieri L, Ruiz-Arlandis G, Gath J, Jensen PH, Habenstein B, Madiona K, Olieric V, Böckmann A, Meier BH *et al* (2013) Structural and functional characterization of two alpha-synuclein strains. *Nat Commun* 4: 2575

Braak H, Braak E (2000) Pathoanatomy of Parkinson's disease. *J Neurol* 247 Suppl 2: Ii3–10
Braak H, Del Tredici K, Rüb U, de Vos RA, Jansen Steur EN, Braak E (2003) Staging of brain pathology related to sporadic Parkinson's disease. *Neurobiol Aging* 24: 197–211

Brás IC & Outeiro TF (2021) Alpha-Synuclein: Mechanisms of Release and Pathology Progression in Synucleinopathies. *Cells* 10: 375

Bräuer S, Schniewind I, Dinter E & Falkenburger BH (2025) Recursive seed amplification detects distinct α-synuclein strains in cerebrospinal fluid of patients with Parkinson's disease. *Acta Neuropathol Commun* 13: 13

Brockmann K, Schulte C, Hauser A-K, Lichtner P, Huber H, Maetzler W, Berg D & Gasser T (2013) SNCA: Major genetic modifier of age at onset of Parkinson's disease. *Mov Disord* 28: 1217–1221

Brockmann K, Srulijes K, Pflederer S, Hauser A-K, Schulte C, Maetzler W, Gasser T & Berg D (2015) GBA-associated Parkinson's disease: Reduced survival and more rapid progression in a prospective longitudinal study. *Mov Disord* 30: 407–411

Brown HJ, Fan RZ, Bell R, Salehe SS, Martínez CM, Lai Y, Tieu K (2025) Imbalanced mitochondrial dynamics in human PD and α-synuclein mouse brains. *Neurobiol Dis* 212: 106976

Bruick RK (2000) Expression of the gene encoding the proapoptotic Nip3 protein is induced by hypoxia. *Proc Natl Acad Sci USA* 97: 9082–9087

Burman JL, Pickles S, Wang C, Sekine S, Vargas JNS, Zhang Z, Youle AM, Nezich CL, Wu X, Hammer JA *et al* (2017) Mitochondrial fission facilitates the selective mitophagy of protein aggregates. *J Cell Biol* 216: 3231–3247

Burré J, Sharma M, Tsetsenis T, Buchman V, Etherton MR & Südhof TC (2010) Alpha-synuclein promotes SNARE-complex assembly in vivo and in vitro. *Science* 329: 1663–1667

Burré J, Sharma M, Südhof TC (2014) α-Synuclein assembles into higher-order multimers upon membrane binding to promote SNARE complex formation. *Proc Natl Acad Sci USA*111: E4274–4283

Byers B, Cord B, Nguyen HN, Schüle B, Fenno L, Lee PC, Deisseroth K, Langston JW, Pera RR, Palmer TD (2011) SNCA Triplication Parkinson's Patient's iPSC-derived DA Neurons Accumulate α-Synuclein and Are Susceptible to Oxidative Stress. *PLoS ONE* 6: e26159

Campêlo CLdC, Silva RH (2017) Genetic Variants in SNCA and the Risk of Sporadic Parkinson's Disease and Clinical Outcomes: A Review. *Parkinson's Dis* 2017: 4318416

Casalino E, Stine LB, Corin AJ, Thai C-T, Quiroz J, Wilson SC, Labow M, Mittal S (2022) A novel high-throughput screening strategy for targeting alpha-synuclein and other long-lived proteins. *SLAS Discov* 27: 349–357

Cascella R, Bigi A, Cremades N, Cecchi C (2022) Effects of oligomer toxicity, fibril toxicity and fibril spreading in synucleinopathies. *Cell Mol Life Sci* 79: 174

Cavaliere F, Cerf L, Dehay B, Ramos-Gonzalez P, De Giorgi F, Bourdenx M, Bessede A, Obeso JA, Matute C, Ichas F *et al* (2017) In vitro α-synuclein neurotoxicity and spreading among neurons and astrocytes using Lewy body extracts from Parkinson disease brains. *Neurobiol Dis* 103: 101–112

Chandra S, Gallardo G, Fernández-Chacón R, Schlüter OM & Südhof TC (2005) Alpha-synuclein cooperates with CSPalpha in preventing neurodegeneration. *Cell* 123: 383–396

Chartier-Harlin MC, Kachergus J, Roumier C, Mouroux V, Douay X, Lincoln S, Levecque C, Larvor L, Andrieux J, Hulihan M *et al* (2004) Alpha-synuclein locus duplication as a cause of familial Parkinson's disease. *Lancet* 364: 1167–1169

Chattaragada MS, Riganti C, Sassoe M, Principe M, Santamorena MM, Roux C, Curcio C, Evangelista A, Allavena P, Salvia R *et al* (2018) FAM49B, a novel regulator of mitochondrial function and integrity that suppresses tumor metastasis. *Oncogene* 37: 697–709

Chen C, McDonald D, Blain A, Mossman E, Atkin K, Marusich MF, Capaldi R, Bone L, Smith A, Filby A *et al* (2023) Parkinson's disease neurons exhibit alterations in mitochondrial quality control proteins. *npj Parkinson's Dis* 9: 120

Chen M, Maimaitili M, Habekost M, Gill KP, Mermet-Joret N, Nabavi S, Febbraro F, Denham M (2020) Rapid generation of regionally specified CNS neurons by sequential patterning and conversion of human induced pluripotent stem cells. *Stem Cell Res* 48: 101945

Chen K, Martens YA, Meneses A, Ryu DH, Lu W, Raulin AC, Li F, Zhao J, Chen Y, Jin Y, *et al* (2022) LRP1 is a neuronal receptor for α-synuclein uptake and spread. *Mol Neurodegener* 17: 57

Chi C, Leonard A, Knight WE, Beussman KM, Zhao Y, Cao Y, Londono P, Aune E, Trembley MA, Small EM *et al* (2019) LAMP-2B regulates human cardiomyocyte function by mediating autophagosome-lysosome fusion. *Proc Natl Acad Sci USA* 116: 556–565

Chinta SJ, Mallajosyula JK, Rane A, Andersen JK (2010) Mitochondrial alpha-synuclein accumulation impairs complex I function in dopaminergic neurons and results in increased mitophagy in vivo. *Neurosci Lett* 486: 235–239

Cho SW, Kim S, Kim JM, Kim J-S (2013) Targeted genome engineering in human cells with the Cas9 RNA-guided endonuclease. *Nature Biotechnol* 31: 230–232

Choi ML, Chappard A, Singh BP, Maclachlan C, Rodrigues M, Fedotova EI, Berezhnov AV, De S, Peddie CJ, Athauda D *et al* (2022) Pathological structural conversion of α-synuclein at the mitochondria induces neuronal toxicity. *Nature Neurosci* 25: 1134–1148

Choubey V, Safiulina D, Vaarmann A, Cagalinec M, Wareski P, Kuum M, Zharkovsky A, Kaasik A (2011) Mutant A53T alpha-synuclein induces neuronal death by increasing mitochondrial autophagy. *J Biol Chem* 286: 10814–10824

Chu Y, Dodiya H, Aebischer P, Olanow CW, Kordower JH (2009) Alterations in lysosomal and proteasomal markers in Parkinson's disease: relationship to alpha-synuclein inclusions. *Neurobiol Dis* 35: 385–398

Chu Y, Hirst WD, Federoff HJ, Harms AS, Stoessl AJ & Kordower JH (2024) Nigrostriatal tau pathology in parkinsonism and Parkinson's disease. *Brain* 147: 444–457

Chung CY, Khurana V, Auluck PK, Tardiff DF, Mazzulli JR, Soldner F, Baru V, Lou Y, Freyzon Y, Cho S *et al* (2013) Identification and rescue of α-synuclein toxicity in Parkinson patient-derived neurons. *Science* 342: 983–987

Clark LN, Ross BM, Wang Y, Mejia-Santana H, Harris J, Louis ED, Cote LJ, Andrews H, Fahn S, Waters C, *et al* (2007) Mutations in the glucocerebrosidase gene are associated with early-onset Parkinson disease. *Neurology* 69: 1270–1277

Coelho M, Ferreira JJ (2012) Late-stage Parkinson disease. *Nat Rev Neurol* 8: 435–442

Colla E, Coune P, Liu Y, Pletnikova O, Troncoso JC, Iwatsubo T, Schneider BL, Lee MK (2012) Endoplasmic reticulum stress is important for the manifestations of α-synucleinopathy in vivo. *J Neurosci* 32: 3306–3320

Cong L, Ran FA, Cox D, Lin S, Barretto R, Habib N, Hsu PD, Wu X, Jiang W, Marraffini LA *et al* (2013) Multiplex Genome Engineering Using CRISPR/Cas Systems. *Science* 339: 819–823

Cooper AA, Gitler AD, Cashikar A, Haynes CM, Hill KJ, Bhullar B, Liu K, Xu K, Strathearn KE, Liu F *et al* (2006) Alpha-synuclein blocks ER-Golgi traffic and Rab1 rescues neuron loss in Parkinson's models. *Science* 313: 324–328

Cooper CA, Jain N, Gallagher MD, Weintraub D, Xie SX, Berlyand Y, Espay AJ, Quinn J, Edwards KL, Montine T, *et al* (2017) Common variant rs356182 near SNCA defines a Parkinson's disease endophenotype. *Ann Clin Transl Neurol* 4: 15–25

Cooper O, Seo H, Andrabi S, Guardia-Laguarta C, Graziotto J, Sundberg M, McLean JR, Carrillo-Reid L, Xie Z, Osborn T *et al* (2012) Pharmacological rescue of mitochondrial deficits in iPSC-derived neural cells from patients with familial Parkinson's disease. *Sci Transl Med* 4: 141ra190

Cornacchia D, Studer L (2017) Back and forth in time: Directing age in iPSC-derived lineages. *Brain Rese* 1656: 14–26

Courte J, Bousset L, Boxberg YV, Villard C, Melki R, Peyrin J-M (2020) The expression level of alpha-synuclein in different neuronal populations is the primary determinant of its prion-like seeding. *Sci Rep* 10: 4895

Cramb KML, Belen Malpartida A, Caiazza MC, Ryan B, Wade-Martins R (2023) Differentiation of human Dopamine Neurons (DaNs) from induced pluripotent stem cells (iPSCs). *Protocols.io*

Cronin KD, Ge D, Manninger P, Linnertz C, Rossoshek A, Orrison BM, Bernard DJ, El-Agnaf OMA, Schlossmacher MG, Nussbaum RL, et al (2009) Expansion of the Parkinson disease-associated SNCA-Rep1 allele upregulates human α-synuclein in transgenic mouse brain. *Hum Mol Genet* 18: 3274–3285

Cuervo AM, Stefanis L, Fredenburg R, Lansbury PT, Sulzer D (2004) Impaired degradation of mutant alpha-synuclein by chaperone-mediated autophagy. *Science* 305: 1292–1295

Dada ST, Hardenberg MC, Toprakcioglu Z, Mrugalla LK, Cali MP, McKeon MO, Klimont E, Michaels TCT, Knowles TPJ, Vendruscolo M (2023) Spontaneous nucleation and fast aggregate-dependent proliferation of α-synuclein aggregates within liquid condensates at neutral pH. *Proc Natl Acad Sci USA* 120: e2208792120

Das G, Misra AK, Das SK, Ray K & Ray J (2009) Microtubule-associated protein tau (*MAPT*) influences the risk of Parkinson's disease among Indians. *Neurosci Lett* 460: 16–20

Davis AA, Andruska KM, Benitez BA, Racette BA, Perlmutter JS & Cruchaga C (2016) Variants in *GBA*, *SNCA*, and *MAPT* influence Parkinson disease risk, age at onset, and progression. *Neurobiol Aging* 37: 209.e1-209.e7

Davis MY, Johnson CO, Leverenz JB, Weintraub D, Trojanowski JQ, Chen-Plotkin A, Van Deerlin VM, Quinn JF, Chung KA, Peterson-Hiller AL, *et al* (2016) Association of GBA Mutations and the E326K Polymorphism With Motor and Cognitive Progression in Parkinson Disease. *JAMA Neurol* 73: 1217–1224

Day JO, Mullin S (2021) The Genetics of Parkinson's Disease and Implications for Clinical Practice. *Genes (Basel)* 12

de Oliveira GAP, Silva JL (2019) Alpha-synuclein stepwise aggregation reveals features of an early onset mutation in Parkinson's disease. *Commun Biol* 2: 374

Dehay B, Bové J, Rodríguez-Muela N, Perier C, Recasens A, Boya P, Vila M (2010) Pathogenic lysosomal depletion in Parkinson's disease. *J Neurosci* 30: 12535–12544

Dehay B, Ramirez A, Martinez-Vicente M, Perier C, Canron MH, Doudnikoff E, Vital A, Vila M, Klein C, Bezard E (2012) Loss of P-type ATPase ATP13A2/PARK9 function induces general lysosomal deficiency and leads to Parkinson disease neurodegeneration. *Proc Natl Acad Sci USA* 109: 9611–9616

Dehestani M, Liu H, Sreelatha AAK, Schulte C, Bansal V & Gasser T (2022) Mitochondrial and autophagy-lysosomal pathway polygenic risk scores predict Parkinson's disease. *Mol Cell Neurosci* 121: 103751

Delenclos M, Burgess JD, Lamprokostopoulou A, Outeiro TF, Vekrellis K, McLean PJ (2019) Cellular models of alpha-synuclein toxicity and aggregation. *J Neurochem* 150: 566–576

Del Tredici K & Braak H (2016) Sporadic Parkinson's disease: development and distribution of α-synuclein pathology. *Neuropathol Appl Neurobiol* 42: 33–50

Desplats P, Lee H-J, Bae E-J, Patrick C, Rockenstein E, Crews L, Spencer B, Masliah E, Lee S-J (2009) Inclusion formation and neuronal cell death through neuron-to-neuron transmission of α-synuclein. *Proc Natl Acad Sci USA* 106: 13010–13015

Devi L, Raghavendran V, Prabhu BM, Avadhani NG, Anandatheerthavarada HK (2008) Mitochondrial Import and Accumulation of α-Synuclein Impair Complex I in Human Dopaminergic Neuronal Cultures and Parkinson Disease Brain. *J Biol Chem* 283: 9089–9100

Di Maio R, Barrett PJ, Hoffman EK, Barrett CW, Zharikov A, Borah A, Hu X, McCoy J, Chu CT, Burton EA *et al* (2016) α-Synuclein binds to TOM20 and inhibits mitochondrial protein import in Parkinson's disease. *Sci Transl Med* 8: 342ra378–342ra378

Diao X, Wang F, Becerra-Calixto A, Soto C, Mukherjee A (2021) Induced Pluripotent Stem Cell-Derived Dopaminergic Neurons from Familial Parkinson's Disease Patients Display α-Synuclein Pathology and Abnormal Mitochondrial Morphology. *Cells* doi: 10.3390/cells10092402 [PREPRINT]

Diaz-Ortiz ME, Seo Y, Posavi M, Carceles Cordon M, Clark E, Jain N, Charan R, Gallagher MD, Unger TL, Amari N *et al* (2022) GPNMB confers risk for Parkinson's disease through interaction with α-synuclein. *Science* 377: eabk0637

Ding X, Ren F (2020) Leucine-rich repeat kinase 2 inhibitors: a patent review (2014-present). *Expert Opin Ther Pat* 30: 275–286

Do CB, Tung JY, Dorfman E, Kiefer AK, Drabant EM, Francke U, Mountain JL, Goldman SM, Tanner CM, Langston JW *et al* (2011) Web-Based Genome-Wide Association Study Identifies Two Novel Loci and a Substantial Genetic Component for Parkinson's Disease. *PLOS Genet* 7: e1002141

Doherty KM, Silveira-Moriyama L, Parkkinen L, Healy DG, Farrell M, Mencacci NE, Ahmed Z, Brett FM, Hardy J, Quinn N *et al* (2013) Parkin Disease: A Clinicopathologic Entity? *JAMA Neurol* 70: 571–579

Doostparast Torshizi A, Truong DT, Hou L, Smets B, Whelan CD & Li S (2024) Proteogenomic network analysis reveals dysregulated mechanisms and potential mediators in Parkinson's disease. *Nat Commun* 15: 6430

Dorsey ER, Constantinescu R, Thompson JP, Biglan KM, Holloway RG, Kieburtz K, Marshall FJ, Ravina BM, Schifitto G, Siderowf A *et al* (2007) Projected number of people with Parkinson disease in the most populous nations, 2005 through 2030. *Neurology* 68: 384–386

Dorsey ER, De Miranda BR, Hussain S, Bloem BR, Elbaz A, Llibre-Guerra J, Lo RY, Goldman SM & Tanner CM (2025) Environmental toxicants and Parkinson's disease: recent evidence, risks, and prevention opportunities. *Lancet Neurol* 24: 976–986

Dorsey ER, Elbaz A, Nichols E, Nooshin Abbasi FA-A, Ahmed Abdelalim, Jose C Adsuar, Mustafa Geleto Ansha, Carol Brayne, Jee-Young J Choi, Daniel Collado-Mateo, Nabila Dahodwala, Huyen Phuc Do, Dumessa Edessa, Matthias Endres, Seyed-Mohammad Fereshtehnejad, Kyle J Foreman, Fortune Gbetoho Gankpe, Rahul Gupta, Samer Hamidi, Graeme J Hankey, Simon I Hay, Mohamed I Hegazy, Desalegn T Hibstu, Amir Kasaeian, Yousef Khader, Ibrahim Khalil, Young-Ho Khang, Yun Jin Kim, Yoshihiro Kokubo, Giancarlo Logroscino, João Massano, Norlinah Mohamed Ibrahim, Mohammed A Mohammed, Alireza Mohammadi, Maziar Moradi-Lakeh, Mohsen Naghavi, Binh Thanh Nguyen, Yirga Legesse Nirayo, Felix Akpojene Ogbo, Mayowa Ojo Owolabi, David M Pereira, Maarten J Postma, Mostafa Qorbani, Muhammad Aziz Rahman, Kedir T Roba, Hosein Safari, Saeid Safiri, Maheswar Satpathy, Monika Sawhney, Azadeh Shafieesabet, Mekonnen Sisay Shiferaw, Mari Smith, Cassandra E I Szoeke, Rafael Tabarés-Seisdedos, Nu Thi Truong, Kingsley Nnanna Ukwaja, Narayanaswamy Venketasubramanian, Santos Villafaina, Kidu Gidey Weldegwergs, Ronny Westerman, Tissa Wijeratne, Andrea S Winkler, Bach Tran Xuan, Naohiro Yonemoto, Valery L Feigin, Theo Vos, Christopher J L Murray (2018) Global, regional, and national

burden of Parkinson's disease, 1990-2016: a systematic analysis for the Global Burden of Disease Study 2016. *Lancet Neurol* 17: 939–953

Dumitriu A, Pacheco CD, Wilk JB, Strathearn KE, Latourelle JC, Goldwurm S, Pezzoli G, Rochet J-C, Lindquist S, Myers RH (2011) Cyclin-G-associated kinase modifies α-synuclein expression levels and toxicity in Parkinson's disease: results from the GenePD Study. *Hum Mol Genet* 20: 1478–1487

Edwards TL, Scott WK, Almonte C, Burt A, Powell EH, Beecham GW, Wang L, Züchner S, Konidari I, Wang G *et al* (2010) Genome-Wide Association Study Confirms SNPs in SNCA and the MAPT Region as Common Risk Factors for Parkinson Disease. *Ann Hum Genet* 74: 97–109

El-Agnaf OMA, Salem SA, Paleologou KE, Cooper LJ, Fullwood NJ, Gibson MJ, Curran MD, Court JA, Mann DMA, Ikeda S-I, *et al* (2003) α-Synuclein implicated in Parkinson's disease is present in extracellular biological fluids, including human plasma. *FASEB J* 17: 1–16

El-Agnaf OMA, Salem SA, Paleologou KE, Curran MD, Gibson MJ, Court JA, Schlossmacher MG & Allsop D (2006) Detection of oligomeric forms of α-synuclein protein in human plasma as a potential biomarker for Parkinson's disease. *FASEB J* 20: 419–425

Emin D, Zhang YP, Lobanova E, Miller A, Li X, Xia Z, Dakin H, Sideris DI, Lam JYL, Ranasinghe RT *et al* (2022) Small soluble α-synuclein aggregates are the toxic species in Parkinson's disease. *Nat Commun* 13: 5512

Emmenegger M, De Cecco E, Hruska-Plochan M, Eninger T, Schneider MM, Barth M, Tantardini E, de Rossi P, Bacioglu M, Langston RG, *et al* (2021) LAG3 is not expressed in human and murine neurons and does not modulate α-synucleinopathies. *EMBO Mol Med* 13: EMMM202114745

Endlicher R, Drahota Z, Štefková K, Červinková Z, Kučera O (2023) The Mitochondrial Permeability Transition Pore-Current Knowledge of Its Structure, Function, and Regulation, and Optimized Methods for Evaluating Its Functional State. *Cells* 12

Escott-Price V, Consortium for the IPDG, Nalls MA, Morris HR, Lubbe S, Brice A, Gasser T, Heutink P, Wood NW, Hardy J, *et al* (2015) Polygenic risk of Parkinson disease is correlated with disease age at onset. *Ann Neurology* 77: 582–591

Eskelinen EL, Illert AL, Tanaka Y, Schwarzmann G, Blanz J, Von Figura K, Saftig P (2002) Role of LAMP-2 in lysosome biogenesis and autophagy. *Mol Biol Cell* 13: 3355–3368

Espay AJ, Brundin P, Lang AE (2017) Precision medicine for disease modification in Parkinson disease. *Nat Rev Neurol* 13: 119–126

Espay AJ, Kalia LV, Gan-Or Z, Williams-Gray CH, Bedard PL, Rowe SM, Morgante F, Fasano A, Stecher B, Kauffman MA *et al* (2020) Disease modification and biomarker development in Parkinson disease: Revision or reconstruction? *Neurology* 94: 481–494

Evers B, Jastrzebski K, Heijmans JPM, Grernrum W, Beijersbergen RL, Bernards R (2016) CRISPR knockout screening outperforms shRNA and CRISPRi in identifying essential genes. *Nature Biotechnol* 34: 631–633

Fang T-SZ, Sun Y, Pearce AC, Eleuteri S, Kemp M, Luckhurst CA, Williams R, Mills R, Almond S, Burzynski L, *et al* (2023) Knockout or inhibition of USP30 protects dopaminergic neurons in a Parkinson's disease mouse model. *Nat Commun* 14: 7295

Farrow SL, Cooper AA, O'Sullivan JM (2022a) Redefining the hypotheses driving Parkinson's diseases research. *NPJ Parkinson's Dis* 8: 45

Farrow SL, Schierding W, Gokuladhas S, Golovina E, Fadason T, Cooper AA, O'Sullivan JM (2022b) Establishing gene regulatory networks from Parkinson's disease risk loci. *Brain* 145: 2422–2435

Fernandes HJR, Patikas N, Foskolou S, Field SF, Park JE, Byrne ML, Bassett AR, Metzakopian E (2020) Single-Cell Transcriptomics of Parkinson's Disease Human In Vitro Models Reveals Dopamine Neuron-Specific Stress Responses. *Cell Rep* 33: 108263

Fernandopulle MS, Prestil R, Grunseich C, Wang C, Gan L, Ward ME (2018) Transcription Factor-Mediated Differentiation of Human iPSCs into Neurons. *Curr Protoc Cell Biol* 79: e51

Fiesel FC, Ando M, Hudec R, Hill AR, Castanedes-Casey M, Caulfield TR, Moussaud-Lamodière EL, Stankowski JN, Bauer PO, Lorenzo-Betancor O *et al* (2015) Patho-physiological relevance of PINK1-dependent ubiquitin phosphorylation. *EMBO Rep* 16: 1114–1130

Fløtnes IH, Toker L, Sandnes DA, Castelli M, Mostafavi S, Lura N, Shadad O, Fernandez-Vizarra E, Painous C, Pérez-Soriano A *et al* (2024) Mitochondrial complex I deficiency stratifies idiopathic Parkinson's disease. *Nature Commun* 15: 3631

Foo JN, Chew EGY, Chung SJ, Peng R, Blauwendraat C, Nalls MA, Mok KY, Satake W, Toda T, Chao Y *et al* (2020) Identification of Risk Loci for Parkinson Disease in Asians and Comparison of Risk Between Asians and Europeans: A Genome-Wide Association Study. *JAMA Neurol* 77: 746–754

Franks SNJ, Heon-Roberts R, Ryan BJ (2024) CRISPRi: a way to integrate iPSC-derived neuronal models. *Biochem Soc Trans* 52: 539–551

Freeman D, Cedillos R, Choyke S, Lukic Z, McGuire K, Marvin S, Burrage AM, Sudholt S, Rana A, O'Connor C *et al* (2013) Alpha-synuclein induces lysosomal rupture and cathepsin dependent reactive oxygen species following endocytosis. *PLoS ONE* 8: e62143

Fujiwara H, Hasegawa M, Dohmae N, Kawashima A, Masliah E, Goldberg MS, Shen J, Takio K, Iwatsubo T (2002) α-Synuclein is phosphorylated in synucleinopathy lesions. *Nat Cell Biol* 4: 160–164

Fulco CP, Munschauer M, Anyoha R, Munson G, Grossman SR, Perez EM, Kane M, Cleary B, Lander ES, Engreitz JM (2016) Systematic mapping of functional enhancer-promoter connections with CRISPR interference. *Science* 354: 769–773

Fung HC, Scholz S, Matarin M, Simón-Sánchez J, Hernandez D, Britton A, Gibbs JR, Langefeld C, Stiegert ML, Schymick J *et al* (2006) Genome-wide genotyping in Parkinson's disease and neurologically normal controls: first stage analysis and public release of data. *Lancet Neurol* 5: 911–916

Fusco G, Pape T, Stephens AD, Mahou P, Costa AR, Kaminski CF, Kaminski Schierle GS, Vendruscolo M, Veglia G, Dobson CM *et al* (2016) Structural basis of synaptic vesicle assembly promoted by α-synuclein. *Nat Commun* 7: 12563

Galvagnion C, Buell AK, Meisl G, Michaels TCT, Vendruscolo M, Knowles TPJ, Dobson CM (2015) Lipid vesicles trigger α-synuclein aggregation by stimulating primary nucleation. *NatChem Biol* 11: 229–234

Gan-Or Z, Bar-Shira A, Mirelman A, Gurevich T, Giladi N & Orr-Urtreger A (2012) The Age at Motor Symptoms Onset in LRRK2-Associated Parkinson's Disease is Affected by a Variation in the MAPT Locus: A Possible Interaction. *J Mol Neurosci* 46: 541–544

Gegg ME, Burke D, Heales SJ, Cooper JM, Hardy J, Wood NW, Schapira AH (2012) Glucocerebrosidase deficiency in substantia nigra of parkinson disease brains. *Ann Neurol* 72: 455–463

Geisler S, Holmström KM, Skujat D, Fiesel FC, Rothfuss OC, Kahle PJ, Springer W (2010a) PINK1/Parkin-mediated mitophagy is dependent on VDAC1 and p62/SQSTM1. *Nat Cell Biol* 12: 119–131

Geisler S, Holmström KM, Treis A, Skujat D, Weber SS, Fiesel FC, Kahle PJ, Springer W (2010b) The PINK1/Parkin-mediated mitophagy is compromised by PD-associated mutations. *Autophagy* 6: 871–878

Gilbert LA, Horlbeck MA, Adamson B, Villalta JE, Chen Y, Whitehead EH, Guimaraes C, Panning B, Ploegh HL, Bassik MC *et al* (2014) Genome-Scale CRISPR-Mediated Control of Gene Repression and Activation. *Cell* 159: 647–661

Gilbert LA, Larson MH, Morsut L, Liu Z, Brar GA, Torres SE, Stern-Ginossar N, Brandman O, Whitehead EH, Doudna JA *et al* (2013) CRISPR-mediated modular RNA-guided regulation of transcription in eukaryotes. *Cell* 154: 442–451

Goedert M, Spillantini MG, Del Tredici K, Braak H (2013) 100 years of Lewy pathology. *Nat Rev Neurol* 9: 13–24

Gonçalves SA, Macedo D, Raquel H, Simões PD, Giorgini F, Ramalho JS, Barral DC, Ferreira Moita L, Outeiro TF (2016) shRNA-Based Screen Identifies Endocytic Recycling Pathway Components That Act as Genetic Modifiers of Alpha-Synuclein Aggregation, Secretion and Toxicity. *PLOS Genet* 12: e1005995

Grassi D, Howard S, Zhou M, Diaz-Perez N, Urban NT, Guerrero-Given D, Kamasawa N, Volpicelli-Daley LA, LoGrasso P, Lasmézas CI (2018) Identification of a highly neurotoxic α-synuclein species inducing mitochondrial damage and mitophagy in Parkinson's disease. *Proc Natl Acad Sci USA* 115: E2634–E2643

Grenn FP, Kim JJ, Makarious MB, Iwaki H, Illarionova A, Brolin K, Kluss JH, Schumacher-Schuh AF, Leonard H, Faghri F *et al* (2020) The Parkinson's Disease Genome-Wide Association Study Locus Browser. *Mov Disord* 35: 2056–2067

Groveman BR, Orrù CD, Hughson AG, Raymond LD, Zanusso G, Ghetti B, Campbell KJ, Safar J, Galasko D & Caughey B (2018) Rapid and ultra-sensitive quantitation of disease-associated α-synuclein seeds in brain and cerebrospinal fluid by αSyn RT-QuIC. *Acta Neuropathol Commun* 6: 7

Grover S, Kumar Sreelatha AA, Pihlstrom L, Domenighetti C, Schulte C, Sugier P-E, Radivojkov-Blagojevic M, Lichtner P, Mohamed O, Portugal B, *et al* (2022) Genome-wide Association and Meta-analysis of Age at Onset in Parkinson Disease. *Neurology* 99: e698–e710

Guardia-Laguarta C, Area-Gomez E, Rüb C, Liu Y, Magrané J, Becker D, Voos W, Schon EA, Przedborski S (2014) α-Synuclein is localized to mitochondria-associated ER membranes. *J Neurosci* 34: 249–259

Guo W, Wang H, Kumar Tharkeshwar A, Couthouis J, Braems E, Masrori P, Van Schoor E, Fan Y, Ahuja K, Moisse M *et al* (2023) CRISPR/Cas9 screen in human iPSC-derived cortical neurons

identifies NEK6 as a novel disease modifier of C9orf72 poly(PR) toxicity. *Alzheimers Dement* 19: 1245–1259

Guzman JN, Sánchez-Padilla J, Chan CS, Surmeier DJ (2009) Robust pacemaking in substantia nigra dopaminergic neurons. *J Neurosci* 29: 11011–11019

Hamza TH, Zabetian CP, Tenesa A, Laederach A, Montimurro J, Yearout D, Kay DM, Doheny KF, Paschall J, Pugh E *et al* (2010) Common genetic variation in the HLA region is associated with late-onset sporadic Parkinson's disease. *Nat Genet* 42: 781–785

Hanss Z, Larsen SB, Antony P, Mencke P, Massart F, Jarazo J, Schwamborn JC, Barbuti PA, Mellick GD, Krüger R (2021) Mitochondrial and Clearance Impairment in p.D620N VPS35 Patient-Derived Neurons. *Mov Disord* 36: 704–715

Hashem SI, Murphy AN, Divakaruni AS, Klos ML, Nelson BC, Gault EC, Rowland TJ, Perry CN, Gu Y, Dalton ND, *et al* (2017) Impaired mitophagy facilitates mitochondrial damage in Danon disease. *J Mol Cell Cardiol* 108: 86–94

Hatton C, Reeve A, Lax NZ, Blain A, Ng YS, El-Agnaf O, Attems J, Taylor J-P, Turnbull D & Erskine D (2020) Complex I reductions in the nucleus basalis of Meynert in Lewy body dementia: the role of Lewy bodies. *Acta Neuropathol Commun* 8: 103

Heikkila RE, Hess A, Duvoisin RC (1984) Dopaminergic neurotoxicity of 1-methyl-4-phenyl-1,2,5,6-tetrahydropyridine in mice. *Science* 224: 1451–1453

Heintze J, Luft C, Ketteler R (2013) A CRISPR CASe for high-throughput silencing. *Front Genet* Volume 4 – 2013

Heman-Ackah SM, Manzano R, Hoozemans JJM, Scheper W, Flynn R, Haerty W, Cowley SA, Bassett AR, Wood MJA (2017) Alpha-synuclein induces the unfolded protein response in Parkinson's disease SNCA triplication iPSC-derived neurons. *Hum Mol Genet* 26: 4441–4450

Henrich MT, Geibl FF, Lakshminarasimhan H, Stegmann A, Giasson BI, Mao X, Dawson VL, Dawson TM, Oertel WH & Surmeier DJ (2020) Determinants of seeding and spreading of α-synuclein pathology in the brain. *Sci Adv* 6: eabc2487

Höglinger GU, Adler CH, Berg D, Klein C, Outeiro TF, Poewe W, Postuma R, Stoessl AJ, Lang AE (2024) A biological classification of Parkinson's disease: the SynNeurGe research diagnostic criteria. *Lancet Neurol* 23: 191–204

Höllerhage M, Duan L, Chua OWH, Moebius C, Bothe SH, Losse K, Kotzur R, Lau K, Hopfner F, Richter F *et al* (2025) A genome-wide RNA interference screening reveals protectiveness of SNX5 knockdown in a Parkinson’s disease cell model. *Transl Neurodegener* 14: 27

Hoozemans JJ, van Haastert ES, Eikelenboom P, de Vos RA, Rozemuller JM, Scheper W (2007) Activation of the unfolded protein response in Parkinson's disease. *Biochem Biophys Res Commun* 354: 707–711

Horlbeck MA, Gilbert LA, Villalta JE, Adamson B, Pak RA, Chen Y, Fields AP, Park CY, Corn JE, Kampmann M *et al* (2016) Compact and highly active next-generation libraries for CRISPR-mediated gene repression and activation. *eLife* 5

Hou X, Chen TH-Y, Koga S, Bredenberg JM, Faroqi AH, Delenclos M, Bu G, Wszolek ZK, Carr JA, Ross OA *et al* (2023) Alpha-synuclein-associated changes in PINK1-PRKN-mediated mitophagy are disease context dependent. *Brain Pathol* 33: e13175

Hou X, Fiesel FC, Truban D, Castanedes Casey M, Lin W-l, Soto AI, Tacik P, Rousseau LG, Diehl NN, Heckman MG *et al* (2018) Age- and disease-dependent increase of the mitophagy marker phospho-ubiquitin in normal aging and Lewy body disease. *Autophagy* 14: 1404–1418

Howe FS, Russell A, Lamstaes AR, El-Sagheer A, Nair A, Brown T, Mellor J (2017) CRISPRi is not strand-specific at all loci and redefines the transcriptional landscape. *elife* 6

Hsieh C-H, Li L, Vanhauwaert R, Nguyen KT, Davis MD, Bu G, Wszolek ZK, Wang X (2019) Miro1 Marks Parkinson's Disease Subset and Miro1 Reducer Rescues Neuron Loss in Parkinson's Models. *Cell Metab* 30: 1131–1140.e1137

Hsieh CH, Shaltouki A, Gonzalez AE, Bettencourt da Cruz A, Burbulla LF, St Lawrence E, Schüle B, Krainc D, Palmer TD, Wang X (2016) Functional Impairment in Miro Degradation and Mitophagy Is a Shared Feature in Familial and Sporadic Parkinson's Disease. *Cell Stem Cell* 19: 709–724

Hsu PD, Scott DA, Weinstein JA, Ran FA, Konermann S, Agarwala V, Li Y, Fine EJ, Wu X, Shalem O *et al* (2013) DNA targeting specificity of RNA-guided Cas9 nucleases. *Nat Biotechnol* 31: 827–832

Hultquist Judd F, Schumann K, Woo Jonathan M, Manganaro L, McGregor Michael J, Doudna J, Simon V, Krogan Nevan J, Marson A (2016) A Cas9 Ribonucleoprotein Platform for Functional Genetic Studies of HIV-Host Interactions in Primary Human T Cells. *Cell Rep* 17: 1438–1452

Iannielli A, Luoni M, Giannelli SG, Ferese R, Ordazzo G, Fossati M, Raimondi A, Opazo F, Corti O, Prehn JHM *et al* (2022) Modeling native and seeded Synuclein aggregation and related cellular dysfunctions in dopaminergic neurons derived by a new set of isogenic iPSC lines with SNCA multiplications. *Cell Death Dis* 13: 881

Ibáñez P, Bonnet AM, Débarges B, Lohmann E, Tison F, Pollak P, Agid Y, Dürr A, Brice A (2004) Causal relation between alpha-synuclein gene duplication and familial Parkinson's disease. *Lancet* 364: 1169–1171

Iljina M, Garcia GA, Horrocks MH, Tosatto L, Choi ML, Ganzinger KA, Abramov AY, Gandhi S, Wood NW, Cremades N *et al* (2016) Kinetic model of the aggregation of alpha-synuclein provides insights into prion-like spreading. *Proc Nat Acad Sci USA* 113: E1206–E1215

Imaizumi Y, Okada Y, Akamatsu W, Koike M, Kuzumaki N, Hayakawa H, Nihira T, Kobayashi T, Ohyama M, Sato S *et al* (2012) Mitochondrial dysfunction associated with increased oxidative stress and α-synuclein accumulation in PARK2 iPSC-derived neurons and postmortem brain tissue. *Mol Brain* 5: 35

International Parkinson's Disease Genomics C, Wellcome Trust Case Control C (2011) A Two-Stage Meta-Analysis Identifies Several New Loci for Parkinson's Disease. *PLOS Genet* 7: e1002142

Ishihara N, Jofuku A, Eura Y, Mihara K (2003) Regulation of mitochondrial morphology by membrane potential, and DRP1-dependent division and FZO1-dependent fusion reaction in mammalian cells. *Biochem Biophys Res Commun* 301: 891–898

Iwaki H, Blauwendraat C, Leonard HL, Liu G, Maple-Grødem J, Corvol JC, Pihlstrøm L, van Nimwegen M, Hutten SJ, Nguyen KH *et al* (2019) Genetic risk of Parkinson disease and progression:: An analysis of 13 longitudinal cohorts. *Neurol Genet* 5: e348

Jacobs BM, Belete D, Bestwick J, Blauwendraat C, Bandres-Ciga S, Heilbron K, Dobson R, Nalls MA, Singleton A, Hardy J *et al* (2020) Parkinson's disease determinants, prediction and gene-environment interactions in the UK Biobank. *J Neurol Neurosurg Psychiatry* 91: 1046–1054

Jankovic J, McDermott M, Carter J, Gauthier S, Goetz C, Golbe L, Huber S, Koller W, Olanow C, Shoulson I *et al* (1990) Variable expression of Parkinson's disease: a base-line analysis of the DATATOP cohort. The Parkinson Study Group. *Neurology* 40: 1529–1534

Javitch JA, Snyder SH (1984) Uptake of MPP(+) by dopamine neurons explains selectivity of parkinsonism-inducing neurotoxin, MPTP. *Eur J Pharmacol* 106: 455–456

Jellinger KA (2009) A critical evaluation of current staging of α-synuclein pathology in Lewy body disorders. *Biochim Biophys Acta* 1792: 730–740

Jin SM, Lazarou M, Wang C, Kane LA, Narendra DP, Youle RJ (2010) Mitochondrial membrane potential regulates PINK1 import and proteolytic destabilization by PARL. *J Cell Biol* 191: 933–942

Jinek M, Chylinski K, Fonfara I, Hauer M, Doudna JA, Charpentier E (2012) A Programmable Dual-RNA Guided DNA Endonuclease in Adaptive Bacterial Immunity. *Science* 337: 816–821

Jing X, Liu Z, Li W, Ma K, Zhang J, Yan Z, Zhang S, Lin J, Zhao J, Ong KK *et al* (2025) Protein-truncating variants in UQCRC1 are associated with Parkinson's disease: evidence from half-million people. *NPJ Parkinsons Dis* 11: 120

Jinn S, Drolet RE, Cramer PE, Wong AH, Toolan DM, Gretzula CA, Voleti B, Vassileva G, Disa J, Tadin-Strapps M *et al* (2017) TMEM175 deficiency impairs lysosomal and mitochondrial function and increases α-synuclein aggregation. *Proc Nat Acad Sci USA* 114: 2389–2394

Jones-Tabah J, He K, Karpilovsky N, Senkevich K, Deyab G, Pietrantonio I, Goiran T, Cousineau Y, Nikanorova D, Goldsmith T *et al* (2024) The Parkinson's disease risk gene cathepsin B promotes fibrillar alpha-synuclein clearance, lysosomal function and glucocerebrosidase activity in dopaminergic neurons. *Mol Neurodegener* 19: 88

Jost M, Santos DA, Saunders RA, Horlbeck MA, Hawkins JS, Scaria SM, Norman TM, Hussmann JA, Liem CR, Gross CA *et al* (2020) Titrating gene expression using libraries of systematically attenuated CRISPR guide RNAs. *Nat Biotechnol* 38: 355–364

Kalia LV, Lang AE (2015) Parkinson's disease. *Lancet* 386: 896–912

Kamp F, Exner N, Lutz AK, Wender N, Hegermann J, Brunner B, Nuscher B, Bartels T, Giese A, Beyer K *et al* (2010) Inhibition of mitochondrial fusion by α-synuclein is rescued by PINK1, Parkin and DJ-1. *EMBO J* 29: 3571–3589

Kanfer G, Sarraf SA, Maman Y, Baldwin H, Dominguez-Martin E, Johnson KR, Ward ME, Kampmann M, Lippincott-Schwartz J, Youle RJ (2021) Image-based pooled whole-genome CRISPRi screening for subcellular phenotypes. *J Cell Biol* 220

Kang UJ, Boehme AK, Fairfoul G, Shahnawaz M, Ma TC, Hutten SJ, Green A & Soto C (2019) Comparative study of cerebrospinal fluid α-synuclein seeding aggregation assays for diagnosis of Parkinson's disease. *Mov Disord* 34: 536–544

Kassambra A, 2023. rstatix: Pipe-Friendly Framework for Basic Statistical Tests.

Khoo TK, Yarnall AJ, Duncan GW, Coleman S, O'Brien JT, Brooks DJ, Barker RA, Burn DJ (2013) The spectrum of nonmotor symptoms in early Parkinson disease. *Neurology* 80: 276–281

Kia DA, Zhang D, Guelfi S, Manzoni C, Hubbard L, Reynolds RH, Botía J, Ryten M, Ferrari R, Lewis PA, *et al* (2021) Identification of Candidate Parkinson Disease Genes by Integrating Genome-Wide Association Study, Expression, and Epigenetic Data Sets. *JAMA Neurol* 78: 464–472

Kim HS, Lee K, Kim SJ, Cho S, Shin HJ, Kim C, Kim JS (2018) Arrayed CRISPR screen with image-based assay reliably uncovers host genes required for coxsackievirus infection. *Genome Res* 28: 859–868

Kim MS, Ra EA, Kweon SH, Seo BA, Ko HS, Oh Y, Lee G (2023) Advanced human iPSC-based preclinical model for Parkinson's disease with optogenetic alpha-synuclein aggregation. *Cell Stem Cell* 30: 973–986.e911

Kitada T, Asakawa S, Hattori N, Matsumine H, Yamamura Y, Minoshima S, Yokochi M, Mizuno Y, Shimizu N (1998) Mutations in the parkin gene cause autosomal recessive juvenile parkinsonism. *Nature* 392: 605–608

Klebe S, Golmard J-L, Nalls MA, Saad M, Singleton AB, Bras JM, Hardy J, Simon-Sanchez J, Heutink P, Kuhlenbäumer G, *et al* (2013) The Val158Met COMT polymorphism is a modifier of the age at onset in Parkinson's disease with a sexual dimorphism. *J Neurol Neurosurg Psychiatry* 84: 666–673

Knowles TPJ, Vendruscolo M, Dobson CM (2014) The amyloid state and its association with protein misfolding diseases. *Nat Rev Mol Cell Biol* 15: 384–396

Kobayashi H, Ujike H, Hasegawa J, Yamamoto M, Kanzaki A & Sora I (2006) Correlation of tau gene polymorphism with age at onset of Parkinson's disease. *Neurosci Lett* 405: 202–206

Koch S, Laabs B-H, Kasten M, Vollstedt E-J, Becktepe J, Brüggemann N, Franke A, Krämer UM, Kuhlenbäumer G, Lieb W *et al* (2021) Validity and Prognostic Value of a Polygenic Risk Score for Parkinson's Disease. *Genes* doi: 10.3390/genes12121859 [PREPRINT]

Koike-Yusa H, Li Y, Tan EP, Velasco-Herrera MDC, Yusa K (2014) Genome-wide recessive genetic screening in mammalian cells with a lentiviral CRISPR-guide RNA library. *Nat Biotechnol* 32: 267–273

Köppen J, Schulze A, Machner L, Wermann M, Eichentopf R, Guthardt M, Hähnel A, Klehm J, Kriegeskorte M-C, Hartlage-Rübsamen M *et al* (2020) Amyloid-Beta Peptides Trigger Aggregation of Alpha-Synuclein In Vitro. *Molecules* doi: 10.3390/molecules25030580 [PREPRINT]

Koss DJ, Erskine D, Porter A, Palmoski P, Menon H, Todd OGJ, Leite M, Attems J, Outeiro TF (2022) Nuclear alpha-synuclein is present in the human brain and is modified in dementia with Lewy bodies. *Acta Neuropathol Commun* 10: 98

Koyano F, Okatsu K, Kosako H, Tamura Y, Go E, Kimura M, Kimura Y, Tsuchiya H, Yoshihara H, Hirokawa T *et al* (2014) Ubiquitin is phosphorylated by PINK1 to activate parkin. *Nature* 510: 162–166

Kriks S, Shim J-W, Piao J, Ganat YM, Wakeman DR, Xie Z, Carrillo-Reid L, Auyeung G, Antonacci C, Buch A *et al* (2011) Dopamine neurons derived from human ES cells efficiently engraft in animal models of Parkinson's disease. *Nature* 480: 547–551

Krüger R, Kuhn W, Müller T, Woitalla D, Graeber M, Kösel S, Przuntek H, Epplen JT, Schols L, Riess O (1998) AlaSOPro mutation in the gene encoding α-synuclein in Parkinson's disease. *Nature Genet* 18: 106–108

Kuusisto E, Parkkinen L, Alafuzoff I (2003) Morphogenesis of Lewy Bodies: Dissimilar Incorporation of α-Synuclein, Ubiquitin, and p62. *J Neuropathol Exp Neurol* 62: 1241–1253

Kuusisto E, Salminen A, Alafuzoff I (2001) Ubiquitin-binding protein p62 is present in neuronal and glial inclusions in human tauopathies and synucleinopathies. *Neuroreport* 12: 2085–2090

Kuzuhara S, Mori H, Izumiyama N, Yoshimura M, Ihara Y (1988) Lewy bodies are ubiquitinated. A light and electron microscopic immunocytochemical study. *Acta Neuropathol* 75: 345–353

Lam I, Ndayisaba A, Lewis AJ, Fu Y, Sagredo GT, Kuzkina A, Zaccagnini L, Celikag M, Sandoe J, Sanz RL *et al* (2024) Rapid iPSC inclusionopathy models shed light on formation, consequence, and molecular subtype of α-synuclein inclusions. *Neuron* 112: 2886–2909.e2816

Langston JW (2006) The Parkinson's complex: parkinsonism is just the tip of the iceberg. *Ann Neurol* 59: 591–596

Langston JW, Ballard P, Tetrud JW, Irwin I (1983) Chronic Parkinsonism in humans due to a product of meperidine-analog synthesis. *Science* 219: 979–980

Langston JW, Irwin I, Langston EB, Forno LS (1984) 1-Methyl-4-phenylpyridinium ion (MPP+): identification of a metabolite of MPTP, a toxin selective to the substantia nigra. *Neurosci Lett* 48: 87–92

Larbalestier H, Keatinge M, Watson L, White E, Gowda S, Wei W, Koler K, Semenova SA, Elkin AM, Rimmer N *et al* (2022) GCH1 Deficiency Activates Brain Innate Immune Response and Impairs Tyrosine Hydroxylase Homeostasis. *J Neurosci* 42: 702–716

Lautenschläger J, Stephens AD, Fusco G, Ströhl F, Curry N, Zacharopoulou M, Michel CH, Laine R, Nespovitaya N, Fantham M *et al* (2018) C-terminal calcium binding of α-synuclein modulates synaptic vesicle interaction. *Nat Commun* 9: 712

Lawton M, Ben-Shlomo Y, May MT, Baig F, Barber TR, Klein JC, Swallow DMA, Malek N, Grosset KA, Bajaj N *et al* (2018) Developing and validating Parkinson's disease subtypes and their motor and cognitive progression. *J Neurol Neurosurg Psychiatry* 89: 1279–1287

Lazarou M, Sliter DA, Kane LA, Sarraf SA, Wang C, Burman JL, Sideris DP, Fogel AI, Youle RJ (2015) The ubiquitin kinase PINK1 recruits autophagy receptors to induce mitophagy. *Nature* 524: 309–314

le Sage C, Lawo S, Panicker P, Scales TME, Rahman SA, Little AS, McCarthy NJ, Moore JD, Cross BCS (2017) Dual direction CRISPR transcriptional regulation screening uncovers gene networks driving drug resistance. *Sci Rep* 7: 17693

Leal TP, Waldo E, Duarte-Zambrano F, Inca-Martinez M, Ramchandra J, Chaparro-Solano HM, Anello AE, Borda V, Gouveia MH, Teixeira-dos-Santos D *et al* (2025) Genotype-phenotype association study conducted on LARGE-PD reveals novel loci associated with Parkinson’s Disease. *medRxiv* 2025.2007.2018.25331793

Lee H-J, Khoshaghideh F, Patel S, Lee S-J (2004) Clearance of α-Synuclein Oligomeric Intermediates via the Lysosomal Degradation Pathway. *J Neurosci* 24: 1888–1896

Lee H-J, Suk J-E, Bae E-J, Lee S-J (2008) Clearance and deposition of extracellular α-synuclein aggregates in microglia. *Biochem Biophys Res Commun* 372: 423–428

Lee RG, Balasubramaniam S, Stentenbach M, Kralj T, McCubbin T, Padman B, Smith J, Riley LG, Priyadarshi A, Peng L *et al* (2022) Deleterious variants in CRLS1 lead to cardiolipin deficiency and cause an autosomal recessive multi-system mitochondrial disease. *Hum Mol Genet* 31: 3597–3612

Li H, Ham A, Ma TC, Kuo SH, Kanter E, Kim D, Ko HS, Quan Y, Sardi SP, Li A *et al* (2019a) Mitochondrial dysfunction and mitophagy defect triggered by heterozygous GBA mutations. *Autophagy* 15: 113–130

Li J, Amoh BK, McCormick E, Tarkunde A, Zhu KF, Perez A, Mair M, Moore J, Shulman JM, Al-Ramahi I, *et al* (2023) Integration of transcriptome-wide association study with neuronal dysfunction assays provides functional genomics evidence for Parkinson's disease genes. *Hum Mol Genet* 32: 685–695

Li Y, Muffat J, Omer Javed A, Keys HR, Lungjangwa T, Bosch I, Khan M, Virgilio MC, Gehrke L, Sabatini DM *et al* (2019b) Genome-wide CRISPR screen for Zika virus resistance in human neural cells. *Proc Nat Acad Sci USA* 116: 9527–9532

Li Y, Xiong Y, Wang Z, Han J, Shi S, He J, Shen N, Wu W, Wang R, Lv W *et al* (2021) FAM49B promotes breast cancer proliferation, metastasis, and chemoresistance by stabilizing ELAVL1 protein and regulating downstream Rab10/TLR4 pathway. *Cancer Cell Int* 21: 534

Li YI, van de Geijn B, Raj A, Knowles DA, Petti AA, Golan D, Gilad Y & Pritchard JK (2016) RNA splicing is a primary link between genetic variation and disease. *Science* 352: 600–604

Li YI, Wong G, Humphrey J, Raj T (2019c) Prioritizing Parkinson's disease genes using population-scale transcriptomic data. *Nat Commun* 10: 994

Lill CM, Roehr JT, McQueen MB, Kavvoura FK, Bagade S, Schjeide BM, Schjeide LM, Meissner E, Zauft U, Allen NC *et al* (2012) Comprehensive research synopsis and systematic meta-analyses in Parkinson's disease genetics: The PDGene database. *PLoS Genet* 8: e1002548

Little D, Luft C, Mosaku O, Lorvellec M, Yao Z, Paillusson S, Kriston-Vizi J, Gandhi S, Abramov AY, Ketteler R *et al* (2018) A single cell high content assay detects mitochondrial dysfunction in iPSC-derived neurons with mutations in SNCA. *Sci Rep* 8: 9033

Liu G, Boot B, Locascio JJ, Jansen IE, Winder-Rhodes S, Eberly S, Elbaz A, Brice A, Ravina B, van Hilten JJ, *et al* (2016) Specifically neuropathic Gaucher's mutations accelerate cognitive decline in Parkinson's. *Ann Neurology* 80: 674–685

Liu G, Peng J, Liao Z, Locascio JJ, Corvol J-C, Zhu F, Dong X, Maple-Grødem J, Campbell MC, Elbaz A, *et al* (2021) Genome-wide survival study identifies a novel synaptic locus and polygenic score for cognitive progression in Parkinson's disease. *Nat Genet* 53: 787–793

Liu GH, Qu J, Suzuki K, Nivet E, Li M, Montserrat N, Yi F, Xu X, Ruiz S, Zhang W *et al* (2012a) Progressive degeneration of human neural stem cells caused by pathogenic LRRK2. *Nature* 491: 603–607

Liu L, Feng D, Chen G, Chen M, Zheng Q, Song P, Ma Q, Zhu C, Wang R, Qi W *et al* (2012b) Mitochondrial outer-membrane protein FUNDC1 mediates hypoxia-induced mitophagy in mammalian cells. *Nat Cell Biol* 14: 177–185

Liu SJ, Horlbeck MA, Cho SW, Birk HS, Malatesta M, He D, Attenello FJ, Villalta JE, Cho MY, Chen Y *et al* (2017) CRISPRi-based genome-scale identification of functional long noncoding RNA loci in human cells. *Science* 355: eaah7111

Liu X, Li F, Stubblefield EA, Blanchard B, Richards TL, Larson GA, He Y, Huang Q, Tan AC, Zhang D *et al* (2012c) Direct reprogramming of human fibroblasts into dopaminergic neuron-like cells. *Cell Res* 22: 321–332

Liu X, Liao X, Rao X, Wang B, Zhang J, Xu G, Jiang X, Qin X, Chen C, Zou Z (2020) The lysosomal membrane protein LAMP-2 is dispensable for PINK1/Parkin-mediated mitophagy. *FEBS Lett* 594: 823–840

Liu XS, Wu H, Ji X, Stelzer Y, Wu X, Czauderna S, Shu J, Dadon D, Young RA, Jaenisch R (2016) Editing DNA Methylation in the Mammalian Genome. *Cell* 167: 233–247.e217

Lobanova E, Whiten D, Ruggeri FS, Taylor CG, Kouli A, Xia Z, Emin D, Zhang YP, Lam JYL, Williams-Gray CH, *et al* (2022) Imaging protein aggregates in the serum and cerebrospinal fluid in Parkinson's disease. *Brain* 145: 632–643

Lövestam S, Schweighauser M, Matsubara T, Murayama S, Tomita T, Ando T, Hasegawa K, Yoshida M, Tarutani A, Hasegawa M *et al* (2021) Seeded assembly in vitro does not replicate the structures of α-synuclein filaments from multiple system atrophy. *FEBS Open Bio* 11: 999–1013

Ludtmann MHR, Angelova PR, Horrocks MH, Choi ML, Rodrigues M, Baev AY, Berezhnov AV, Yao Z, Little D, Banushi B *et al* (2018) α-synuclein oligomers interact with ATP synthase and open the permeability transition pore in Parkinson's disease. *Nat Commun* 9: 2293

Luk KC, Kehm V, Carroll J, Zhang B, O'Brien P, Trojanowski JQ & Lee VM-Y (2012) Pathological α-Synuclein Transmission Initiates Parkinson-like Neurodegeneration in Nontransgenic Mice. *Science* 338: 949–953

Luk KC, Kehm VM, Zhang B, O'Brien P, Trojanowski JQ, Lee VMY (2012) Intracerebral inoculation of pathological α-synuclein initiates a rapidly progressive neurodegenerative α-synucleinopathy in mice. *J Exp Med* 209: 975–986

Luk KC, Song C, O'Brien P, Stieber A, Branch JR, Brunden KR, Trojanowski JQ, Lee VM-Y (2009) Exogenous α-synuclein fibrils seed the formation of Lewy body-like intracellular inclusions in cultured cells. *Proc Nat Acad Sci USA* 106: 20051–20056

Luth ES, Stavrovskaya IG, Bartels T, Kristal BS, Selkoe DJ (2014) Soluble, prefibrillar α-synuclein oligomers promote complex I-dependent, Ca2+-induced mitochondrial dysfunction. *J Biol Chem* 289: 21490–21507

Maccioni R, Travisan C, Badman J, Zerial S, Wagener A, Andrade-Talavera Y, Picciau F, Grassi C, Chen G, Lemoine L *et al* (2024) Signal peptide peptidase-like 2b modulates the amyloidogenic pathway and exhibits an Aβ-dependent expression in Alzheimer's disease. *Prog Neurobiol* 235: 102585

Mahul-Mellier A-L, Burtscher J, Maharjan N, Weerens L, Croisier M, Kuttler F, Leleu M, Knott GW, Lashuel HA (2020) The process of Lewy body formation, rather than simply α-synuclein fibrillization, is one of the major drivers of neurodegeneration. *Proc Nat Acad Sci USA* 117: 4971–4982

Mali P, Yang L, Esvelt KM, Aach J, Guell M, DiCarlo JE, Norville JE, Church GM (2013) RNA-Guided Human Genome Engineering via Cas9. *Science* 339: 823–826

Mandegar MA, Huebsch N, Frolov EB, Shin E, Truong A, Olvera MP, Chan AH, Miyaoka Y, Holmes K, Spencer CI *et al* (2016) CRISPR Interference Efficiently Induces Specific and Reversible Gene Silencing in Human iPSCs. *Cell Stem Cell* 18: 541–553

Mao X, Ou MT, Karuppagounder SS, Kam T-I, Yin X, Xiong Y, Ge P, Umanah GE, Brahmachari S, Shin J-H, *et al* (2016) Pathological α-synuclein transmission initiated by binding lymphocyte-activation gene 3. *Science* 353: aah3374

Maraganore DM, de Andrade M, Lesnick TG, Strain KJ, Farrer MJ, Rocca WA, Pant PV, Frazer KA, Cox DR, Ballinger DG (2005) High-resolution whole-genome association study of Parkinson disease. *Am J Hum Genet* 77: 685–693

Marinković M, Šprung M, Novak I (2021) Dimerization of mitophagy receptor BNIP3L/NIX is essential for recruitment of autophagic machinery. *Autophagy* 17: 1232–1243

Martín-Bórnez M, Shar N, Nour MA, Murphy D, Elsayed I, Nanjundaswamy MS, Nwaokorie F, Olusanya A, Kuznetsov N, Bandres-Ciga S, *et al* (2025) Does COMT Play a Role in Parkinson's Disease Susceptibility across Diverse Ancestral Populations? *Mov Disord* 40: 2819–2824

Martínez Carrasco A, Real R, Lawton M, Hertfelder Reynolds R, Tan M, Wu L, Williams N, Carroll C, Corvol J-C, Hu M, *et al* (2023) Genome-wide Analysis of Motor Progression in Parkinson Disease. *Neurology: Genetics* 9: e200092

Masuda-Suzukake M, Nonaka T, Hosokawa M, Oikawa T, Arai T, Akiyama H, Mann DMA, Hasegawa M (2013) Prion-like spreading of pathological α-synuclein in brain. *Brain* 136: 1128–1138

Mata IF, Leverenz JB, Weintraub D, Trojanowski JQ, Chen-Plotkin A, Van Deerlin VM, Ritz B, Rausch R, Factor SA, Wood-Siverio C, *et al* (2016) GBA Variants are associated with a distinct pattern of cognitive deficits in Parkinson's disease. *Mov Disord* 31: 95–102

Matsuda N, Sato S, Shiba K, Okatsu K, Saisho K, Gautier CA, Sou YS, Saiki S, Kawajiri S, Sato F *et al* (2010) PINK1 stabilized by mitochondrial depolarization recruits Parkin to damaged mitochondria and activates latent Parkin for mitophagy. *J Cell Biol* 189: 211–221

Matsuda W, Furuta T, Nakamura KC, Hioki H, Fujiyama F, Arai R, Kaneko T (2009) Single Nigrostriatal Dopaminergic Neurons Form Widely Spread and Highly Dense Axonal Arborizations in the Neostriatum. *J Neurosci* 29: 444

Mazzulli Joseph R, Xu Y-H, Sun Y, Knight Adam L, McLean Pamela J, Caldwell Guy A, Sidransky E, Grabowski Gregory A, Krainc D (2011) Gaucher Disease Glucocerebrosidase and α-Synuclein Form a Bidirectional Pathogenic Loop in Synucleinopathies. *Cell* 146: 37–52

Mazzulli JR, Zunke F, Isacson O, Studer L, Krainc D (2016a) α-Synuclein-induced lysosomal dysfunction occurs through disruptions in protein trafficking in human midbrain synucleinopathy models. *Proc Nat Acad Sci USA* 113: 1931–1936

Mazzulli JR, Zunke F, Tsunemi T, Toker NJ, Jeon S, Burbulla LF, Patnaik S, Sidransky E, Marugan JJ, Sue CM *et al* (2016b) Activation of β-Glucocerebrosidase Reduces Pathological α-Synuclein and Restores Lysosomal Function in Parkinson's Patient Midbrain Neurons. *J Neurosci* 36: 7693–7706

McGlinchey RP, Lee JC (2015) Cysteine cathepsins are essential in lysosomal degradation of α-synuclein. *Proc Nat Acad Sci USA* 112: 9322–9327

McWilliams TG, Prescott AR, Montava-Garriga L, Ball G, Singh F, Barini E, Muqit MMK, Brooks SP, Ganley IG (2018) Basal Mitophagy Occurs Independently of PINK1 in Mouse Tissues of High Metabolic Demand. *Cell Metab* 27: 439–449.e435

Mestre TA, Fereshtehnejad SM, Berg D, Bohnen NI, Dujardin K, Erro R, Espay AJ, Halliday G, van Hilten JJ, Hu MT *et al* (2021) Parkinson's Disease Subtypes: Critical Appraisal and Recommendations. *J Parkinsons Dis* 11: 395–404

Miyazono Y, Hirashima S, Ishihara N, Kusukawa J, Nakamura K-i, Ohta K (2018) Uncoupled mitochondria quickly shorten along their long axis to form indented spheroids, instead of rings, in a fission-independent manner. *Sci Rep* 8: 350

Mohammadi R, Shirazi M, Sadat-Madani SF, Yeo Cheng Long MZ, Singh CL, Tan JY, Deng X, Hashemi Fard SM, Ng SYE, Ng ASL *et al* (2025) Common SNCA Genetic Variants and Parkinson's Disease Risk: A Systematic Review and Meta-Analysis. *Int J Mol Sci* 26

Morgens DW, Deans RM, Li A, Bassik MC (2016) Systematic comparison of CRISPR/Cas9 and RNAi screens for essential genes. *Nat Biotechnol* 34: 634–636

Munoz DM, Cassiani PJ, Li L, Billy E, Korn JM, Jones MD, Golji J, Ruddy DA, Yu K, McAllister G *et al* (2016) CRISPR Screens Provide a Comprehensive Assessment of Cancer Vulnerabilities but Generate False-Positive Hits for Highly Amplified Genomic Regions. *Cancer Discov* 6: 900–913

Murakawa T, Yamaguchi O, Hashimoto A, Hikoso S, Takeda T, Oka T, Yasui H, Ueda H, Akazawa Y, Nakayama H *et al* (2015) Bcl-2-like protein 13 is a mammalian Atg32 homologue that mediates mitophagy and mitochondrial fragmentation. *Nat Commun* 6: 7527

Nag S, Szederkenyi K, Yip CM, McQuibban GA (2023) Protocol for evaluating mitochondrial morphology changes in response to CCCP-induced stress through open-source image processing software. *STAR Protoc* 4: 102745

Nakamura K, Nemani VM, Azarbal F, Skibinski G, Levy JM, Egami K, Munishkina L, Zhang J, Gardner B, Wakabayashi J *et al* (2011) Direct membrane association drives mitochondrial fission by the Parkinson disease-associated protein alpha-synuclein. *J Biol Chem* 286: 20710–20726

Nalls MA, Blauwendraat C, Vallerga CL, Heilbron K, Bandres-Ciga S, Chang D, Tan M, Kia DA, Noyce AJ, Xue A *et al* (2019) Identification of novel risk loci, causal insights, and heritable risk for Parkinson's disease: a meta-analysis of genome-wide association studies. *Lancet Neurol* 18: 1091–1102

Nalls MA, Plagnol V, Hernandez DG, Sharma M, Sheerin UM, Saad M, Simón-Sánchez J, Schulte C, Lesage S, Sveinbjörnsdóttir S *et al* (2011) Imputation of sequence variants for identification of genetic risks for Parkinson's disease: a meta-analysis of genome-wide association studies. *Lancet* 377: 641–649

Narendra D, Tanaka A, Suen D-F, Youle RJ (2008) Parkin is recruited selectively to impaired mitochondria and promotes their autophagy. *J Cell Biol* 183: 795–803

Narendra DP, Jin SM, Tanaka A, Suen D-F, Gautier CA, Shen J, Cookson MR, Youle RJ (2010) PINK1 Is Selectively Stabilized on Impaired Mitochondria to Activate Parkin. *PLOS Biol* 8: e1000298

Narkiewicz J, Giachin G, Legname G (2014) In vitro aggregation assays for the characterization of α-synuclein prion-like properties. *Prion* 8: 19–32

Nehme R, Zuccaro E, Ghosh SD, Li C, Sherwood JL, Pietilainen O, Barrett LE, Limone F, Worringer KA, Kommineni S *et al* (2018) Combining NGN2 Programming with Developmental Patterning Generates Human Excitatory Neurons with NMDAR-Mediated Synaptic Transmission. *Cell Rep* 23: 2509–2523

Neupane S, Nikolić L, Maraio L, Goiran T, Karpilovsky N, Sellitto S, Bouris V, Yin J-A, Melki R, Fon EA *et al* (2025) Large-scale bidirectional arrayed genetic screens identify *OXR1* and *EMC4* as modifiers of α-synuclein aggregation. *bioRxiv*: 2025.2006.2010.658866
Ngo KJ, Paul KC, Wong D, Kusters CDJ, Bronstein JM, Ritz B, Fogel BL (2024) Lysosomal genes contribute to Parkinson's disease near agriculture with high intensity pesticide use. *NPJ Parkinsons Dis* 10: 87

Nguyen HD (2025) Elucidate biomarkers and the molecular pathways associated with genetic variants that contribute to the etiology of Parkinson's disease. *Acta Neurol Belg* 125: 1621–1641

Nichols WC, Pankratz N, Marek DK, Pauciulo MW, Elsaesser VE, Halter CA, Rudolph A, Wojcieszek J, Pfeiffer RF & Foroud T (2009) Mutations in GBA are associated with familial Parkinson disease susceptibility and age at onset. *Neurology* 72: 310–316

Nicklas WJ, Vyas I, Heikkila RE (1985) Inhibition of NADH-linked oxidation in brain mitochondria by 1-methyl-4-phenyl-pyridine, a metabolite of the neurotoxin, 1-methyl-4-phenyl-1,2,5,6-tetrahydropyridine. *Life Sci* 36: 2503–2508

Nishimura K, Nitta T, Doi K, Takata K (2022) Rapid Conversion of Human Induced Pluripotent Stem Cells into Dopaminergic Neurons by Inducible Expression of Two Transcription Factors. *Stem Cells Dev* 31: 269–277

Niu J, Yu M, Wang C, Xu Z (2012) Leucine-rich repeat kinase 2 disturbs mitochondrial dynamics via Dynamin-like protein. *J Neurochem* 122: 650–658

Noyce AJ, Bestwick JP, Silveira-Moriyama L, Hawkes CH, Giovannoni G, Lees AJ, Schrag A (2012) Meta-analysis of early nonmotor features and risk factors for Parkinson disease. *Ann Neurol* 72: 893–901

Nuñez JK, Chen J, Pommier GC, Cogan JZ, Replogle JM, Adriaens C, Ramadoss GN, Shi Q, Hung KL, Samelson AJ *et al* (2021) Genome-wide programmable transcriptional memory by CRISPR-based epigenome editing. *Cell* 184: 2503–2519.e2517

Nybø CJ, Gustavsson EK, Farrer MJ, Aasly JO (2020) Neuropathological findings in PINK1-associated Parkinson's disease. *Parkinsonism Relat Disord* 78: 105–108

Ordonez DG, Lee MK, Feany MB (2018) α-synuclein Induces Mitochondrial Dysfunction through Spectrin and the Actin Cytoskeleton. *Neuron* 97: 108–124.e106

Outeiro TF, Putcha P, Tetzlaff JE, Spoelgen R, Koker M, Carvalho F, Hyman BT, McLean PJ (2008) Formation of toxic oligomeric alpha-synuclein species in living cells. *PLoS ONE* 3: e1867

Owen OE, Kalhan SC, Hanson RW (2002) The Key Role of Anaplerosis and Cataplerosis for Citric Acid Cycle Function*. *J Biol Chem* 277: 30409–30412

Pagano G, Dam T, Kerchner GA, Galpern WR, Biagioni M, Karan R, Jennings D, Peterschmitt MJ, Nikolcheva T, Brundin P (2024) Biologically defined neuronal synuclein disease as a tool to advance drug development. *NPJ Parkinson's Dis* 10: 235

Paillusson S, Gomez-Suaga P, Stoica R, Little D, Gissen P, Devine MJ, Noble W, Hanger DP, Miller CCJ (2017) α-Synuclein binds to the ER-mitochondria tethering protein VAPB to disrupt Ca(2+) homeostasis and mitochondrial ATP production. *Acta Neuropathol* 134: 129–149

Paisán-Ruíz C, Jain S, Evans EW, Gilks WP, Simón J, van der Brug M, López de Munain A, Aparicio S, Gil AM, Khan N *et al* (2004) Cloning of the gene containing mutations that cause PARK8-linked Parkinson's disease. *Neuron* 44: 595–600

Pals P, Lincoln S, Manning J, Heckman M, Skipper L, Hulihan M, Van den Broeck M, De Pooter T, Cras P, Crook J *et al* (2004) α-Synuclein promoter confers susceptibility to Parkinson's disease. *Ann Neurol* 56: 591–595

Pankratz N, Foroud T (2007) Genetics of Parkinson disease. *Genet Med* 9: 801–811

Pankratz N, Wilk JB, Latourelle JC, DeStefano AL, Halter C, Pugh EW, Doheny KF, Gusella JF, Nichols WC, Foroud T *et al* (2009) Genomewide association study for susceptibility genes contributing to familial Parkinson disease. *Hum Genet* 124: 593–605

Parihar MS, Parihar A, Fujita M, Hashimoto M, Ghafourifar P (2008) Mitochondrial association of alpha-synuclein causes oxidative stress. *Cellular and molecular life sciences : CMLS* 65: 1272–1284
Parkinson J (2002) An essay on the shaking palsy. 1817. *J Neuropsychiatry Clin Neurosci* 14: 223–236; discussion 222

Patterson JR, Polinski NK, Duffy MF, Kemp CJ, Luk KC, Volpicelli-Daley LA, Kanaan NM, Sortwell CE (2019) Generation of Alpha-Synuclein Preformed Fibrils from Monomers and Use In Vivo. *J Vis Exp*

Paul KC, Schulz J, Bronstein JM, Lill CM, Ritz BR (2018) Association of Polygenic Risk Score With Cognitive Decline and Motor Progression in Parkinson Disease. *JAMA Neurol* 75: 360–366

Paumier KL, Luk KC, Manfredsson FP, Kanaan NM, Lipton JW, Collier TJ, Steece-Collier K, Kemp CJ, Celano S, Schulz E, *et al* (2015) Intrastriatal injection of pre-formed mouse α-synuclein fibrils into rats triggers α-synuclein pathology and bilateral nigrostriatal degeneration. *Neurobiol Dis* 82: 185–199

Pedersen CC, Lange J, Førland MGG, Macleod AD, Alves G & Maple-Grødem J (2021) A systematic review of associations between common SNCA variants and clinical heterogeneity in Parkinson’s disease. *NPJ Parkinsons Dis* 7: 54

Picard M, Shirihai OS (2022) Mitochondrial signal transduction. *Cell Metab* 34: 1620–1653

Pietrocola F, Galluzzi L, Bravo-San Pedro José M, Madeo F, Kroemer G (2015) Acetyl Coenzyme A: A Central Metabolite and Second Messenger. *Cell Metab* 21: 805–821

Pihlstrøm L, Axelsson G, Bjørnarå KA, Dizdar N, Fardell C, Forsgren L, Holmberg B, Larsen JP, Linder J, Nissbrandt H *et al* (2013) Supportive evidence for 11 loci from genome-wide association studies in Parkinson's disease. *Neurobiol Aging* 34: 1708.e1707–1713

Plotegher N, Gratton E, Bubacco L (2014) Number and Brightness analysis of alpha-synuclein oligomerization and the associated mitochondrial morphology alterations in live cells. *Biochim Biophys Acta* 1840: 2014–2024

Polinski NK, Volpicelli-Daley LA, Sortwell CE, Luk KC, Cremades N, Gottler LM, Froula J, Duffy MF, Lee VMY, Martinez TN *et al* (2018) Best Practices for Generating and Using Alpha-Synuclein Pre-Formed Fibrils to Model Parkinson's Disease in Rodents. *J Parkinsons Dis* 8: 303–322

Polymeropoulos MH, Lavedan C, Leroy E, Ide SE, Dehejia A, Dutra A, Pike B, Root H, Rubenstein J, Boyer R *et al* (1997) Mutation in the alpha-synuclein gene identified in families with Parkinson's disease. *Science* 276: 2045–2047

Powell SK, O'Shea C, Townsley K, Prytkova I, Dobrindt K, Elahi R, Iskhakova M, Lambert T, Valada A, Liao W *et al* (2023) Induction of dopaminergic neurons for neuronal subtype-specific modeling of psychiatric disease risk. *Mol Psychiatry* 28: 1970–1982

Pringsheim T, Jette N, Frolkis A, Steeves TD (2014) The prevalence of Parkinson's disease: a systematic review and meta-analysis. *Mov Disord* 29: 1583–1590

Pujols J, Peña-Díaz S, Conde-Giménez M, Pinheiro F, Navarro S, Sancho J, Ventura S (2017) High-Throughput Screening Methodology to Identify Alpha-Synuclein Aggregation Inhibitors. *Int J Mol Sci* 18: 478

Puspita L, Chung SY & Shim J (2017) Oxidative stress and cellular pathologies in Parkinson's disease. *Mol Brain* 10: 53

Qi LS, Larson MH, Gilbert LA, Doudna JA, Weissman JS, Arkin AP, Lim WA (2013) Repurposing CRISPR as an RNA-guided platform for sequence-specific control of gene expression. *Cell* 152: 1173–1183

Real R, Martinez-Carrasco A, Reynolds RH, Lawton MA, Tan MMX, Shoai M, Corvol J-C, Ryten M, Bresner C, Hubbard L, *et al* (2023) Association between the LRP1B and APOE loci and the development of Parkinson's disease dementia. *Brain* 146: 1873–1887

Reeve AK, Ludtmann MH, Angelova PR, Simcox EM, Horrocks MH, Klenerman D, Gandhi S, Turnbull DM, Abramov AY (2015) Aggregated α-synuclein and complex I deficiency: exploration of their relationship in differentiated neurons. *Cell Death Dis* 6: e1820–e1820

Replogle JM, Bonnar JL, Pogson AN, Liem CR, Maier NK, Ding Y, Russell BJ, Wang X, Leng K, Guna A *et al* (2022) Maximizing CRISPRi efficacy and accessibility with dual-sgRNA libraries and optimal effectors. *eLife* 11: e81856

Ritz B, Rhodes SL, Bordelon Y & Bronstein J (2012) α-Synuclein Genetic Variants Predict Faster Motor Symptom Progression in Idiopathic Parkinson Disease. *PLOS ONE* 7: e36199

Rizig M, Bandres-Ciga S, Makarious MB, Ojo OO, Crea PW, Abiodun OV, Levine KS, Abubakar SA, Achoru CO, Vitale D *et al* (2023) Identification of genetic risk loci and causal insights associated with Parkinson's disease in African and African admixed populations: a genome-wide association study. *Lancet Neurol* 22: 1015–1025

Robak LA, Jansen IE, van Rooij J, Uitterlinden AG, Kraaij R, Jankovic J, Heutink P, Shulman JM (2017) Excessive burden of lysosomal storage disorder gene variants in Parkinson's disease. *Brain* 140: 3191–3203

Rogov VV, Suzuki H, Marinković M, Lang V, Kato R, Kawasaki M, Buljubašić M, Šprung M, Rogova N, Wakatsuki S *et al* (2017) Phosphorylation of the mitochondrial autophagy receptor Nix enhances its interaction with LC3 proteins. *Sci Rep* 7: 1131

Röntgen A, Toprakcioglu Z, Morris OM, Vendruscolo M (2025) Amyloid-β modulates the phase separation and aggregation of α-synuclein. *Proc Nat Acad Sci USA* 122: e2501987122

Rosa F, Dhingra A, Uysal B, Mendis GDC, Loeffler H, Elsen G, Mueller S, Schwarz N, Castillo-Lizardo M, Cuddy C *et al* (2020) In Vitro Differentiated Human Stem Cell-Derived Neurons Reproduce Synaptic Synchronicity Arising during Neurodevelopment. *Stem Cell Rep* 15: 22–37

Rosenbluh J, Xu H, Harrington W, Gill S, Wang X, Vazquez F, Root DE, Tsherniak A, Hahn WC (2017) Complementary information derived from CRISPR Cas9 mediated gene deletion and suppression. *Nature Commun* 8: 15403

Ross-Thriepland D, Bornot A, Butler L, Desai A, Jaiswal H, Peel S, Hunter MR, Odunze U, Isherwood B, Gianni D (2020) Arrayed CRISPR Screening Identifies Novel Targets That Enhance the Productive Delivery of mRNA by MC3-Based Lipid Nanoparticles. *SLAS Discov* 25: 605–617

Rossi A, Kontarakis Z, Gerri C, Nolte H, Hölper S, Krüger M, Stainier DYR (2015) Genetic compensation induced by deleterious mutations but not gene knockdowns. *Nature* 524: 230–233

Rousseaux MWC, Vázquez-Vélez GE, Al-Ramahi I, Jeong H-H, Bajić A, Revelli J-P, Ye H, Phan ET, Deger JM, Perez AM *et al* (2018) A Druggable Genome Screen Identifies Modifiers of α-Synuclein Levels via a Tiered Cross-Species Validation Approach. *J Neurosci* 38: 9286–9301

Rowlands J, Moore DJ (2024) VPS35 and retromer dysfunction in Parkinson's disease. *Philos. Trans. R. Soc. B Biol. Sci* 379: 20220384

Russo MJ, Orru CD, Concha-Marambio L, Giaisi S, Groveman BR, Farris CM, Holguin B, Hughson AG, LaFontant D-E, Caspell-Garcia C, *et al* (2021) High diagnostic performance of independent alpha-synuclein seed amplification assays for detection of early Parkinson's disease. *Acta Neuropathol Commun* 9: 179

Ryan BJ, Bengoa-Vergniory N, Williamson M, Kirkiz E, Roberts R, Corda G, Sloan M, Saqlain S, Cherubini M, Poppinga J *et al* (2021) REST Protects Dopaminergic Neurons from Mitochondrial and α-Synuclein Oligomer Pathology in an Alpha Synuclein Overexpressing BAC-Transgenic Mouse Model. *J Neurosci* 41: 3731–3746

Ryan SD, Dolatabadi N, Chan SF, Zhang X, Akhtar MW, Parker J, Soldner F, Sunico CR, Nagar S, Talantova M *et al* (2013) Isogenic human iPSC Parkinson's model shows nitrosative stress-induced dysfunction in MEF2-PGC1α transcription. *Cell* 155: 1351–1364

Ryan T, Bamm VV, Stykel MG, Coackley CL, Humphries KM, Jamieson-Williams R, Ambasudhan R, Mosser DD, Lipton SA, Harauz G *et al* (2018) Cardiolipin exposure on the outer mitochondrial membrane modulates α-synuclein. *Nat Commun* 9: 817

Samaranch L, Lorenzo-Betancor O, Arbelo JM, Ferrer I, Lorenzo E, Irigoyen J, Pastor MA, Marrero C, Isla C, Herrera-Henriquez J *et al* (2010) PINK1-linked parkinsonism is associated with Lewy body pathology. *Brain* 133: 1128–1142

Sanchez-Martinez A, Martinez A, Whitworth AJ (2023) FBXO7/ntc and USP30 antagonistically set the ubiquitination threshold for basal mitophagy and provide a target for Pink1 phosphorylation in vivo. *PLoS Biol* 21: e3002244

Sanchez CG, Acker CM, Gray A, Varadarajan M, Song C, Cochran NR, Paula S, Lindeman A, An S, McAllister G *et al* (2021) Genome-wide CRISPR screen identifies protein pathways modulating tau protein levels in neurons. *Commun Biol* 4: 736

Sandor C, Robertson P, Lang C, Heger A, Booth H, Vowles J, Witty L, Bowden R, Hu M, Cowley SA *et al* (2017) Transcriptomic profiling of purified patient-derived dopamine neurons identifies convergent perturbations and therapeutics for Parkinson's disease. *Hum Mol Genet* 26: 552–566

Sanson KR, Hanna RE, Hegde M, Donovan KF, Strand C, Sullender ME, Vaimberg EW, Goodale A, Root DE, Piccioni F *et al* (2018) Optimized libraries for CRISPR-Cas9 genetic screens with multiple modalities. *Nat Commun* 9: 5416

Santhosh Kumar S, Naseri NN, Pather SR, Hallacli E, Ndayisaba A, Buenaventura C, Acosta K, Roof J, Fazelinia H, Spruce LA *et al* (2024) Sequential CRISPR screening reveals partial NatB inhibition as a strategy to mitigate alpha-synuclein levels in human neurons. *Sci Adv* 10: eadj4767

Saramowicz K, Siwecka N, Galita G, Kucharska-Lusina A, Rozpędek-Kamińska W, Majsterek I (2023) Alpha-Synuclein Contribution to Neuronal and Glial Damage in Parkinson's Disease. *Int J Mol Sci* 25

Sarraf SA, Raman M, Guarani-Pereira V, Sowa ME, Huttlin EL, Gygi SP, Harper JW (2013) Landscape of the PARKIN-dependent ubiquitylome in response to mitochondrial depolarization. *Nature* 496: 372–376

Satake W, Nakabayashi Y, Mizuta I, Hirota Y, Ito C, Kubo M, Kawaguchi T, Tsunoda T, Watanabe M, Takeda A *et al* (2009) Genome-wide association study identifies common variants at four loci as genetic risk factors for Parkinson's disease. *Nat Genet* 41: 1303–1307

Saunders-Pullman R, Mirelman A, Alcalay RN, Wang C, Ortega RA, Raymond D, Mejia-Santana H, Orbe-Reilly M, Johannes BA, Thaler A, *et al* (2018) Progression in the LRRK2-Associated Parkinson Disease Population. *JAMA Neurol* 75: 312–319

Sazanov LA (2015) A giant molecular proton pump: structure and mechanism of respiratory complex I. *Nat Rev Mol Cell Biol* 16: 375–388

Schaeffer E, Kluge A, Schulte C, Deuschle C, Bunk J, Welzel J, Maetzler W & Berg D (2024) Association of Misfolded α-Synuclein Derived from Neuronal Exosomes in Blood with Parkinson's Disease Diagnosis and Duration. *J Parkinson's Dis* 14: 667–679

Schapira AH, Cooper JM, Dexter D, Clark JB, Jenner P, Marsden CD (1990a) Mitochondrial complex I deficiency in Parkinson's disease. *J Neurochem* 54: 823–827

Schapira AHV, Mann VM, Cooper JM, Dexter D, Daniel SE, Jenner P, Clark JB, Marsden CD (1990b) Anatomic and Disease Specificity of NADH CoQ1 Reductase (Complex I) Deficiency in Parkinson's Disease. *J Neurochem* 55: 2142–2145

Schmidt R, Steinhart Z, Layeghi M, Freimer JW, Bueno R, Nguyen VQ, Blaeschke F, Ye CJ, Marson A (2022) CRISPR activation and interference screens decode stimulation responses in primary human T cells. *Science* 375: eabj4008

Schmidt SI, Okarmus J, Madsen DA, Hansen JS, Gregersen E, Gram H, Winkelmann LS, Oliveira AS, Heon-Roberts R, Ryan BJ *et al* (2025) Formation of seeding-competent α-synuclein aggregates in parkin-deficient iPSC-derived human neurons. *NPJ Parkinsons Dis* 11: 180

Scholz K, Pattanayak R, Ekkatine R, Pair FS, Nobles A, Stone WJ, Yacoubian TA (2025) Rab27b Promotes Lysosomal Function and Alpha-Synuclein Clearance in Neurons. *J Neurosci* 45

Schweers RL, Zhang J, Randall MS, Loyd MR, Li W, Dorsey FC, Kundu M, Opferman JT, Cleveland JL, Miller JL *et al* (2007) NIX is required for programmed mitochondrial clearance during reticulocyte maturation. *Proc Nat Acad Sci USA* 104: 19500–19505

Serdiuk T, Fleischmann Y, Ghosh D, Delparente A, Reber V, Frey L, Rhyner D, Gerez J, Volkmar N, Kralickova L *et al* (2025) Alpha-synuclein interacts with regulators of ATP homeostasis in mitochondria. *Nat Commun* 16: 7651

Shahmoradian SH, Lewis AJ, Genoud C, Hench J, Moors TE, Navarro PP, Castaño-Díez D, Schweighauser G, Graff-Meyer A, Goldie KN *et al* (2019) Lewy pathology in Parkinson's disease consists of crowded organelles and lipid membranes. *Nat Neurosci* 22: 1099–1109

Shahnawaz M, Mukherjee A, Pritzkow S, Mendez N, Rabadia P, Liu X, Hu B, Schmeichel A, Singer W, Wu G, *et al* (2020) Discriminating α-synuclein strains in Parkinson's disease and multiple system atrophy. *Nature* 578: 273–277

Shalem O, Sanjana NE, Hartenian E, Shi X, Scott DA, Mikkelsen TS, Heckl D, Ebert BL, Root DE, Doench JG *et al* (2014) Genome-Scale CRISPR-Cas9 Knockout Screening in Human Cells. *Science* 343: 84–87

Shaltouki A, Hsieh CH, Kim MJ, Wang X (2018) Alpha-synuclein delays mitophagy and targeting Miro rescues neuron loss in Parkinson's models. *Acta Neuropathol* 136: 607–620

Sheta R, Teixeira M, Idi W, Pierre M, de Rus Jacquet A, Emond V, Zorca CE, Vanderperre B, Durcan TM, Fon EA *et al* (2022) Combining NGN2 programming and dopaminergic patterning for a rapid and efficient generation of hiPSC-derived midbrain neurons. *Sci Rep* 12: 17176

Shiba-Fukushima K, Ishikawa K-I, Inoshita T, Izawa N, Takanashi M, Sato S, Onodera O, Akamatsu W, Okano H, Imai Y *et al* (2017) Evidence that phosphorylated ubiquitin signaling is involved in the etiology of Parkinson's disease. *Hum Mol Genet* 26: 3172–3185

Sidransky E, Nalls MA, Aasly JO, Aharon-Peretz J, Annesi G, Barbosa ER, Bar-Shira A, Berg D, Bras J, Brice A *et al* Multicenter Analysis of Glucocerebrosidase Mutations in Parkinson's Disease. *N Engl J Med* 361: 1651–1661

Siekevitz P (1957) Powerhouse of the Cell. *Sci Am* 197: 131–144

Simón-Sánchez J, Schulte C, Bras JM, Sharma M, Gibbs JR, Berg D, Paisan-Ruiz C, Lichtner P, Scholz SW, Hernandez DG *et al* (2009) Genome-wide association study reveals genetic risk underlying Parkinson's disease. *Nat Genet* 41: 1308–1312

Simuni T, Chahine LM, Poston K, Brumm M, Buracchio T, Campbell M, Chowdhury S, Coffey C, Concha-Marambio L, Dam T *et al* (2024) A biological definition of neuronal α-synuclein disease: towards an integrated staging system for research. *Lancet Neurol* 23: 178–190

Singh F, Prescott AR, Rosewell P, Ball G, Reith AD, Ganley IG (2021) Pharmacological rescue of impaired mitophagy in Parkinson's disease-related LRRK2 G2019S knock-in mice. *eLife* 10: e67604

Singleton AB, Farrer M, Johnson J, Singleton A, Hague S, Kachergus J, Hulihan M, Peuralinna T, Dutra A, Nussbaum R *et al* (2003) α-Synuclein Locus Triplication Causes Parkinson's Disease. *Science* 302: 841–841

Smith L, Schapira AHV (2022) GBA Variants and Parkinson Disease: Mechanisms and Treatments. *Cells* 11

Soutar MPM, Melandri D, O'Callaghan B, Annuario E, Monaghan AE, Welsh NJ, D'Sa K, Guelfi S, Zhang D, Pittman A *et al* (2022) Regulation of mitophagy by the NSL complex underlies genetic risk for Parkinson's disease at 16q11.2 and MAPT H1 loci. *Brain* 145: 4349–4367

Sowter HM, Ratcliffe PJ, Watson P, Greenberg AH, Harris AL (2001) HIF-1-dependent regulation of hypoxic induction of the cell death factors BNIP3 and NIX in human tumors. *Cancer Res* 61: 6669–6673

Spillantini MG, Crowther RA, Jakes R, Hasegawa M, Goedert M (1998) α-Synuclein in filamentous inclusions of Lewy bodies from Parkinson's disease and dementia with Lewy bodies. *Proc Nat Acad Sci USA* 95: 6469–6473

Spillantini MG, Schmidt ML, Lee VMY, Trojanowski JQ, Jakes R, Goedert M (1997) α-Synuclein in Lewy bodies. *Nature* 388: 839–840

Spinelli JB, Haigis MC (2018) The multifaceted contributions of mitochondria to cellular metabolism. *Nat Cell Biol* 20: 745–754

Spinelli JB, Yoon H, Ringel AE, Jeanfavre S, Clish CB, Haigis MC (2017) Metabolic recycling of ammonia via glutamate dehydrogenase supports breast cancer biomass. *Science* 358: 941–946

Staats R, Michaels TCT, Flagmeier P, Chia S, Horne RI, Habchi J, Linse S, Knowles TPJ, Dobson CM, Vendruscolo M (2020) Screening of small molecules using the inhibition of oligomer formation in α-synuclein aggregation as a selection parameter. *Commun Chem* 3: 191

Step K, Leal TP, Waldo E, Madula L, Swart Y, Hernández CF, Kim JJ, Bandres-Ciga S, Program GPsG, Mata IF *et al* (2025) Genome-wide association analyses reveal susceptibility variants linked to Parkinson's disease in the South African population using inferred global and local ancestry. *medRxiv*: 2025.2008.2001.25331910

Strappazzon F, Nazio F, Corrado M, Cianfanelli V, Romagnoli A, Fimia GM, Campello S, Nardacci R, Piacentini M, Campanella M *et al* (2015) AMBRA1 is able to induce mitophagy via LC3 binding, regardless of PARKIN and p62/SQSTM1. *Cell Death Differ* 22: 419–432

Strezoska Ž, Perkett MR, Chou ET, Maksimova E, Anderson EM, McClelland S, Kelley ML, Vermeulen A, Smith AvB (2017) High-content analysis screening for cell cycle regulators using arrayed synthetic crRNA libraries. *J Biotechnol* 251: 189–200

Su YC, Qi X (2013) Inhibition of excessive mitochondrial fission reduced aberrant autophagy and neuronal damage caused by LRRK2 G2019S mutation. *Hum Mol Genet* 22: 4545–4561

Sun W, Schulte C, Gasser T & Tan M (2025) TMEM175, SCARB2 and CTSB associations with Parkinson's disease risk across populations. *NPJ Parkinsons Dis* 11: 348

Sun X, Dou K, Xue L, Xie Y, Yang Y & Xie A (2024) Comprehensive analysis of clinical and biological features in Parkinson's disease associated with the LRRK2 G2019S mutation: Data from the PPMI study. *Clin Transl Sci* 17: e13720

Svanbergsson A, Ek F, Martinsson I, Rodo J, Liu D, Brandi E, Haikal C, Torres-Garcia L, Li W, Gouras G *et al* (2021) FRET-Based Screening Identifies p38 MAPK and PKC Inhibition as Targets for Prevention of Seeded α-Synuclein Aggregation. *Neurotherapeutics* 18: 1692–1709

Szklarczyk D, Nastou K, Koutrouli M, Kirsch R, Mehryary F, Hachilif R, Hu D, Peluso ME, Huang Q, Fang T, *et al* (2025) The STRING database in 2025: protein networks with directionality of regulation. *Nucleic Acids Res* 53: D730–D737

Szwedo AA, Pedersen CC, Ushakova A, Forsgren L, Tysnes O-B, Counsell CE, Alves G, Lange J, Macleod AD & Maple-Grødem J (2020) Association of SNCA Parkinson's Disease Risk Polymorphisms With Disease Progression in Newly Diagnosed Patients. *Front Neurol* 11: 620585

Takanashi M, Li Y, Hattori N (2016) Absence of Lewy pathology associated with PINK1 homozygous mutation. *Neurology* 86: 2212–2213

Tam V, Patel N, Turcotte M, Bossé Y, Paré G & Meyre D (2019) Benefits and limitations of genome-wide association studies. *Nat Rev Genet* 20: 467–484

Tan J, Martin SE (2016) Validation of Synthetic CRISPR Reagents as a Tool for Arrayed Functional Genomic Screening. *PLoS ONE* 11: e0168968

Tang FL, Erion JR, Tian Y, Liu W, Yin DM, Ye J, Tang B, Mei L, Xiong WC (2015) VPS35 in Dopamine Neurons Is Required for Endosome-to-Golgi Retrieval of Lamp2a, a Receptor of Chaperone-Mediated Autophagy That Is Critical for α-Synuclein Degradation and Prevention of Pathogenesis of Parkinson's Disease. *J Neurosci* 35: 10613–10628

Tan MMX, Lawton MA, Jabbari E, Reynolds RH, Iwaki H, Blauwendraat C, Kanavou S, Pollard MI, Hubbard L, Malek N, *et al* (2021) Genome-Wide Association Studies of Cognitive and Motor Progression in Parkinson's Disease. *Mov Disord* 36: 424–433

Tan MMX, Lawton MA, Pollard MI, Brown E, Real R, Carrasco AM, Bekadar S, Jabbari E, Reynolds RH, Iwaki H, *et al* (2024) Genome-wide determinants of mortality and motor progression in Parkinson's disease. *NPJ Parkinsons Dis* 10: 113

Tanaka M, Kim YM, Lee G, Junn E, Iwatsubo T & Mouradian MM (2004) Aggresomes Formed by α-Synuclein and Synphilin-1 Are Cytoprotective*. *J Biol Chem* 279: 4625–4631

Tanik SA, Schultheiss CE, Volpicelli-Daley LA, Brunden KR, Lee VM (2013) Lewy body-like α-synuclein aggregates resist degradation and impair macroautophagy. *J Biol Chem* 288: 15194–15210

Tanner CM, Kamel F, Ross GW, Hoppin JA, Goldman SM, Korell M, Marras C, Bhudhikanok GS, Kasten M, Chade AR *et al* (2011) Rotenone, paraquat, and Parkinson's disease. *Environ Health Perspect* 119: 866–872

Tanner CM, Ottman R, Goldman SM, Ellenberg J, Chan P, Mayeux R, Langston JW (1999) Parkinson disease in twins: an etiologic study. *JAMA* 281: 341–346

Tanudjojo B, Shaikh SS, Fenyi A, Bousset L, Agarwal D, Marsh J, Zois C, Heman-Ackah S, Fischer R, Sims D *et al* (2021) Phenotypic manifestation of α-synuclein strains derived from Parkinson's disease and multiple system atrophy in human dopaminergic neurons. *Nat Commun* 12: 3817

Tarutani A, Suzuki G, Shimozawa A, Nonaka T, Akiyama H, Hisanaga S, Hasegawa M (2016) The Effect of Fragmented Pathogenic α-Synuclein Seeds on Prion-like Propagation. *J Biol Chem* 291: 18675–18688

The Global Parkinson's Genetics P, Leonard HL (2025) Novel Parkinson's Disease Genetic Risk Factors Within and Across European Populations. *medRxiv*: 2025.2003.2014.24319455

Thoma EC, Wischmeyer E, Offen N, Maurus K, Sirén A-L, Schartl M, Wagner TU (2012) Ectopic Expression of Neurogenin 2 Alone is Sufficient to Induce Differentiation of Embryonic Stem Cells into Mature Neurons. *PLoS ONE* 7: e38651

Tian R, Abarientos A, Hong J, Hashemi SH, Yan R, Dräger N, Leng K, Nalls MA, Singleton AB, Xu K *et al* (2021) Genome-wide CRISPRi/a screens in human neurons link lysosomal failure to ferroptosis. *Nat Neurosci* 24: 1020–1034

Tian R, Gachechiladze MA, Ludwig CH, Laurie MT, Hong JY, Nathaniel D, Prabhu AV, Fernandopulle MS, Patel R, Abshari M *et al* (2019) CRISPR Interference-Based Platform for Multimodal Genetic Screens in Human iPSC-Derived Neurons. *Neuron* 104: 239–255.e212

Toomey CE, Heywood WE, Evans JR, Lachica J, Pressey SN, Foti SC, Al Shahrani M, D'Sa K, Hargreaves IP, Heales S *et al* (2022) Mitochondrial dysfunction is a key pathological driver of early stage Parkinson's. *Acta Neuropathol Commun* 10: 134

Toulorge D, Schapira AHV, Hajj R (2016) Molecular changes in the postmortem parkinsonian brain. *J Neurochem* 139: 27–58

Tran J, Anastacio H, Bardy C (2020) Genetic predispositions of Parkinson's disease revealed in patient-derived brain cells. *NPJ Parkinson's Dis* 6: 8

Tropea TF, Mak J, Guo MH, Xie SX, Suh E, Rick J, Siderowf A, Weintraub D, Grossman M, Irwin D, *et al* (2019) TMEM106B Effect on cognition in Parkinson disease and frontotemporal dementia. *Ann Neurology* 85: 801–811

Tsubouchi A, An Y, Kawamura Y, Yanagihashi Y, Nakayama H, Murata Y, Teranishi K, Ishiguro S, Aburatani H, Yachie N *et al* (2024) Pooled CRISPR screening of high-content cellular phenotypes using ghost cytometry. *Cell Rep Methods* 4

Tsujimura A, Taguchi K, Watanabe Y, Tatebe H, Tokuda T, Mizuno T, Tanaka M (2015) Lysosomal enzyme cathepsin B enhances the aggregate forming activity of exogenous α-synuclein fibrils. *Neurobiol Dis* 73: 244–253

Twig G, Elorza A, Molina AJ, Mohamed H, Wikstrom JD, Walzer G, Stiles L, Haigh SE, Katz S, Las G *et al* (2008) Fission and selective fusion govern mitochondrial segregation and elimination by autophagy. *EMBO J* 27: 433–446

Valdés P, Mercado G, Vidal RL, Molina C, Parsons G, Court FA, Martinez A, Galleguillos D, Armentano D, Schneider BL *et al* (2014) Control of dopaminergic neuron survival by the unfolded protein response transcription factor XBP1. *Proc Nat Acad Sci USA* 111: 6804–6809

Valente EM, Abou-Sleiman PM, Caputo V, Muqit MM, Harvey K, Gispert S, Ali Z, Del Turco D, Bentivoglio AR, Healy DG *et al* (2004) Hereditary early-onset Parkinson's disease caused by mutations in PINK1. *Science* 304: 1158–1160

van Duijn CM, Dekker MC, Bonifati V, Galjaard RJ, Houwing-Duistermaat JJ, Snijders PJ, Testers L, Breedveld GJ, Horstink M, Sandkuijl LA *et al* (2001) Park7, a novel locus for autosomal recessive early-onset parkinsonism, on chromosome 1p36. *Am J Hum Genet* 69: 629–634

Van Laar AD, Webb KR, Keeney MT, Van Laar VS, Zharikov A, Burton EA, Hastings TG, Glajch KE, Hirst WD, Greenamyre JT *et al* (2023) Transient exposure to rotenone causes degeneration and progressive parkinsonian motor deficits, neuroinflammation, and synucleinopathy. *NPJ Parkinsons Dis* 9: 121

Vanderperre B, Muraleedharan A, Dorion M-F, Larroquette F, Del Cid Pellitero E, Rajakulendran N, Chen CX-Q, Larivière R, Michaud-Tardif C, Chidiac R *et al* (2024) A genome-wide CRISPR/Cas9 screen identifies genes that regulate the cellular uptake of α-synuclein fibrils by modulating heparan sulfate proteoglycans. *bioRxiv*: 2023.2009.2029.560170

Volpicelli-Daley LA, Luk KC, Lee VMY (2014) Addition of exogenous α-synuclein preformed fibrils to primary neuronal cultures to seed recruitment of endogenous α-synuclein to Lewy body and Lewy neurite–like aggregates. *Nat Protoc* 9: 2135–2146

Volpicelli-Daley Laura A, Luk Kelvin C, Patel Tapan P, Tanik Selcuk A, Riddle Dawn M, Stieber A, Meaney David F, Trojanowski John Q, Lee Virginia MY (2011) Exogenous α-Synuclein Fibrils Induce Lewy Body Pathology Leading to Synaptic Dysfunction and Neuron Death. *Neuron* 72: 57–71

Wald NJ, Old R (2019) The illusion of polygenic disease risk prediction. *Genet Med* 21: 1705–1707

Wall CE, Rose CM, Adrian M, Zeng YJ, Kirkpatrick DS, Bingol B (2019) PPEF2 Opposes PINK1-Mediated Mitochondrial Quality Control by Dephosphorylating Ubiquitin. *Cell Rep* 29: 3280–3292.e3287

Walsh CT, Tu BP, Tang Y (2018) Eight Kinetically Stable but Thermodynamically Activated Molecules that Power Cell Metabolism. *Chem Rev* 118: 1460–1494

Walton RT, Singh A, Blainey PC (2022) Pooled genetic screens with image-based profiling. *Mol Syst Biol* 18: e10768

Wang C, Ward ME, Chen R, Liu K, Tracy TE, Chen X, Xie M, Sohn PD, Ludwig C, Meyer-Franke A *et al* (2017) Scalable Production of iPSC-Derived Human Neurons to Identify Tau-Lowering Compounds by High-Content Screening. *Stem Cell Rep* 9: 1221–1233

Wang S, DeLeon C, Sun W, Quake SR, Roth BL, Südhof TC (2024) Alternative splicing of latrophilin-3 controls synapse formation. *Nature* 626: 128–135

Wang T, Birsoy K, Hughes NW, Krupczak KM, Post Y, Wei JJ, Lander ES, Sabatini DM (2015) Identification and characterization of essential genes in the human genome. *Science* 350: 1096–1101

Wang T, Wei JJ, Sabatini DM, Lander ES (2014) Genetic Screens in Human Cells Using the CRISPR-Cas9 System. *Science* 343: 80–84

Wang X, Becker K, Levine N, Zhang M, Lieberman AP, Moore DJ, Ma J (2019) Pathogenic alpha-synuclein aggregates preferentially bind to mitochondria and affect cellular respiration. *Acta Neuropathol Commun* 7: 41

Watanabe Y, Tatebe H, Taguchi K, Endo Y, Tokuda T, Mizuno T, Nakagawa M, Tanaka M (2013) p62/SQSTM1-Dependent Autophagy of Lewy Body-Like α-Synuclein Inclusions. *PLoS ONE* 7: e52868

Wauters F, Cornelissen T, Imberechts D, Martin S, Koentjoro B, Sue C, Vangheluwe P, Vandenberghe W (2020) LRRK2 mutations impair depolarization-induced mitophagy through inhibition of mitochondrial accumulation of RAB10. *Autophagy* 16: 203–222

Weiner WJ (2008) There is no Parkinson disease. *Arch Neurol* 65: 705–708

Weston LJ, Bowman AM, Osterberg VR, Meshul CK, Woltjer RL, Unni VK (2022) Aggregated Alpha-Synuclein Inclusions within the Nucleus Predict Impending Neuronal Cell Death in a Mouse Model of Parkinsonism. *Int J Mol Sci* 23

Wiedenheft B, Sternberg SH, Doudna JA (2012) RNA-guided genetic silencing systems in bacteria and archaea. *Nature* 482: 331–338

Williamson MG, Heon-Roberts R, Franks SNJ, Mock E, Jones HBL, Britti E, Malpartida A, Bassal M, Lavelle M, Connor J *et al* (2025) USP30 inhibition improves mitochondrial health through both PINK1-dependent and independent mechanisms. *bioRxiv*: 2025.2002.2003.636341

Williamson MG, Madureira M, McGuinness W, Heon-Roberts R, Mock ED, Naidoo K, Cramb KML, Caiazza M-C, Malpartida AB, Lavelle M *et al* (2023) Mitochondrial dysfunction and mitophagy defects in LRRK2-R1441C Parkinson's disease models. *Hum Mol Genet* 32: 2808–2821

Winder-Rhodes SE, Evans JR, Ban M, Mason SL, Williams-Gray CH, Foltynie T, Duran R, Mencacci NE, Sawcer SJ & Barker RA (2013) Glucocerebrosidase mutations influence the natural history of Parkinson's disease in a community-based incident cohort. *Brain* 136: 392–399

Winslow AR, Chen CW, Corrochano S, Acevedo-Arozena A, Gordon DE, Peden AA, Lichtenberg M, Menzies FM, Ravikumar B, Imarisio S *et al* (2010) α-Synuclein impairs macroautophagy: implications for Parkinson's disease. *J Cell Biol* 190: 1023–1037

Wu D, Poddar A, Ninou E, Hwang E, Cole MA, Liu SJ, Horlbeck MA, Chen J, Replogle JM, Carosso GA *et al* (2022) Dual genome-wide coding and lncRNA screens in neural induction of induced pluripotent stem cells. *Cell Genom* 2

Xu S, Chen M, Feng T, Zhan L, Zhou L, Yu G (2021) Use ggbreak to Effectively Utilize Plotting Space to Deal With Large Datasets and Outliers. *Front Genet* Volume 12 – 2021

Xue C, Lin TY, Chang D & Guo Z (2017) Thioflavin T as an amyloid dye: fibril quantification, optimal concentration and effect on aggregation. *R Soc Open Sci* 4: 160696

Xue Y, Zhan X, Sun S, Karuppagounder SS, Xia S, Dawson VL, Dawson TM, Laterra J, Zhang J, Ying M (2019) Synthetic mRNAs Drive Highly Efficient iPS Cell Differentiation to Dopaminergic Neurons. *Stem Cells Transl Med* 8: 112–123

Yamashita S-i, Sugiura Y, Matsuoka Y, Maeda R, Inoue K, Furukawa K, Fukuda T, Chan DC, Kanki T (2024) Mitophagy mediated by BNIP3 and NIX protects against ferroptosis by downregulating mitochondrial reactive oxygen species. *Cell Death Differ* 31: 651–661

Yang Y, Ouyang Y, Yang L, Beal MF, McQuibban A, Vogel H, Lu B (2008) Pink1 regulates mitochondrial dynamics through interaction with the fission/fusion machinery. *Proc Nat Acad Sci USA* 105: 7070–7075

Yang Y, Shi Y, Schweighauser M, Zhang X, Kotecha A, Murzin AG, Garringer HJ, Cullinane PW, Saito Y, Foroud T *et al* (2022) Structures of α-synuclein filaments from human brains with Lewy pathology. *Nature* 610: 791–795

Yap TL, Gruschus JM, Velayati A, Westbroek W, Goldin E, Moaven N, Sidransky E, Lee JC (2011) α-Synuclein Interacts with Glucocerebrosidase Providing a Molecular Link between Parkinson and Gaucher Diseases*. *J Biol Chem* 286: 28080–28088

Yin JA, Frick L, Scheidmann MC, Liu T, Trevisan C, Dhingra A, Spinelli A, Wu Y, Yao L, Vena DL *et al* (2025) Arrayed CRISPR libraries for the genome-wide activation, deletion and silencing of human protein-coding genes. *Nat Biomed Eng* 9: 127–148

Yin Y, Liu Y, Xu M, Zhang X & Li C (2021) Association of COMT rs4680 and MAO-B rs1799836 polymorphisms with levodopa-induced dyskinesia in Parkinson's disease—a meta-analysis. *Neurol Sci* 42: 4085–4094

Youle RJ, van der Bliek AM (2012) Mitochondrial Fission, Fusion, and Stress. *Science* 337: 1062–1065

Yu M, Ye H, De-Paula RB, Mangleburg CG, Wu T, Lee TV, Li Y, Duong D, Phillips B, Cruchaga C *et al* (2023) Functional screening of lysosomal storage disorder genes identifies modifiers of alpha-synuclein neurotoxicity. *PLOS Genet* 19: e1010760

Yuki KE, Marei H, Fiskin E, Eva MM, Gopal AA, Schwartzentruber JA, Majewski J, Cellier M, Mandl JN, Vidal SM *et al* (2019) CYRI/FAM49B negatively regulates RAC1-driven cytoskeletal remodelling and protects against bacterial infection. *Nat Microbiol* 4: 1516–1531

Zambon F, Cherubini M, Fernandes HJR, Lang C, Ryan BJ, Volpato V, Bengoa-Vergniory N, Vingill S, Attar M, Booth HDE *et al* (2019) Cellular α-synuclein pathology is associated with bioenergetic dysfunction in Parkinson's iPSC-derived dopamine neurons. *Hum Mol Genet* 28: 2001–2013

Zhang F, Wu Z, Long F, Tan J, Gong N, Li X, Lin C (2022) The Roles of ATP13A2 Gene Mutations Leading to Abnormal Aggregation of α-Synuclein in Parkinson's Disease. *Front Cell Neurosci* 16: 927682

Zhang Y, Pak C, Han Y, Ahlenius H, Zhang Z, Chanda S, Marro S, Patzke C, Acuna C, Covy J *et al* (2013) Rapid single-step induction of functional neurons from human pluripotent stem cells. *Neuron* 78: 785–798

Zimprich A, Biskup S, Leitner P, Lichtner P, Farrer M, Lincoln S, Kachergus J, Hulihan M, Uitti RJ, Calne DB *et al* (2004) Mutations in LRRK2 cause autosomal-dominant parkinsonism with pleomorphic pathology. *Neuron* 44: 601–607